2-27-2018 2:30 PM

Calcium Isotopes in Natural and Experimental Carbonated Silicate Melts

Matthew Maloney, *The University of Western Ontario*

Supervisor: Bouvier, Audrey, *The University of Western Ontario*
Co-Supervisor: Withers, Tony, *The University of Western Ontario*
A thesis submitted in partial fulfillment of the requirements for the Master of Science degree in Geology

Abstract

The calcium stable isotopic compositions of mantle-sourced rocks and minerals were investigated to better understand the carbon cycle in the Earth's mantle. Bulk carbonatites and kimberlites were analyzed to identify a geochemical signature of carbonatite magmatism, while inter-mineral fractionation was measured in co-existing Ca-bearing carbonate and silicate minerals. Bulk samples show a range of composition deviating from the bulk silicate Earth $\delta^{44/40}$Ca composition indicating signatures of magmatic processes or marine carbonate addition to source materials. $\Delta^{44/40}Ca_{carbonate\text{-}silicate}$ values range from -0.55‰ to +1.82‰ and positively correlate with Ca/Mg ratios in pyroxenes. A series of experiments designed to equilibrate clinopyroxene with carbonated melts of varying compositions were conducted to constrain the systematics of Ca isotopic fractionation in these systems. Results show significant fractionation between phases, with $\delta^{44/40}$Ca in Cpx ranging from +0.37 to +2.75‰ heavier than quenched melts. However, the influence of thermal diffusion on these results is not fully understood.

Keywords

Calcium Isotopes, Stable Isotopic Fractionation, Experiment, Carbonatites, Kimberlites, Peridotites, Carbonatite Magmatism, Mantle Geochemistry,

Acknowledgements

First and foremost, I must thank my co-supervisors Dr. Audrey Bouvier and Dr. Tony Withers for giving me the opportunity to study here at Western and for providing me with continued guidance and support throughout this project. In addition to being model examples of what it takes to be a successful scientist, you have taught me the skills that are required to be an independent, critical thinker. You have challenged me to be a better researcher and a better person.

I want to thank Dr. R. Bastian Georg for providing me with many hours of patient support and assistance while teaching me how to use the Neptune at the Trent Water Quality Centre and for conducting my strontium and iron isotopic analyses. You made the many trips to Trent University more enjoyable and infinitely more successful, and I always looked forward to the dinner at St. Veronus that became a tradition.

Thank you to the staff and fellow students with whom I have shared the GEOMETRIC clean lab during my time here, whether it was assistance with a specific task, or simply some company during a long day (and/or night) running columns. A special thanks to Blair Gibson for his assistance operating the ICPMS and conducting the major, minor, and trace element analyses for many of my samples.

Finally, I would like to thank my family for always being there for me throughout the many long years of academic endeavours; I would not be here without you. Thank you to all the great friends I have been lucky to make while here at Western, you made this experience better than I could have hoped. And a very special thank you to my partner, Heather. You gave me the encouragement to pursue my goals and the support to achieve them.

Table of Contents

Abstract i

Acknowledgements ii

Table of Contents iii

List of Tables vii

List of Figures x

Chapter 1 1

1. Introduction 1

1.1 Earth's Carbon Cycle 1

1.2 Carbonate Melts and Carbon-Rich Rocks 2

1.2. Carbonatites 4

1.3 High-Pressure and High-Temperature Experimental Work 7

1.3.1 Experiments on the Origin of Carbonatites and Carbon-Bearing Melts 8

1.3.2 Experiments Using Geochemical Tracers 14

1.3.3 Experimental Determination of Stable Isotope Fractionation 15

1.3.4 Thermal Diffusion 18

1.4 Isotope Geochemistry 20

1.4.1 Calcium Isotopes 20

1.5 Thesis Objectives 28

Chapter 2 29

2. Methods & Analytical Techniques 29

2.1 Sample Selection 29

2.2 Natural Sample Preparation 29

2.3 Experimental Sample Design and Preparation 30

2.4 Electron Probe Microanalyses 34
2.5 Silicate Mineral Acid Leaching Procedure 34
2.6 Sample Dissolution Procedure 35
2.7 Calcium Purification 36
2.8 Iron Purification 40
2.9 Quadrupole Inductively Couple Plasma Mass Spectrometry (ICP-MS) 41
2.10 Multi-Collector Inductively Coupled Plasma Mass Spectrometry (MC-ICP-MS) 42
Chapter 3 46
3. Sample Descriptions 46
3.1 Carbonatites 46
3.1.1 Oka Carbonatites 46
3.1.2 Phalaborwa Carbonatites 47
3.1.3 Lueshe Carbonatite 48
3.1.4 Nemegos Carbonatite 48
3.1.5 Cape Verde Archipelago Carbonatites 49
3.1.6 Tamazert Massif (Morocco) Carbonatites 50
3.2 Kimberlites and Related Rocks 50
3.2.1 Kimberley Area Kimberlite 51
3.2.2 Kaapvaal Craton Peridotites 51
3.3 External Standards 52
3.3.1 San Carlos Peridotite 52
3.3.2 Kilbourne Hole Peridotite 53
3.3.3 BCR-2 53
3.4 Other Samples 54
3.4.1 Bancroft Marble 54

3.4.2 Twin Sisters Ultramafic Complex 55
Chapter 4 56
4. Results 56
4.1 Microprobe Data 56
4.2 XRF Data 59
4.3 Minor and Trace Element Data 59
4.4 Calcium Isotopic Data for Natural Samples 61
4.4.1 SRM915b and External Standards 62
4.4.2 Carbonatites 65
4.4.3 Kimberlites and Related Samples 68
4.4.4 Other Natural Samples 70
4.4.5 Coexisting Carbonates and Pyroxenes 72
4.5 Strontium Isotopic Data for Natural Samples 74
4.6 Experimental Results 76
4.6.1 Clinopyroxene + Carbonate Melt Experiments 77
4.6.2 Clinopyroxene + Silicate Melt Experiment 84
4.6.3 Clinopyroxene + Carbonated Silicate Melt Experiments 85
4.6.4 Iron Isotope Data 93
Chapter 5 96
5. Discussion 96
5.1 Natural Samples 96
5.1.1 Bulk Carbonatites 96
5.1.2 Cape Verde and Tamazert Carbonatites 100
5.1.3 Bulk Kimberlites and Related Peridotites 103
5.1.4 Carbonate – Pyroxene Fractionation 105

5.1.5 Olivine – Pyroxene Fractionation 108
5.2 Experimental Work 109
5.2.1 Attainment of Equilibrium 109
5.2.2 Experimentally Determined Fractionation Factors 110
5.2.3 Ca-O Bond Lengths 111
5.2.4 Experimental Pyroxenes vs. Melts as a Proxy for BSE vs. Basalts 114
5.2.5 Temperature Effect 116
5.2.6 Thermal Diffusion 119
Chapter 6 128
6 Conclusion 128
6.1 Future Natural Sample Work 129
6.2 Future Experiments 130
References 132
Appendix A 149
Appendix B 152
Curriculum Vitae 158

List of Tables

Table 1 - Possible deep carbon reservoirs. Table redrawn from Hazen et al., (2012). 3
Table 2 - Experiment Starting Materials in wt% 31
Table 3 - Experiment ID's, run conditions and apparatus used for all the experiments conducted in this study. 32
Table 4 - Step 1 calcium purification procedure 37
Table 5 - Step 2 calcium purification procedure 37
Table 6 - Preliminary calcium purification procedure for very low Ca samples 39
Table 7 - Iron purification procedure 41
Table 8 - Oka carbonatite samples included in this study. 46
Table 9 - Phalaborwa carbonatite samples included in this study. 47
Table 10 - Lueshe carbonatite samples included in this study. 48
Table 11 - Nemegos carbonatite samples included in this study. 49
Table 12 - Cape Verde carbonatite samples included in this study. 50
Table 13 - Tamazert carbonatites included in this study. 50
Table 14 - Kimberley kimberlites included in this study. 51
Table 15 - Kaapvaal peridotites included in this study. 52
Table 16 - San Carlos peridotite samples included in this study. 52
Table 17 - Kilbourne Hole peridotites included in this study. 53
Table 18 - Major element concentrations in USGS reference material BCR-2. Table redrawn from Wilson (1997) 54
Table 19 - Bancroft marble samples included in this study. 54
Table 20 - Twin Sisters peridotite samples included in this study. 55
Table 21 - Major element compositions of carbonate mineral separates from carbonatite samples in this study. CO_2 totals were calculated by difference. 56
Table 22 - Major element compositions for silicate mineral separates from carbonatite samples in this study. 57
Table 23 - Major element compositions of carbonate and silicate mineral separates from Kimberley kimberlite and Kaapvaal peridotite samples in this study. CO_2 totals were calculated by difference. 57

Table 24 - Major element compositions of carbonate and silicate mineral separates from Bancroft marble samples in this study. CO_2 totals were calculated by difference. 58
Table 25 - Major element compositions of silicate mineral separates for Twin Sisters and Kilbourne Hole peridotite samples in this study. 58
Table 26 - Major element concentrations of bulk rock samples analyzed using XRF in this study (in %). BDL = Below Detection Limit. 59
Table 27 - Minor and trace element concentrations of bulk rock samples in this study (all concentrations in parts per million). 60
Table 28 – $\delta^{44/42}$Ca values for SRM915b samples analyzed in this study. 62
Table 29 - Calcium isotopic compositions of external standards analyzed in this study. Published values for San Carlos and Kilbourne Hole samples are from Huang et al. (2010), published value for BCR-2 is from Valdes et al. (2014). 64
Table 30 – Calcium isotopic composition of carbonatites analyzed in this study. 65
Table 31 – Calcium isotopic compositions of kimberlites and related samples analyzed in this study. 69
Table 32 – Calcium isotopic compositions of other natural samples analyzed in this study..... 70
Table 33 – Calcium isotopic compositions of coexisting pyroxene and carbonate minerals analyzed in this study. 73
Table 34 – Bulk rock $^{87}Sr/^{86}Sr$ ratios of samples in this study. 75
Table 35 - Major element compositions of Cpx + Carbonate Melt experiments. CO_2 wt.% in quenched melt calculated by difference. 80
Table 36 - Calcium isotopic composition of Cpx + Carbonate Melt experiments. 81
Table 37 - Major element compositions of Cpx + Silicate Melt experiment. H_2O content of melt phase calculated by difference 84
Table 38 - Calcium isotopic composition of Cpx + Silicate Melt experiment. 85
Table 39 - Major element compositions of Cpx + Carbonated Silicate Melt experiments. CO_2 wt.% in melt phases calculated by difference. 88
Table 40 - Calcium isotopic compositions of Cpx + Carbonated Silicate Melt experiments..... 89
Table 41 - Iron isotopic compositions of Cpx + Carbonated Silicate Melt experiments..... 93
Table 42 - Estimated amounts of ancient marine carbonate added to the mantle source for Cape Verde and Tamazert carbonatites and the amount of the total Ca budget contributed by this

carbonate addition. Calculations are based on the calcium isotopic compositions measured in this study paired with the models and theory from Huang et al. (2011)..... 102
Table 43 - Crystals-Quenched melt fractionation factors for experimental samples..... 110
Table 44 - Estimated Ca-O bond lengths for Ca-bearing minerals and melts. Opx, Cpx, and calcite bond lengths are from Huang et al. (2010), carbonate melt bond length from Genge et al. (1995), silicate melt bond length estimated from Sun et al. (2011)..... 111
Table 45 - Estimated rates of change to $\delta^{44/40}$Ca and $\delta^{57/54}$Fe caused by thermal diffusion compared to data from this study..... 122
Table 46 – Estimated temperature variation within experimental capsules calculated based on the measured $\Delta^{44/40}Ca_{crystals\text{-}melt}$ in this study and effect of thermal diffusion driven fractionation for calcium isotopes averaged from Richter et al. (2009) and Huang et al. (2010)..... 124

List of Figures

Figure 1 - Carbonatite classification diagram. Redrawn from Woolley and Kempe (1989). 5
Figure 2 - Experiments in the carbonated peridotite system showing the carbonate ledge. (a) illustrates the basic topology and (b) illustrates the effect of bulk silicate composition. Figure from Hammouda and Keshav (2015). 9
Figure 3 - Overview of the carbon geodynamical cycle, illustrating areas where carbonatite melts may occur. Figure from Hammouda and Keshav (2015). 12
Figure 4 - Comparison of $^{26}Mg/^{24}Mg$ fractionation factors for magnesite-forsterite (Mgs-Fo), orthopyroxene-forsterite (Opx-Fo), and spinel-forsterite (Sp-Fo) mineral pairs. Figure from Young et al., (2015). 16
Figure 5 - Fe-O bond length increases with coordination number in high-temperature Fe-bearing minerals. Figure redrawn from Sossi and O'Neill, (2017). 17
Figure 6 - $\Delta^{57}Fe_{mineral\text{-}fluid}$ decreases with increased Fe-O bond length. The increased $\Delta^{57}Fe_{mineral\text{-}fluid}$ of magnetite is due to its higher oxidation state. Figure redrawn from Sossi and O'Neill, (2017). 18
Figure 7 - Correlated major element fractionations caused by thermal diffusion. Figure from Richter et al., (2009) 19
Figure 8 - Summary of published Ca isotope data compiled and presented in Fantle and Tipper (2014). Figure redrawn from Fantle and Tipper (2014). 23
Figure 9 – $\delta^{44/40}Ca$ vs. Ca-O bond length in low temperature minerals (calcite, aragonite, barite) calculated using mineral-seawater fractionation factors from Gussone et al., (2005) and Griffith et al., (2008), and coexisting Opx and Cpx in mantle peridotites measured by Huang et al., (2010). Figure redrawn from Huang et al. (2010). 25
Figure 10 - Compilation of published terrestrial and meteorite Ca data (excluding low temperature terrestrial systems). Vertical red line indicates the average $\delta^{44/40}Ca$ value for terrestrial basalts (+0.90 ± 0.04‰, Valdes et al., 2014), vertical blue line indicates the average $\delta^{44/40}Ca$ value for the BSE (+1.05 ± 0.04‰, Huang et al. 2010), and vertical yellow line indicates the average $\delta^{44/40}Ca$ value for seawater (+1.92 ± 0.20‰, Fantle and Tipper, 2014). Data and sources are given in Appendix A and Appendix B. Any data that was not reported as $\delta^{44/40}Ca$ relative to SRM915a in the original source was converted using the methods given in Chapter 2 or using conversion values from Fantle and Tipper, (2014).... 27

Figure 11 - Photographs taken while opening experiment B797. Left image shows a cluster of clinopyroxene crystals removed from the capsule, the image on the right shows the open capsule with fragments of quenched melt and Cpx crystals inside. For scale: diameter of the capsule is 3 mm. 33
Figure 12 - Photographs taken while opening experiment M824. Left image shows crystals within the open capsule, the image on the right shows the transition from crystals to quenched melt within the capsule. For scale: diameter of the capsule is 3 mm. 33
Figure 13 - Elution curve for calcium purification step 1 38
Figure 14 - Elution curve for calcium purification step 2 38
Figure 15 - Elution curve for low Ca samples preliminary cation exchange column matrix removal step. 40
Figure 16 - SRM915b long-term reproducibility. Red line indicates the average of all measurements (0.00 ± 0.07‰, N = 16). 44
Figure 17 - San Carlos clinopyroxenes were used as external standards in this study to test the accuracy of the chemical purification methods. Each replicate matched the published value from Huang et al. (2010) within error. 45
Figure 18 - Chondrite normalized rare-earth element spider plots for samples in this study: A) Lueshe carbonatite, Nemegos carbonatite, and Bancroft marble samples; B) Oka carbonatite samples; C) Phalaborwa carbonatite samples; D) Kimberley kimberlite and Kaapvaal peridotite samples. Normalizing values for chondrite are from McDonough and Sun (1995). 61
Figure 19 - Long-term reproducibility of SRM915b standard over duration of this study (0.00 ± 0.07‰, n = 16). 63
Figure 20 - Ca isotope data for external standards in this study compared to previously published values. 65
Figure 21 - Ca isotope data for carbonatite samples. Squares = bulk rock samples, Circles = carbonates, Diamonds = pyroxenes, Triangles = apatite. 67
Figure 22 - Ca isotope data for bulk rock carbonatite samples grouped by locality. 68
Figure 23 - Ca isotope data for kimberlites and related peridotite samples 69
Figure 24 - Ca isotope data for other natural samples 71

Figure 25 - Ca isotopic composition of San Carlos and Kilbourne Hole olivine mineral separates compared to coexisting clinopyroxenes and orthopyroxenes. 72
Figure 26 – Ca isotope data for coexisting carbonate and pyroxene mineral separates 74
Figure 27 - Comparison of $\delta^{44/40}$Ca vs. $^{87}Sr/^{86}Sr$ values in bulk rock samples analyzed in this study. 76
Figure 28 - Schematic of typical experimental capsule and resulting phases. 77
Figure 29 - BSE images of all Cpx + Carbonate Melt experiments. 'X' suffix indicates crystals, 'M' suffix indicates quenched melt, 'G' suffix indicates glassy quenched melt in experiment B798. White patch in the image for B796-X is the result of a gas bubble that formed on the surface of the sample during analysis and does not reflect a compositional change in the Cpx crystals. Scale bars are provided but vary for each image. 79
Figure 30 - Ca isotopic data for Cpx + Carbonate Melt experiments 82
Figure 31 - Ca isotopic data for pyroxenes compared to quenched melt in Cpx + Carbonate Melt experiments 82
Figure 32 – $\delta^{44/40}$Ca difference between crystals and quenched melt as a function of temperature in Cpx + Carbonate Melt experiments 83
Figure 33 - $\delta^{44/40}$Ca difference between crystals and quenched melt as a function of sample mass in Cpx + Carbonate Melt experiments 83
Figure 34 - BSE images for Cpx + Silicate Melt experiment. 84
Figure 35 - Ca isotope data for Cpx + Silicate Melt experiment 85
Figure 36 - BSE images for all Cpx + Carbonated Silicate Melt experiments. Experiment M824 images were taken during a different session and therefore differences in colour or shade compared to the other experiments do not necessarily reflect differences in composition. The image for Cbt-02-M also includes a smaller fragment of Cpx crystal, the quenched melt is the larger fragment. Scale bars are provided for each image. Cpx = clinopyroxene, Opx = orthopyroxene, Gt = Garnet. 87
Figure 37 - Ca isotope data for Cpx + Carbonated Silicate Melt experiments. 90
Figure 38 - $\delta^{44/40}$Ca difference between crystals and quenched melt as a function of temperature in Cpx + Carbonated Silicate Melt experiments. 90
Figure 39 - $\delta^{44/40}$Ca difference between crystals and quenched melt as a function of sample mass in Cpx + Carbonated Silicate Melt experiments. 91

Figure 40 - $\delta^{44/40}$Ca difference between crystals and quenched melt as a function of pressure in Cpx + Carbonated Silicate Melt experiments. 92
Figure 41 - $\delta^{44/40}$Ca difference between crystals and quenched melt in experiment Cbt-01 and the effect of leaching on crystals. 92
Figure 42 - Fe isotope data for Cpx + Carbonated Silicate Melt experiments reported as $\delta^{57/54}$Fe. 94
Figure 43 – $\Delta^{44/40}$Ca vs. $\Delta^{57/54}$Fe in Cpx + Carbonated Silicate Melt experiments. 95
Figure 44 - Bulk rock $\delta^{44/40}$Ca values for carbonatites in this study compared to the BSE $\delta^{44/40}$Ca value of Huang et al. (2010). 97
Figure 45 – Positive correlation between Lu and Yb concentrations and $\delta^{44/40}$Ca values in Oka carbonatite bulk rock samples. 98
Figure 46 - Positive correlation between Lu and Yb concentrations and $\delta^{44/40}$Ca values in Oka carbonatite and Nemegos carbonatite bulk rock samples with HIMU type mantle reservoir origins. 99
Figure 47 – $^{87}Sr/^{86}Sr$ ratios vs $\delta^{44/40}$Ca values for bulk carbonatite samples in this study. Estimated Sr ratio ranges for mantle reservoirs overlain (Zindler and Hart, 1986). DM = Depleted Mantle, HIMU = High μMantle, EM I = Enriched Mantle I, EM II = Enriched Mantle II. 100
Figure 48 - Bulk rock $\delta^{44/40}$Ca values for Cape Verde and Tamazert carbonatites in this study compared to the BSE $\delta^{44/40}$Ca value of Huang et al. (2010). 102
Figure 49 - Estimated amounts of ancient marine carbonate added to Cape Verde and Tamazert carbonatites with 0% and 5% end members plotted for reference. 103
Figure 50 - Bulk rock $\delta^{44/40}$Ca values for Kimberley kimberlite (R841) and Kaapvaal peridotite (16962) in this study compared to the BSE $\delta^{44/40}$Ca value of Huang et al. (2010). 104
Figure 51 - Positive correlation between Lu and Yb concentrations and $\delta^{44/40}$Ca values in Kimberley kimberlite and Kaapvaal peridotite bulk rock samples with EM I type mantle reservoir origins. 104
Figure 52 - Positive correlation between Ca/Mg ratio in pyroxene and $\Delta^{44/40}Ca_{carbonate\text{-}pyroxene}$ .. 107
Figure 53 - Positive correlation between Ca/Mg ratio in pyroxene and $\Delta^{44/40}Ca_{carbonate\text{-}pyroxene}$ with extrapolated estimate for Opx. 108
Figure 54 - Negative correlation between Ca/Mg ratio in Opx and $\Delta^{44/40}Ca_{Opx\text{-}Olivine}$. 109

Figure 55 - Positive correlation between Ca-O bond length and $\delta^{44/40}$Ca for all experiments conducted. 113
Figure 56 – $\delta^{44/40}$Ca values for BSE vs. terrestrial basalt average compared to the average $\delta^{44/40}$Ca values for Cpx vs. quenched melt in experiments. 115
Figure 57 - Systematic trends in ultramafic rock $\delta^{44/40}$Ca data compared to basalts. Data from Amini et al. (2009). 115
Figure 58 - Positive correlation between temperature and $\Delta^{44/40}Ca_{crystals\text{-}melt}$ in Cpx + Carbonated Silicate Melt experiments.....117
Figure 59 - Positive correlation between temperature and $\Delta^{44/40}Ca_{crystals\text{-}melt}$ in Cpx + Carbonate Melt experiments.....117
Figure 60 - Positive correlation between sample mass and $\Delta^{44/40}Ca_{crystals\text{-}melt}$ in Cpx + Carbonate Melt experiments. 118
Figure 61 - Temperature gradients within a piston-cylinder apparatus. Figure from Richter et al. (2009)..... 121
Figure 62 – $\Delta^{44/40}$Ca/$\Delta^{57/54}$Fe relationship for the Cpx + Carbonated Silicate Melt experiments in this study compared to the $\Delta^{44/40}$Ca/$\Delta^{57/54}$Fe caused by thermal diffusion according to Richter et al. (2009) and Huang et al. (2010) 123
Figure 63 - Schematic of two possible scenarios describing the temperature driven fractionation in high pressure experiments. 125

Chapter 1

1. Introduction

1.1 Earth's Carbon Cycle

Carbon is the basis of all biomolecules and inextricably linked to the sustainability of all life on Earth. Carbon-rich gases in the atmosphere (e.g. CO_2) affect Earth's variable climate conditions, while carbon-based fuels supply most of the energy that powers society. From food to plastics, strong structural materials to soft textiles, carbon plays a role in such a wide array of useful materials unmatched by any other element. However, despite its importance, the properties and behaviour of carbon-bearing systems more than several hundred meters beneath the Earth's surface remain poorly understood. Previous investigations of the global carbon cycle have focused primarily on shallow surface environments, oceans, and the atmosphere, with the understanding that these carbon reservoirs essentially act as a closed system. The transfer of carbon between biotic and abiotic reservoirs in the near surface carbon cycle is influenced by living systems, combustion of organic matter, burial of sediments, and transfer of CO_2 between the oceans and atmosphere (Berner, 2004). The distribution of near-surface fossil fuels and carbon-bearing rocks such as carbonates and organic-rich shales have been mapped, their abundances and ages estimated, and their contributions to the carbon cycle have been established. In contrast, relatively little is known about the deep interior carbon cycle, which may contain more than 90% of the Earth's total carbon (Javoy, 1997). Many major questions remain poorly constrained:

- What is the abundance of carbon in the Earth's deep interior?
- What reservoirs contain this carbon and what is the nature and extent of these reservoirs in time and space?
- How is carbon exchanged among reservoirs?
- What is the flux of carbon between the deep interior and the surface of the Earth?

Primitive chondritic meteorites, which are believed to be one proxy for the composition of the Earth at the time of its formation (Marty et al., 2013), contain several weight percent carbon. Yet the current, albeit not well constrained, estimates for Earth's total carbon are much lower. A better understanding of the deep carbon cycle through a comprehensive characterization of the

mantle carbon reservoirs may be part of the answer to this question of missing carbon. Possible deep carbon reservoirs include volumetrically large but diffuse reservoirs such as silicate minerals and melts and concentrated reservoirs such as carbonate magmas (Table 1).

The nature and extent of these various carbon reservoirs in Earth's interior is important for gaining a better overall understanding of carbon in the Earth. Further research and technological advances are still required to answer many of these questions about the abundance and mobility of deep carbon (Jones et al., 2013).

1.2 Carbonate Melts and Carbon-Rich Rocks

Carbonates have been identified as a possible deep carbon reservoir (Table 1) and carbonate melts could possibly play an important role in providing a vertical pathway for carbon transferral from the mantle to the surface of the Earth (Jones et al., 2013). The study of carbonate magmas and their related rocks could therefore aid in the characterization of deep carbon and its role in the global carbon cycle.

Table 1 - Possible deep carbon reservoirs. Table redrawn from Hazen et al., (2012).

Reservoir	Composition	Structure	[C] (mole %)	Depth (km)	Abundance (wt%)
Diamond	C	Diamond	100	>150	<<1
Graphite	C	Graphite	100	<150	<<1
Carbides	SiC, FeC, Fe_3C	Moissanite, Cohenite	25-50	?	?
Carbonates	$(Ca,Mg,Fe)CO_3$	Unknown	20	0 to ?	?
Metal	Fe,Ni	Kamecite/ Awaruite	Minor?	?	?
Silicates	Mg-Si-O	Various	Trace?	?	?
Oxides	Mg-Fe-O	Various	Trace?	?	?
Sulfides	Fe-S	Various	Trace?	?	?
Silicate Melts	Mg-Si-O		Trace?	?	?
CHON fluids	C-H-O-N		Variable	?	?
Methane	CH_4		20	?	?
Methane clathrate	$[H_2O+CH_4]$	Clathrate	Variable	?	?
Hydrocarbons	C_nH_{2n+2}		Variable	?	?
Organic species	C-H-O-N		Variable	?	?
Deep life	C-H-O-N-P-S		Variable	<15	?

Carbonate magmas are often temporally associated with alkaline silicate melts, but are distinguished by their unique physical properties. They have very high solubilities for elements that are typically rare in silicate melts, as well as for dissolved volatiles such as water and halogens. Carbonate melts remain mobile over a wide range of temperatures and are noted for their very low viscosity (Dobson et al., 1996; Wolff, 1994), implicating them in geochemical enrichment processes within the mantle related to metasomatism and making them efficient transporters of carbon from mantle to crust (Jones et al., 2013). They are also noted for their high electrical conductivity and their presence has been used to explain anomalously conductive regions in the mantle (Gaillard et al., 2008). Perhaps the most fundamental property of carbonate

melts is their atomic structure itself - ionic liquids consisting of metal cations and carbonate CO_3^{2-} molecular anions related via coulombic interactions. This sets them apart from silicate melts, which are characterized by polymerized network structures (Mysen, 1983).

Direct evidence of mantle carbonate sources is not well preserved at the Earth's surface. Oldoinyo Lengai in Tanzania is the only active carbonate volcano, but it erupts highly alkaline carbonate lavas that do not match the Ca-rich or Mg-rich carbonates found in other carbonatite occurrences worldwide (Chen et al., 2013). Therefore, carbonatite liquids must be studied using experimental methods and through investigations of rocks that are believed to have formed through interactions with carbon-rich magmas such as carbonatites and kimberlites.

1.2. Carbonatites

Carbonatites are magmatic rocks that contain more than 50 wt% carbonate minerals derived from carbonate magma (Streckeisen, 1980), less than 20% SiO_2 (Le Maitre, 2002), and high abundances of Sr, Ba, P, and light rare-earth elements (LREE), usually three or more orders of magnitude higher than chondritic meteorite values (Nelson et al., 1988). They can be subdivided based on their dominant carbonate mineral and corresponding major element geochemistry (Figure 1). Carbonatites often occur not just as one single rock unit but as a suite with alkaline silicate rocks, with only ~20% of carbonatite occurrences not having associated silicate rocks (Woolley and Kjarsgaard, 2008). Based on these associated silicate rocks, Mitchell (2005)

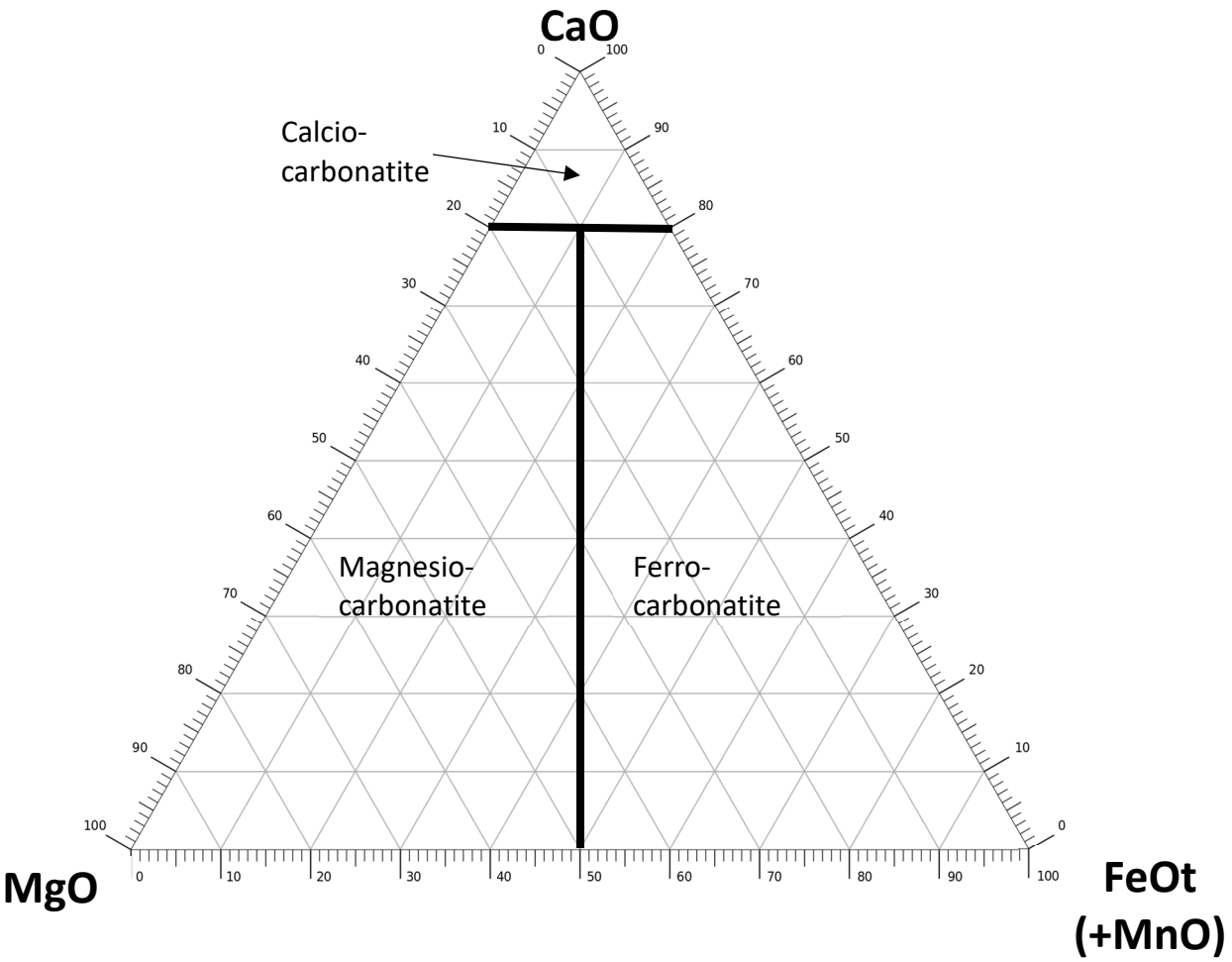

Figure 1 - Carbonatite classification diagram. Redrawn from Woolley and Kempe (1989).

further classifies magmatic carbonatites into groups associated with nephelinite, melilitite, kimberlite, and specific mantle-derived silicate magmas formed by partial melting.

Carbonatites are most commonly found in continental crust in stable, intraplate settings, many in regions that are peripheral to orogenic belts and often related to continental rift related tectonics (Veizer et al., 1992). However, there are increasing numbers of carbonatites reported from other tectonic settings such as oceanic islands, ophiolites, and deep subduction zones, and any understanding of the origins of carbonatites must be able to take these into account (Jones et al., 2013). Woolley and Kjarsgaard (2008) published a detailed and comprehensive world map of all known carbonatite occurrences to date. The ages of these carbonatite occurrences range from Archaean to present but appear to increase in frequency with decreasing age. The Phalaborwa carbonatite in South Africa is reported to be the oldest carbonatite at an age of 2063 to 2013 Ma (Masaki et al., 2005).

There is significant scientific evidence indicating a mantle origin for carbonatites including: Sr-Nd isotopic data, stable isotope compositions, noble gases and experimental phase equilibria (Jones et al., 2013). Steep LREE enriched patterns without significant europium anomalies are typical for carbonatites and consistent with mantle origins. The extremely low concentrations of Pb in carbonatites offers a clear distinction from crustal carbonates, and the Pb isotopic composition of carbonatites further indicates a lack of crustal contamination and could be used to explore the isotope geochemical signature of mantle carbon reservoirs (Jones et al., 2013). Even with substantial evidence for the mantle origin for carbonatites, the limit to their depth of origin is not known, but needs to be constrained since their possible existence in the lower mantle may have an important influence on the long-term storage and mobility of deep carbon (Kaminsky et al., 2009).

Despite the consensus that carbonatites originate in the mantle, one single theory for their formation has yet to be agreed upon (Jones et al., 2013). Currently, three main theories exist to explain the origin of carbonatites:

1. Residual melts of fractionated carbonated nephelinite or melilitite (Gittins 1989; Gittins and Jago 1998).
2. Immiscible melt fractions of CO_2-saturated silicate melts (Freestone and Hamilton, 1980; Amundsen, 1987; Kjarsgaard and Hamilton 1988, 1989; Brooker and Hamilton 1990; Kjarsgaard and Peterson 1991; Church and Jones 1995; Lee and Wyllie 1997; Dawson 1998; Halama at al., 2005; Brooker and Kjarsgaard, 2011).
3. Primary mantle melts generated through partial melting of CO_2-bearing peridotite (Wallace and Green 1988; Sweeney 1994; Harmer and Gittins 1998; Harmer et al., 1998; Ying et al., 2004; Dasgupta et al., 2004b).

Combinations of some or all three of these theories have also been proposed for carbonatite genesis (e.g. Yaxley and Brey, 2004). Despite the lack of consensus on the exact origin of carbonatites, their derivation from the mantle with minimal effects of crustal contamination make them powerful geochemical probes for understanding the Earth's mantle (Jones et al., 2013).

Geochemical analyses, experiments, and general observations have linked carbonatites to other ultramafic carbon-rich rocks, specifically kimberlites, and some have even obscured the

distinction between carbonatite and kimberlite volcanism (Sparks et al., 2009). Kimberlites are rare, highly alkaline, mantle-derived rocks found primarily within Archaean cratons and are the deepest terrestrial magmas best known as carriers of diamonds from deep within the Earth to the surface. Woolley and Bailey (2012) argue in favour of a direct link between carbonatites, kimberlites, and a common underlying source of deep mantle carbon. Evidence for a genetic link between carbonatites and kimberlites include:

- Shared geochemical trace element signatures (Hornig-Kjarsgaard, 1998; Le Roex et al., 2003),
- Experimentally determined relationship between group II kimberlites and carbonate melts in the same mantle source region (Ulmer and Sweeney, 2002), and
- Metasomatized mantle xenoliths that display a geochemical signature that is transitional between carbonatites and kimberlites (Jones, 1989).

However, there are others that argue against a genetic association between carbonatites and kimberlites (Anderson, 2008; Mitchell, 2005). Evidently there are still questions to answer regarding the petrogenesis of carbonatites and carbonate melts within the deep mantle that obscure our comprehension of the exact origin of carbonatites and their relationship to other mantle rocks, including kimberlites, the deepest known mantle magmas.

1.3 High-Pressure and High-Temperature Experimental Work

Despite the still evolving body of knowledge regarding the origin of carbonatites and carbon-bearing magmas in the Earth's mantle, much of what we do understand has been discovered through decades of experimental studies in high-pressure and high-temperature systems. Mantle pressures and temperatures can be achieved in laboratories using piston cylinder and multi-anvil experimental apparatus, allowing for carefully controlled experiments under mantle conditions. As a result, there is a significant amount of experimental evidence for the involvement of carbon in mantle magmatism.

1.3.1 Experiments on the Origin of Carbonatites and Carbon-Bearing Melts

Melting of carbonated peridotite and carbonate-silicate phase equilibria in this system is important for understanding the generation of magmas that require CO_2 such as carbonatites and kimberlites. Early experimental work in the carbonated peridotite system was conducted by Wyllie and co-workers and by Eggler and co-workers. The main finding of these early works was the transition in the type of melts that are generated, silicate melts formed in the low-pressure regions (<2 GPa) and carbonatite or kimberlite type melts formed in the high-pressure region (2-3 GPa). The transition in the type of melt that is produced appears to correspond with a distinct change in the slope of the carbonated peridotite solidus in the systems $MgO\text{-}SiO_2\text{-}CO_2$ ($MS\text{-}CO_2$), $CaO\text{-}MgO\text{-}SiO_2\text{-}CO_2$ ($CMS\text{-}CO_2$), and $CaO\text{-}MgO\text{-}Al_2O_3\text{-}SiO2\text{-}CO_2$ ($CMAS\text{-}CO_2$). The solidus for the model carbonated peridotite has a positive slope from 1 to 2 GPa, a negative slope above 2.5 GPa, and then a positive slope again as pressure is increased above 3 GPa (Figure 2) (Eggler, 1973, 1974, 1975, 1976; Wyllie and Huang, 1975a, 1975b, 1976a, 1976b). The negatively sloped region of the solidus is called the carbonate "ledge" (Eggler, 1987a, 1987b) and is the most pronounced feature in its topology. The classical peridotite-carbonate phase diagrams describe the reaction that occurs at the carbonate ledge as:

Clinopyroxene + Olivine + Vapour = Orthopyroxene + Carbonate Melt,

with the vapour-bearing assemblage on the low pressure/low temperature side of the ledge, and the melt-bearing assemblage on the high pressure/high temperature side of the ledge (Figure 2). Experimentally, the ledge can occur because the melting temperature of carbonated peridotite decreases by 200-300°C compared to dry peridotite when the vapour-carbonate reaction meets the model carbonated peridotite solidus curve (Wyllie and Huang, 1975a, 1975b, 1976a, 1976b). However, extensive debate followed regarding the details of this transition – the cause for such a transition, the exact pressure at which it occurs, and its sharpness.

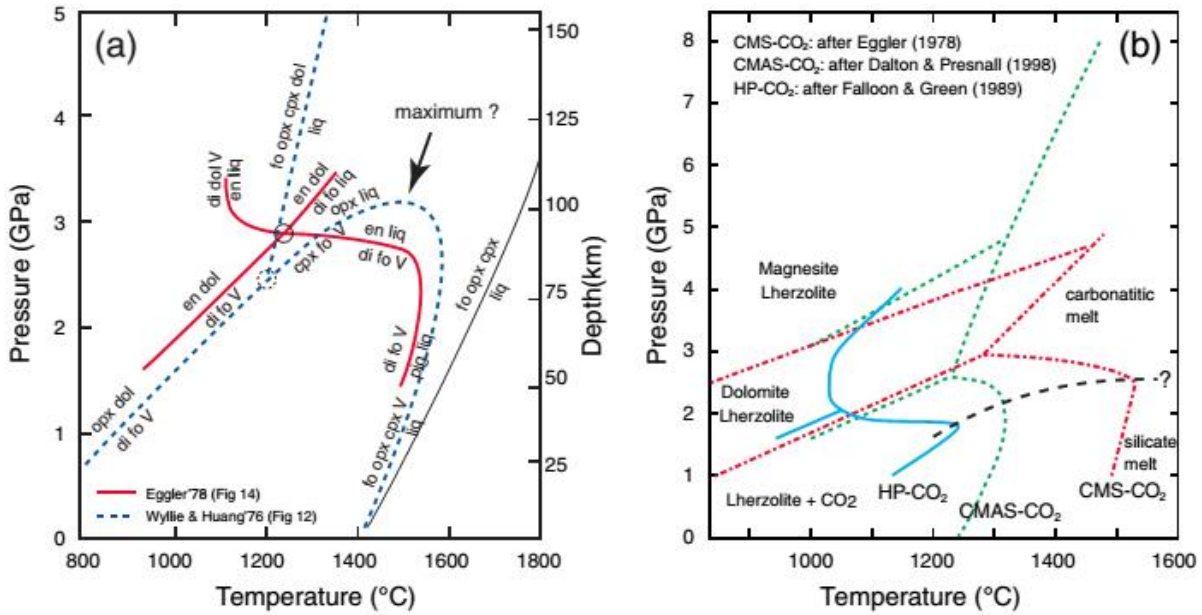

Figure 2 - Experiments in the carbonated peridotite system showing the carbonate ledge. (a) illustrates the basic topology and (b) illustrates the effect of bulk silicate composition. Figure from Hammouda and Keshav (2015).

The Wyllie and co-worker's interpretation of the carbonate ledge was that it was caused by an invariant point in P-T space at the intersection of two curves, where vapour, carbonate, and liquid all coexisted with mantle peridotite in the MS-CO_2 and CMS-CO_2 systems. This invariant point was also found in the CMAS-CO_2 system at approximately 2.6 GPa (Dalton and Presnall, 1998). Additional experimental studies of the carbonate ledge by Wyllie and Huang using the CMS-CO_2 system (1975a, 1975b) as well as the simpler MS-CO_2 system (1976a) indicated that the liquid that was in equilibrium with the other phases at this point was a model carbonatite (~40 wt.% CO_2). Therefore, they concluded that the liquid is a model carbonatite over the pressure range of approximately 2.5 to 4.4 GPa, only when P-T invariance occurs, and regardless of the system utilized. In their phase equilibria scheme, immediately before the liquid becomes a carbonatite, it is essentially basaltic in composition (White and Wyllie, 1992)

The interpretation of the carbonate ledge by Eggler and co-workers was that it was caused by the gradual increase in CO_2 solubility in the liquid between 2-3 GPa (Eggler, 1973, 1974, 1975, 1976, 1978). Starting at 2 GPa, the liquid was an undersaturated basalt with approximately 5 wt.% CO_2, but with increasing pressure the solubility of CO_2 in the liquid increased,

transitioning through a melilitic composition, and eventually to a kimberlitic composition between 2.6-3 GPa with ~20-25 wt.% CO_2 (Eggler 1976). This gradual transition across the carbonate ledge contrasts with the sharp transition suggested by Wyllie and co-workers.

More recent studies of the carbonate ledge using the CMAS-CO_2 system (Keshav and Gudfinnsson, 2013; Novella et al., 2014) also indicates that the amount of CO_2 in the melt increases between 1.9 and 2.1 GPa along the carbonated peridotite solidus, causing a shift from a silicate melt at 1.9 GPa to a carbonatite melt at 2.1 GPa. Both types of melts are in equilibrium with olivine, orthopyroxene, clinopyroxene, spinel, and vapour on the solidus. These studies suggest that the carbonated peridotite solidus meets a P-T invariance at 2 GPa, precisely where the carbonate ledge appears in the earlier works of Wyllie and Eggler, and it is this invariance that causes the ledge to occur. However, according to these works, the reason this invariance occurs at 2 GPa is because on either side of it there are two distinctly different melt compositions, therefore, the carbonate ledge is interpreted to be caused by the existence of two immiscible liquids (Novella et al., 2014).

The carbonate ledge essentially represents a barrier above which carbonates are no longer stable. This is because on the high-pressure side of the ledge (i.e. greater depths), CO_2 as a vapour does not remain stable as a vapour and instead reacts with silicates to form solid or molten carbonates, whereas on the lower pressure side of the ledge, decarbonation reactions occur and carbonates break down and release CO_2. This decarbonation reaction that occurs at the ledge can explain why carbonates are rarely found in mantle xenoliths (Canil, 1990), and can also prevent carbonatite magmas from reaching the Earth's surface (Dalton and Presnall, 1998). Although there are exceptions where very fast ascent rates can allow carbonatite magmas to escape degassing at the ledge, the carbonate ledge effectively provides an upper bound for the region of the mantle where carbonatite melts can exist.

Whereas the carbonate ledge provides the upper bound for the carbonatite melt present region in the Earth's mantle, a redox front provides the lower bound. The Enstatite + Magnesite = Olivine + Graphite/Diamond (EMOG/D) equilibrium defined by Eggler and Baker (1982) describes carbonate stability in relation to graphite or diamond as a function of oxygen fugacity. Carbon is stable as carbonate when the oxygen fugacity of the mantle is above the EMOG/D equilibrium, and it is stable as graphite or diamond (a reduced phase) when the oxygen fugacity of the mantle

is below EMOG/D. Since the oxygen fugacity of the mantle decreases with depth (Frost and McCammon, 2008), the region where oxidized carbon is stable as carbonate and can participate in melting is restricted to shallower depths (<150km). If carbonate in the mantle was to descend below this redox front, it would be reduced to graphite or diamond and any carbonate melt would undergo a process called 'redox freezing' (Rohrbach and Schmidt, 2011). This means that carbonate melts are not expected to exist at depths greater than 150km when Fe controlled redox conditions are dominant (Luth, 1999). However, there is the possibility that carbonate-bearing subducted slabs could allow for carbon controlled redox conditions to prevail, allowing for localized areas of oxidized carbon melting deeper in the mantle (Figure 3).

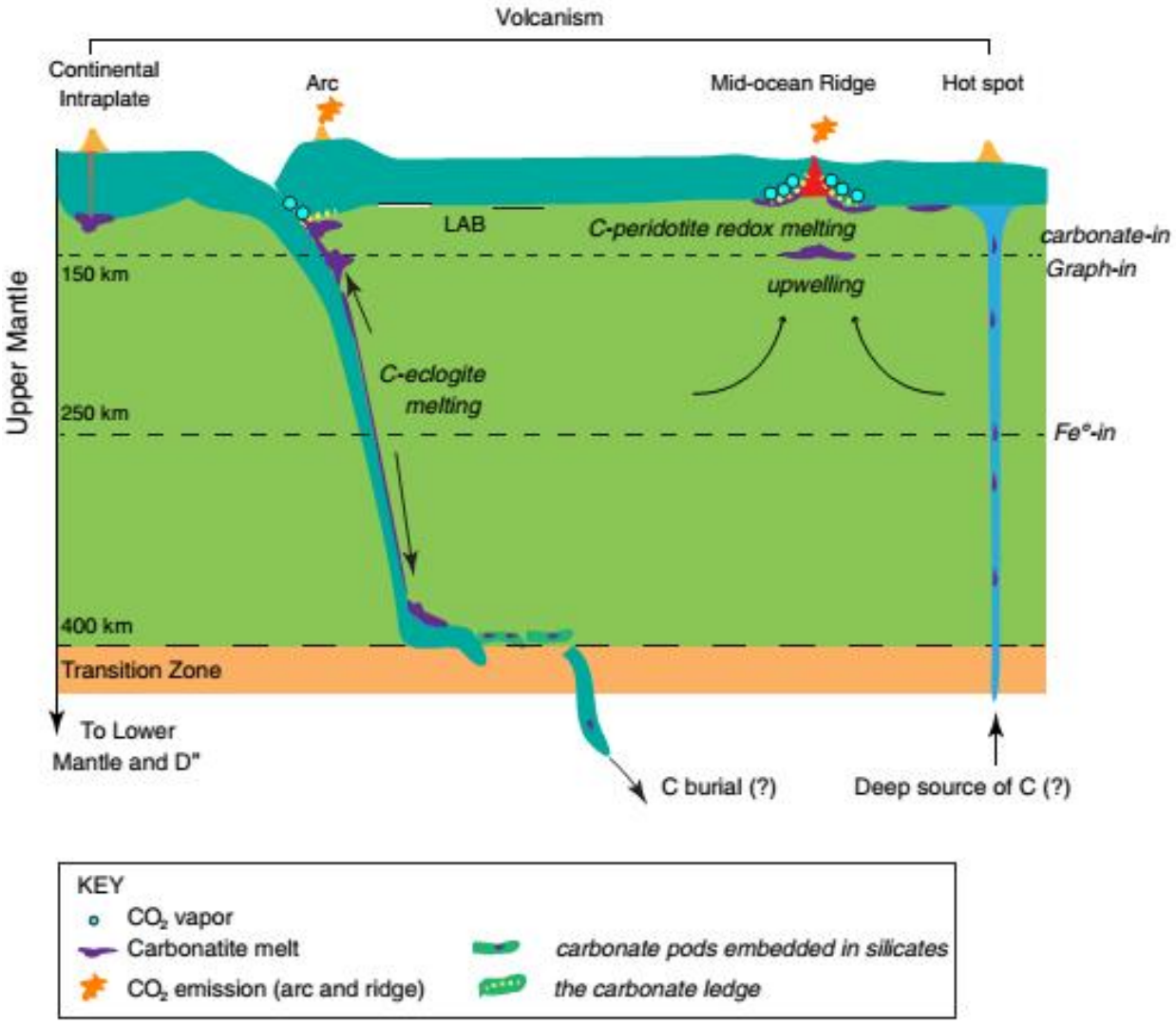

Figure 3 - Overview of the carbon geodynamical cycle, illustrating areas where carbonatite melts may occur. Figure from Hammouda and Keshav (2015).

Like the carbonated peridotite system, phase relations in the carbonated eclogite system are important for understanding carbon-rich magmas in Earth's mantle, but more specifically, the carbonated eclogite system is important in the context of subduction and carbonate recycling (Doucelance et al., 2010, 2014). Early experimental work (Yaxley and Green, 1994) determined that carbonates could be subducted to mantle depths greater than 100km, while more recent experimental studies have expanded on this hypothesis.

High-pressure and high-temperature experiments on carbonated eclogites can be more complex than those in the carbonated peridotite system and yield higher variance assemblages. Various experimental studies in the 3-10 GPa range have produced contrasting solidus temperatures and

melt compositions (Hammouda, 2003; Dasgupta et al., 2004a; Yaxley and Brey, 2004). This discrepancy is most likely caused by the variations in bulk compositions of the starting materials used by different experimenters. Regarding these differences, Dasgupta et al. (2004a) argue that there is no single unique solidus for the melting of carbonated eclogite because of the different amounts and compositions of carbonate that can be added during ocean floor alteration.

The carbonate ledge that was reported in the carbonated peridotite system, is identified in some, but not all, experiments on carbonated eclogites. However, the pressures at which the ledge was identified varied between experiments. Hammouda (2003) used a more silica-rich starting composition, produced coesite and stishovite in their run products, and observed the ledge at 5.5 GPa, while the experiments by Dasgupta et al. (2004b) yielded no silica phase in their run products and observed a ledge at lower pressures, much like the carbonated peridotite system. This supports the idea that the variations in results can be attributed to differences in bulk starting compositions, and suggests that the amount of silica in the experiments can have some influence on the carbonate ledge in this system.

The existence of the carbonate ledge in the carbonated eclogite system has a profound influence on the survival of carbonates in subducted slabs. Based on the different pressure temperature paths computed for hot versus cold subduction (van Keken et al., 2002), the fate of carbon carried in a subducting plate varies. For hot slab subduction (e.g. young oceanic lithosphere), the P-T path of the carbonates carried by the subducting plate crosses the solidus of the ledge due to its negative slope, suggesting that the carbon cycle would end at shallower depths in the Earth (<200km). However, in the case of cold slab subduction (e.g. old continental lithosphere), it is possible that carbonates in the subducting plate could reach much greater depths. One possible implication of these studies is that the melting of carbonated eclogite could be a potential source of continental carbonatites, while carbonated peridotite is a more likely source of magmatic carbon in oceanic regions (Dasgupta et al., 2004b).

Adding to the body of research on carbonatite melts in carbonated peridotite and eclogite systems, recent research by Dasgupta et al. (2013) highlights the importance of carbonated silicate melts in the Earth's mantle and their influence on the stability of carbonatite melts and the inventory of carbon in the upper mantle. Dasgupta et al. (2013) conducted piston cylinder and multi-anvil experiments using carbonated peridotites and examined the relationship between

near solidus carbonatite melts and higher temperature carbonated silicate melts to constrain the carbonate-silicate melt transition in P-T space. One of their key findings was that the temperature at which carbonated silicate melting can occur is significantly lower than the volatile-free peridotite solidus and that this difference increased with pressure. Their results also suggested that TiO_2, Na_2O, and FeO played an important role in the stabilization of carbonated silicate melts as the temperature at which carbonated silicate melting began in their experiments was approximately 200°C lower than in previous experiments in the more simplified CMAS-CO_2 system (Gudfinnsson and Presnall, 2005). Overall, this study proposes that the first melt formed beneath ridges in an upwelling mantle is a carbonated silicate melt at depths of up to 250-220km, and this deep onset of carbonated silicate melting suggests that a kimberlitic melt, not a carbonatite melt, exerts the most control over the flux of incompatible elements including CO_2 at mid-ocean ridges.

1.3.2 Experiments Using Geochemical Tracers

Evidently, experimental studies on carbonated peridotites and carbonated eclogites are robust approaches for studying the origin of carbonatite magmas. However, other tools exist for tracing the sources of mantle carbon, including the use of geochemical tracers. The first and most obvious choice would be to use carbon isotopes since carbon is a major element in carbonatites and the carbon isotope ratios for various reservoirs such as the mantle ($\delta^{13}C$ = -5.5‰), sedimentary carbonates ($\delta^{13}C$ = 0‰), and organic carbon ($\delta^{13}C$ < -20‰) are all relatively well constrained (Deines, 2002). Therefore, any recycled sedimentary carbon integrated into carbonatite magmas should yield a noticeably heavier carbon isotope signature. However, nearly all the carbon isotope measurements made on carbonatites yield mantle values (Deines, 1989). The main problem is that the systematics of carbon isotope fractionation at high pressures and temperatures is relatively unknown. There were some limited earlier experimental works on the fractionation between CO_2 and silicate melts that reported variable results (Javoy et al., 1978; Mattey et al., 1990; Mattey, 1991) and a more recent study on silicate melts in equilibrium with a reduced fluid (Mysen et al., 2009). However, there is insufficient experimental work that has been done to be able to interpret the carbon isotope signatures of mantle derived sources like carbonatites.

Still, other useful geochemical tracers for the origin of carbonatites and mantle carbon may exist, with calcium being another potential candidate. Compared to carbon, calcium has the advantage of being present in both silicate and carbonate fractions of mantle minerals or melts whereas all carbon will be sequestered into the carbonate fractions. To interpret the isotopic data of carbonatites for any geochemical tracer, there must be a good understanding of the various natural isotopic reservoirs, as well as some experimental evidence for the systematics of isotopic fractionation between different phases at high temperatures and pressures. Fortunately, there is recent evidence showing that the fractionation of stable isotopes between phases that equilibrated at high temperatures and pressures can be experimentally determined.

1.3.3 Experimental Determination of Stable Isotope Fractionation

To effectively use the ratios of non-traditional stable isotopes to study rocks formed at high temperatures, accurate and reliable equilibrium fractionation factors between phases are of critical importance. Young et al. (2015) assert that even in studies where stable isotopes are used as geochemical tracers of mantle reservoirs or other studies where the fractionation between phases is not the focus, a robust understanding of fractionation factors is vital for interpretations of bulk rock data sets. These fractionation factors can often be predicted by computational methods, but require confirmation using carefully controlled experiments.

Computational predictions of inter-mineral fractionation are often based on the general rule that heavier isotopes concentrate where bonds are stiffer (i.e. bond lengths are shorter), which in turn is affected by crystal chemical controls such as coordination number. Young et al. (2015) illustrated that experiments have confirmed these computational methods are often successful in predicting the direction and magnitudes of fractionation factors for stable isotopes such as Mg, Si, and Fe. The experimentally determined $^{26}Mg/^{24}Mg$ fractionation factors for spinel-forsterite and magnesite-forsterite mineral pairs (Macris et al., 2013) matched well with those predicted computationally using density functional perturbation theory (DFPT, Schauble, 2011) (Figure 4). Experimentally determined $^{57}Fe/^{54}Fe$ fractionation factors between magnetite and fayalite (Shahar et al., 2008) also matched the ionic model predictions of Young et al. (2015). In terms of using stable isotopes to identify unseen geochemical reservoirs, experimental determination of silicon isotope fractionation factors between Fe-rich metal and mantle-like silicates (e.g. Shahar

et al., 2009; Shahar et al., 2011) have been used to help assess the significance of isotopic partitioning between the Earth's core and mantle.

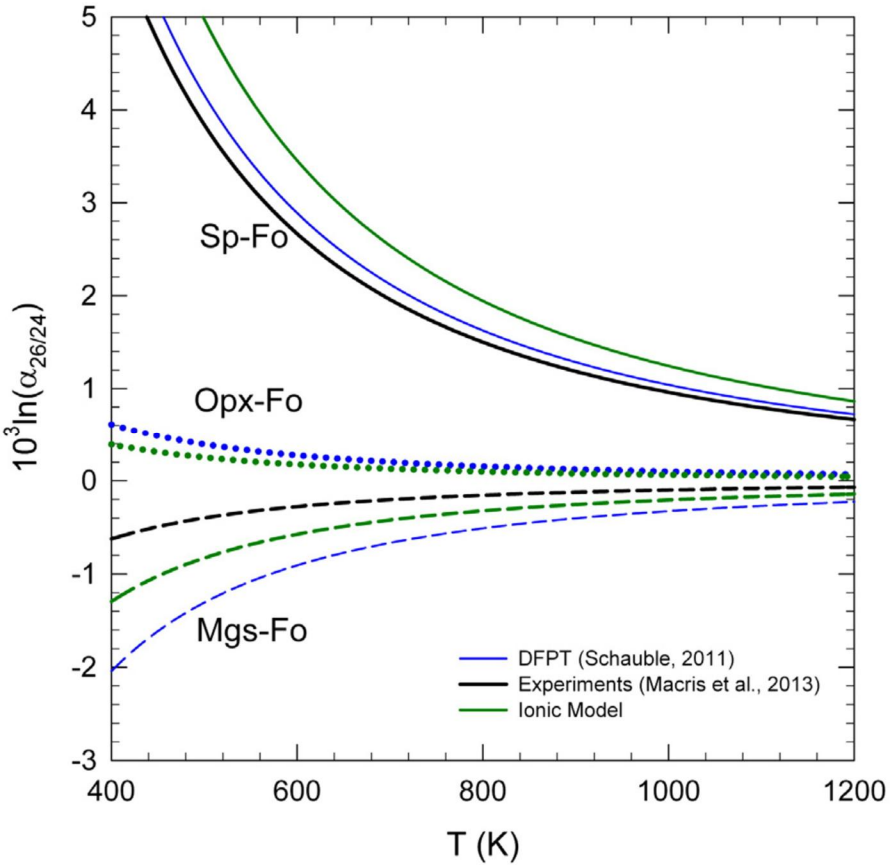

Figure 4 - Comparison of $^{26}Mg/^{24}Mg$ fractionation factors for magnesite-forsterite (Mgs-Fo), orthopyroxene-forsterite (Opx-Fo), and spinel-forsterite (Sp-Fo) mineral pairs. Figure from Young et al., (2015).

More recently, Sossi and O'Neill (2017) conducted a series of piston cylinder experiments at 800°C and 1 GPa to determine the iron (Fe) fractionation factors ($\Delta^{57}Fe$) for pairs of common Fe-bearing high temperature minerals and to characterize the effect of coordination number and oxidation state on their isotopic compositions. They explicitly state that quantifying stable isotope fractionation under controlled experimental conditions is key to understanding the systematics of fractionation in nature. Sossi and O'Neill (2017) conducted their experiments by growing a single solid phase from a mix of oxide powders corresponding to the bulk composition of the mineral of choice in equilibrium with a buffering fluid of 2M $FeCl_2{\cdot}4H_2O_{(l)}$ as a common reference phase. By assuming that the bonding environment of Fe was the same in the fluid of all the experiments, they calculated the mineral-mineral fractionation factors by simply subtracting

the fluid phase. Fractionation factors between mineral phases for stable iron isotopes under equilibrium conditions is dependent on the strength of the Fe-O bonds (shorter = stronger) in the mineral (Urey, 1947; Schauble, 2004), which is influenced by coordination number and oxidation state. Some of the main findings of Sossi and O'Neill (2017) were:

1) Average Fe-O bond lengths increased with increasing coordination numbers (Figure 5).
2) Fractionation between the mineral and the buffering fluid decreased with increasing coordination number (i.e. increasing Fe-O bond lengths, weaker bonds) (Figure 6).
3) Fractionation between the mineral and the buffering fluid increased with increasing oxidation states (as exhibited by magnetite in Figure 6).

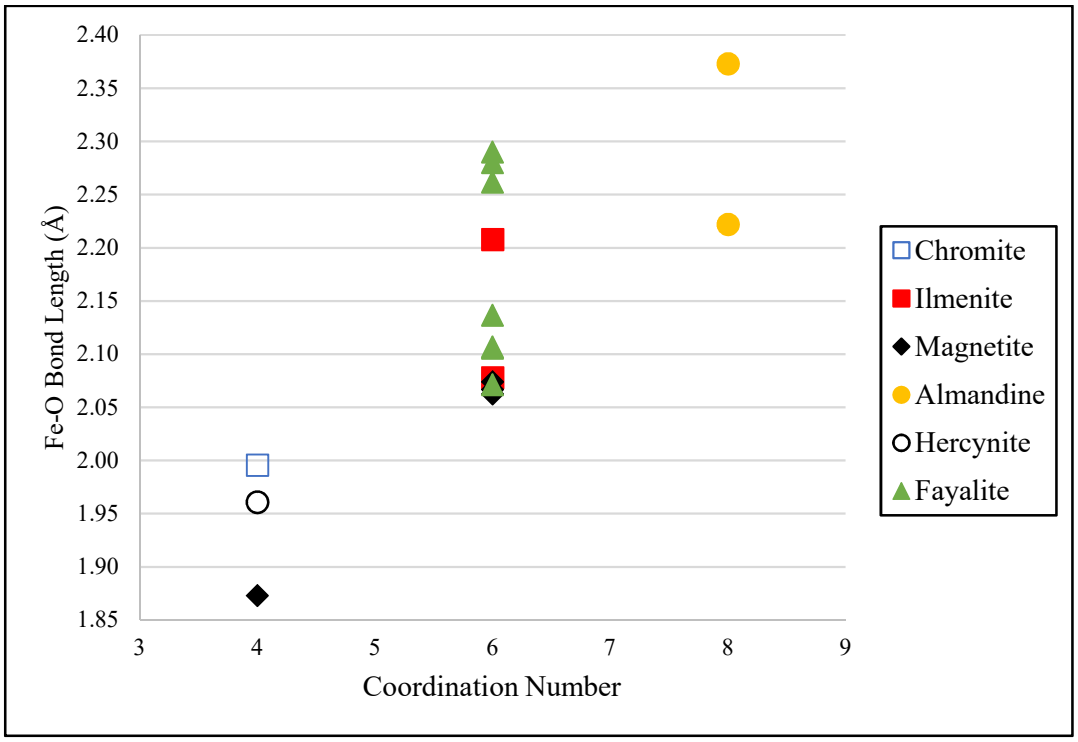

Figure 5 - Fe-O bond length increases with coordination number in high-temperature Fe-bearing minerals. Figure redrawn from Sossi and O'Neill, (2017).

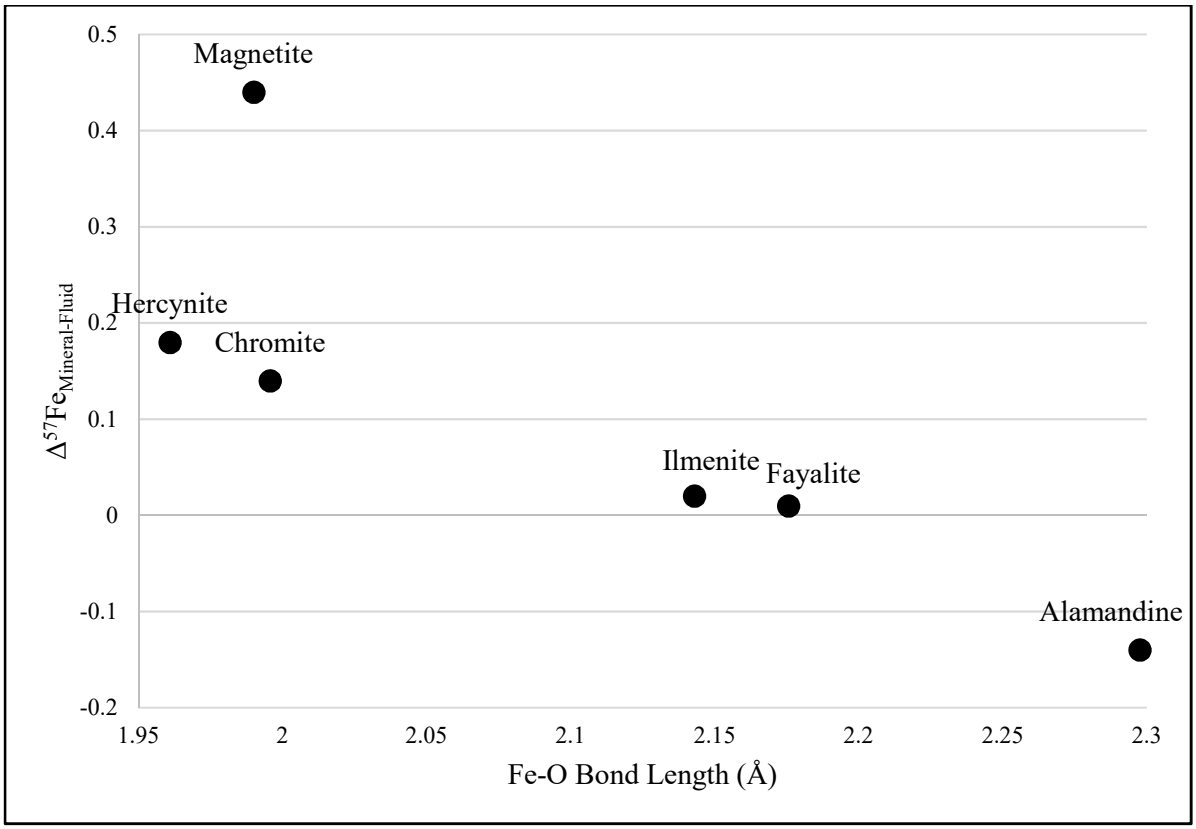

Figure 6 - $\Delta^{57}Fe_{mineral\text{-}fluid}$ decreases with increased Fe-O bond length. The increased $\Delta^{57}Fe_{mineral\text{-}fluid}$ of magnetite is due to its higher oxidation state. Figure redrawn from Sossi and O'Neill, (2017).

The importance of the Sossi and O'Neill (2017) study relevant to this work is that it demonstrates again that fractionation factors and the systematics of fractionation for stable isotopes in phases equilibrated at high temperatures or pressures can be determined experimentally.

1.3.4 Thermal Diffusion

While experimentally determined fractionation factors for stable isotopes in high temperature systems are critical to understanding natural systems, there are some difficulties associated with conducting these types of experiments. Piston cylinder experiments on silicate melts have been shown to produce thermal isotopic fractionation effects for the stable isotopes of major elements (Richter et al., 2008, 2009; Huang et al., 2009, 2010). Thermal diffusion, otherwise known as the Ludwig-Soret effect (Ludwig, 1856; Soret, 1879) or just Soret diffusion, refers to mass

diffusions or chemical fluxes driven by differences in temperature. The experiments conducted by Richter et al. (2008, 2009) utilized a 10mm long capsule in a piston cylinder apparatus and intentionally created a 160°C temperature gradient between the two ends of the capsule. The experiments were run for 100 hours at just over 1 GPa and were considered to have reached a steady state. The results showed fractionations caused by thermal diffusion for the major elements Si, Mg, Ca, Fe, and O that were all correlated but with different sensitivities to temperature (Figure 7). The thermal isotopic fractionations were described in terms of the parameter Ω_i, which is defined as the fractionation in per mil per 100°C per atomic mass difference between the isotopes. Richter et al. (2009) reported values of $\Omega_{Ca} = 1.6$, $\Omega_{Fe} = 1.1$, $\Omega_{Si} = 0.6$, $\Omega_O = 1.5$, and Richter et al. (2008) reported $\Omega_{Mg} = 3.6$. For Ca this corresponds to a thermal isotopic fractionation of $\delta^{44/40}Ca = 0.064‰$ per 1°C. The values reported by Richter et al. (2008, 2009) are comparable to those that were also reported by Huang et al. (2010).

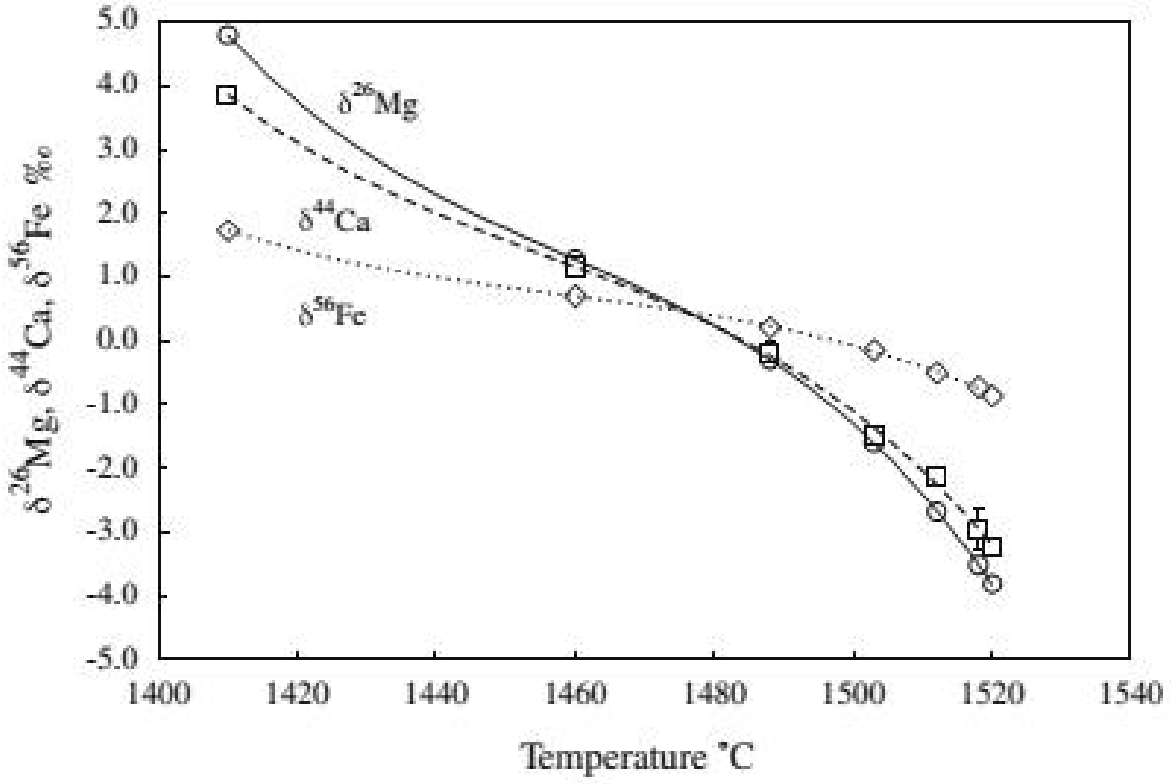

Figure 7 - Correlated major element fractionations caused by thermal diffusion. Figure from Richter et al., (2009)

Interestingly, the results of these thermal diffusion experiments consistently showed that the heavier isotopes would be enriched in the colder end of the experimental capsule, regardless of

whether the concentration of the parent element increased towards the same end. These results suggest that even very small temperature differences of a few degrees or a few tens of degrees will fractionate the isotopes of major elements in silicate liquids and that these fractionations will be correlated and predictable, and therefore can be distinguished from fractionation caused by other processes (Richter et al., 2009). This unique fingerprint of positive co-variation of stable isotope fractionation provides an important diagnostic tool for potentially recognizing if these processes occur in nature and future studies using non-traditional stable isotopes could provide information to determine if thermal diffusion could be a significant process of igneous differentiation on Earth (Huang et al., 2010). However, any experimental work involving stable isotopes must account for this process and take precautions to limit temperature gradients within experimental capsules.

1.4 Isotope Geochemistry

With recent advances in modern analytical geochemistry techniques, non-traditional stable isotopes such as Mg, Si, Ca, and Fe formerly not thought to fractionate during magmatic processes have become a very powerful tool in the field of high temperature geochemistry (Huang et al., 2010). With the Ca cycle closely linked to the C cycle in the Earth (DePaolo, 2004; Fantle and Tipper, 2014), studying the Ca isotopic composition of carbonatites may be able to add to our understanding of deep carbon and its role in the global carbon cycle.

1.4.1 Calcium Isotopes

Calcium is the fifth most abundant element in the Earth's crust and an important rock forming element. It has six isotopes (^{40}Ca, 96.941%; ^{42}Ca, 0.647%; ^{43}Ca, 0.135%; ^{44}Ca, 2.086%; ^{46}Ca, 0.004%; ^{48}Ca, 0.187%) with the largest relative mass difference between the heaviest and lightest isotope (Δm/m = 20%) except for H and He, which amplifies mass-dependent fractionation and makes it a cosmochemical and geochemical tracer with great potential (DePaolo, 2004). Calcium-bearing carbonate minerals can coexist with calcium-bearing silicate minerals in carbonatites, and recent geochemical research has shown that the Ca isotopic variation in silicate minerals that equilibrated at high temperatures in the mantle can be accurately measured (Huang

et al., 2010; Valdes et al., 2014). Calcium is a good candidate for isotopic studies of the mantle because, as a refractory lithophile element, it does not partition into planetary cores during the accretion and differentiation processes that occur during planetary formation (Valdes et al., 2014). Therefore, the calcium isotopic composition of the mantle may represent the bulk Earth composition.

Like other stable isotopes, calcium isotope fractionation is reported in the conventional delta notation:

$$\delta^{44/40}\text{Ca} = \{[(^{44}\text{Ca}/^{40}\text{Ca})_{\text{sample}} - (^{44}\text{Ca}/^{40}\text{Ca})_{\text{standard}}]/[(^{44}\text{Ca}/^{40}\text{Ca})_{\text{standard}}]\}$$

Delta notation reports the ratio of stable isotopes relative to a standard because the differences in isotopic ratios can be measured more precisely than the absolute ratios. Delta notation is reported in per mil (‰) units, or parts per thousand. A positive δ value indicates the ratio of heavy to light isotope is higher in the sample than in the standard and a negative δ value indicates the opposite. The fractionation factor between two substances or phases (A and B) can also be reported as:

$$\alpha_{A\text{-}B} = (1000 + \delta_A)/(1000 + \delta_B)$$

Values of α are often very close to unity, normally in the order 1 ± 10^{-3}, and for this reason, other useful methods of reporting fractionation are the 10^3 ln α value and the Δ ('big delta') value. 10^3 ln $(1 + x\ 10^{-3})$ is approximately equal to just x, and the Δ value ($\Delta_{A\text{-}B} = \delta_A - \delta_B$) is approximately equal to 10^3 ln α so both are useful for reporting the isotopic fractionation between two substances.

Many of the isotopic exchanges that occur in nature are near-equilibrium reactions and therefore they can be modeled using classical equilibrium thermodynamics. The precipitation of mineral phases (e.g. carbonates, phosphates) in water is one example of a low-temperature equilibrium process, whereas crystallization is generally an equilibrium process at high temperatures. In general, equilibrium fractionation between two phases is determined by the differences in bond strength of the different isotopes of any element, with the heavier isotope forming stronger bonds and being concentrated in whichever phase also has 'stiffer' or stronger bonds. General rules for equilibrium isotopic fractionation are described by Schauble (2004):

1) Fractionation between two phases generally decreases with increasing temperatures as described by the relationship $1/T^2$
2) Fractionation is generally greater for elements with a larger mass ratio determined by the equation $(m_{heavy} - m_{light})/(m_{heavy}m_{light})$
3) Heavy isotopes are preferentially partitioned into the sites with the stiffest bonds (strongest and shortest bonds) and bond stiffness is increased by
    a. High oxidation states
    b. Lighter elements
    c. Covalent bonds
    d. Low coordination number

It is the first rule regarding the relationship between fractionation and temperature which has made high temperature isotope geochemistry for some stable isotopes difficult until recent technological advancements in mass spectrometry. The δ values for Ca can now be measured to a precision as good as ±0.05 (2 standard deviations) or better, using high resolution multi-collector inductively coupled mass spectrometry, representing a minimum improvement by a factor of 10 from very early measurements conducted using double-spike thermal ionization mass spectrometry techniques (Schiller et al., 2012).

Calcium isotopic fractionation has been well studied in low-temperature systems, with most previous research focused on marine carbonates and sulfates and limited work on Ca isotopes in igneous systems (Fantle and Tipper, 2014). Low temperature systems showing Ca isotopic fractionation include: inorganic and biotic Ca-mineral precipitation (e.g. Gussone et al., 2003), ion exchange (Russell and Papanastassiou, 1978), and plant uptake (e.g. Schmitt and Stille, 2005). Russell et al. (1978) were the first to publish a study of Ca isotopes that included igneous rocks, however, the analytical precision (δ^{44}Ca ±0.5‰, 2 standard deviations) was not precise enough to resolve most isotopic fractionations. Data compiled from more recent studies shows large variations in the $\delta^{44/40}$Ca values (+0.62‰ to +1.54‰) for terrestrial basalts (Kang et al., 2017). Fantle and Tipper (2014) conducted a review of recent Ca isotope research and compiled data from more than 70 published studies (Figure 8). Generally, seawater is the heaviest isotopically speaking with a mean value of δ^{44}Ca = +1.92‰ while plants are isotopically lighter at only δ^{44}Ca = +0.01‰. Other important trends that were reported were the difference between

ancient (δ^{44}Ca = +0.54‰) and modern marine carbonates (δ^{44}Ca = +0.74‰), and the fact that the marine carbonates yielded typically lower δ^{44}Ca values than silicates (δ^{44}Ca = +0.99‰).

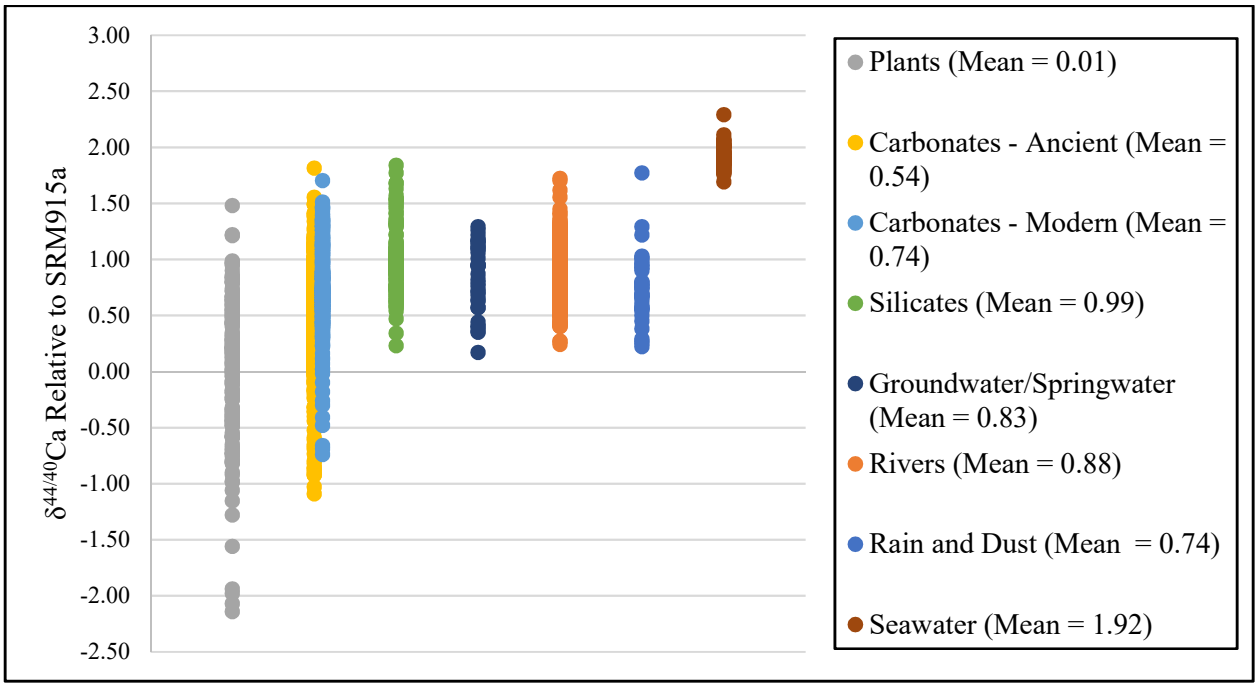

Figure 8 - Summary of published Ca isotope data compiled and presented in Fantle and Tipper (2014). Figure redrawn from Fantle and Tipper (2014).

As with most published Ca isotope studies, Fantle and Tipper (2014) reported their $\delta^{44/40}$Ca values relative to the NIST reference standard SRM915a which is a calcium carbonate. However, this reference standard has since been exhausted and replaced with SRM915b, another calcium carbonate. Whereas most samples are heavier isotopically than the SRM915a, the SRM915b is much closer to the bulk silicate earth values for δ^{44}Ca and therefore it has been argued that it is a better reference standard for use in Ca isotopic studies (Schiller et al., 2012).

Amini et al. (2009) provided Ca isotopes for widely available reference material as well as a wider range of igneous and metamorphic rock types than was available in the literature at the time. They reported, for the first time, mantle rocks such as peridotites that were enriched in heavy Ca isotopes compared to basalts. They indicated that Ca isotopes can be fractionated at high temperatures but did not identify the igneous and metamorphic processes by which this may occur. However, they did postulate that inter-mineral fractionation may play a role in the Ca isotope variations they measured in ultramafic rocks, and that changes in mineral assemblages or the abundances of different minerals within samples may cause Ca isotope variability. They

suggested that a more in-depth analysis of rock assemblages including mineral separates was required to further constrain the fractionation mechanism.

Huang et al. (2010) reported the first evidence for Ca isotopic fractionation between co-existing clinopyroxene (Cpx) and orthopyroxene (Opx) in mantle peridotites with the $^{44}Ca/^{40}Ca$ in orthopyroxenes being +0.36 to +0.75‰ higher than that of the clinopyroxenes. This fractionation between co-existing minerals was attributed to differences in the Ca-O bond length, with the shorter Ca-O bond leading to a stronger bond and a heavier Ca isotopic composition (Figure 9). Due to the large variability in the Ca isotopic composition of basalts (DePaolo, 2004), and the fact that their study showed Ca isotopic fractionation due to igneous processes, Huang et al. (2010) reconstructed the mantle $^{44}Ca/^{40}Ca$ value based on mantle peridotites. They based their estimate on the proportion of Opx and Cpx (the principal Ca-bearing minerals) in the upper mantle and assumed the Ca isotopic composition of the minerals in their study were representative of the mantle. Their estimate for the mantle or Bulk Silicate Earth (BSE) $\delta^{44/40}Ca$ was +1.05±0.04 which was higher than the average for their measured basalts (+0.97±0.04), consistent with the results of Amini et al. (2009). Huang et al. (2010) concluded by asserting their BSE $\delta^{44/40}Ca$ was not final, but rather that additional samples should be analyzed to better characterize the Ca isotopic composition of the mantle. The importance of establishing a stable terrestrial mantle value for Ca isotopes extends beyond terrestrial samples, it is also important to effectively compare the Ca isotopic compositions of meteorites and other planetary bodies with the BSE (Simon and DePaolo, 2010; Valdes et al., 2014; Amsellem et al., 2017). Subsequent studies of the Ca isotopic composition of mantle peridotites have continued to expand our understanding of the mechanisms behind the observed Ca isotopic fractionation.

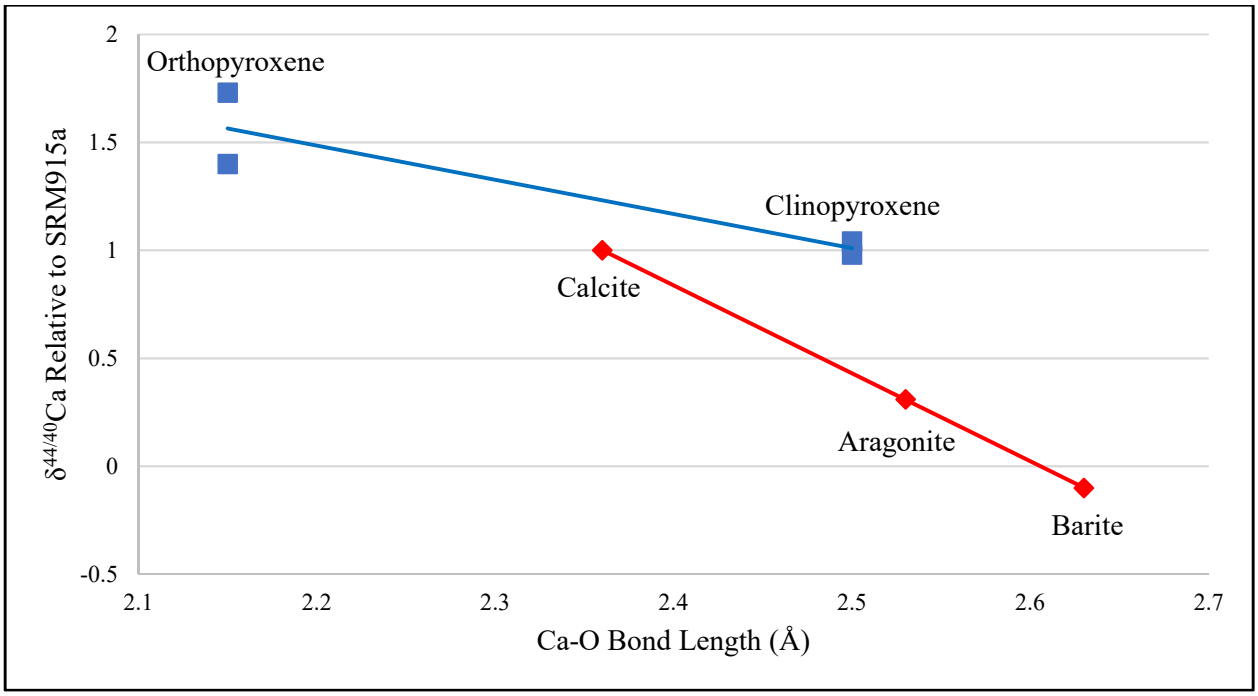

Figure 9 – $\delta^{44/40}$Ca vs. Ca-O bond length in low temperature minerals (calcite, aragonite, barite) calculated using mineral-seawater fractionation factors from Gussone et al., (2005) and Griffith et al., (2008), and coexisting Opx and Cpx in mantle peridotites measured by Huang et al., (2010). Figure redrawn from Huang et al. (2010).

Kang et al. (2016) provided Ca isotope data for coexisting Cpx and Opx in mantle xenoliths from Eastern China. They found Opx-Cpx Ca isotope fractionations ranging from −0.01 to +1.11 that increased with decreasing Ca/Mg values in the orthopyroxenes. Their $\delta^{44/40}$Ca for the bulk peridotites ranged from +0.76 to +1.04‰, positively correlated with CaO content and negatively correlated with MgO content. These correlations were explained by a two end-member mixing model between a fertile mantle and a depleted one with low $\delta^{44/40}$Ca caused by carbonate metasomatism followed by melt extraction. Kang et al. (2016) argued their study showed that Ca isotopes could be useful for studying mantle evolution.

Kang et al. (2017) further expanded the database of Ca isotopes in mantle peridotites to better constrain the Ca isotopic composition of the BSE. Their results showed that fertile peridotites had a consistent $\delta^{44/40}$Ca value of +0.94±0.05‰ which they proposed as the BSE value. They also indicated that the mantle processes of melt extraction and metasomatism may slightly elevate and decrease respectively the $\delta^{44/40}$Ca values of mantle peridotites, particularly in low-Ca rocks. They assert that the results of their study provide the benchmark for using Ca isotopes for

the study of planet formation, mantle evolution, and crustal recycling. Figure 10 represents a summary of the high-temperature Ca isotope data that has been published to date. The data and sources for Figure 10 are also provided in Appendix A (meteorite samples) and Appendix B (terrestrial samples).

In addition to these studies of natural samples, theoretical research has also been conducted by Feng et al. (2014) into the mechanisms behind the Ca isotope fractionation between coexisting Opx and Cpx. The mantle and crust are the largest reservoirs of Ca in the Earth and Ca cycles between the mantle and crust are achieved by crustal growth and recycling (e.g. Dasgupta et al., 2004a). Since carbonates typically have $\delta^{44/40}$Ca values distinct from the mantle and much higher Ca contents, recycling of marine carbonates at subduction zones can alter the Ca isotope compositions of the mantle (Huang et al., 2011). Due to the coupling of Ca and C cycles, Ca isotopes can be used to monitor the global carbon cycle throughout Earth's history (e.g. Fantle and DePaolo, 2005) and subsequently, Feng et al. (2014) emphasized the necessity for a detailed investigation into how Ca isotopes are fractionated between silicate minerals. In order to use Ca isotopes as tracers in mantle geochemistry, equilibrium fractionation factor of Ca isotopes between mantle minerals are of critical importance, and to date there have been no experiments to determine these all-important fractionation factors (Feng et al., 2014). Feng et al. (2014) showed for the first time, a compositional effect on equilibrium stable isotope fractionation that matched the observations on natural mantle minerals from Huang et al. (2010). They confirmed the belief that the Opx-Cpx fractionation that was measured in the San Carlos and Kilbourne Hole peridotites (Huang et al., 2010) was controlled by Ca-O bond lengths, while also showing that the Ca-O bond length in Opx can vary when Ca is a minor element. Lower Ca/Mg values in Opx results in a shorter Ca-O bond length and an enrichment in heavier Ca isotopes, which explains the +0.36 to +0.75‰ variation in Opx-Cpx fractionation measured between the San Carlos and Kilbourne Hole peridotites.

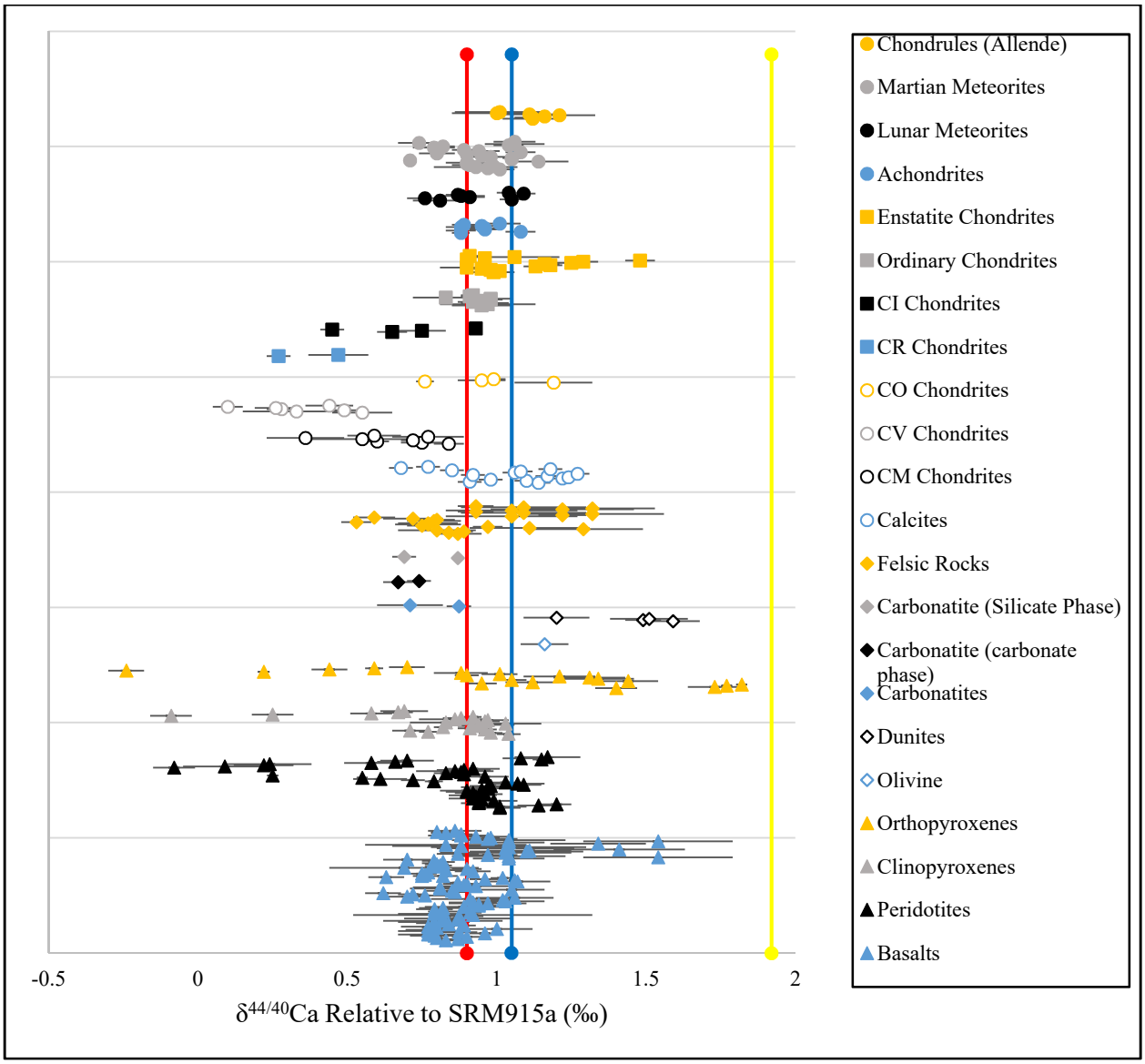

Figure 10 - Compilation of published terrestrial and meteorite Ca data (excluding low temperature terrestrial systems). Vertical red line indicates the average $\delta^{44/40}$Ca value for terrestrial basalts (+0.90 ± 0.04‰, Valdes et al., 2014), vertical blue line indicates the average $\delta^{44/40}$Ca value for the BSE (+1.05 ± 0.04‰, Huang et al. 2010), and vertical yellow line indicates the average $\delta^{44/40}$Ca value for seawater (+1.92 ± 0.20‰, Fantle and Tipper, 2014). Data and sources are given in Appendix A and Appendix B. Any data that was not reported as $\delta^{44/40}$Ca relative to SRM915a in the original source was converted using the methods given in Chapter 2 or using conversion values from Fantle and Tipper, (2014).

1.5 Thesis Objectives

- Add to the growing database of Ca isotopic data for mantle rocks (e.g. peridotites, carbonatites, kimberlites) and improve our understanding of the Ca isotopic composition of the mantle
- Use natural carbonatite samples to investigate the potential differences in Ca isotopic compositions between carbonates and silicate minerals with the same evolutionary history
- Add further constraints to the use of Ca isotopes as geochemical tracers of carbonatite metasomatism
- Measure the Ca isotopic compositions of co-existing silicate and carbonate minerals
- Conduct a series of experiments at a range of pressure and temperature conditions to constrain the systematics of Ca isotopic fractionation between mantle minerals and melts of different compositions ranging from carbonate to silicate melts.

Chapter 2

2. Methods & Analytical Techniques

2.1 Sample Selection

Both natural and experimental samples were analyzed for their Ca isotopic compositions in this study. Experimental samples were not collected, but instead synthesized in the laboratory and will be described in a subsequent section. Natural samples were selected with an emphasis on rocks derived from the Earth's mantle such as peridotites, carbonatites, kimberlites, and mantle xenoliths. Ten of these samples were obtained from the Suffel Collection at the University of Western Ontario, a collection of more than 200,000 catalogued samples from ore deposits around the world. Four samples were taken from the personal collections of Dr. Audrey Bouvier and Dr. Tony Withers. One sample was obtained from the rock and mineral collection at the University of Minnesota, and six samples were obtained from Dr. Regis Doucelance at Clermont University.

2.2 Natural Sample Preparation

Preparation of each sample for calcium isotopic analysis varied slightly depending on the physical state of the sample upon acquisition as well as their rock and mineral matrices, but with the same objective of breaking down the bulk rock and separating it into its distinct mineral phases. Mineral separation began by breaking down the bulk rock into more manageable pieces using a diamond-edged rock saw, isolating portions of the whole rock that contained higher concentrations of the Ca-bearing minerals of interest. These smaller pieces were broken down further using a disc mill to crush them into grain sized fragments and then separated by grain size using handheld sieves (>425μm, 250-425μm, 150-250μm, <150μm). If necessary, the 150-250μm sized grains were passed on a S.G. Frantz Co. LB-1 Magnetic Barrier Laboratory Separator to help separate and concentrate the different mineral phases based on their magnetic susceptibilities. The final step of mineral separation for all samples was hand-picking mineral grains using forceps under a binocular microscope, selecting only the cleanest grains with no visible impurities. In addition to mineral separates, a homogenized bulk rock powder for each sample was also reserved for various whole-rock analyses

2.3 Experimental Sample Design and Preparation

Piston cylinder and multi-anvil experiments were designed with starting bulk compositions given in Table 2. Experiments were designed with the strategy of producing clinopyroxene and quenched melt in approximately equal proportions. Clinopyroxene and melt compositions were chosen to reflect appropriate compositions for a mantle assemblage that would be in equilibrium with a low degree carbonated silicate melt. In other words, the starting materials used for experiments were constructed such that the clinopyroxene and melt compositions would match those found to be in equilibrium with a peridotite assemblage (Dasgupta et al., 2013). This means that the melt composition is that of a low-melt-fraction, high-pressure carbonated silicate melt, such as might form under oxidising conditions in a carbon-bearing peridotite mantle, even though the melt fraction in the experiment is close to 0.5. In addition, the compositions of the two phases in the target assemblage were calculated to match those shown to be in equilibrium with olivine, orthopyroxene and garnet (Dasgupta et al., 2013), even though these other minerals are not part of the target experimental assemblage. Capsules were packed at UWO and pressed at the University of Minnesota. Prior to weighing, K_2CO_3 was dried at 500 °C for eight hours, and Na_2CO_3 and $CaCO_3$ were dried at 400 °C, for twelve and four hours, respectively. Reagent SiO_2, Al_2O_3 and MgO were calcined at 1100 °C for 95 hours. All K_2O and Na_2O was added to the starting material as K_2CO_3 and Na_2CO_3, while CaO was added as both $CaCO_3$ and $CaSiO_3$ to achieve the required amount of CO_2 in each experiment. To achieve the intended levels of H_2O in the Cpx + Silicate melt experiment, all MgO was added as $Mg(OH)_2$. Reagents were weighed using an analytical balance and each mix was ground in an agate mortar with isopropanol for a minimum of 45 minutes. Starting materials were stored in glass vials in a desiccator until they were ready to be packed into 3 mm diameter, platinum experimental capsules 4-6 mm in length, and sealed by arc welding. Capsules contained 43-61 mg of starting material.

Table 2 - Experiment Starting Materials in wt%

	Piston Cylinder Cpx + Carbonated Silicate Melt Starting Materials (Experiment Cbt-01)	Multi-Anvil Cpx + Carbonated Silicate Melt Starting Materials (Experiments Cbt-02 and M824)	Piston Cylinder Cpx + Silicate Melt Starting Materials (Experiment A1325)	Piston Cylinder Cpx + Carbonatite Melt Starting Materials (Experiments B795, B796, B797, B798)
SiO_2	38.40	41.56	49.21	29.78
TiO_2	2.90	0.70	-	-
Al_2O_3	4.33	3.54	10.45	2.38
Cr_2O_3	0.51	0.13	-	-
FeO	7.76	7.12	-	-
MnO	0.12	0.18	-	-
MgO	18.24	20.59	12.38	18.57
CaO	14.27	15.10	22.97	27.26
Na_2O	2.26	0.82	-	-
K_2O	0.09	0.03	-	-
CO_2	11.00	10.25	-	21.39
H_2O	-	-	5.53	-

All experiments were assembled and conducted at the University of Minnesota's Experimental Petrology Laboratory. Piston cylinder experiments were conducted using an end-loaded piston cylinder apparatus using a $BaCO_3$ pressure medium and type B thermocouple and run times ranged from 44-128 hours. Pressure calibration for this instrument can be found in Xirouchakis et al. (2001). Multi-anvil experiments were conducted using a Walker-style module mounted in a 1000-ton hydraulic press with a modified 12-TEL assembly for large volume experiments (Withers et al., 2011). The modified assembly consisted of 13 mm x 5 mm outside diameter x 4 mm inside diameter graphite furnace. A type C thermocouple was used and the interior of the furnace surrounding the capsule and thermocouple was filled with crushable MgO. The details for the pressure and temperature calibration for this apparatus is given in Dasgupta et al. (2004a). Based on unpublished pyroxene solvus thermometry, experiments with multiple thermocouple junctions, and observations of the solid-liquid boundaries in sphene melting experiments, the temperature gradient within the central 2.5 mm measured along the cylindrical axis of the

furnace in both piston cylinder and (unmodified) multi-anvil assemblies is ≤ 20 °C/mm. The run conditions for each experiment are given in Table 3.

Table 3 - Experiment ID's, run conditions and apparatus used for all the experiments conducted in this study.

Experiment Type	Experiment ID	Pressure (GPa)	Temperature (°C)	Run Time (hours)	Apparatus Used
Cpx + Silicate Melt	A1325	1	1125	128	Piston Cylinder
Cpx + Carbonate Melt	B796	3	1250	72.8	
	B795	3	1350	44.5	
	B797	3	1450	46.3	
	B798	3	1550	44.7	
Cpx + Carbonated Silicate Melt	Cbt-01	3	1375		
	Cbt-02	5	1440	48	Multi-Anvil
	M824	5	1440	48	

Any residual MgO pressure medium was carefully removed from the outside of the experimental capsules before they were carefully opened using forceps and a scalpel under a binocular microscope. Experimental products were slowly removed from their platinum capsules under magnification and collected in glass vials, separating the clinopyroxenes from the melt phase for each experiment (Figures 11 and 12).

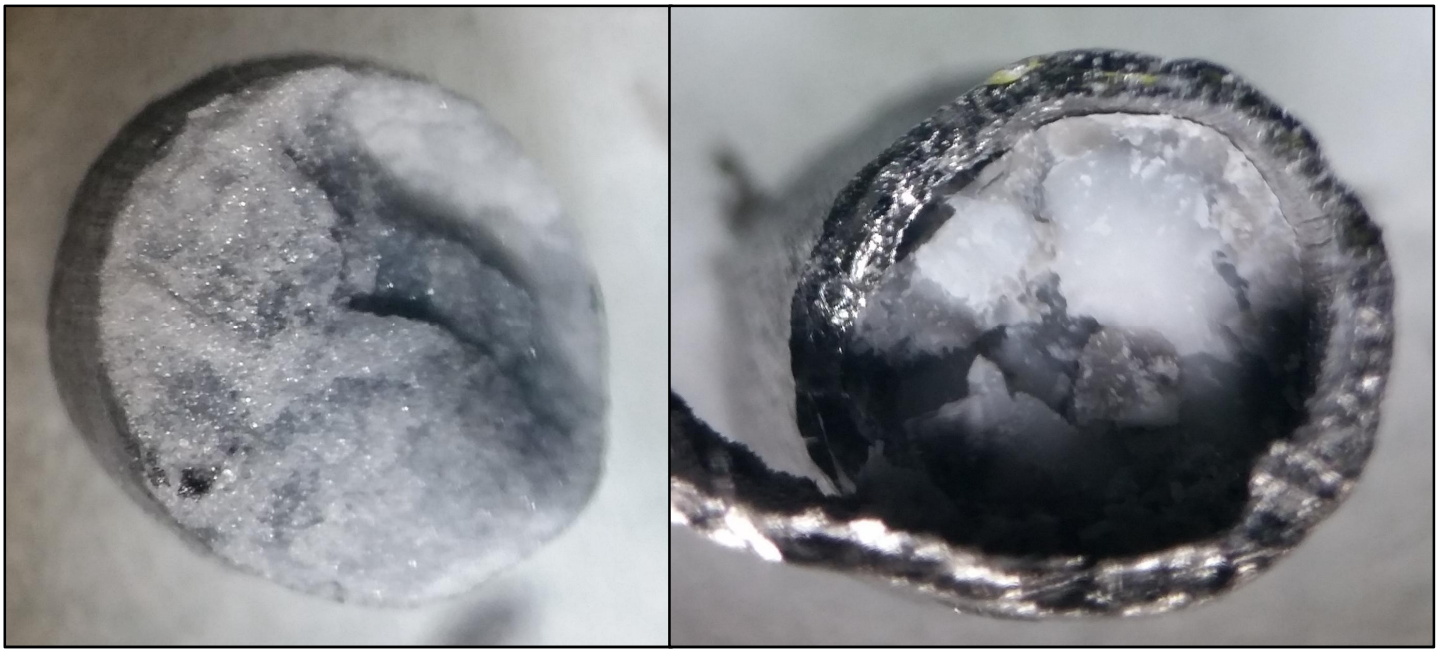

Figure 11 - Photographs taken while opening experiment B797. Left image shows a cluster of clinopyroxene crystals removed from the capsule, the image on the right shows the open capsule with fragments of quenched melt and Cpx crystals inside. For scale: diameter of the capsule is 3 mm.

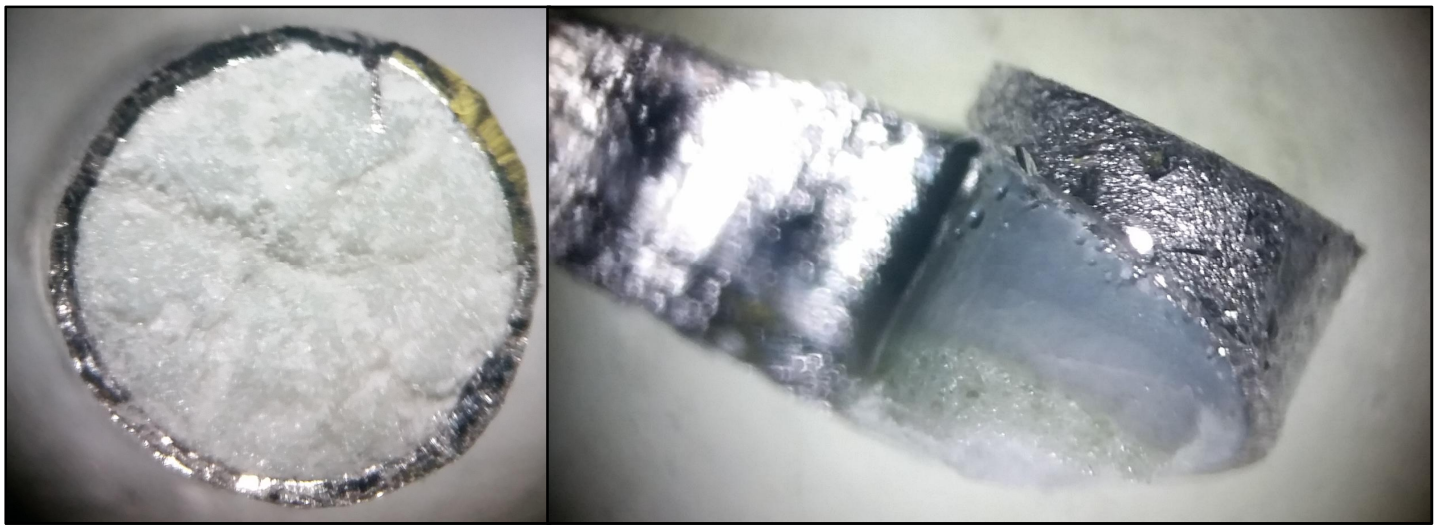

Figure 12 - Photographs taken while opening experiment M824. Left image shows crystals within the open capsule, the image on the right shows the transition from crystals to quenched melt within the capsule. For scale: diameter of the capsule is 3 mm.

2.4 Electron Probe Microanalyses

After sample preparation and mineral separation, the major element compositions of the various calcium-bearing minerals in each sample were analyzed by electron microprobe. This information was required to determine the amount of calcium in each, and therefore establish how much sample mass was to be dissolved for calcium isotope analyses. One sample was mounted as a rock fragment in epoxy while the rest were mounted as individual mineral grains in epoxy or cyanoacrylate on brass mounts. All samples were polished using diamond lapping film and then carbon coated before being analyzed.

All microprobe analyses were done at the Earth and Planetary Materials Analysis (EPMA) Laboratory at the University of Western Ontario using the JEOL JXA-8530F hyperprobe. The electron microprobe allows for non-destructive in situ chemical analysis of solid geological samples. The silicon drift energy dispersive spectrometer (EDS) was used for rapid identification of mineral phases and qualitative elemental analyses before the wavelength dispersive spectrometers (WDS) were used for quantitative chemical analyses of each Ca-bearing silicate and carbonate mineral phase. The backscattered electron (BSE) detector was also used for imaging of mineral grains, especially for experimental samples. The silicate mineral phases were analyzed using a focused beam with a 1 μm spot size, an acceleration voltage of 15 kV, and a beam current of 20 nA. The following standards were employed: San Carlos olivine (Si, Mg), rutile (Ti), Ca-augite (Al), fayalite (Fe), diopside (Ca), albite (Na), millerite (Ni), rhodonite (Mn), orthoclase (K), and chromite (Cr). Carbonate mineral phases were analyzed using a defocused beam with a 25 μm spot size, an acceleration voltage of 15 kV, and a beam current of 5 nA. The following standards were employed: calcite (Ca), dolomite (Mg), siderite (Fe, Mn), strontianite (Sr), barite (Ba), and quartz (Si).

2.5 Silicate Mineral Acid Leaching Procedure

After mineral separation and microprobe analyses, but before sample dissolution, silicate mineral separates were acid leached to remove any potential carbonate residues that would contaminate these samples. Samples were weighed and then soaked in 2 ml 0.5M acetic acid in capped Teflon beakers at 100-120 °C for 30-60 minutes, then placed in an ultrasonic bath for 15 minutes. The liquid was pipetted off and each sample was washed twice with MilliQ water.

2.6 Sample Dissolution Procedure

All sample dissolutions were conducted in the GEOMETRIC Laboratory at the University of Western Ontario under clean conditions using acid-washed Teflon beakers, 18.2 MΩ cm^{-1} MilliQ (purified by Millipore Adavntage 10 and QPOD Element ion-exchange filtration systems) water and ultra-clean distilled acids throughout. The calcium blank for this digestion method was on average 7 ng. Depending on the Ca concentrations of the samples, between 1 and 1000 mg of sample material was weighed into beakers using a Mettler Toledo Excellence Plus XPE105 Analytical Balance. The dissolution procedure varied depending on whether the sample was composed on silicate or carbonate minerals, the method used for each were as follows:

- Silicate Mineral Dissolution

1) Acid leaching procedure (outlined above)
2) Add 10 drops of concentrated HNO_3 (16M) + ~2 ml of concentrated HF (29M)
3) Capped on Hot plate @ 120 °C for minimum 48 hours (often several days is necessary)
4) Dry down on hot plate
5) Add ~20 drops of concentrated $HClO_4$ (enough to cover sample) to break down fluorides and avoid Ca isotopic fractionation into insoluble fluorides
6) Dry down on hot plate @ 180 °C in perchloric fume hood
7) Add H_2O from dropper to rinse down any remaining $HClO_4$ from sides of beaker
8) Dry down on hot plate again in perchloric fume hood
9) Add ~2ml concentrated HNO_3 to convert the samples into a nitride form
10) Dry down on hot plate
11) Uptake in 1M HNO_3
12) Centrifuge to remove any refractory particles not dissolved (e.g. possible organics or metals)

- Carbonate Mineral Dissolution

1) Add ~2 ml 0.5M Acetic Acid or HNO_3 (if necessary) to dissolve only carbonates, not silicate inclusions
2) Hot plate @ 120 °C
3) Centrifuge for 10 mins to remove any particles
4) Collect supernatant, dry down on hot plate
5) Uptake in 1M HNO_3

2.7 Calcium Purification

Samples containing 50-200 μg Ca were purified from matrix elements using column chromatography to prevent elemental and molecular isobaric interferences during mass spectrometry analyses. The calcium purification procedure given in Tables 4 and 5 was adapted from the method described in Valdes et al. (2014). Each step was tested and calibrated to optimize the calcium yields and purity before beginning work with samples. Complete calcium recovery was essential as it has been shown that incomplete recovery can result in fractionation of calcium isotopes (Russell et al., 1978). Figures 13 and 14 display the calibration curves for each step of the calcium purification protocol.

Step 1 used 2 ml of Eichrom DGA ion exchange resin packed in polypropylene Bio-Rad columns. These columns could process a maximum sample load of 20 mg, however, for samples larger than 2-3 mg a second pass was required to further purify the sample (specifically to remove the small residual Ti peak visible in elution steps Ca 1, Ca 2 of the elution curve in Figure 13). Strontium is the only element that was not separated from calcium during this first purification step. After one or two passes through this matrix removal step, samples were dried down and re-dissolved in 3M HNO_3 in preparation for the second purification step. Step 2 used 200μl of Eichrom Sr-specific resin packed in ~3 ml Teflon columns to separate Sr from Ca. Based on the elution curve (Figure 14), only 5 ml of 3M HNO_3 was used after the initial sample load to elute Ca since all the Ca had been eluted at that point and any additional volume started to elute Sr. Samples were then dried down and re-dissolved in 2% HNO_3 for ICP-MS and MC-ICP-MS analyses. Yields for each of these purification steps was measured by quadrupole ICP-MS to be 100% and total procedural blanks were measured to be on average 18.3 ng of Ca which equated to 0.009-0.037% relative to the total Ca in the samples (50-200 μg).

Table 4 - Step 1 calcium purification procedure

Step #1: Matrix removal (Repeated for high matrix samples)		
Eluent	**Volume (ml)**	**Elements Eluted**
15M HNO_3	5	cleaning
1M HNO_3	6	Conditioning
Load sample in 1M HNO_3	1	Matrix
1M HNO_3	5	Matrix
15M HNO_3	12	Ca + Sr
15M HNO_3	5	cleaning
H_2O	5	rinse

Table 5 - Step 2 calcium purification procedure

Step #2: Sr separation		
Eluent	**Volume (ml)**	**Elements Eluted**
3M HNO_3	1 reservoir	cleaning
3M HNO_3	4	Conditioning
Load sample in 3M HNO_3	1	Ca
3M HNO_3	5	Ca
0.01M HNO_3	3	Sr
0.01M HNO_3	1 reservoir	rinse

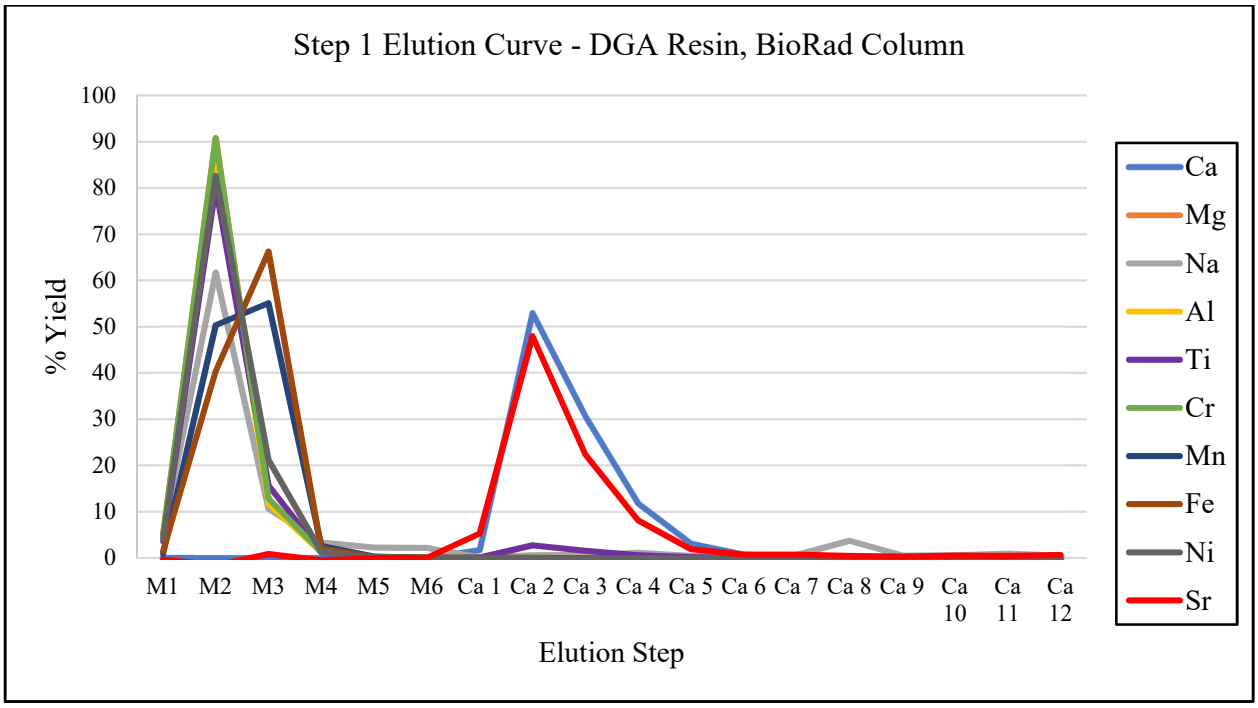

Figure 13 - Elution curve for calcium purification step 1.

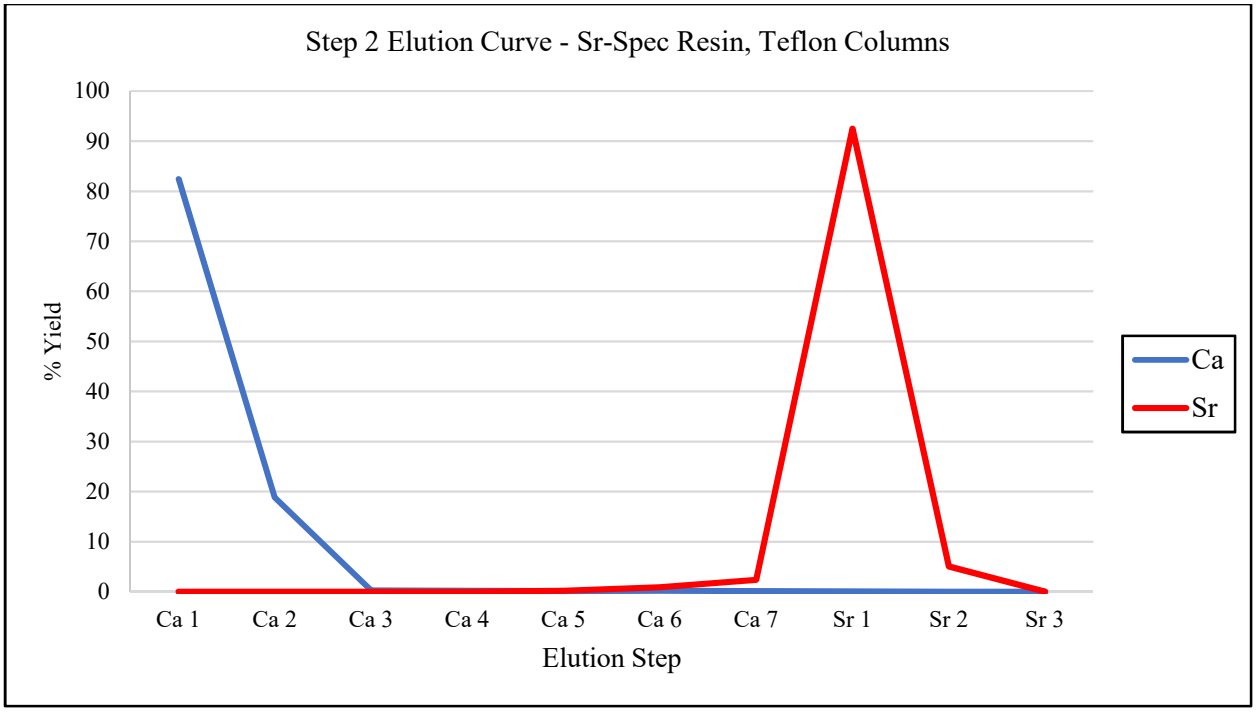

Figure 14 - Elution curve for calcium purification step 2.

For low Ca samples, such as olivines, some bulk rock samples, and some orthopyroxenes, a preliminary pass using cation exchange column was conducted before advancing to the above steps. For these samples, most of the matrix elements were removed from the sample using Teflon columns with Bio-Rad AG50W-X8 200-400 mesh cation exchange resin (11.6 ml, capacity of 270 mg whole-rock sample) (Tera et al., 1970). The procedure for this step is given in Table 6 and the calibration curve is given in Figure 15. The eluates collected from this preliminary matrix removal step were dried down, re-dissolved in 1M HNO_3, and passed through the remaining steps of the Ca column chemistry protocol. The yield for this step was measured to be 98% (with an estimated error of ±5% by qICPMS).

Table 6 - Preliminary calcium purification procedure for very low Ca samples

Low Ca Samples Preliminary Matrix Removal		
Eluent	**Volume (ml)**	**Elements Eluted**
2.5M HCl	35	Conditioning
Load Sample in 2.5M HCl	3	Matrix
Rinse 2.5M HCl	27	Matrix Elements
2.5M HCl	25	Ca
H_2O	10	Backwash
2M HF	60	Cleaning
6M HCl	60	Cleaning
H_2O	10	Backwash & Store

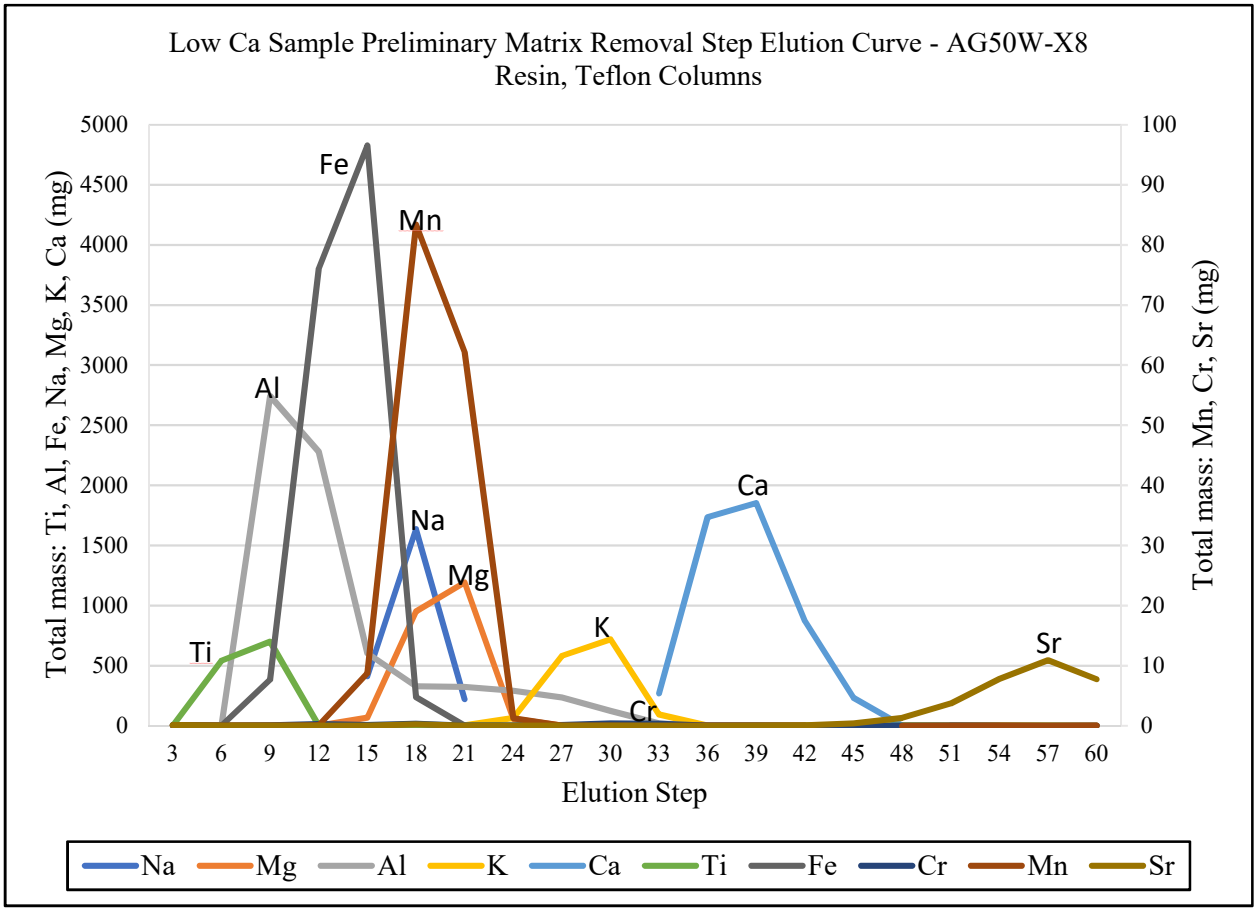

Figure 15 - Elution curve for low Ca samples preliminary cation exchange column matrix removal step.

2.8 Iron Purification

In addition to calcium, several samples were analyzed for their Fe isotopic composition. Sample aliquots containing 5 μg Fe were purified from matrix elements using column chromatography to prevent elemental and molecular isobaric interferences during mass spectrometry analyses. The purification procedure used 2 ml of 100-200 mesh Bio-Rad AG MP-1 strong anion exchange resin packed into polypropylene Bio-Rad type columns. The Fe purification protocol was adapted from Chapman et al., (2006) and the details are outlined in Table 7.

Table 7 - Iron purification procedure

Fe Purification Protocol		
Eluent	**Volume (ml)**	**Elements Eluted**
6M HCl	1 reservoir	Cleaning
H_2O	1 reservoir	Cleaning
7M HCl	6	Conditioning
Load sample in 7M HCl	1	Matrix
7M HCl	33	Matrix
2M HCl	25	Fe
H_2O	1 reservoir	Rinse

2.9 Quadrupole Inductively Couple Plasma Mass Spectrometry (ICP-MS)

Quadrupole inductively coupled plasma mass spectrometry (qICP-MS) was used extensively to measure major and trace elements throughout various steps of the sample preparation process. All ICP-MS analyses were conducted using a Thermo iCAP Q quadrupole ICP-MS in the GEOMETRIC Laboratory at the University of Western Ontario. Some of the many uses of the ICP-MS included: major element analyses of samples including determining the calcium concentration of each, analyzing column calibration results including measuring sample yields, trace element analyses of samples, and measuring chemistry procedural blanks. All samples were analyzed in 2% HNO_3 solutions and each run included a set of calibration standards, blank, and internal standard. For major element analyses of samples, typically a 1% sample aliquot was diluted into 10 ml of 2% HNO_3. Calcium was the most frequent analyte, and solutions were analyzed at concentrations ranging from the detection limit of approximately 2-5 ppb up to 5-10 ppm. However, concentrations in the range of 100-500 ppb were typical for most calcium analyses. ICP-MS measurements were critical to determine the Ca concentration of samples before column chemistry to ensure that the columns were not overloaded, as well as essential for measuring the concentrations of samples after chemical purification to ensure complete yields. It was also used to ensure that each sample was diluted to the same concentration and that the concentrations matched that of the standards before isotopic analyses.

2.10 Multi-Collector Inductively Coupled Plasma Mass Spectrometry (MC-ICP-MS)

All high-precision Ca isotope analyses were conducted using a Thermo Neptune multi-collector inductively coupled plasma mass spectrometer (MC-ICP-MS) operating at high resolution at the Water Quality Centre at Trent University. After chemical purification, calcium samples were dissolved in 2% HNO_3 and diluted to a concentration of 4 ppm. Samples were introduced to the MC-ICP-MS plasma source using an ESI SC-4 DX autosampler and an ESI Apex Q desolvating nebulizer sample introduction system which helped increase sensitivity and decrease rinse-out times. Samples were aspirated at an approximate rate of 0.150 ml/min and the samples gas flow rate was typically in the range of 0.800-1.000 L/min. The cones used were a TF1001-Ni/Cu nickel sampler cone with a copper core, along with either a T1002A-Ni nickel skimmer cone or a TF1002X-Ni nickel X-skimmer cone with a copper core. The X-skimmer cone typically allowed for greater sensitivity but less stability, so the skimmer cone that was used depended on the instrument conditions. A static 6 Faraday cup configuration was used with the ^{42}Ca, ^{43}Ca, ^{44}Ca, ^{46}Ca, ^{47}Ti, and ^{48}Ca ion beams measured on L4, L2, L1, H1, H2, and H3 cups respectively. Each analysis consisted of one block of 25 cycles with integration times of 8.389 s and was preceded by a baseline measurement. Tuning parameters were adjusted each day during analyses to ensure optimal instrument stability and sensitivity.

The standard-sample bracketing technique was used for all isotope measurements to correct for instrument drift throughout the course of the analyses. NIST SRM915b was used as the bracketing standard for all measurements. The SRM915b standard contains a level of Sr that would affect the accuracy of measurements, so it was first passed through one round of Sr removal chemistry. The conventional delta notation was used to report all calcium isotope variations in per mil units (‰) relative to the bracketing standard:

$$\delta^{44/42}Ca = \{[(^{44}Ca/^{42}Ca)_{sample} - (^{44}Ca/^{42}Ca)_{SRM915b}]/[(^{44}Ca/^{42}Ca)_{SRM915b}]\} \text{ (eqn 1)}$$

$$\delta^{44/40}Ca = \{[(^{44}Ca/^{40}Ca)_{sample} - (^{44}Ca/^{40}Ca)_{SRM915a}]/[(^{44}Ca/^{40}Ca)_{SRM915a}]\} \text{ (eqn 2)}$$

Since $^{40}Ar^{+}$ is used as the ionizing gas when using MC-ICP-MS for analyses, it is not possible to measure the more conventionally reported $^{44}Ca/^{40}Ca$ ratios. However, assuming mass dependency the $^{44}Ca/^{42}Ca$ ratio that was measured in this study was converted to $^{44}Ca/^{40}Ca$ ratios

using the equation $\delta^{44/40}Ca = \delta^{44/42}Ca/\beta$ where $\beta = 0.488$ (Colla et al., 2013), allowing for better comparisons to values reported in the existing literature. Mass independent fractionation is assumed to have no effect on these conversions since all Ca isotopic fractionations measured thus far in terrestrial samples are mass dependent (Moynier and Fujii, 2017). Furthermore, most of the existing literature reported their $\delta^{44}Ca$ values relative to the calcium standard SRM915a, the supply of which has since been exhausted and replaced with SRM915b. Valdes et al. (2014) measured the $\delta^{42/44}Ca$ value of SRM915b relative to SRM915a to be −0.35 ± 0.01‰ or, assuming mass dependency, a $\delta^{44/40}Ca$ of +0.71 ± 0.02‰. These conversion values were also in good agreement with other published studies (Heuser and Eisenhauer, 2008; Hindshaw et al., 2011; Lehn et al., 2013) and so were used to convert the data and report it relative to SRM915a for better comparisons to the existing literature. Ultimately, all data was measured and calculated as $\delta^{44/42}Ca$ relative to SRM915b (see equation 1) but was subsequently converted to $\delta^{44/40}Ca$ relative to SRM915a (equation 2) using the equation $\delta^{44/40}Ca = (\delta^{44/42}Ca/0.488) + 0.71$.

SRM915b aliquots were always passed through the full chemistry procedure alongside samples and these aliquots were routinely measured relative to the regular SRM915b bracketing standard. This was done to ensure that the chemistry method was not introducing any fractionation as well as to monitor the instrument stability and long-term reproducibility of the analyses. The long-term average of SRM915b from September 2016 to September 2017 was 0.00 ± 0.07‰ (n = 16) (Figure 16). The errors associated with these SRM915b measurements are comparable to recent Ca isotopic studies that used MC-ICP-MS, for example, Schiller et al. (2012) processed a

SRM915b aliquot using their full chemistry procedure and reported a value of $\delta^{44/42}Ca = +0.04 \pm 0.09$ (error is two times the standard deviation).

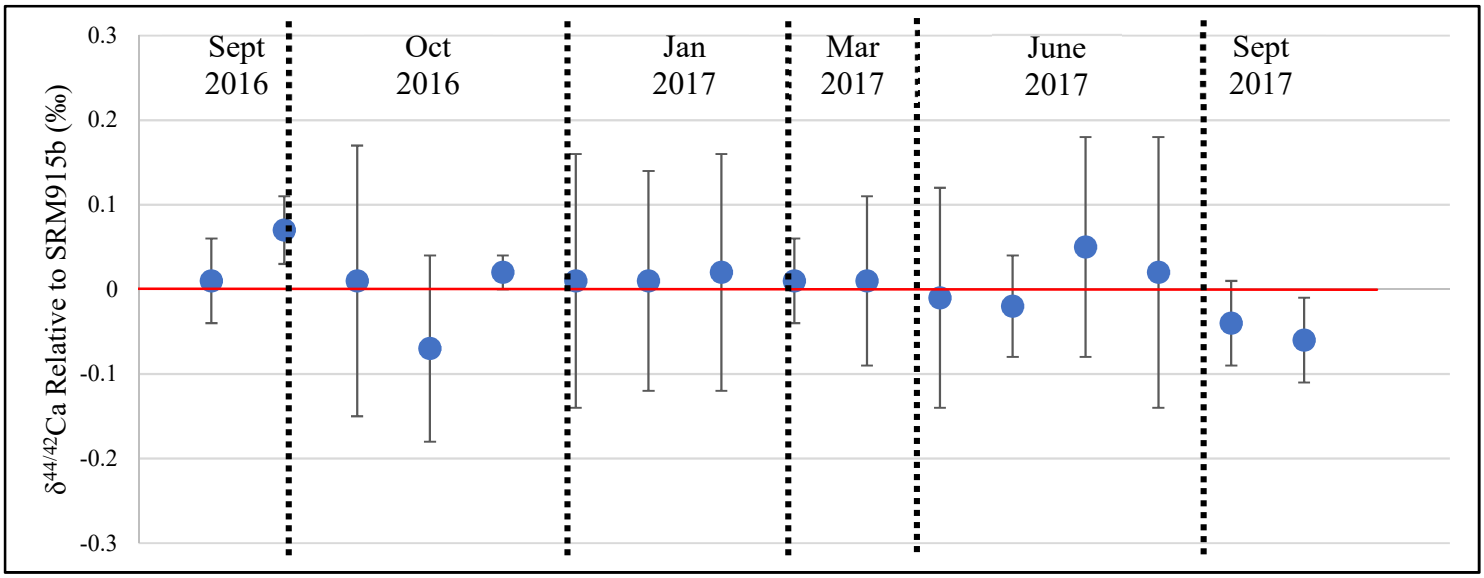

Figure 16 - SRM915b long-term reproducibility. Red line indicates the average of all measurements (0.00 ± 0.07‰, N = 16).

Additional samples were utilized as external standards to ensure the efficacy of the chemistry and analyses. These included clinopyroxene and orthopyroxene mineral separates from the San Carlos and Kilbourne Hole peridotites, as well as the USGS rock standard BCR-2. These samples were used because their Ca isotope data has already been published (e.g. Huang et al., 2010). Each was found to be identical within error to the previously published values. Leached and unleached samples of the San Carlos and Kilbourne Hole clinopyroxenes were found to be identical within error. San Carlos clinopyroxenes that underwent one pass through the matrix removal step #1 chemistry were identical within error to a sample that underwent two passes, and full procedural replicates from dissolution to purification were also identical (Figure 17).

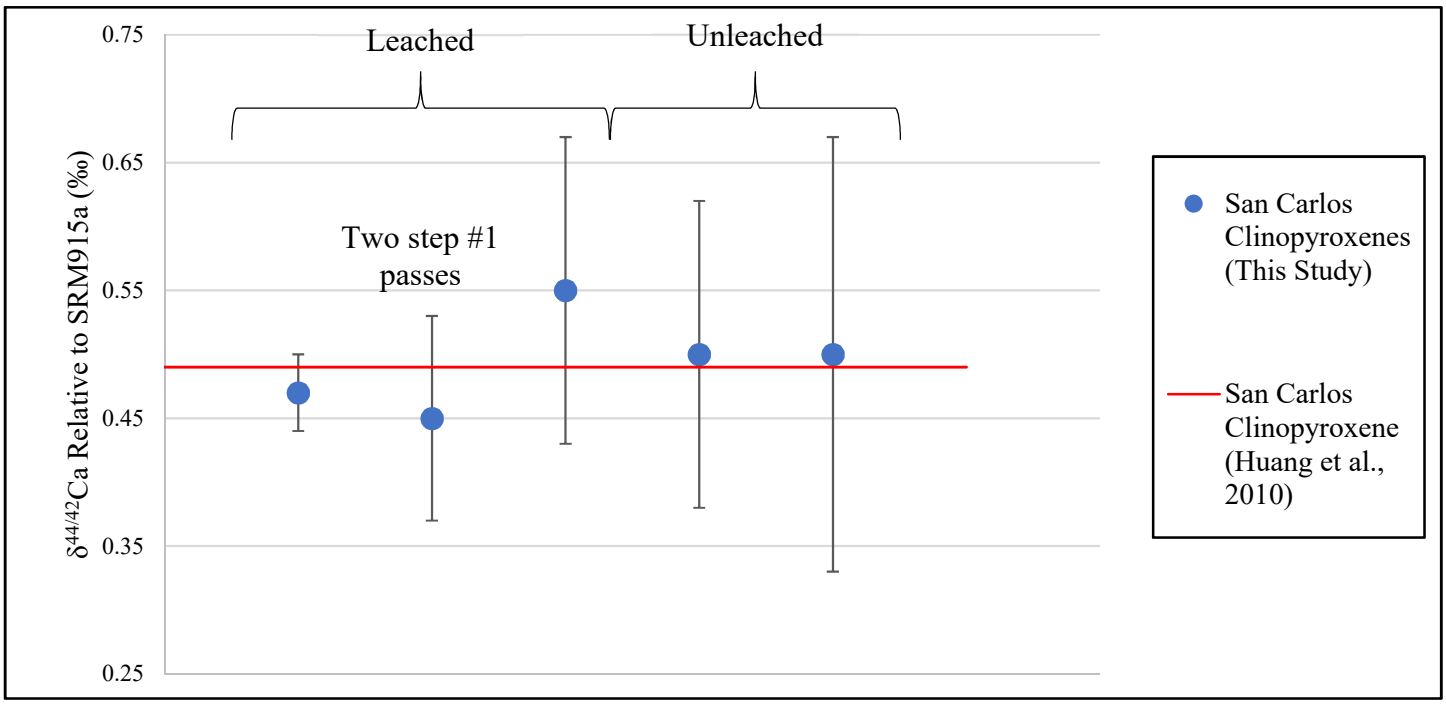

Figure 17 - San Carlos clinopyroxenes were used as external standards in this study to test the accuracy of the chemical purification methods. Each replicate matched the published value from Huang et al. (2010) within error.

Chapter 3

3. Sample Descriptions

3.1 Carbonatites

This work includes 14 carbonatite samples from 6 localities.

3.1.1 Oka Carbonatites

The Oka carbonatite complex is located 40km west of Montreal, Quebec, Canada. It is one of the most westerly plutons of the Monteregian Igneous Province, intruded into Precambrian Grenville basement rocks (Gold, 1972; Gold et al., 1986). There are two clear intrusive centres that make up northern and southern ring structures and give the complex a distorted figure eight appearance (Gold et al., 1967; Gold, 1972). Both ring structures contain an outer region of alkalic silica-rich rocks and carbonatite along with a later central region of carbonatite (Treiman and Essene, 1985). The Oka carbonatite complex has been mined for niobium, which is found at three main occurrences – St. Lawrence Columbium Deposit (SLC), the Bond Zone, and the NIOCAN deposit. It is also one of the youngest carbonatite occurrences in North America with U-Pb ages ranging between 113 Ma and 135 Ma (Chen and Simonetti, 2014). Oxygen and carbon isotope compositions of Oka carbonatites suggest a primary igneous origin (Dennis and Schrag, 2010). This study includes three samples from the Oka carbonatite complex acquired from the Suffel Collection at the University of Western Ontario (Table 8).

Table 8 - Oka carbonatite samples included in this study.

Sample #	Sample Fractions Analyzed for Ca Isotopes	Sample Location Info
20346	- Bulk Rock (20346-Bulk) - Calcite mineral separate (20346-C)	- SLC deposit at the Oka complex
12162	- Bulk Rock (12162-Bulk) - Calcite mineral separate (12162-C)	- SLC deposit at the Oka complex
9399	- Bulk Rock (9399-Bulk) - Calcite mineral separate (9399-C) - Clinopyroxene mineral separate (9399-P)	- Unknown location at the Oka complex

3.1.2 Phalaborwa Carbonatites

The Phalaborwa (or Palabora) carbonatite complex is in northeastern Transvaal, South Africa, within the Kaapvaal craton. It is well-known as the only carbonatite occurrence containing copper mineralization of economic value. It is a concentrically zoned structure with a central pipe-like feature known as Loolekop. There are two distinct types of carbonatites in this location. The first is a medium- to coarse-grained banded carbonatite, and the second is a transgressive carbonatite in veinlets caused by subsequent fracturing of the Loolekop Pipe (Phalaborwa Mining Company Limited Mine Geological and Mineralogical staff, 1976). The transgressive carbonatite is where the Cu mineralization occurs and contains both calcite and dolomite, whereas the banded carbonatite contains just calcite. The banded and transgressive carbonatites have both been dated using U-Pb isotopes to an age of 2060 Ma (Wu et al., 2011). One other unique feature of Phalaborwa carbonatites is high and variable Sr isotopic compositions (Wu et al., 2011). Based on Sr, Nd, and Hf isotopic analyses of Phalaborwa carbonatites, a primary igneous origin derived from different batches of enriched and heterogeneous mantle sources is suggested (Wu et al., 2011). This study includes three carbonatite samples from the Phalaborwa carbonatite complex acquired from the Suffel Collection at the University of Western Ontario (Table 9).

Table 9 - Phalaborwa carbonatite samples included in this study.

Sample #	Sample Fractions Analyzed for Ca Isotopes	Sample Location Info
25865	- Bulk Rock (25865-Bulk) - Calcite mineral separate (25865-C)	- Sample of banded Phalaborwa carbonatite
25869	- Bulk Rock (25869-Bulk) - Mixed (calcite + dolomite) carbonate mineral separate (25869-C)	- Sample of transgressive Phalaborwa carbonatite
20414	- Bulk Rock (20414-Bulk) - Mixed (calcite + dolomite) carbonate mineral separate (20414-C)	- Undetermined but believed to be sample of transgressive Phalaborwa carbonatite

3.1.3 Lueshe Carbonatite

The Lueshe carbonatite complex is in the Rwindi Mountains in the northeastern Democratic Republic of Congo. It is a sub-elliptical pluton that intrudes into a 1100 Ma metamorphic rock sequence. The complex includes a core of syenite and a ring dyke structure of coarse-grained calcic carbonatite, as well as one area of medium to fine-grained dolomitic carbonatite in the southeast portion of the complex. The carbonatites here can contain microscopic sized veins of hydrothermal alteration and in some areas experienced significant weathering, especially in the dolomitic carbonatites (Nasraoui and Bilal, 2000). Despite the presence of altered and weathered carbonatites, stable carbon and oxygen isotope data for the calcic Lueshe carbonatites (Pineau and Javoy, 1969; Denaeyer, 1970) plot within the carbonatite field for unaltered carbonatites as defined by Taylor et al. (1967). Kramm et al. (1997) also suggest a primary magmatic origin for the Lueshe carbonatites based on Sr and Nd isotope data and REE distribution patterns. K-Ar dating gives an age of 516±26 Ma for the carbonatites (Bellon and Pouclet, 1980), while more recent Rb-Sr dating gives an age of about 558 Ma (Kramm et al., 1997). This study includes one sample from the Lueshe carbonatite complex acquired from the Suffel Collection at the University of Western Ontario (Table 10).

Table 10 - Lueshe carbonatite samples included in this study.

Sample #	Sample Fractions Analyzed for Ca Isotopes	Sample Location Info
10690	- Bulk Rock (10690-Bulk) - Calcite mineral separate (10690-C) - Orthopyroxene mineral separate (10690-P)	- Sample of coarse-grained, calcic Lueshe carbonatite

3.1.4 Nemegos Carbonatite

The Lackner Lake Complex is an alkalic syenite – carbonatite pluton that has intruded Archean gneisses near Nemegos, Ontario, Canada. It is a circular complex approximately 5.5 km in diameter and borders the Ivanhoe Lake fault zone, which is the boundary between the Wawa Subprovince and the Abitibi Subprovince (Symons, 1989). The complex is primarily composed of coarse-grained syenites with smaller zones of carbonatites, as well as veins of carbonatites

that contain niobium-rich pyrochlores (Symons, 1989). According to K-Ar dating, the age of the complex is 1086 ± 60 Ma (Lowden et al., 1963), while Rb-Sr dating has given ages of 1078 ± 7 Ma (Owen and Faure, 1977) and 1058 ± 22 Ma (Bell and Blenkinsop, 1980). This study includes one sample of carbonatite from the Lackner Lake Complex at Nemegos acquired from the Suffel Collection at the University of Western Ontario (Table 11).

Table 11 - Nemegos carbonatite samples included in this study.

Sample #	Sample Fractions Analyzed for Ca Isotopes	Sample Location Info
10673b	- Bulk Rock (10673b-Bulk) - Calcite mineral separate (10673b-C) - Clinopyroxene mineral separate (10673b-P) - Apatite mineral separate (10673b-A)	- Sample from undisclosed location at the Nemegos carbonatite deposit

3.1.5 Cape Verde Archipelago Carbonatites

The Cape Verde archipelago is a chain of 10 volcanic islands and several smaller islets located 450 km off the coast of Senegal in western Africa. They are situated on top of the Cape Verde Rise, an oceanic mega-swell considered to be the result of a mantle plume (e.g. Montelli et al., 2006; Zhao, 2007). The islands are renowned as one of the only occurrences of oceanic carbonatites on Earth. The carbonatites here are intrusive and are relatively young, with Brava carbonatites dated to about 1.55 Ma (Madeira et al., 2010), and Fogo carbonatites dated to approximately 3.4 Ma (Lancelot and Allegre, 1974). As one of the rare occurrences of oceanic carbonatites, they have been studied using many different isotopic systems in recent years including: Sr-Nd (Doucelance et al., 2010), noble gases and C (Mata et al., 2010), as well as Ce-Nd and Pb (Doucelance et al., 2014). These isotopic studies suggest that the origin of the Cape Verde carbonatites involves a mixing of a depleted mantle source and either recycled marine carbonates or a deep primordial mantle source, with the more recent Ce-Nd isotopic study favouring the recycling of marine carbonates (Doucelance et al., 2014). This study includes three samples from the Cape Verde archipelago acquired from Dr. Regis Doucelance at Clermont Université, France (Table 12).

Table 12 - Cape Verde carbonatite samples included in this study.

Sample #	Sample Fractions Analyzed for Ca Isotopes	Sample Location Info
F1C	- Bulk rock sample only	- Ca-carbonatite from Fogo Island
CY 250	- Bulk rock sample only	- Ca-carbonatite from Brava Island
CY 114	- Bulk rock sample only	- Mg-carbonatite from Brava Island

3.1.6 Tamazert Massif (Morocco) Carbonatites

The Tamazert Massif of the High Central Atlas Range of Morocco contains some of the largest occurrences of outcropping carbonatites in northern Africa. The High Atlas Range extends for more than 2000km in an east-west direction from Morocco to Algeria and Tunisia and the Tamazert complex is found on the north side of the central region of this range. It is an elliptically shaped intrusion (17km x 5km) that covers around 70 km^2 consisting of silica-undersaturated alkaline rocks and carbonatites that have intruded into Jurassic carbonates. The carbonatites have been dated to an age of 39 Ma (Bouabdellah et al., 2010). Ce-Nd and Pb isotopic studies by Doucelance et al., (2014) indicate a similar origin for the Tamazert and Cape Verde carbonatites. This study includes three carbonatite samples from the Tamazert Massif acquired from Dr. Regis Doucelance at Clermont Université, France (Table 13).

Table 13 - Tamazert carbonatites included in this study.

Sample #	Sample Fractions Analyzed for Ca Isotopes	Sample Location Info
TA 2a92	- Bulk rock sample only	- Ca-carbonatite from Tamazert Massif
TA 1692	- Bulk rock sample only	- Ca-carbonatite from Tamazert Massif
TA 1792	- Bulk rock sample only	- Ca-carbonatite from Tamazert Massif

3.2 Kimberlites and Related Rocks

This work includes one kimberlite sample along with two kimberlite related peridotite samples.

3.2.1 Kimberley Area Kimberlite

The area surrounding Kimberley, South Africa is home to a cluster of kimberlite pipe deposits including five major deposits and many smaller pipes. The discovery of diamonds and their association with these kimberlites in the late 19th century sparked a rush of diamond mining in the area and led to the discovery of many diamond mines in South Africa (Field et al., 2008). The Kimberley area kimberlites intrude Archean-aged basement gneisses of the Kaapvaal Craton. The age of this cluster of kimberlite pipes has been dated at 84 ± 3 Ma (Clement et al., 1979). Kimberlites from the major kimberlite pipes in the Kimberley area have been classified as group I kimberlites (Le Roex et al., 2003) This study includes one kimberlite sample from Kimberley, South Africa acquired from the rock and mineral collections at the University of Minnesota (Table 14).

Table 14 - Kimberley kimberlites included in this study.

Sample #	Sample Fractions Analyzed for Ca Isotopes	Sample Location Info
R841	- Bulk Rock (R841-Bulk) - Calcite mineral separate (R841-C) - Clinopyroxene mineral separate (R841-P) - Two amphibole mineral separates (R841-Am1 and R841-Am2)	- Sample from undisclosed location around Kimberley, South Africa

3.2.2 Kaapvaal Craton Peridotites

The Kaapvaal Craton covers an area of approximately 1.2 x 10^6 km^2 and consists of mainly tonalitic gneisses and granite greenstones that formed and stabilized sometime between 3.7 and 2.6 Ga (de Wit et al., 1992). It has been subdivided into four terranes: The Western Terrane, the Southeastern Terrane, the Central Terrane, and the Pietersburg Terrane (Begg et al., 2009). The area of Kimberley, South Africa, and its many kimberlite pipes, can be found in the Western Terrane of the Kaapvaal Craton. Along with diamonds, kimberlite pipes in this region often carry mantle peridotite xenoliths to the Earth's surface (Le Roex et al., 2003). This study includes two peridotite samples from the Kaapvaal craton acquired from the Suffel Collection at the University of Western Ontario (Table 15).

Table 15 - Kaapvaal peridotites included in this study.

Sample #	Sample Fractions Analyzed for Ca Isotopes	Sample Location Info
16965	- Orthopyroxene mineral separate only (16965-P)	- Peridotite sample from diatreme in the Kaapvaal craton, unknown location
16962	- Bulk rock (16962-Bulk) - Orthopyroxene mineral separate (16962-P)	- Peridotite sample from diatreme in the Kaapvaal craton, unknown location

3.3 External Standards

This study includes three samples that were used as external standards since their Ca isotopic composition has already been published in one or more scientific works.

3.3.1 San Carlos Peridotite

The San Carlos ultramafic inclusion region is located on Peridot Mesa within the San Carlos Apache Reservation, approximately 30 km east of Globe, Arizona, USA. The region is known for abundant, large and coarse-grained peridotite inclusions. The San Carlos peridotites can be divided into two groups, Group I xenoliths which are more Cr and Mg rich and dominated by spinel lherzolites, and Group II xenoliths which are Fe and Ti rich, contain a wide variety of rock types, and are much less common (Frey and Prinz, 1978). The Ca isotopic composition of clinopyroxenes and orthopyroxenes from the San Carlos mantle peridotites have been published by Huang et al. (2010). The San Carlos mantle peridotite samples in this study were collected and provided by Dr. Audrey Bouvier (Table 16).

Table 16 - San Carlos peridotite samples included in this study.

Sample #	Sample Fractions Analyzed for Ca Isotopes	Sample Location Info
San Carlos	- Clinopyroxene mineral separate (SC-Cpx) - Orthopyroxene mineral separate (SC-Opx) - Olivine mineral separate (SC-Olv)	- San Carlos peridotites from the San Carlos ultramafic inclusion

3.3.2 Kilbourne Hole Peridotite

The Kilbourne Hole maar is an eruptive center in the Potrillo Volcanic Field in the Rio Grande Rift in southern New Mexico. It is sub-elliptical in shape, around 3 km wide, and 100-125 m deep. The age of the maar eruption has been dated at approximately 20,000 years ago using ^{3}He surface exposure dating (Anthony and Poths, 1992; Williams, 1999). The eruption brought an abundant supply of mantle xenoliths to the surface. The types of xenoliths include peridotite (lherzolite, harzburgites, and dunites) and clinopyroxenites, with the dominant lithology being lherzolite peridotites (Irving, 1980). Huang et al. (2010) analyzed the Ca isotopic compositions of the clinopyroxenes and orthopyroxenes in Kilbourne Hole peridotites. The Kilbourne Hole mantle peridotite samples in this study were provided by Dr. Tony Withers (Table 17).

Table 17 - Kilbourne Hole peridotites included in this study.

Sample #	Sample Fractions Analyzed for Ca Isotopes	Sample Location Info
Kilbourne Hole	- Clinopyroxene mineral separate (KH-Cpx) - Orthopyroxene mineral separate (KH-Opx) - Olivine mineral separate (KH-Olv)	- Kilbourne Hole peridotites from the Kilbourne Hole maar

3.3.3 BCR-2

Basalt, Columbia River (BCR-2) is a United States Geological Survey (USGS) reference material. The material used to prepare BCR-2 was collected in 1996 from the Bridal Veil Flow Quarry, located approximately 29 miles east of Portland, Oregon, USA, under the direction of Stephen A. Wilson, U.S. Geological Survey (Wilson, 1997). The elemental concentrations were determined during an extensive study involving twenty international laboratories (Table 18). The Ca isotopic composition of BCR-2 has already been published in many scientific papers (e.g. Valdes et al., 2014; Kang et al., 2017).

Table 18 - Major element concentrations in USGS reference material BCR-2. Table redrawn from Wilson (1997).

Oxide	Wt %	±
Al_2O_3	13.5	0.2
CaO	7.12	0.11
$Fe_2O_{3\ tot}$	13.8	0.2
K_2O	1.79	0.05
MgO	3.59	0.05
Na_2O	3.16	0.11
P_2O_5	0.35	0.02
SiO_2	54.1	0.8
TiO_2	2.26	0.05

3.4 Other Samples

This work includes two additional samples that do not fall into any of the other sample categories.

3.4.1 Bancroft Marble

This sample of marble from Bancroft, Ontario, Canada was collected and provided by Dr. Tony Withers (Table 19). Not much is known about the tectonic history or geologic setting of where this sample originated from, nor is the age of the sample known. Despite the relative paucity of information regarding this sample, it was available in abundance and contained both carbonate and silicate minerals and therefore was used as a preliminary sample in this study to fine-tune sample preparation and chemical purification procedures without using more valuable samples.

Table 19 - Bancroft marble samples included in this study.

Sample #	Sample Fractions Analyzed for Ca Isotopes	Sample Location Info
Bancroft Marble	- Clinopyroxene mineral separate (BC-Cpx) - Calcite mineral separate (BC-C)	- Bancroft, Ontario, Canada

3.4.2 Twin Sisters Ultramafic Complex

The Twin Sisters ultramafic complex is in Washington, USA, in the North Cascades Mountains of the North American Cordillera approximately 6km southwest of Mount Baker. It is an elliptical shaped body around 6 x 16 km and is believed to extend to a depth of approximately 2 km based on gravity modeling (Thompson and Robinson, 1975; Brown et al., 1987). The Twin Sisters complex consists of only ultramafic rocks, dominated by dunite and harzburgite peridotites, with several generations of orthopyroxenite and clinopyroxenite veins, all of which are of mantle origin (Ragan, 1961) and experienced natural deformation processes in the upper mantle (Kruckenberg et al., 2013). The age of the Twin Sisters complex is currently unknown, but it provides access to some of the world's most pristine outcrops of upper mantle materials. The Twin Sisters mantle peridotite samples in this study were collected and provided by Dr. Tony Withers (Table 20)

Table 20 - Twin Sisters peridotite samples included in this study.

Sample #	Sample Fractions Analyzed for Ca Isotopes	Sample Location Info
Twin Sisters	- Clinopyroxene mineral separate (TS-Cpx) - Orthopyroxene mineral separate (TS-Opx) - Bulk rock dunite (TS-WR)	- Mantle peridotites from undisclosed location in the Twin Sisters ultramafic complex

Chapter 4

4. Results

4.1 Microprobe Data

Major element compositions for mineral separates analyzed in this study were determined using electron microprobe analysis at the University of Western Ontario. Data for carbonate and silicate mineral separates in carbonatite, kimberlite, and other samples are given in Tables 21-25.

Table 21 - Major element compositions of carbonate mineral separates from carbonatite samples in this study. CO_2 totals were calculated by difference.

	Nemegos		Lueshe		Oka					
	10673b-C (Calcite)		10690-C (Calcite)		20346-C (Calcite)		9399-C (Calcite)		12162-C (Calcite)	
SiO_2	0.02	±0.01	0.03	±0.02	0.00	±0.01	0.02	±0.01	0.01	±0.01
MgO	0.10	±0.01	0.23	±0.02	0.10	±0.03	0.04	±0.02	0.11	±0.02
CaO	52.45	±0.65	53.27	±0.21	54.64	±0.40	55.46	±0.47	54.71	±0.19
BaO	0.07	±0.05	0.06	±0.04	0.12	±0.04	0.05	±0.06	0.23	±0.07
FeO	0.42	±0.09	0.77	±0.04	0.05	±0.03	0.02	±0.04	0.02	±0.03
MnO	0.23	±0.03	0.51	±0.03	0.20	±0.03	0.03	±0.03	0.17	±0.05
K_2O	0.00	±0.00	0.00	±0.00	-	-	-		-	-
SrO	2.34	±0.54	1.02	±0.10	1.72	±0.18	1.44	±0.13	1.37	±0.06
CO_2	44.37		44.11		43.17		42.94		43.38	
Total	100.00		100.00		100.00		100.00		100.00	
n	9		9		6		5		5	
	Phalaborwa									
	25865-C (Calcite)		25869-C (Calcite)		25869-C (Dolomite)		20414-C (Calcite)		20414-C (Dolomite)	
SiO_2	0.03	±0.02	0.01	±0.02	0.01	±0.01	0.00	±0.01	0.00	±0.01
MgO	2.42	±0.55	1.68	±0.16	20.38	±0.23	2.51	±0.14	19.63	±0.13
CaO	51.69	±0.74	52.82	±0.10	30.59	±0.17	51.00	±0.50	30.66	±0.17
BaO	0.12	±0.06	0.03	±0.06	0.00	±0.06	0.00	±0.05	0.03	±0.05
FeO	0.39	±0.05	0.32	±0.02	1.41	±0.09	0.64	±0.00	2.33	±0.23
MnO	0.07	±0.05	0.09	±0.02	0.12	±0.02	0.27	±0.02	0.25	±0.01
K_2O	-	-	-	-	-	-	-		-	-
SrO	0.51	±0.07	0.74	±0.03	0.36	±0.02	1.03	±0.11	0.55	±0.07
CO_2	44.77		44.31		47.13		44.55		46.55	
Total	100.00		100.00		100.00		100.00		100.00	
n	5		3		3		3		3	

Table 22 - Major element compositions for silicate mineral separates from carbonatite samples in this study.

	Nemegos		Lueshe		Oka	
	10673b-P		10690-P		9399-P	
SiO_2	49.47	±0.53	51.54	±0.13	35.88	±0.15
Al_2O_3	0.51	±0.16	2.26	±0.20	0.04	±0.02
Na_2O	1.87	±0.17	12.49	±0.07	0.03	±0.03
MgO	5.24	±0.72	0.26	±0.03	17.93	±0.17
TiO_2	0.13	±0.08	0.24	±0.02	0.04	±0.03
CaO	19.66	±0.38	0.48	±0.09	32.62	±0.17
FeO	19.84	±0.79	27.24	±0.28	7.66	±0.40
MnO	1.11	±0.05	0.01	±0.01	4.74	±0.16
K_2O	0.00	±0.00	0.00	±0.00	0.00	±0.01
NiO	0.00	±0.00	0.01	±0.01	0.01	±0.01
Cr_2O_3	0.01	±0.02	0.01	±0.01	0.00	±0.01
Total	97.84	±0.44	94.54	±0.22	98.95	±0.30
n	5		8		5	

Table 23 - Major element compositions of carbonate and silicate mineral separates from Kimberley kimberlite and Kaapvaal peridotite samples in this study. CO_2 totals were calculated by difference.

	Kimberley	
	R841-C (Calcite)	
SiO_2	0.03	±0.02
MgO	0.01	±0.01
CaO	57.27	±0.26
BaO	0.00	±0.03
FeO	0.00	±0.02
MnO	0.00	±0.01
K_2O	-	-
SrO	0.37	±0.30
CO_2	42.32	
Total	100.00	
n	4	

	Kimberley				Kaapvaal			
	R841-P		R841-Am		16962-P		16965-P	
SiO_2	54.40	±0.16	54.69	±0.52	57.87	±0.38	55.46	±0.06
Al_2O_3	2.42	±0.38	1.16	±0.03	0.80	±0.01	3.04	±0.18
Na_2O	1.92	±0.28	3.40	±0.09	0.13	±0.02	0.02	±0.00
MgO	16.30	±0.71	22.30	±0.49	36.74	±0.06	34.30	±0.23
TiO_2	0.06	±0.04	0.34	±0.03	0.00	±0.02	0.00	±0.01
CaO	20.28	±0.13	6.93	±0.03	0.29	±0.02	0.84	±0.09
FeO	2.20	±0.30	2.73	±0.03	3.46	±0.05	4.50	±0.07
MnO	0.05	±0.03	0.04	±0.01	0.08	±0.02	0.12	±0.04
K_2O	0.02	±0.01	3.91	±0.06	0.01	±0.01	0.01	±0.01
NiO	0.06	±0.02	0.07	±0.02	0.10	±0.02	0.07	±0.01
Cr_2O_3	1.67	±0.04	0.31	±0.01	0.38	±0.02	0.77	±0.06
Total	99.38	±0.21	95.88	±1.10	99.86	±0.43	99.13	±0.18
n	7		6		5		5	

Table 24 - Major element compositions of carbonate and silicate mineral separates from Bancroft marble samples in this study. CO_2 totals were calculated by difference.

	Bancroft			Bancroft	
	BC-C (Calcite)			BC-Cpx	
SiO_2	0.02	±0.02	SiO_2	53.91	±0.27
MgO	0.36	±0.03	Al_2O_3	0.53	±0.12
CaO	55.58	±0.28	Na_2O	0.48	±0.17
BaO	0.00	±0.06	MgO	16.26	±0.78
FeO	0.19	±0.03	TiO_2	0.03	±0.02
MnO	0.04	±0.03	CaO	24.77	±0.49
K_2O	0.00	±0.01	FeO	3.11	±1.05
SrO	0.33	±0.04	MnO	0.18	±0.05
CO_2	43.48		K_2O	0.00	±0.00
Total	100.00		NiO	0.00	±0.01
n	18		Cr_2O_3	-	-
			Total	99.27	±0.22
			n	33	

Table 25 - Major element compositions of silicate mineral separates for Twin Sisters and Kilbourne Hole peridotite samples in this study.

	Twin Sisters				Kilbourne Hole					
	TS-Cpx		TS-Opx		KH-Cpx		KH-Opx		KH-Olv	
SiO_2	53.69	±0.19	56.42	±0.09	51.51	±0.12	54.32	±0.04	40.38	±0.13
Al_2O_3	0.89	±0.09	0.87	±0.05	7.27	±0.12	4.95	±0.09	0.02	±0.01
Na_2O	0.30	±0.02	0.01	±0.01	1.57	±0.07	0.09	±0.01	0.00	±0.01
MgO	17.70	±0.12	34.68	±0.18	14.92	±0.07	32.34	±0.12	48.45	±0.19
TiO_2	0.03	±0.01	0.02	±0.01	0.53	±0.02	0.11	±0.02	0.01	±0.01
CaO	23.91	±0.12	0.39	±0.08	19.97	±0.12	0.70	±0.01	0.07	±0.00
FeO	1.74	±0.10	5.82	±0.11	2.91	±0.08	6.39	±0.03	10.02	±0.07
MnO	0.07	±0.01	0.15	±0.02	0.09	±0.01	0.15	±0.01	0.16	±0.01
K_2O	0.00	±0.00	0.00	±0.00	0.00	±0.01	0.00	±0.00	0.01	±0.00
NiO	0.04	±0.01	0.10	±0.01	0.03	±0.02	0.08	±0.03	0.36	±0.03
Cr_2O_3	0.72	±0.04	0.40	±0.03	0.74	±0.04	0.32	±0.02	0.01	±0.01
Total	99.09	±0.15	98.86	±0.17	99.54	±0.25	99.45	±0.13	99.49	±0.27
n	7		7		6		6		6	

4.2 XRF Data

Bulk rock major element compositions were determined using X-ray fluorescence (XRF) at the University of Western Ontario for several of the samples in this study (Table 26).

Table 26 - Major element concentrations of bulk rock samples analyzed using XRF in this study (in %). BDL = Below Detection Limit.

	Kimberley kimberlite	Nemegos carbonatite	Lueshe carbonatite	Oka carbonatite
	R841	**10673b**	**10690**	**9399**
SiO2	41.01	1.75	9.08	4.03
TiO2	0.67	0.10	0.11	0.25
Al2O3	5.64	0.21	0.50	0.71
Fe2O3	7.58	3.65	7.69	2.17
MnO	0.12	0.23	0.37	0.46
MgO	25.95	0.53	0.46	2.08
CaO	4.50	46.92	41.18	44.53
K2O	1.26	0.02	0.02	0.25
Na2O	1.45	0.22	2.14	0.24
P2O5	0.46	3.65	1.45	4.42
Cr2O3	0.18	BDL	BDL	BDL
BaO	0.05	0.06	0.04	0.13
SrO	0.05	1.97	0.70	0.90
LOI	11.53	35.13	31.67	31.26
Total	100.44	94.42	95.38	91.43

4.3 Minor and Trace Element Data

Minor and trace element analyses of bulk rock samples in this study were conducted using ICP-MS at the University of Western Ontario. The complete results of these analyses are provided in Table 27. Figure 18 plots chondrite-normalized rare-earth element (REE) data for these samples.

Table 27 - Minor and trace element concentrations of bulk rock samples in this study (all concentrations in parts per million).

	Bancroft	10690	10673b	R841	12162	16962	9399	20346	20414	16965	25865	25869
K	2529	< 1229	< 1229	10028	2609	2917	2669	1160	26958	388	783	387
Sc	2.5	3.2	1.4	13.2	0.8	4.9	1.1	0.8	10.6	5.7	7.1	4.3
Ti	611	836	737	4141	1309	939	1732	761	2910	17	479	177
V	41.5	389.6	16.5	91.9	165.0	32.2	123.2	139.5	128.7	32.2	22.7	1.6
Cr	10	< 7.5	< 7.5	1167	5	1640	4	17	21	2519	19	5
Mn	862	3068	1991	905	5054	725	4505	2499	1444	813	693	762
Fe	17662	51694	22000	56001	30283	46908	17406	10037	94528	52355	19460	43657
Co	4	2	5	72	1	96	2	1	102	104	11	133
Ni	8	< 6.5	< 6.5	1251	4	2393	3	19	43	2437	31	188
Cu	7	< 6.5	14	50	6	18	5	4	6944	7	224	18441
Zn	138	7	40	61	153	38	105	44	65	42	14	38
Rb	7.5	0.7	2.2	54.7	24.0	14.8	16.4	9.1	187.4	1.5	1.6	0.9
Sr	1316	6644	20506	590	10714	80	10359	14661	3396	6	3820	5019
Y	38.0	45.1	156.5	11.8	107.8	1.0	115.2	93.8	50.8	0.1	68.4	47.9
Zr	21	219	99	181	86	14	103	34	161	1	59	7
Nb	4.2	3602.6	1403.3	47.9	851.5	9.3	1150.1	1861.7	9.2	0.3	0.7	0.2
Ba	243	331	494	440	2111	91	1429	1161	2106	6	710	159
La	137.4	148.8	738.3	58.5	1106.0	7.2	1584.5	1049.6	319.9	0.3	213.7	305.6
Ce	235.5	317.7	1528.3	117.9	2096.3	14.0	2816.5	1988.1	747.5	0.4	492.2	755.5
Pr	23.1	34.7	173.6	13.1	188.0	1.5	253.2	176.2	90.4	0.0	63.4	94.4
Nd	72.8	120.4	591.2	46.8	617.4	5.8	799.6	563.8	387.2	0.2	278.8	422.4
Sm	10.0	19.3	91.7	7.3	78.0	1.0	93.4	69.8	68.9	0.1	55.3	74.4
Eu	2.2	5.6	26.8	1.9	19.9	0.2	23.2	17.4	14.0	0.0	12.3	11.8
Gd	8.0	15.9	68.7	5.3	51.5	0.6	59.6	45.5	43.7	0.0	41.3	42.0
Tb	1.1	2.1	8.3	0.6	5.5	0.1	6.0	4.8	4.3	0.0	4.5	4.0
Dy	6.0	10.9	39.9	3.0	24.7	0.3	25.8	21.5	16.2	0.0	19.1	14.5
Ho	1.2	2.0	6.7	0.5	4.1	0.0	4.3	3.6	2.1	0.0	2.7	1.9
Er	4.0	5.2	17.2	1.3	10.7	0.1	11.3	9.4	4.4	0.0	5.6	3.9
Tm	0.6	0.7	2.0	0.2	1.3	0.0	1.3	1.1	0.4	0.0	0.5	0.3
Yb	4.3	4.2	11.0	1.0	7.6	0.1	7.7	6.5	2.2	0.0	2.5	1.7
Lu	0.7	0.6	1.3	0.1	1.0	0.0	1.0	0.8	0.3	0.0	0.3	0.2
Hf	0.6	7.4	1.1	4.5	0.3	0.4	0.3	0.2	2.8	0.0	1.4	0.1
Ta	0.1	8.2	8.6	1.1	80.7	0.5	139.9	10.7	0.7	0.0	0.1	0.0
W	0.2	0.6	0.2	1.6	0.8	1.2	0.8	0.3	0.3	0.7	0.2	0.1
Pb	23.1	3.3	14.9	6.8	1.1	1.1	1.3	0.9	4.1	0.3	1.4	4.2
Th	213.2	28.6	117.7	8.6	1.8	0.9	11.8	2.4	50.4	0.0	4.1	55.0
U	52.8	12.7	26.1	2.6	9.4	0.2	23.8	0.5	14.9	0.0	0.8	23.6

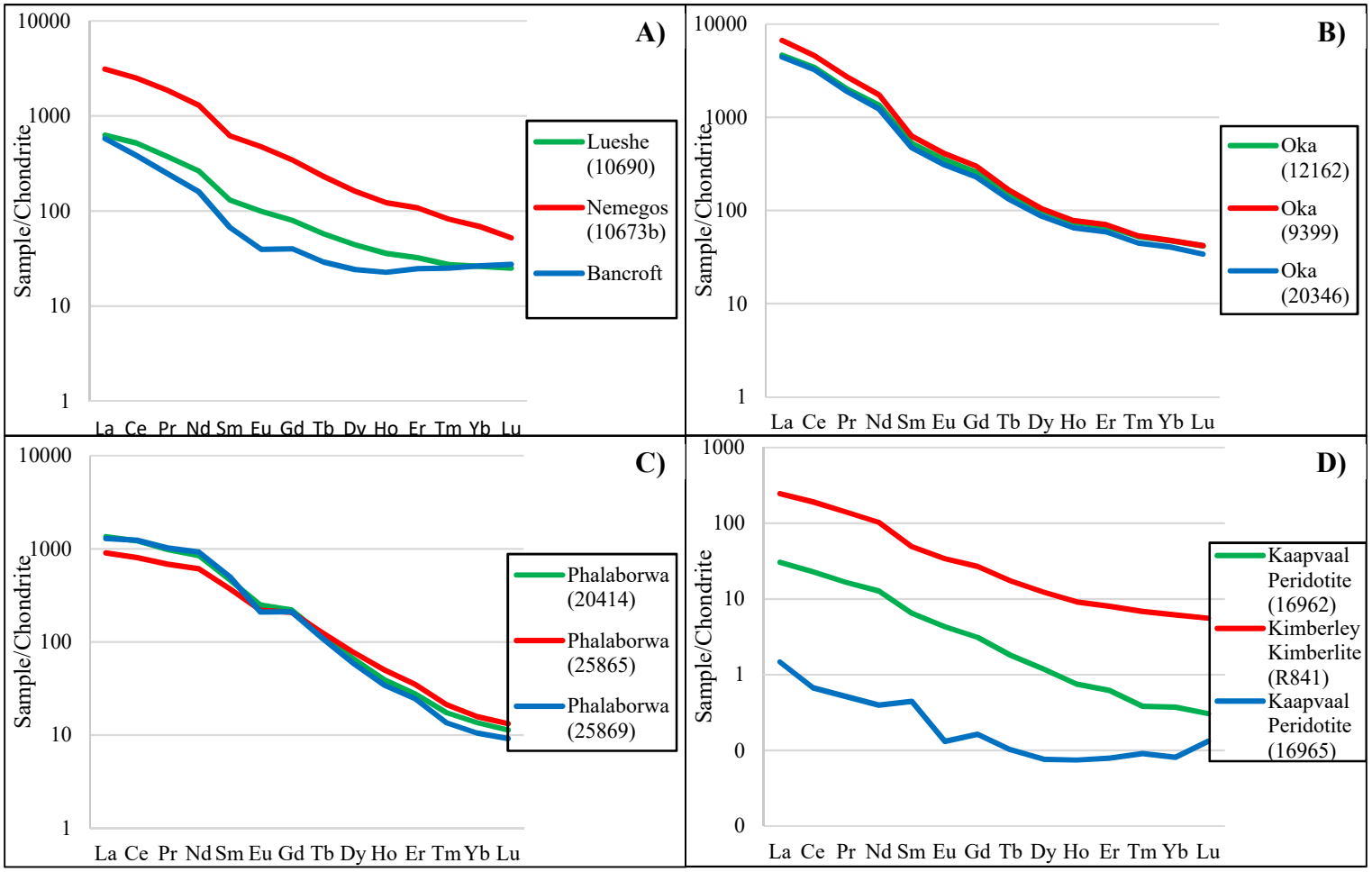

Figure 18 - Chondrite normalized rare-earth element spider plots for samples in this study: A) Lueshe carbonatite, Nemegos carbonatite, and Bancroft marble samples; B) Oka carbonatite samples; C) Phalaborwa carbonatite samples; D) Kimberley kimberlite and Kaapvaal peridotite samples. Normalizing values for chondrite are from McDonough and Sun (1995).

4.4 Calcium Isotopic Data for Natural Samples

Calcium isotopic data are presented in this chapter as $\delta^{44}Ca/^{42}Ca$ relative to SRM915b, $\delta^{44}Ca/^{42}Ca$ relative to SRM915a, and $\delta^{44}Ca/^{40}Ca$ relative to SRM915a. Initial analyses provided data as $\delta^{44}Ca/^{42}Ca$ relative to SRM915b which was subsequently converted using the equations and methods outlined in Chapter 2.

4.4.1 SRM915b and External Standards

The SRM915b Ca isotopic standard that was passed through the full Ca purification procedure along with every set of samples was measured relative to the unprocessed SRM915b bracketing standard during each analytical session. This was done to ensure the chemistry procedure was not introducing any fractionation as well as to monitor instrument stability and long-term reproducibility of the analyses. The calcium isotopic compositions of the SRM915b standards used in this study are provided in Table 28 and the long-term reproducibility (0.00 ± 0.07‰, n = 16) is illustrated in Figure 19.

Table 28 – $\delta^{44/42}$Ca values for SRM915b samples analyzed in this study.

	Date of Analysis	**Mean $\delta^{44/42}$Ca Rel. SRM915b (in ‰)**	**2 SD**	**N (repeats)**
SRM915b Standards	September 2016	+0.01	0.05	3
	October 2016	+0.07	0.04	3
	October 2016	+0.01	0.16	3
	October 2016	−0.07	0.11	3
	October 2016	+0.02	0.02	3
	January 2017	+0.01	0.15	4
	January 2017	+0.01	0.13	3
	January 2017	+0.02	0.14	3
	March 2017	+0.01	0.05	3
	March 2017	+0.01	0.10	4
	June 2017	−0.01	0.13	13
	June 2017	−0.02	0.06	4
	June 2017	+0.05	0.13	3
	June 2017	+0.02	0.16	3
	September 2017	−0.04	0.05	4
	September 2017	−0.06	0.05	4

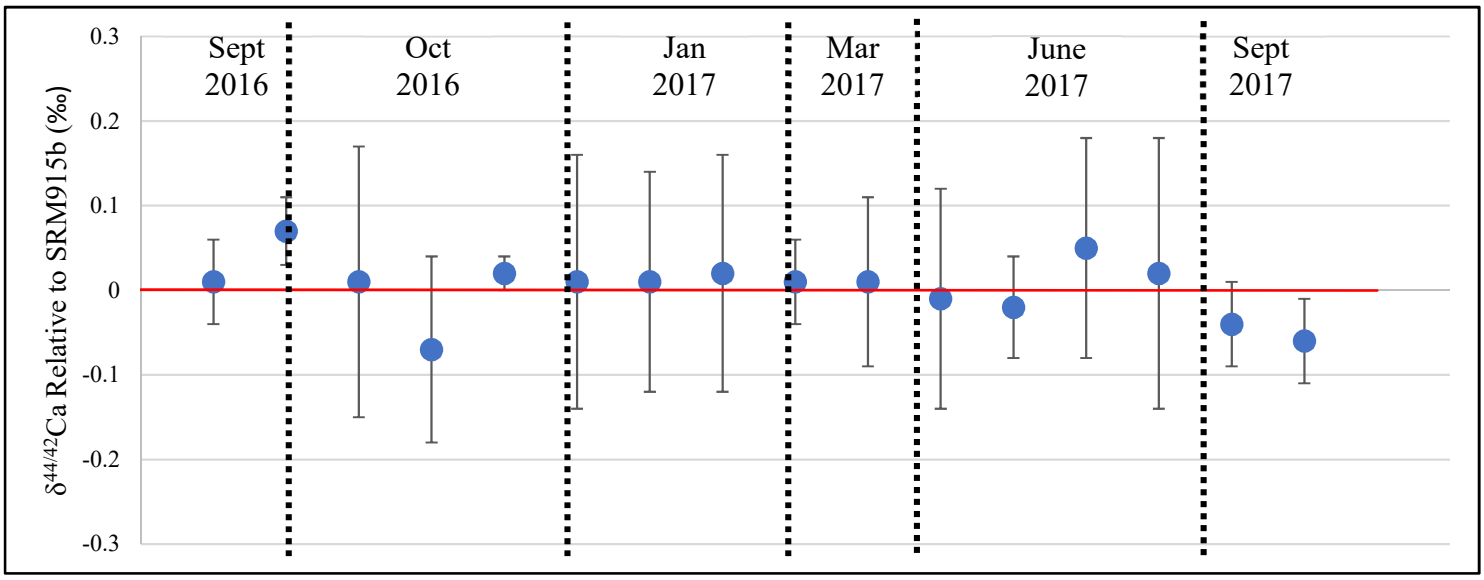

Figure 19 - Long-term reproducibility of SRM915b standard over duration of this study (0.00 ± 0.07‰, n = 16).

The calcium isotopic compositions of external standards used in this study are provided in Table 29. All the analyses of external standards matched within error the data provided in previously published works (Table 29, Figure 20). Full procedural replicates for San Carlos clinopyroxene samples were identical within error (+0.47 ± 0.03‰ and +0.55 ± 0.12‰), as were full procedural replicates for Kilbourne Hole clinopyroxene samples (+0.37 ± 0.08‰ and +0.46 ± 0.05‰) (Figure 20). Unleached samples of both San Carlos clinopyroxenes (+0.50 ± 0.12‰) and Kilbourne Hole clinopyroxenes (+0.39 ± 0.08‰) were identical within error to their respective leached clinopyroxenes (Figure 20). A San Carlos clinopyroxene sample that underwent two rounds of matrix removal step #1 chemistry (+0.45 ± 0.08‰) was also identical within error compared to the samples put through only one round of this purification step (Figure 20).

Table 29 - Calcium isotopic compositions of external standards analyzed in this study. Published values for San Carlos and Kilbourne Hole samples are from Huang et al. (2010), published value for BCR-2 is from Valdes et al. (2014).

	$\delta^{44/42}$Ca Rel. SRM915b (in ‰)	2 SD	N (repeats)	$\delta^{44/42}$Ca Rel. SRM915a (in ‰)	Published $\delta^{44/42}$Ca Rel. SRM915a (in ‰)	2 SD	Difference from Published $\delta^{44/42}$Ca Rel. SRM915a Value (in ‰)
San Carlos							
Clinopyroxene	+0.12	0.03	3	+0.47	+0.49	0.04	−0.02
Clinopyroxene (full replicate)	+0.20	0.12	3	+0.55	+0.49	0.04	+0.06
Clinopyroxene (full replicate with two matrix removal step 1 passes)	+0.10	0.08	3	+0.45	+0.49	0.04	−0.04
Clinopyroxene (unleached)	+0.15	0.12	4	+0.50	+0.49	0.04	+0.01
Clinopyroxene (unleached full replicate)	+0.15	0.17	8	+0.50	+0.49	0.04	+0.01
Orthopyroxene	+0.32	0.07	4	+0.67	+0.64	0.06	+0.03
BCR-2							
Bulk	+0.08	0.1	4	+0.43	+0.43	0.09	0.00
Kilbourne Hole							
Clinopyroxene	+0.02	0.08	3	+0.37	+0.43	0.02	−0.06
Clinopyroxene (full replicate)	+0.11	0.05	4	+0.46	+0.43	0.02	+0.03
Clinopyroxene (Unleached)	+0.04	0.08	3	+0.39	+0.43	0.02	−0.04
Orthopyroxene	+0.41	0.11	4	+0.76	+0.81	0.07	−0.05

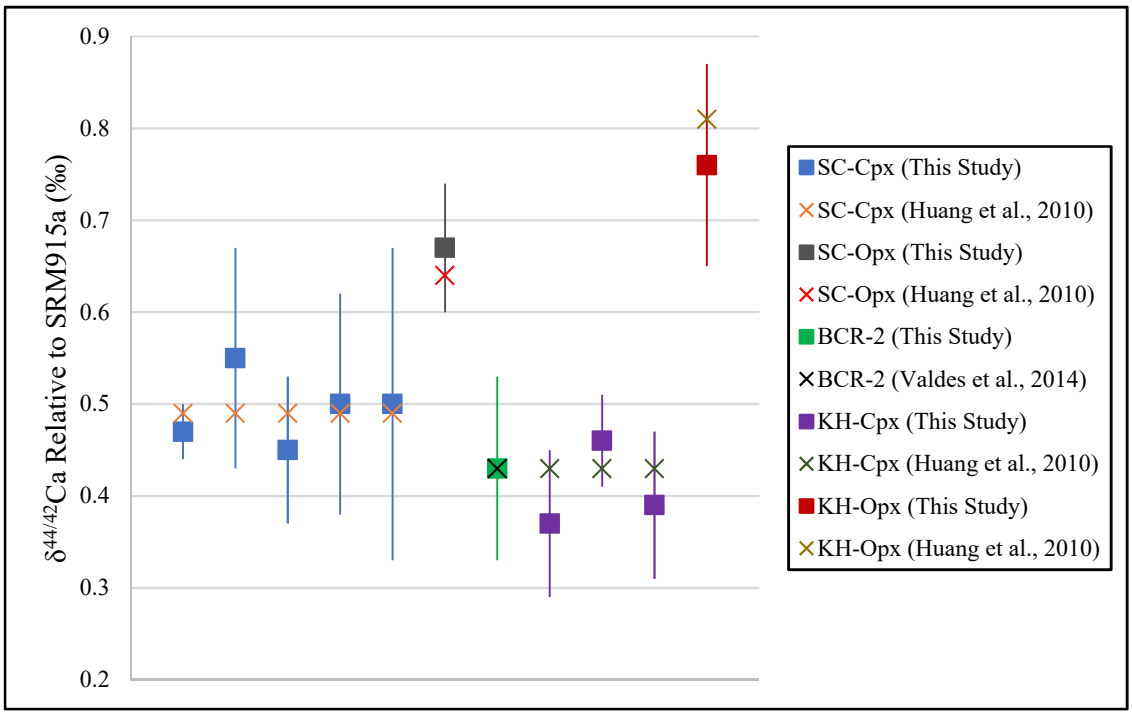

Figure 20 - Ca isotope data for external standards in this study compared to previously published values.

4.4.2 Carbonatites

The calcium isotopic compositions of all carbonatites studied in this work are provided in Table 30 and illustrated in Figure 21. Bulk rock $\delta^{44/40}$Ca data is provided, as well as any Ca-bearing mineral separates that were available for analysis in each sample.

The $\delta^{44/40}$Ca for bulk carbonatites in this study ranges from +0.43 ± 0.18‰ in sample 25865, to +1.29 ± 0.16‰ in sample 10673b, with an overall average value for bulk carbonatites of +0.91‰. Bulk rock $\delta^{44/40}$Ca data for carbonatites is illustrated in Figure 22.

Table 30 – Calcium isotopic composition of carbonatites analyzed in this study.

		$\delta^{44/42}$Ca Rel. SRM915b (in ‰)	2 SD	N (repeats)	$\delta^{44/42}$Ca Rel. SRM915a (in ‰)	$\delta^{44/40}$Ca Rel. SRM915a (in ‰)	2 SD
Nemegos	**10673b**						
	Bulk	+0.28	0.08	4	+0.63	+1.29	0.16
	Carbonate (calcite)	+0.69	0.15	3	+1.04	+2.13	0.31
	Pyroxene (Cpx)	−0.20	0.13	4	+0.15	+0.31	0.27
	Apatite	+0.36	0.06	3	+0.71	+1.45	0.12

Lueshe	**10690**						
	Bulk	+0.18	0.11	3	+0.53	+1.09	0.23
	Carbonate (calcite)	+0.29	0.17	6	+0.64	+1.31	0.35
	Pyroxene (Opx)	+0.05	0.13	3	+0.40	+0.82	0.27
Oka	**20346**						
	Bulk	+0.07	0.07	4	+0.42	+0.86	0.14
	Carbonate (calcite)	+0.20	0.08	3	+0.55	+1.13	0.16
	12162						
	Bulk	+0.16	0.05	4	+0.51	+1.04	0.10
	Carbonate (calcite)	+0.19	0.10	6	+0.54	+1.11	0.20
	9399						
	Bulk	+0.14	0.07	4	+0.49	+1.00	0.14
	Carbonate (calcite)	−0.06	0.10	8	+0.29	+0.59	0.20
	Pyroxene (Cpx)	+0.03	0.07	3	+0.38	+0.78	0.14
Phalaborwa	**25865**						
	Bulk	−0.14	0.09	8	+0.21	+0.43	0.18
	Carbonate (calcite)	+0.03	0.07	4	+0.38	+0.78	0.14
	25869						
	Bulk	+0.17	0.04	4	+0.52	+1.07	0.08
	Carbonate (calcite + dolomite)	−0.08	0.11	3	+0.27	+0.55	0.23
	20414						
	Bulk	+0.02	0.05	4	+0.37	+0.76	0.10
	Carbonate (calcite + dolomite)	−0.14	0.06	3	+0.21	+0.43	0.12
Cape Verde	**F1C**						
	Bulk	+0.12	0.04	4	+0.47	+0.96	0.08
	CY 250						
	Bulk	+0.11	0.04	4	+0.46	+0.94	0.08
	CY 114						
	Bulk	+0.06	0.08	8	+0.41	+0.84	0.16
Tamazert	**TA 1692**						
	Bulk	+0.09	0.07	4	+0.44	+0.90	0.14
	TA 1792						
	Bulk	+0.03	0.11	8	+0.38	+0.78	0.23
	TA 2a92						
	Bulk	+0.05	0.11	8	+0.4	+0.82	0.23

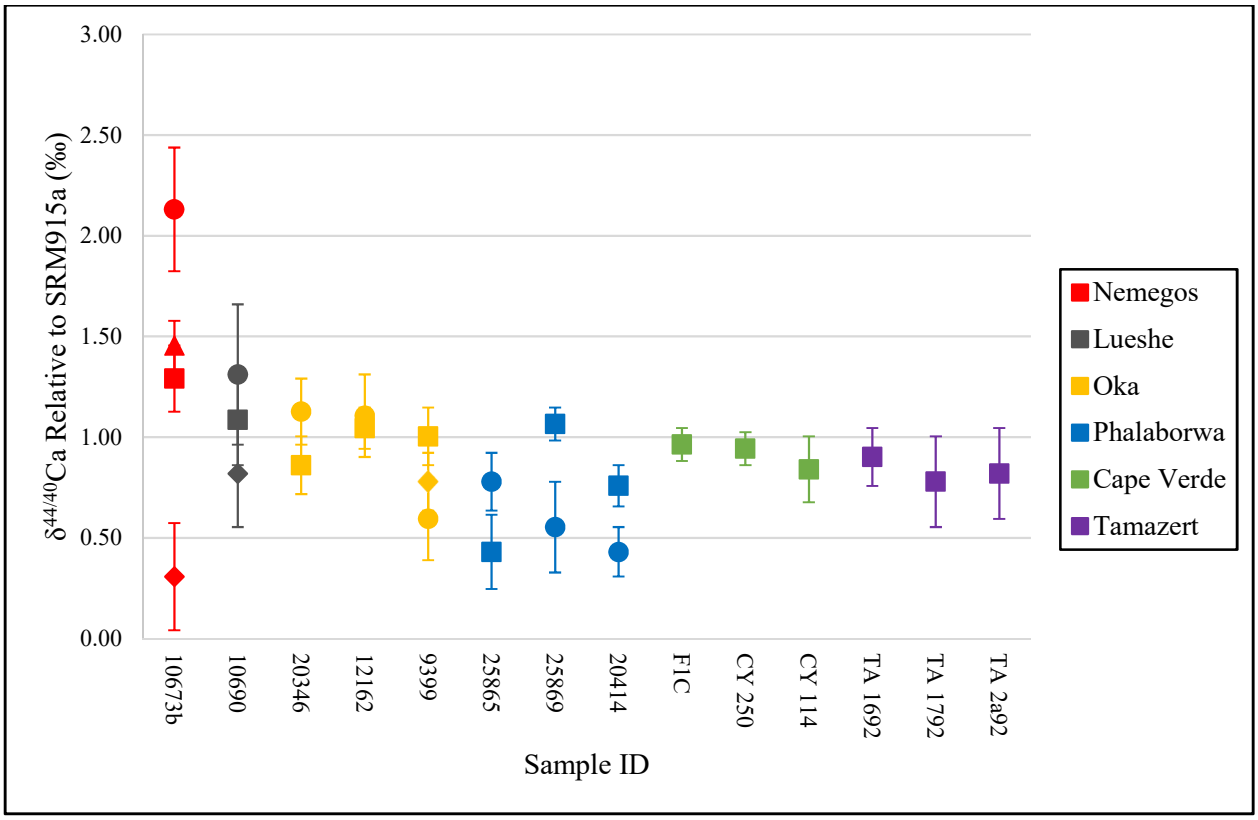

Figure 21 - Ca isotope data for carbonatite samples. Squares = bulk rock samples, Circles = carbonates, Diamonds = pyroxenes, Triangles = apatite.

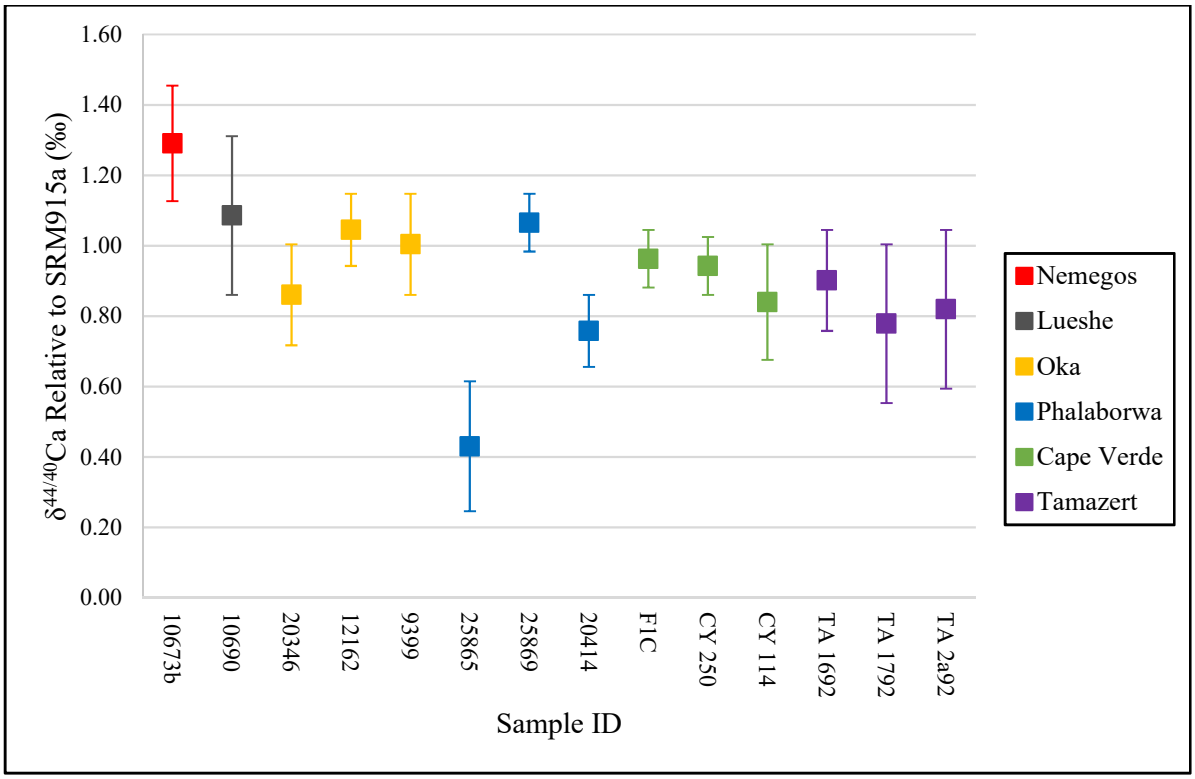

Figure 22 - Ca isotope data for bulk rock carbonatite samples grouped by locality.

4.4.3 Kimberlites and Related Samples

The calcium isotopic compositions of all kimberlite and kimberlite related peridotite samples studied in this work are provided in Table 31 and illustrated in Figure 23.

Table 31 – Calcium isotopic compositions of kimberlites and related samples analyzed in this study.

		$\delta^{44/42}$Ca Rel. SRM915b (in ‰)	2 SD	N (repeats)	$\delta^{44/40}$Ca Rel. SRM915a (in ‰)	$\delta^{44/42}$Ca Rel. SRM915a (in ‰)	2 SD
Kimberley	**R841**						
	Bulk	+0.17	0.09	8	+0.52	+1.07	0.18
	Carbonate (calcite)	−0.21	0.14	7	+0.14	+0.29	0.29
	Pyroxene (Cpx)	+0.06	0.13	7	+0.41	+0.84	0.27
	Amphibole 1	−0.39	0.08	4	−0.04	−0.08	0.16
	Amphibole 2	+0.18	0.09	3	+0.53	+1.09	0.18
Kaapvaal	**16965**						
	Pyroxene (Opx)	+0.27	0.09	4	+0.62	+1.27	0.18
	16962						
	Bulk	+0.02	0.10	4	+0.37	+0.76	0.20
	Pyroxene (Opx)	−0.15	0.14	4	+0.20	+0.41	0.29

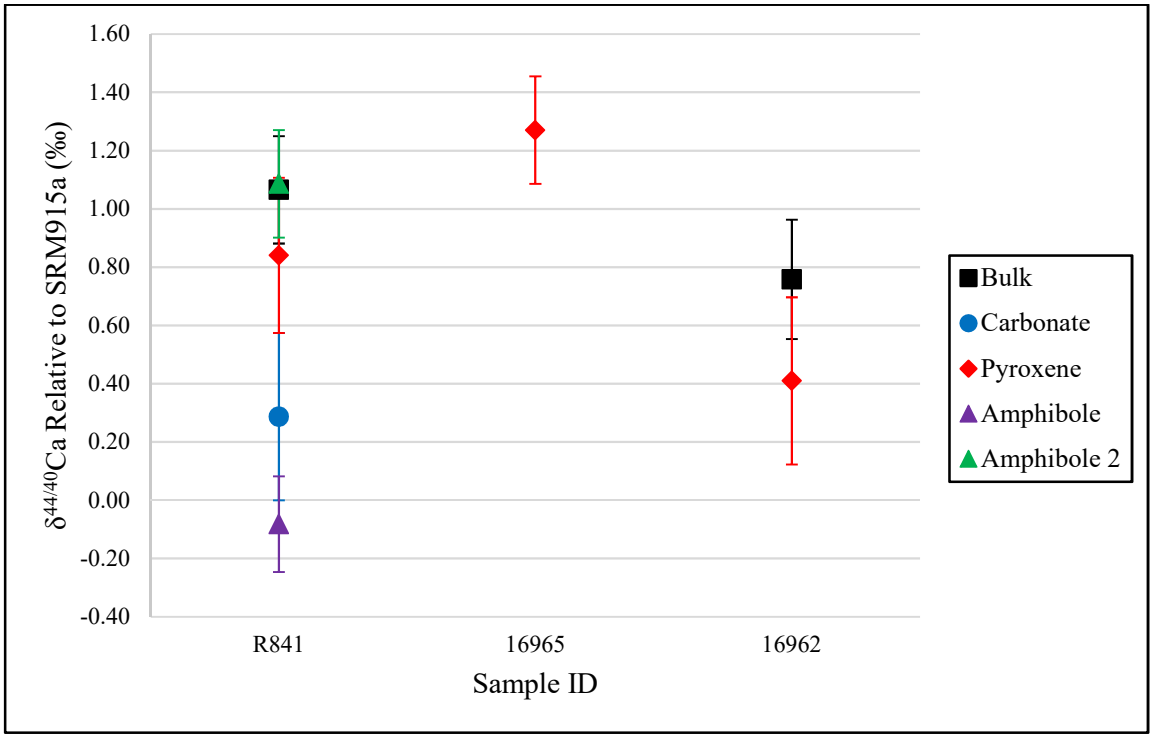

Figure 23 - Ca isotope data for kimberlites and related peridotite samples.

4.4.4 Other Natural Samples

The calcium isotopic compositions of all other samples studied in this work are provided in Table 32 and plotted in Figure 24. These samples include the Bancroft marble, Twin Sisters peridotite and olivine mineral separates from the San Carlos and Kilbourne Hole mantle peridotites. $\delta^{44/40}$Ca values for the olivine mineral separates compared to the coexisting Cpx and Opx minerals in the San Carlos and Kilbourne Hole samples are illustrated in Figure 25.

Table 32 – Calcium isotopic compositions of other natural samples analyzed in this study.

	$\delta^{44/42}$Ca Rel. SRM915b (in ‰)	2 SD	N (repeats)	$\delta^{44/40}$Ca Rel. SRM915a (in ‰)	$\delta^{44/42}$Ca Rel. SRM915a (in ‰)	2 SD
Bancroft Marble						
Carbonate (calcite)	+0.05	0.12	3	+0.40	+0.82	0.25
Carbonate (calcite) replicate	−0.02	0.13	3	+0.33	+0.68	0.27
Carbonate (calcite) average	+0.02	0.14	6	+0.37	+0.76	0.29
Clinopyroxene	0.00	0.06	4	+0.35	+0.72	0.12
Twin Sisters						
Clinopyroxene	−0.19	0.06	3	+0.16	+0.33	0.12
Orthopyroxene	+0.07	0.07	3	+0.42	+0.86	0.14
Dunite Whole Rock	+0.27	0.13	4	+0.62	+1.27	0.27
San Carlos						
Olivine	+0.40	0.07	4	+0.75	+1.54	0.14
Kilbourne Hole						
Olivine	+0.19	0.08	4	+0.54	+1.11	0.16

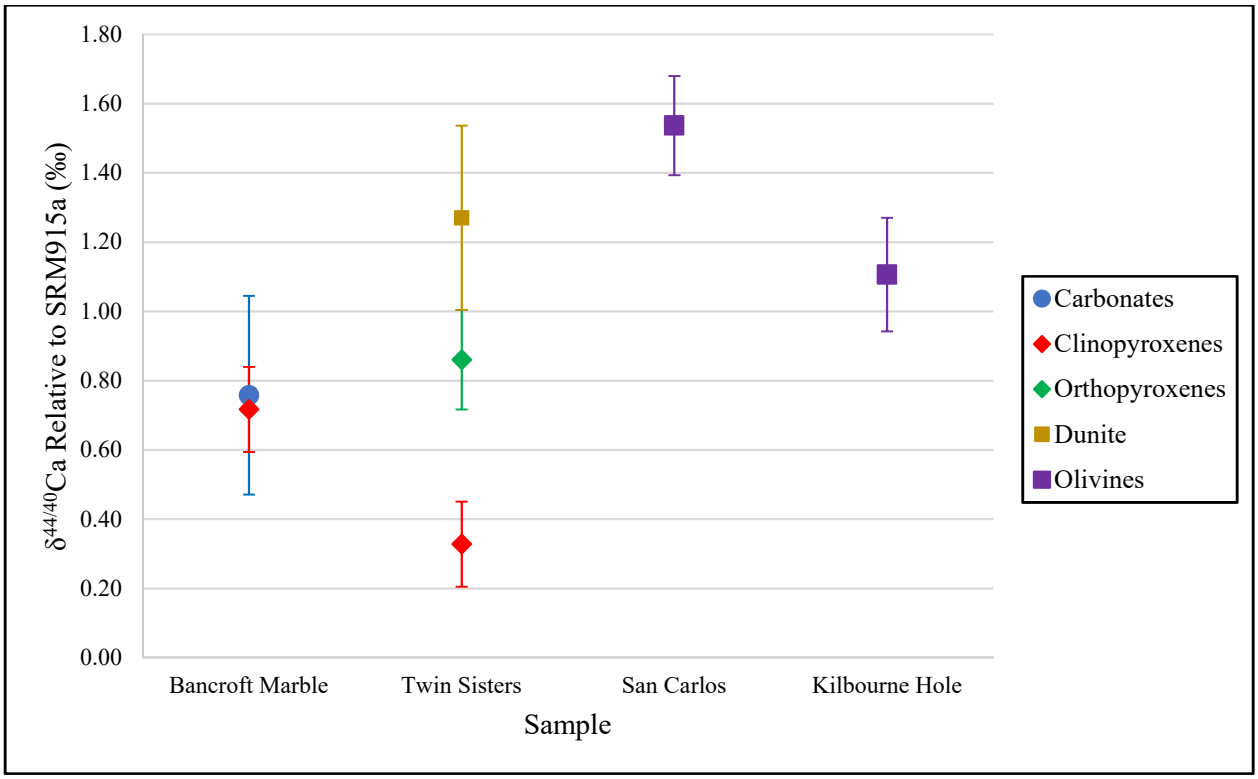

Figure 24 - Ca isotope data for other natural samples

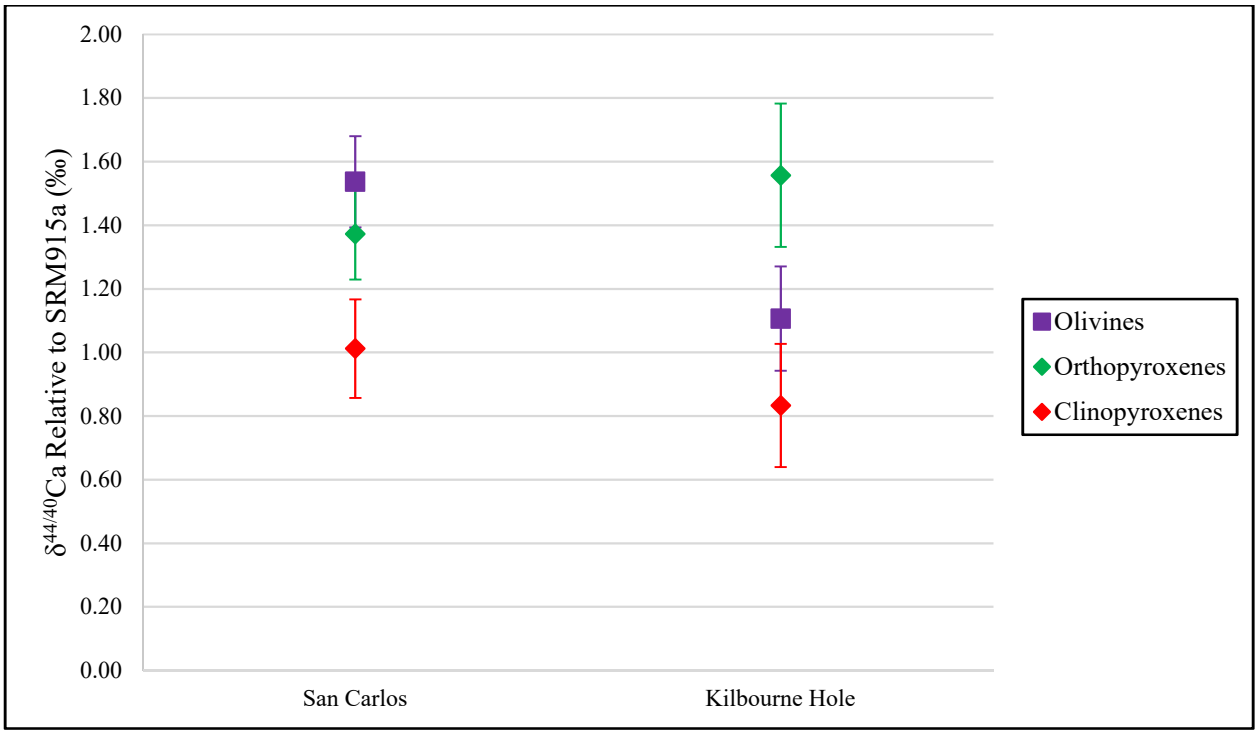

Figure 25 - Ca isotopic composition of San Carlos and Kilbourne Hole olivine mineral separates compared to coexisting clinopyroxenes and orthopyroxenes.

4.4.5 Coexisting Carbonates and Pyroxenes

Several samples contained coexisting pyroxene and carbonate minerals. The $\delta^{44/40}$Ca values for these coexisting minerals is given in Table 33 and illustrated in Figure 26 for comparison. The variations in $\delta^{44/40}$Ca between carbonates and pyroxenes within each sample varies greatly, ranging from +1.82‰ in sample 10673b to –0.55‰ in sample R841.

Table 33 – Calcium isotopic compositions of coexisting pyroxene and carbonate minerals analyzed in this study.

		$\delta^{44/42}$Ca Rel. SRM915b (in ‰)	2 SD	N (repeats)	$\delta^{44/42}$Ca Rel. SRM915a (in ‰)	$\delta^{44/40}$Ca Rel. SRM915a (in ‰)	2 SD
Nemegos	**10673b**						
	Carbonate (calcite)	+0.69	0.15	3	+1.04	+2.13	0.31
	Pyroxene (Cpx)	−0.20	0.13	4	+0.15	+0.31	0.27
Lueshe	**10690**						
	Carbonate (calcite)	+0.29	0.17	6	+0.64	+1.31	0.35
	Pyroxene (Opx)	+0.05	0.13	3	+0.40	+0.82	0.27
Oka	**9399**						
	Carbonate (calcite)	−0.06	0.1	8	+0.29	+0.59	0.20
	Pyroxene (Cpx)	+0.03	0.07	3	+0.38	+0.78	0.14
Kimberley	**R841**						
	Carbonate (calcite)	−0.21	0.14	7	+0.14	+0.29	0.29
	Pyroxene (Cpx)	+0.06	0.13	7	+0.41	+0.84	0.27
Bancroft	**Bancroft Marble**						
	Carbonate (calcite) average	+0.02	0.14	6	+0.37	+0.76	0.29
	Clinopyroxene	+0.00	0.06	4	+0.35	+0.72	0.12

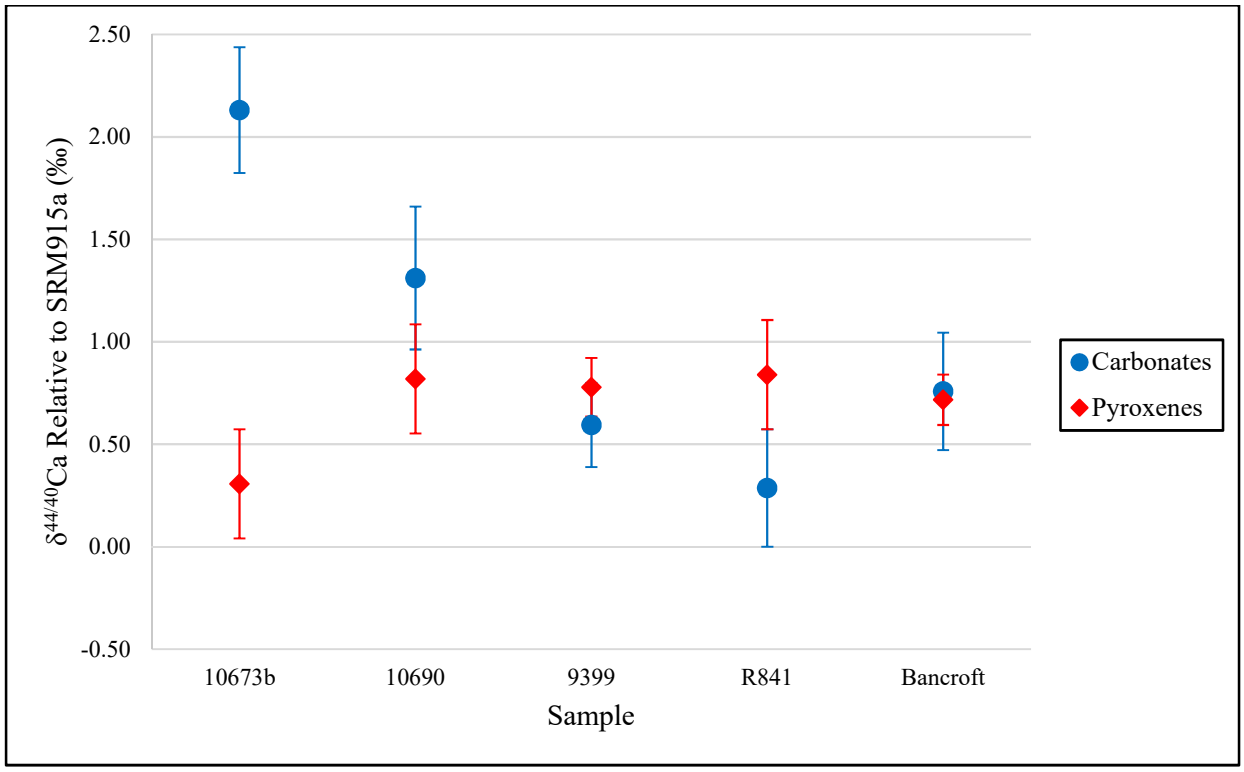

Figure 26 – Ca isotope data for coexisting carbonate and pyroxene mineral separates

4.5 Strontium Isotopic Data for Natural Samples

Most of the samples in this study were also analyzed for their bulk rock strontium isotopic $^{87}Sr/^{86}Sr$ ratios. The results of these analyses are presented in Table 34. $^{87}Sr/^{86}Sr$ ratios ranged from $0.702996 \pm 3.51x10^{-05}$ (sample 10673b) to $0.710230 \pm 2.35x10^{-05}$ (sample 20414). NIST SRM-987 isotopic standard was analyzed twice during the analytical run and yielded values of $0.7103 \pm 2.93x10^{-05}$ and $0.7103 \pm 3.04x10^{-05}$. Figure 27 plots the $^{87}Sr/^{86}Sr$ ratios vs. bulk rock $\delta^{44/40}Ca$ values for samples that have data for both parameters.

Table 34 – Bulk rock $^{87}Sr/^{86}Sr$ ratios of samples in this study.

Sample Type	Sample	$^{87}Sr/^{86}Sr$	SD
Carbonatites	**Oka**		
	20346	0.7033	2.36E-05
	9399	0.7033	2.70E-05
	12162	0.7033	2.90E-05
	Nemegos		
	10673b	0.7030	3.51E-05
	Lueshe		
	10690	0.7032	2.66E-05
	Phalaborwa		
	25865	0.7064	2.91E-05
	25869	0.7040	2.78E-05
	20414	0.7102	2.35E-05
Kimberlites and Related Peridotites	**Kimberley**		
	R841	0.7057	3.32E-05
	Kaapvaal		
	16962	0.7055	2.37E-05
Others	**Bancroft Marble**		
	BC	0.7050	2.81E-05

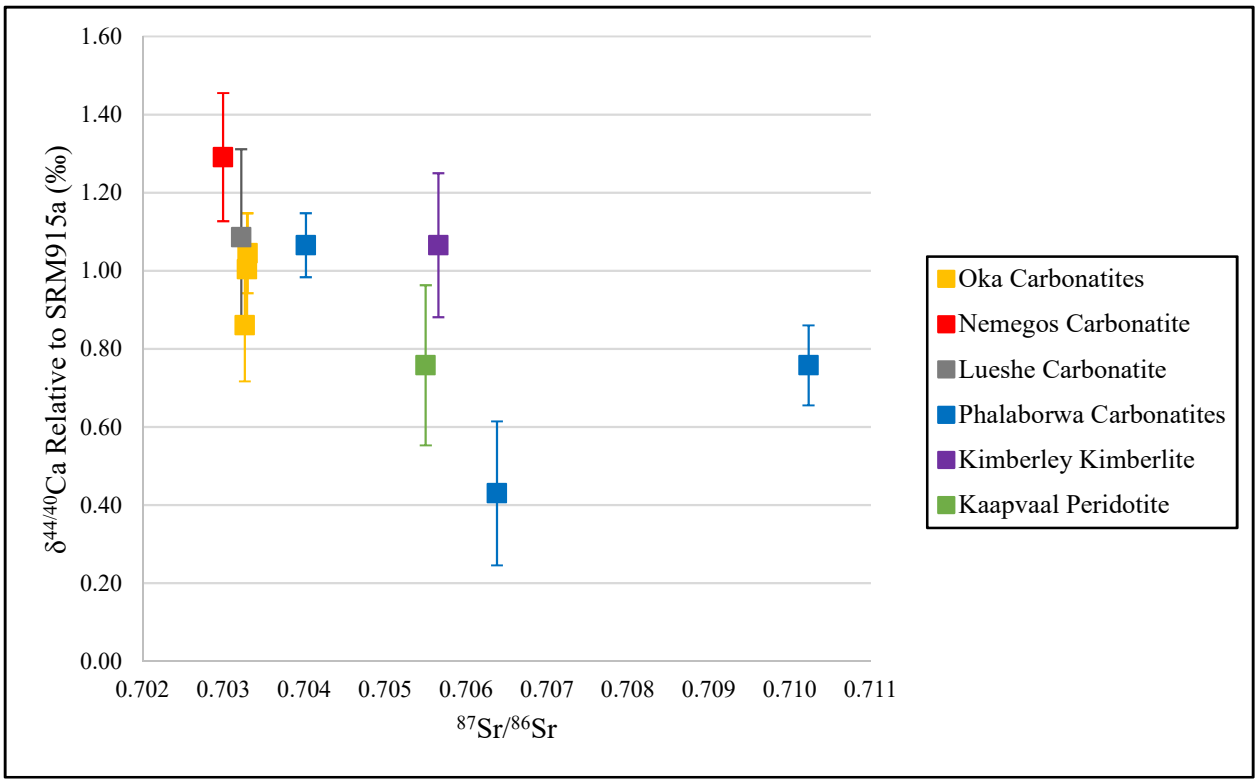

Figure 27 - Comparison of $\delta^{44/40}$Ca vs. ^{87}Sr/^{86}Sr values in bulk rock samples analyzed in this study.

4.6 Experimental Results

This section describes the resulting run products for each experiment and the results of the isotopic analyses of all experimental samples. As intended, most experiments produced a quenched melt phase and a crystal phase (clinopyroxenes) in approximately equal proportions. The crystal phase was typically concentrated in the bottom of the experimental capsule and the quenched melt phase concentrated in the upper half of the capsule (Figure 28). Experimental sample ID's followed by an 'X' indicate crystal phase and ID's followed by an 'M' indicate quenched melt phase (e.g. B796-X, B796-M).

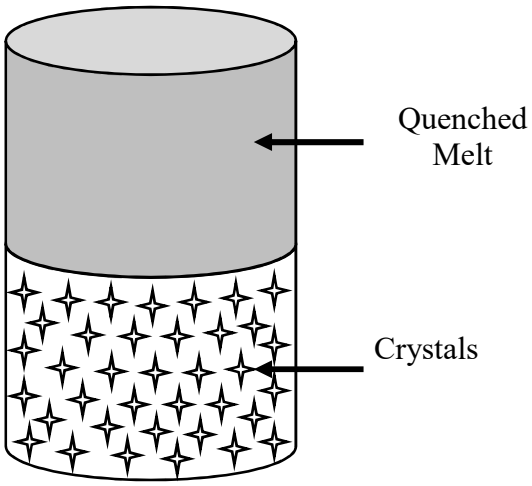

Figure 28 - Schematic of typical experimental capsule and resulting phases.

4.6.1 Clinopyroxene + Carbonate Melt Experiments

Four clinopyroxene + carbonate melt experiments were conducted at 3 GPa and temperatures ranging from 1250 to 1550 °C using the same starting material (Chapter 2). Each experiment produced crystals and quenched melt except for experiment B798. The crystals produced in each experiment were homogeneous clinopyroxenes ranging in size from approximately 1-100 μm. As observed in previous studies (e.g., White and Wyllie, 1992; Dalton and Presnall, 1998), carbonated silicate melt is not preserved as a glass, but rather transforms to a matte of rapidly-grown, feathery 'quench crystals' during the couple of seconds that it talks to cool the experiment to below 500 °C. This quenched carbonate melt in these experiments was opaque and milky white in appearance and sometimes powdery in texture. The quenched melt texture is not completely homogeneous and often appears radiating or fibrous in BSE images (Figure 29). Quench crystals nucleated at the border between the clinopyroxene crystals and quenched melt and appeared to radiate inwards from the edges of the experimental capsule. B798 was the highest temperature experiment (1550 °C) and it produced 100% quenched melt with no (equilibrium) crystals. Part of the resulting quench material appeared to be in the form of a glass (B798-G) or more glass-like than the typical milky-white quenched melt. BSE images for each phase of the four experiments are provided in Figure 29. Major elemental compositions of each phase in the four experiments are provided in Table 35. The results of the Ca isotopic analyses for all experiments are given in Table 36 and illustrated in Figure 30. In experiments that contain both crystals and quenched melt, the $\delta^{44/40}$Ca values are consistently greater in the crystals than

in the quenched melt (Figure 31). The magnitude of this difference in $\delta^{44/40}$Ca values between crystals and quenched melt is positively correlated with increasing temperature (Figure 32), and increasing sample mass (Figure 33) which is as a proxy for the size (i.e. length) of the experimental capsule.

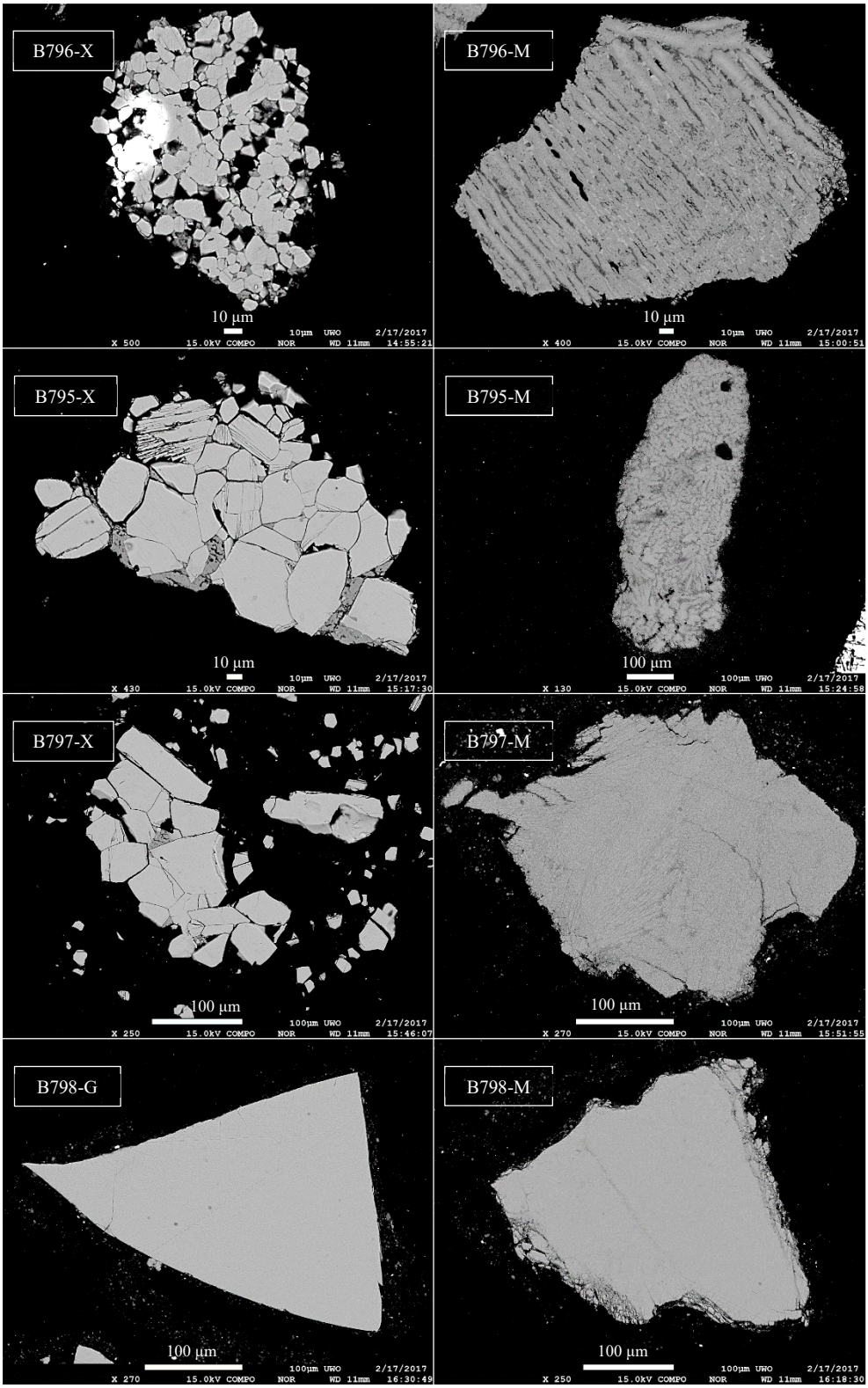

Figure 29 - BSE images of all Cpx + Carbonate Melt experiments. 'X' suffix indicates crystals, 'M' suffix indicates quenched melt, 'G' suffix indicates glassy quenched melt in experiment B798. White patch in the image for B796-X is the result of a gas bubble that formed on the surface of the sample during analysis and does not reflect a compositional change in the Cpx crystals. Scale bars are provided but vary for each image.

Table 35 - Major element compositions of Cpx + Carbonate Melt experiments. CO_2 wt.% in quenched melt calculated by difference.

	B796 (3GPa/1250°C)					B795 (3GPa/1350°C)			
	Pyroxene	**SD**	**Melt**	**SD**		**Pyroxene**	**SD**	**Melt**	**SD**
SiO_2	53.95	0.33	3.44	1.43	SiO_2	55.12	0.22	5.08	5.14
Al_2O_3	3.19	0.43	-	-	Al_2O_3	1.66	0.18	0.93	0.55
MgO	20.15	0.27	13.87	0.85	MgO	20.52	0.09	15	3.51
CaO	21.82	0.21	38.95	1.25	CaO	22.48	0.05	34.66	2.2
CO_2	-	-	43.74	-	CO_2	-	-	44.33	-
TOTAL	99.11	0.24	100		TOTAL	99.78		100	
n	5		6		n	5		9	
	B797 (3GPa/1450°C)					**B798 (3GPa/1550°C)**			
	Pyroxene	**SD**	**Melt**	**SD**		**Glassy**	**SD**	**Melt**	**SD**
SiO_2	54.58	0.2	7.55	6.31	SiO_2	32.18	1.11	33.16	2.05
Al_2O_3	2.43	0.14	2.01	1.58	Al_2O_3	2.78	0.14	2.9	0.11
MgO	20.42	0.33	16.6	3.21	MgO	12.61	0.54	18.82	0.96
CaO	22.2	0.28	35.74	2.39	CaO	24.55	0.23	28.51	0.81
CO_2	-	-	38.1	-	CO_2	27.88	-	16.61	-
TOTAL	99.63		100		TOTAL	100		100	
n	5		8		n	5		15	

Table 36 - Calcium isotopic composition of Cpx + Carbonate Melt experiments.

Experiment Type	Sample ID	P/T	Phase	$\delta^{44/42}$Ca Rel. SRM915b (in ‰)	2 SD	N (repeats)	$\delta^{44/42}$Ca Rel. SRM915a (in ‰)	$\delta^{44/40}$Ca Rel. SRM915a (in ‰)	2 SD
Cpx-Carbonate Melt	CaCO3	N/A	Starting Material	−0.05	0.14	3	+0.30	+0.61	0.29
	B796	3 GPa/1250 °C	Pyroxene	−0.03	0.13	3	+0.32	+0.66	0.27
			Quenched Melt	−0.21	0.11	3	+0.14	+0.29	0.23
			Pyroxene Leachate	+0.20	0.15	7	+0.55	+1.13	0.31
	B795	3 GPa/1350 °C	Pyroxene	+0.04	0.06	3	+0.39	+0.80	0.12
			Quenched Melt	−0.26	0.14	3	+0.09	+0.18	0.29
			Pyroxene Leachate	+0.32	0.16	8	+0.67	+1.37	0.33
	B797	3 GPa/1450 °C	Pyroxene	+0.43	0.12	4	+0.78	+1.60	0.25
			Quenched Melt	−0.20	0.07	3	+0.15	+0.31	0.14
			Pyroxene Leachate	+0.52	0.14	8	+0.87	+1.78	0.29
	B798	3 GPa/1550 °C	Glassy Quenched Melt	−0.14	0.06	4	+0.21	+0.43	0.12
			Quenched Melt	−0.08	0.06	3	+0.27	+0.55	0.12

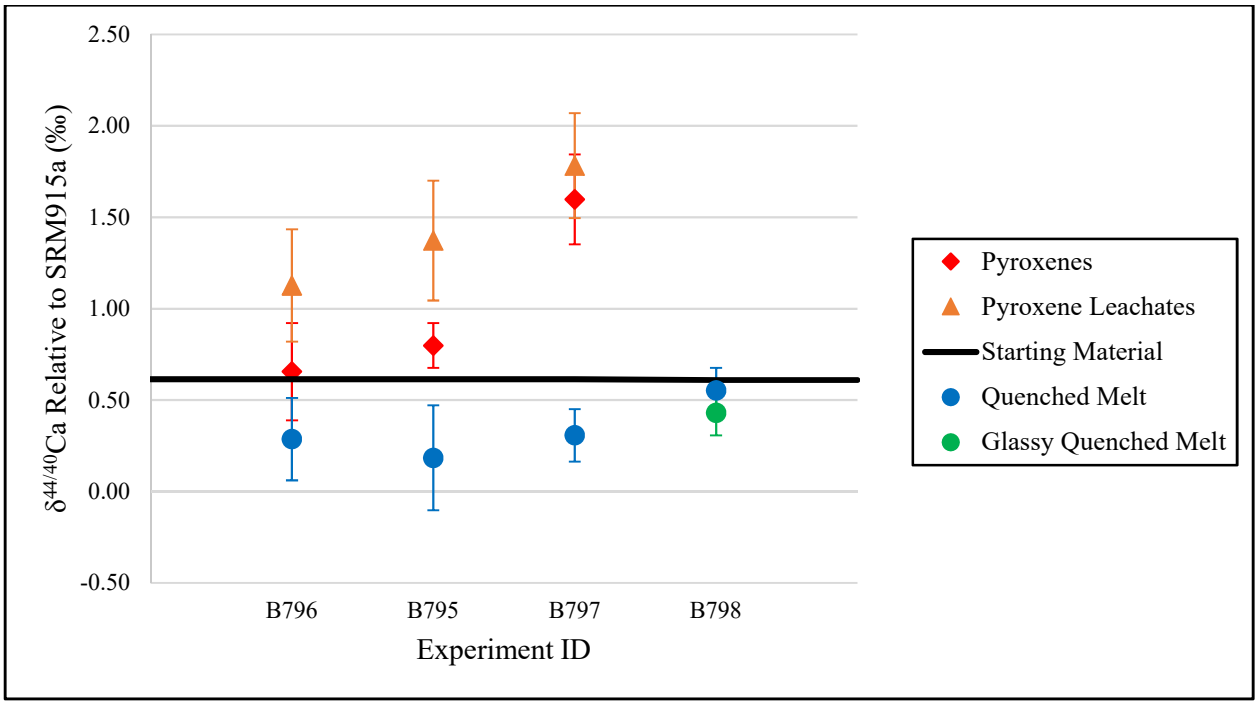

Figure 30 - Ca isotopic data for Cpx + Carbonate Melt experiments

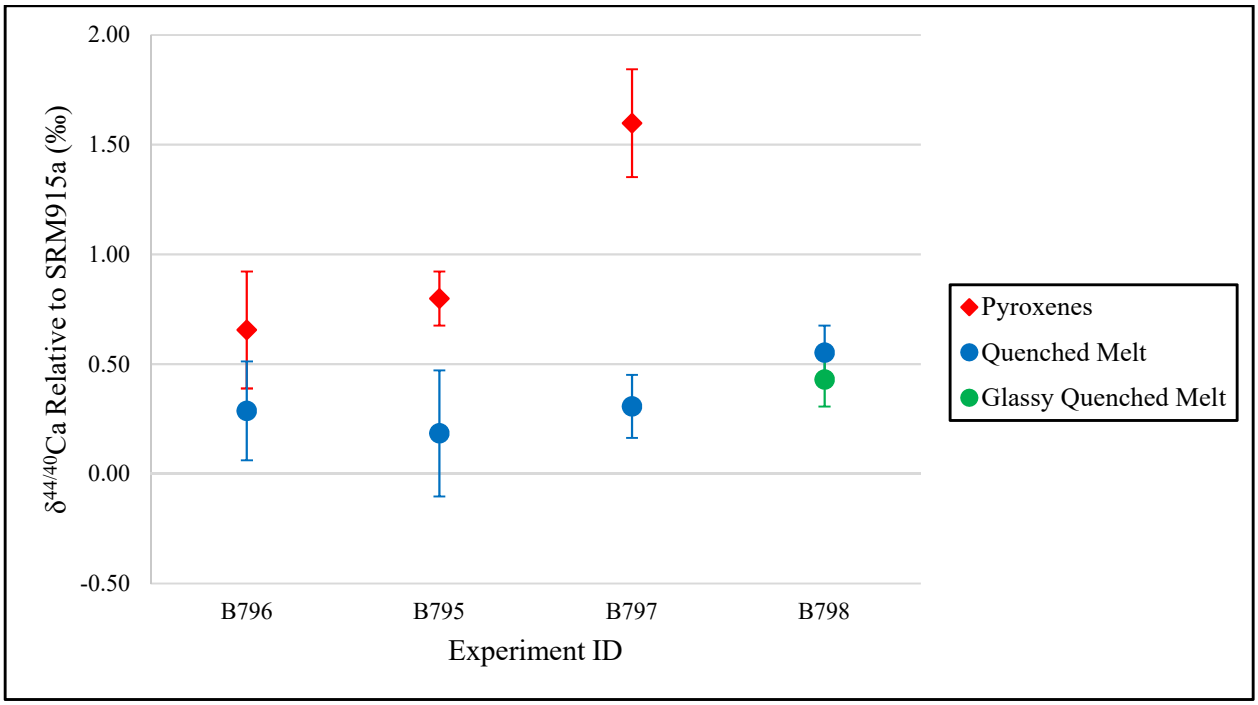

Figure 31 - Ca isotopic data for pyroxenes compared to quenched melt in Cpx + Carbonate Melt experiments

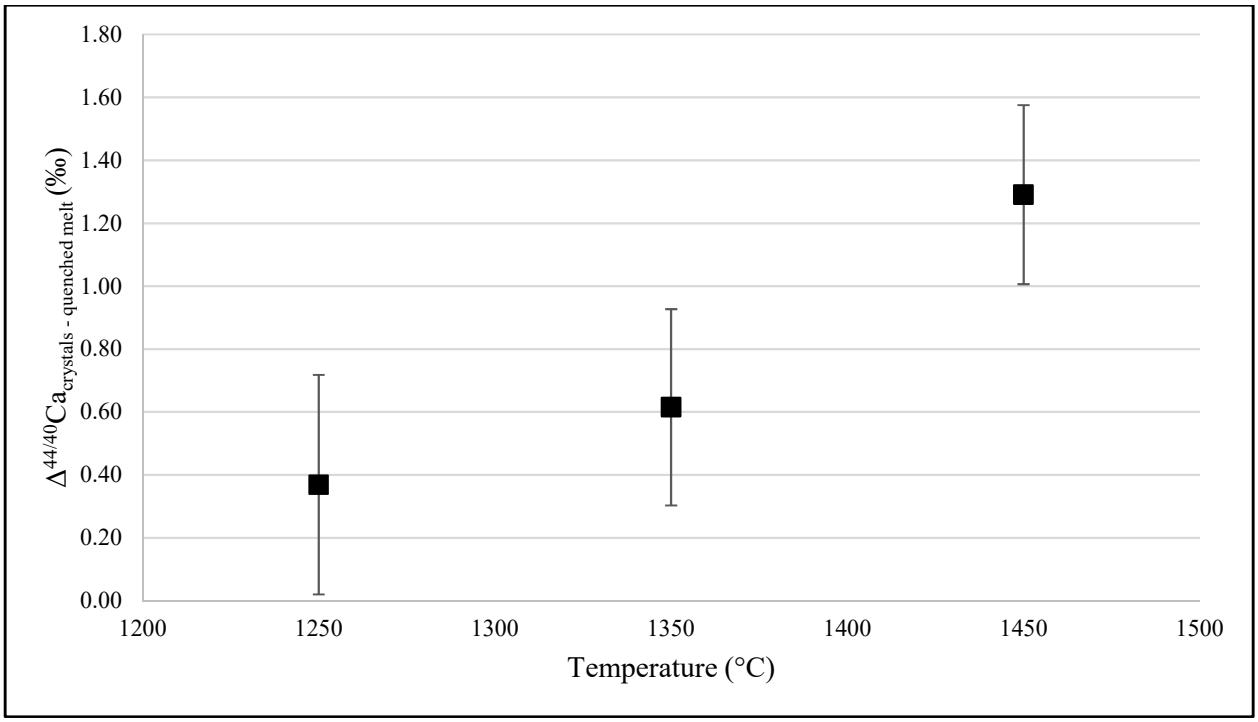

Figure 32 – $\delta^{44/40}$Ca difference between crystals and quenched melt as a function of temperature in Cpx + Carbonate Melt experiments

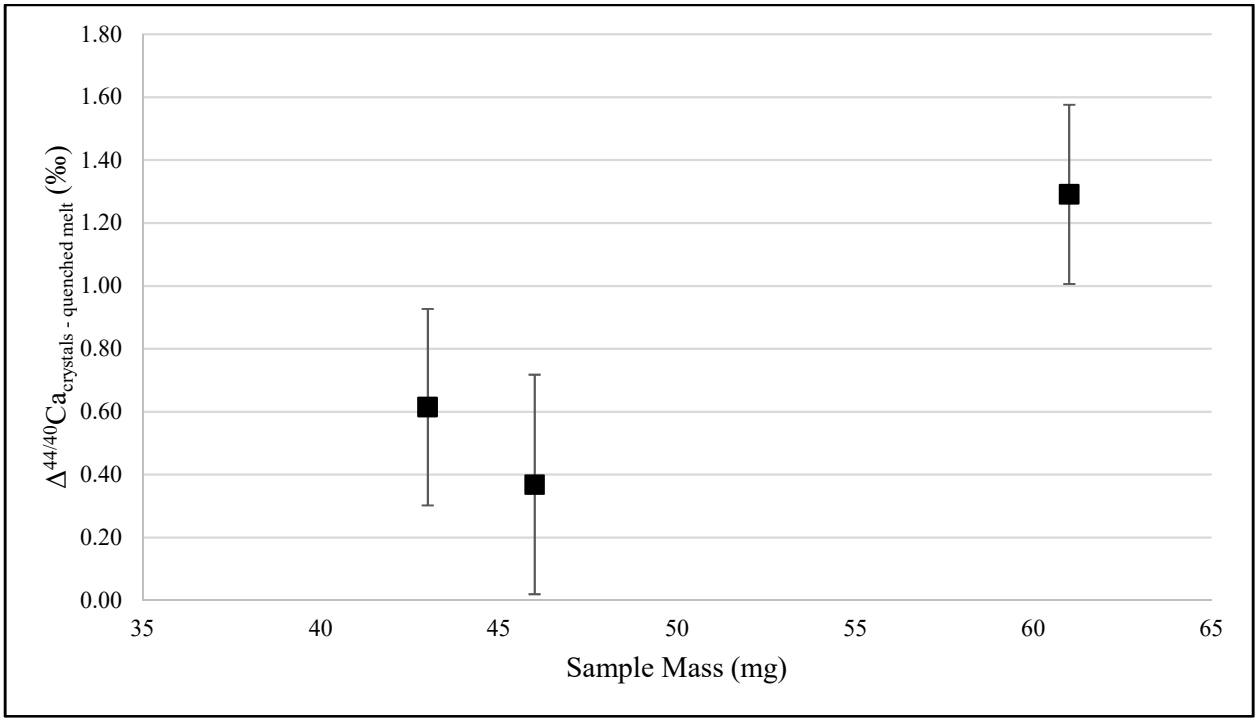

Figure 33 - $\delta^{44/40}$Ca difference between crystals and quenched melt as a function of sample mass in Cpx + Carbonate Melt experiments

4.6.2 Clinopyroxene + Silicate Melt Experiment

One clinopyroxene + silicate melt experiment was conducted at 1 GPa and 1125 °C (Chapter 2). This experiment produced clinopyroxene crystals (A1325-X) and a silicate melt (A1325-M). The crystals were relatively large compared to the other experiments, ranging from approximately 10's of μm up to 500 μm. The quenched silicate melt was in the form of a glass and was colourless. The BSE images for each phase are provided in Figure 34. Major elemental composition of each phase is given in Table 37. The results of the Ca isotopic analyses are given in Table 38 and plotted in Figure 35. Following the same trend as the Cpx + Carbonate melt experiments, the $\delta^{44/40}$Ca values are greater in the crystals than in the quenched melt.

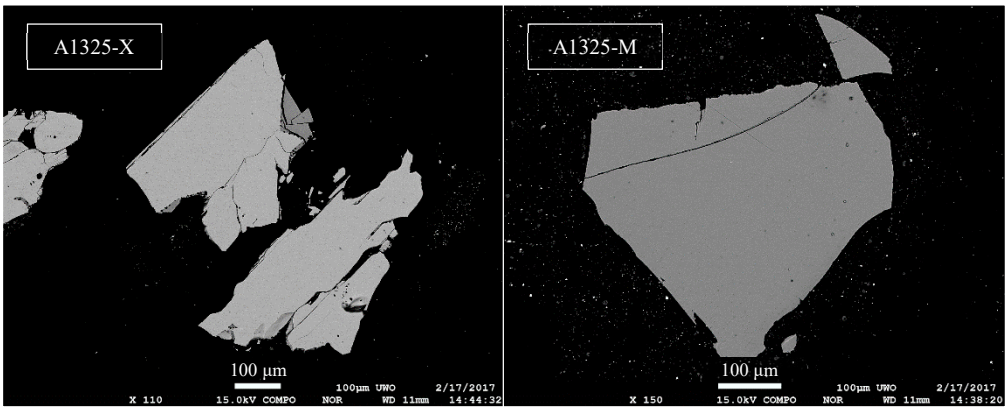

Figure 34 - BSE images for Cpx + Silicate Melt experiment.

Table 37 - Major element compositions of Cpx + Silicate Melt experiment. H_2O content of melt phase calculated by difference

	A1325			
	Pyroxene	**SD**	**Melt**	**SD**
SiO_2	54.16	0.27	46.94	0.21
Al_2O_3	3.29	0.49	18.96	0.19
MgO	18.22	0.22	7.25	0.04
CaO	24.88	0.4	18.09	0.03
H_2O	-	-	8.76	
TOTAL	100.55	0.14	100	0.35
n	5		5	

Table 38 - Calcium isotopic composition of Cpx + Silicate Melt experiment.

Experiment Type	Sample ID	P/T	Phase	$\delta^{44/42}$Ca Rel. SRM915b (in ‰)	2 SD	N (repeats)	$\delta^{44/42}$Ca Rel. SRM915a (in ‰)	$\delta^{44/40}$Ca Rel. SRM915a (in ‰)	2 SD
Cpx-Silicate Melt	$CaSiO_3$	N/A	Starting Material	−0.13	0.06	4	+0.22	+0.45	0.12
	A1325	1 GPa/1125 °C	pyroxene	−0.10	0.11	3	+0.25	+0.51	0.23
			melt	−0.32	0.10	3	+0.03	+0.06	0.20

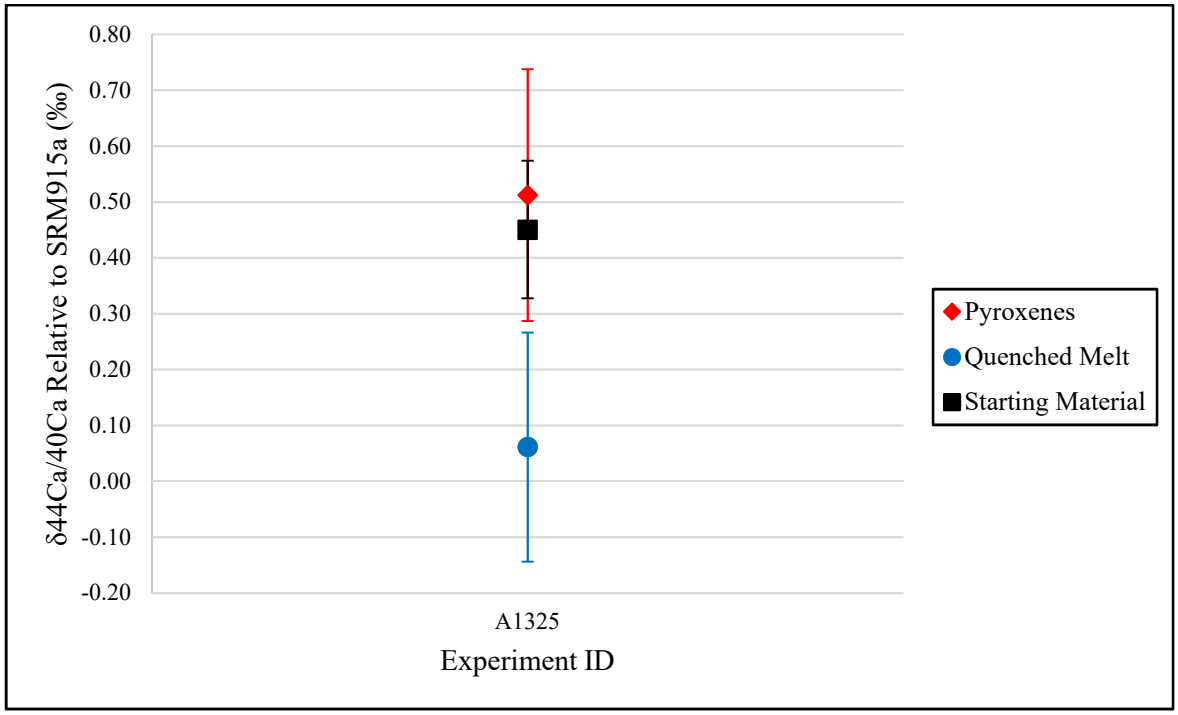

Figure 35 - Ca isotope data for Cpx + Silicate Melt experiment

4.6.3 Clinopyroxene + Carbonated Silicate Melt Experiments

Three clinopyroxene + carbonated silicate melt experiments were conducted at 3 and 5 GPa and 1375 – 1440 °C. Starting compositions were identical for experiments Cbt-02 and M824 but different for experiment Cbt-01 (Chapter 2, Table 2). Each experiment produced crystals and quenched melt, however, experiment M824 unintentionally produced orthopyroxene, and garnet crystals along with clinopyroxene crystals unlike all the other crystal-bearing experiments which

yielded only clinopyroxenes. This mixed mineral crystal phase was treated and analyzed in bulk due to the difficulty of mechanical separation of the different minerals. The BSE images of the crystals and quenched melt for the three experiments are provided in Figure 36. Major element compositions for the crystals and quenched melt in each experiment are provided in Table 39. The results of the Ca isotopic analyses for all experiments are given in Table 40 and plotted in Figure 37. Once again, the $\delta^{44/40}$Ca values are consistently greater in the crystals compared to the quenched melt. Like the Cpx + Carbonate melt experiments, the magnitude of this difference in $\delta^{44/40}$Ca values between crystals and quenched melt is positively correlated with increasing temperature (Figure 38), however, unlike the Cpx + Carbonate melt experiments, it does not increase with increasing sample mass (Figure 39). Also seen in this set of experiments is an increase in the difference in $\delta^{44/40}$Ca between crystals and quenched melt with an increase in pressure (Figure 40). Figure 41 demonstrates the relationship between the crystals and quenched melt in experiment Cbt-01 as well as the negligible effect of leaching on the crystal phase.

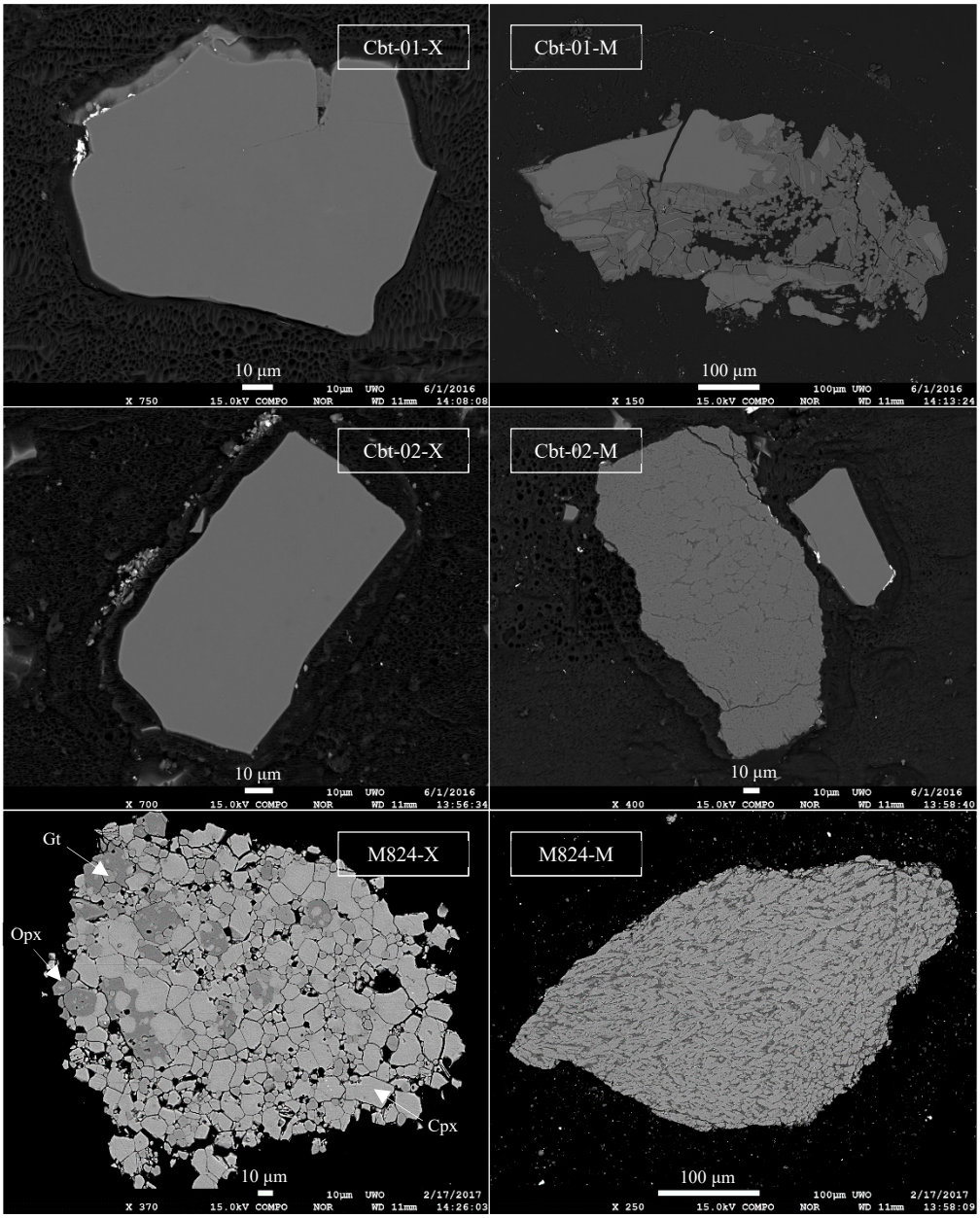

Figure 36 - BSE images for all Cpx + Carbonated Silicate Melt experiments. Experiment M824 images were taken during a different session and therefore differences in colour or shade compared to the other experiments do not necessarily reflect differences in composition. The image for Cbt-02-M also includes a smaller fragment of Cpx crystal, the quenched melt is the larger fragment. Scale bars are provided for each image. Cpx = clinopyroxene, Opx = orthopyroxene, Gt = Garnet.

Table 39 - Major element compositions of Cpx + Carbonated Silicate Melt experiments.

CO_2 wt.% in melt phases calculated by difference.

	Cbt-01 (3GPa/1375°C)			
	Pyroxene	**SD**	**Melt**	**SD**
SiO_2	54.77	0.21	36.13	0.09
Al_2O_3	3.07	0.24	6.57	0.05
Na_2O	1.26	0.02	3.26	0.01
MgO	21.75	0.34	17.65	0.03
TiO_2	0.01	0.01	0.01	0.01
CaO	15.20	0.27	14.79	0.04
FeO	1.84	0.19	2.98	0.05
MnO	0.02	0.01	0.02	0.00
K_2O	0.00	0.00	0.17	0.01
NiO	0.01	0.01	0.00	0.00
Cr_2O_3	1.14	0.13	0.16	0.02
CO_2	-	-	18.26	-
TOTAL	99.05	0.26	100	0.10
n	9		4	

	Cbt-02 (5GPa/1440°C)			
	Pyroxene	**SD**	**Melt**	**SD**
SiO_2	54.99	0.69	26.24	1.53
Al_2O_3	3.36	0.06	3.61	0.14
Na_2O	0.85	0.02	0.21	0.12
MgO	23.12	0.15	16.50	0.78
TiO_2	0.08	0.01	1.18	1.64
CaO	12.47	0.15	18.84	0.5
FeO	3.01	0.23	3.26	0.19
MnO	0.18	0.01	0.23	0.03
K_2O	0.01	0.00	0.05	0.03
NiO	0.01	0.00	0.00	0.00
Cr_2O_3	0.19	0.01	0.04	0.01
CO_2	-	-	29.85	-
TOTAL	98.27	0.68	100.00	2.65
n	9		4	

	M824 (5GPa/1440°C)									
	Cpx	**SD**	**Opx**	**SD**	**Gt**	**SD**	**Silicate AVG**	**SD**	**Melt**	**SD**
SiO_2	55.75	0.09	57.48	0.12	44.07	1.90	55.17	0.26	26.39	1.45
Al_2O_3	3.01	0.14	1.82	0.04	22.78	2.94	4.47	0.37	3.13	0.22
Na_2O	1.00	0.02	0.21	0.01	0.09	0.13	0.70	0.03	0.64	0.07
MgO	21.03	0.25	33.41	0.19	22.75	0.24	24.53	0.23	17.70	0.59
TiO_2	0.14	0.02	0.07	0.01	0.38	0.08	0.14	0.02	1.62	0.35
CaO	14.36	0.50	1.61	0.05	4.85	1.29	10.06	0.45	20.46	0.26
FeO	4.11	0.27	4.99	0.19	5.74	0.37	4.49	0.26	5.13	0.10
MnO	0.17	0.01	0.17	0.02	0.31	0.02	0.18	0.01	0.24	0.01
K_2O	0.00	0.01	0.00	0.00	0.00	0.00	0.00	0.01	0.01	0.01
NiO	0.01	0.02	0.00	0.02	0.00	0.01	0.01	0.02	0.00	0.02
Cr_2O_3	0.13	0.02	0.07	0.01	0.44	0.06	0.14	0.02	0.05	0.01
CO_2	-	-	-	-	-	-	-	-	24.63	-
TOTAL	99.71	0.13	99.83	0.12	101.41	0.32	99.90	0.14	100.00	1.35
n	5		5		5		15		10	

Table 40 - Calcium isotopic compositions of Cpx + Carbonated Silicate Melt experiments.

Experiment Type	Sample ID	P/T	Phase	$\delta^{44/42}$Ca Rel. SRM915b (in ‰)	2 SD	N (repeats)	$\delta^{44/42}$Ca Rel. SRM915a (in ‰)	$\delta^{44/40}$Ca Rel. SRM915a (in ‰)	2 SD
Cpx-Carbonated Silicate Melt	Cbt-01	N/A	Starting Material	−0.01	0.11	3	+0.34	+0.70	0.23
		3 GPa/1375 °C	Pyroxene	+0.36	0.02	2	+0.71	+1.45	0.04
			Quenched Melt	−0.38	0.16	3	−0.03	−0.06	0.33
			Unleached Pyroxene	+0.38	0.09	3	+0.73	+1.50	0.18
			Pyroxene Leachate	+0.09	0.11	3	+0.44	+0.90	0.23
	Cbt-02/M824	N/A	Starting Material	−0.05	0.15	4	+0.30	+0.61	0.31
	Cbt-02	5 GPa/1450 °C	Pyroxene	+0.61	0.08	2	+0.96	+1.97	0.16
			Quenched Melt	−0.42	0.11	6	−0.07	−0.14	0.23
	M824	5 GPa/1440 °C	Pyroxene	+0.73	0.09	4	+1.08	+2.21	0.18
			Quenched Melt	−0.61	0.11	4	−0.26	−0.53	0.23

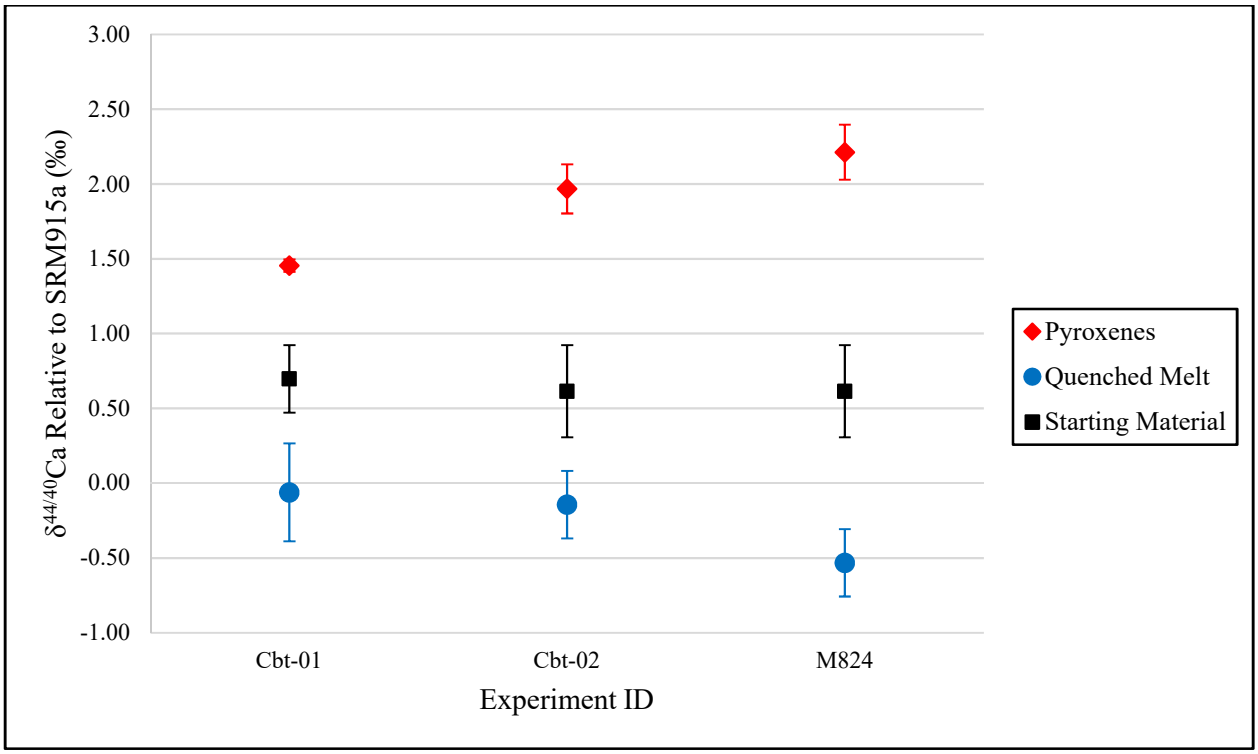

Figure 37 - Ca isotope data for Cpx + Carbonated Silicate Melt experiments.

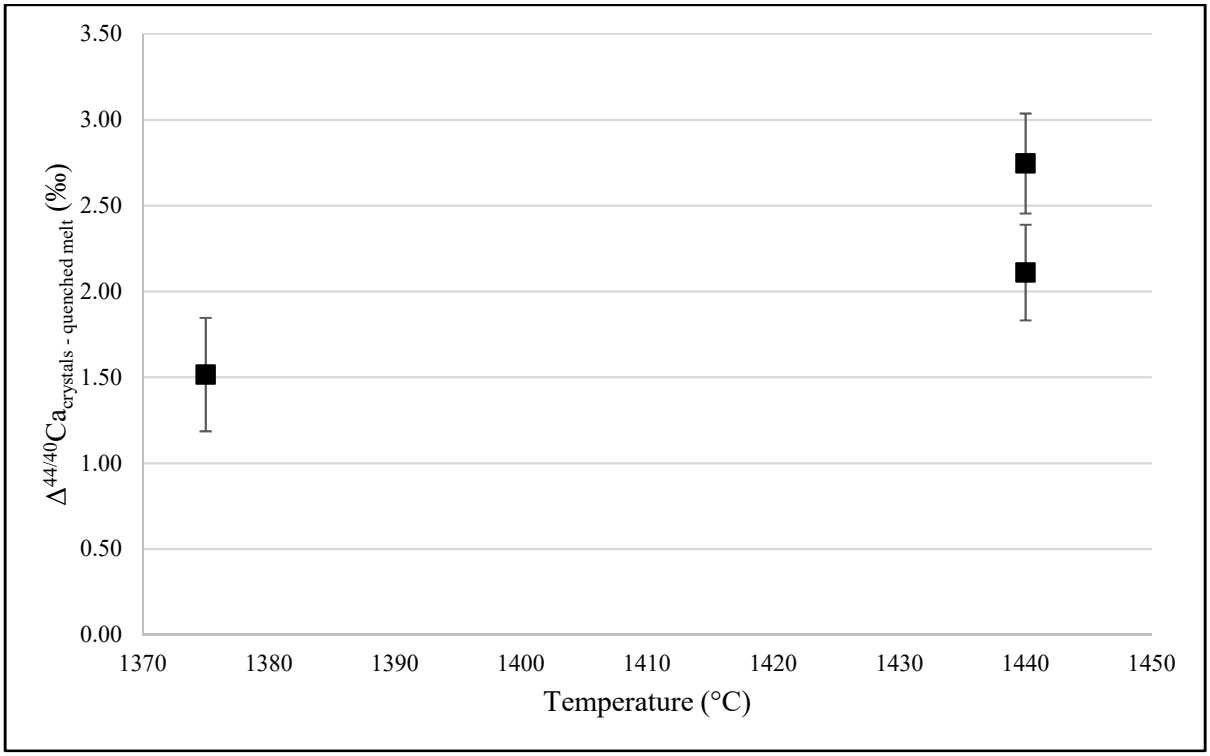

Figure 38 - $\delta^{44/40}$Ca difference between crystals and quenched melt as a function of temperature in Cpx + Carbonated Silicate Melt experiments.

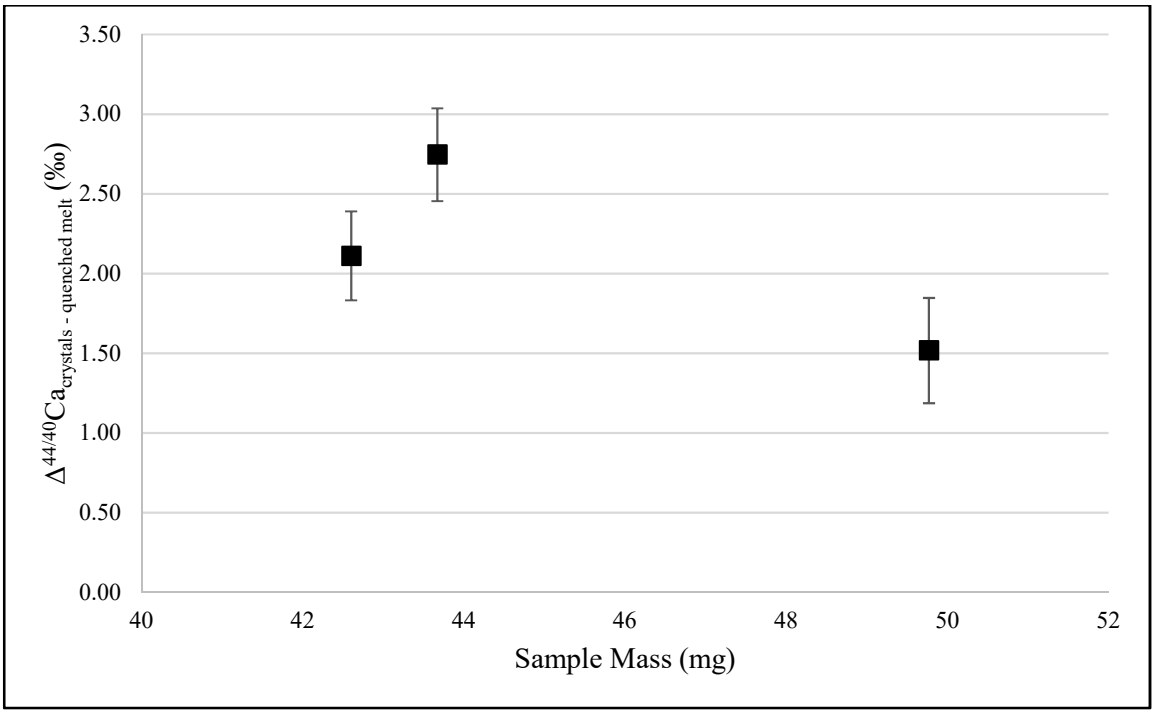

Figure 39 - $\delta^{44/40}$Ca difference between crystals and quenched melt as a function of sample mass in Cpx + Carbonated Silicate Melt experiments.

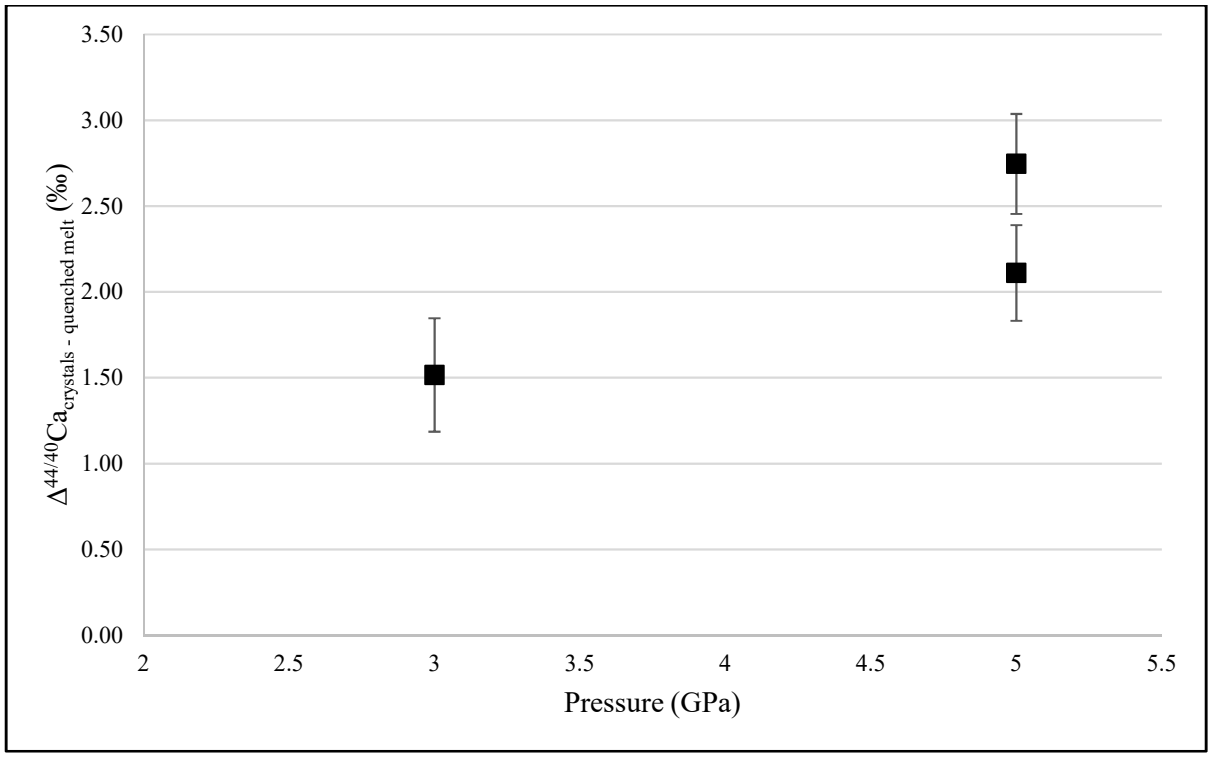

Figure 40 - $\delta^{44/40}$Ca difference between crystals and quenched melt as a function of pressure in Cpx + Carbonated Silicate Melt experiments.

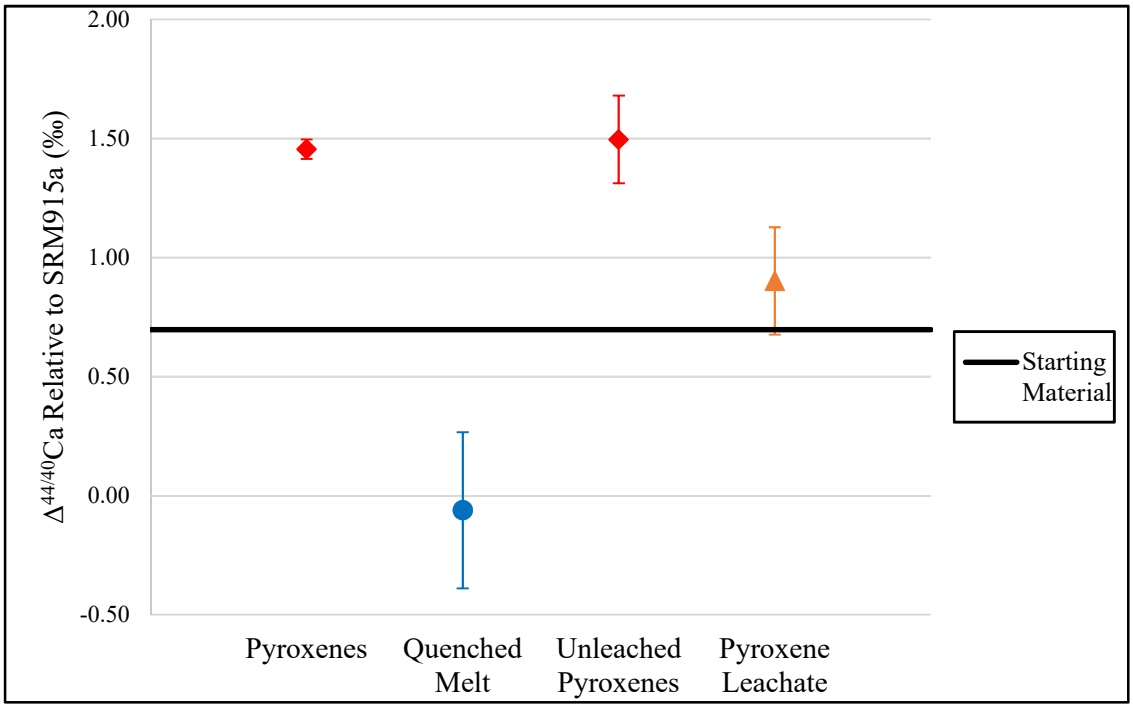

Figure 41 - $\delta^{44/40}$Ca difference between crystals and quenched melt in experiment Cbt-01 and the effect of leaching on crystals.

4.6.4 Iron Isotope Data

The three Cpx + Carbonated Silicate Melt experiments (Cbt-01, Cbt-02, M824) were also analyzed for their iron isotopic compositions. These experiments were chosen for Fe isotopic analysis because they were the only ones that contained iron in their bulk starting compositions. The results of these Fe isotopic analyses are given in Table 41. Like the Ca isotopic analyses, the crystals in each experiment yielded heavier isotopic compositions compared to the quenched melt as illustrated in Figure 42. In all the Cpx + Carbonated Silicate Melt experiments the $\delta^{44/40}$Ca values are positively correlated with $\delta^{57/54}$Fe values (Figure 43).

Table 41 - Iron isotopic compositions of Cpx + Carbonated Silicate Melt experiments.

Experiment Type	Sample ID	P/T	Phase	$\delta^{56/54}$Fe Rel. IRMM-014 (in ‰)	2 SD	N (repeats)	$\delta^{57/54}$Fe Rel. IRMM-014 (in ‰)	2 SD	N (repeats)
Cpx-Carbonated Silicate Melt	Cbt-01	3 GPa/1375 °C	Pyroxene	+3.35	0.04	3	+5.02	0.05	3
			Quenched Melt	+3.14	0.05	3	+4.67	0.07	3
	Cbt-02	5 GPa/1450 °C	Pyroxene	+2.83	0.03	3	+4.30	0.06	3
			Quenched Melt	+2.41	0.02	3	+3.67	0.05	3
	M824	5 GPa/1440 °C	Pyroxene	+2.35	0.07	3	+3.52	0.15	3
			Quenched Melt	+1.50	0.03	3	+2.25	0.07	3

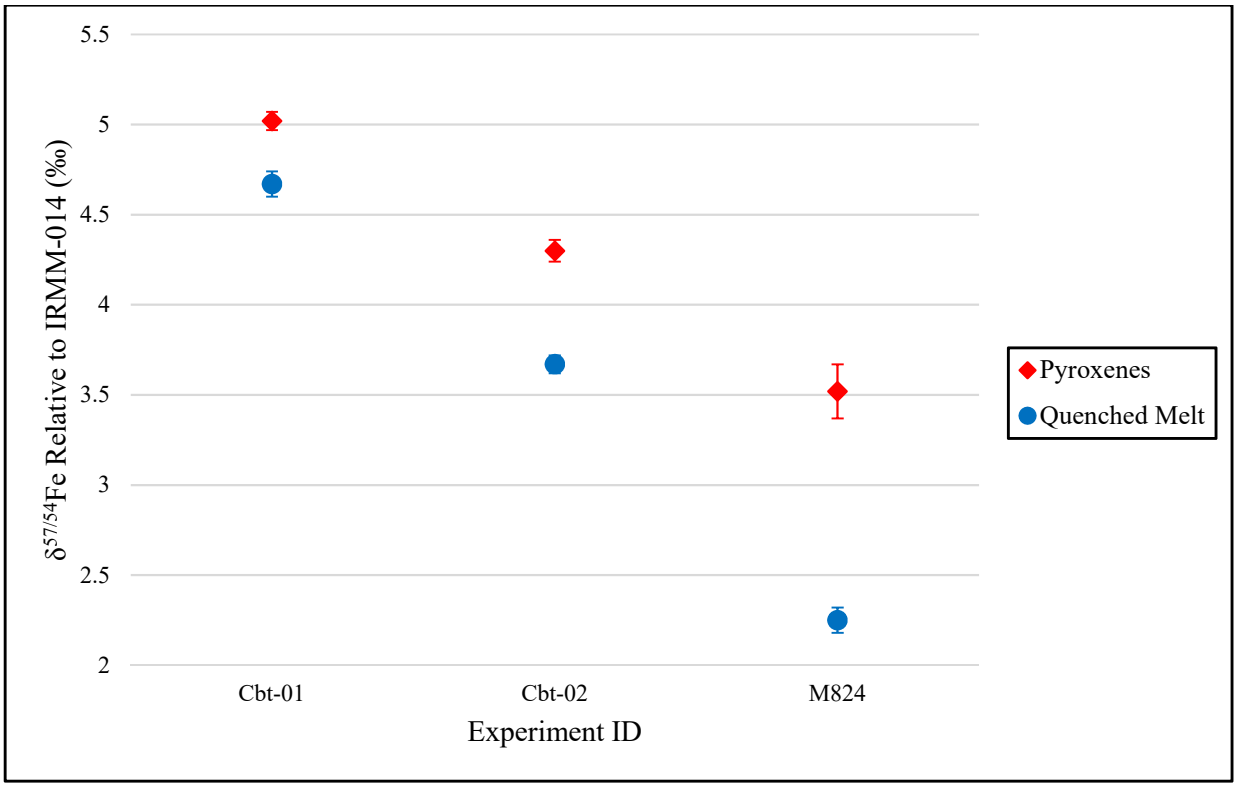

Figure 42 - Fe isotope data for Cpx + Carbonated Silicate Melt experiments reported as $\delta^{57/54}$Fe.

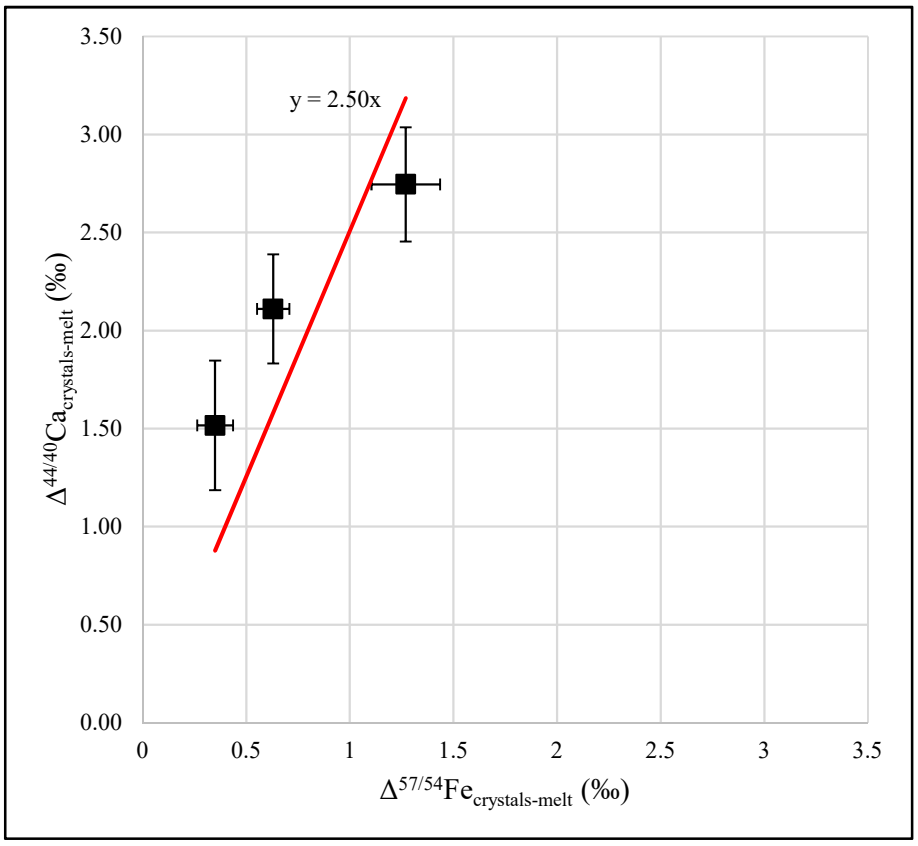

Figure 43 – $\Delta^{44/40}$Ca vs. $\Delta^{57/54}$Fe in Cpx + Carbonated Silicate Melt experiments.

Chapter 5

5. Discussion

5.1 Natural Samples

This study includes elemental and Ca and Sr isotopic analyses of natural samples from different regions and of different rock types. Carbonatites are the prime candidate for this study due to their mantle origins and carbon-rich compositions and they make up the bulk of the natural samples, but mantle peridotites and kimberlite samples are also included. Bulk rock samples as well as mineral separates were analyzed, with the goals being that bulk rock samples could help uncover information about sample origin and unseen reservoirs in the mantle, while mineral separates could be used to study fractionation between high-temperature phases in the Earth's mantle.

5.1.1 Bulk Carbonatites

This section discusses the bulk carbonatites analyzed in this study except for the Cape Verde and Tamazert carbonatites which are discussed as a separate case study in a later section. One of the reasons for conducting bulk rock calcium isotopic analyses of carbonatite samples from different localities was to determine if calcium isotopes could be used as a geochemical indicator of the source of these carbonatites or the processes that contributed to their formation.

Figure 44 compares the $\delta^{44/40}$Ca values of the carbonatites to the $\delta^{44/40}$Ca value for the upper mantle as determined by Huang et al. (2010). Many of the carbonatites (samples 10690, 12162, 9399, 25869) plot within the range of the upper mantle value within error. This suggests an upper mantle source for these carbonatites. Since the upper mantle $\delta^{44/40}$Ca value established by Huang et al. (2010) was calculated using the $\delta^{44/40}$Ca values of Cpx and Opx minerals in mantle peridotites. Since these carbonatites share $\delta^{44/40}$Ca values with the average value for the BSE or upper mantle peridotites this may implicate the carbonated peridotite theory of carbonatite formation for these samples. The $^{87}Sr/^{86}Sr$ ratios for these same samples also suggest a similar type of mantle source Samples 10690, 12162, and 9399 have nearly identical $^{87}Sr/^{86}Sr$ ratios (0.7032, 0.7033, and 0.7033 respectively) and sample 25869 is only slightly higher (0.7040) (Table 34 in Chapter 4). These $^{87}Sr/^{86}Sr$ ratios correspond to a slightly enriched MORB source

(Anderson, 1989), or could be attributed to a high U/Pb mantle (HIMU) source (Zindler and Hart, 1986).

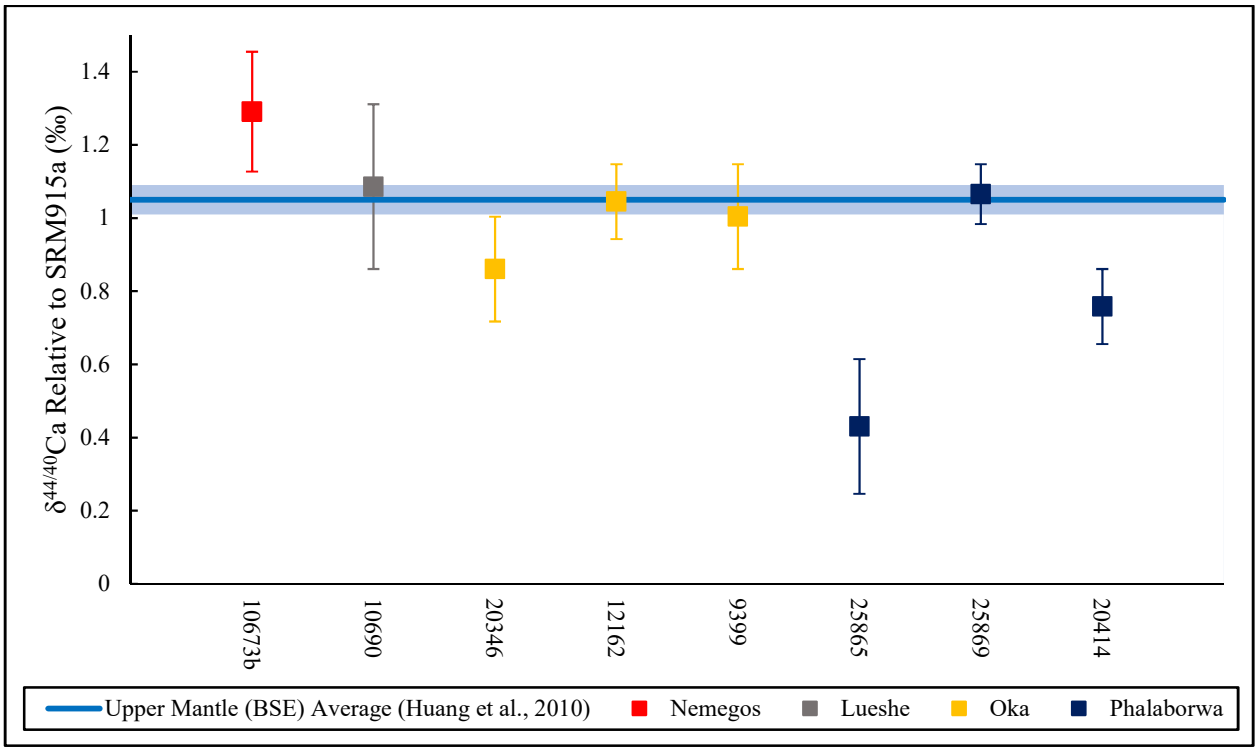

Figure 44 - Bulk rock $\delta^{44/40}$Ca values for carbonatites in this study compared to the BSE $\delta^{44/40}$Ca value of Huang et al. (2010).

The $\delta^{44/40}$Ca value for sample 20346 is only very slightly below the $\delta^{44/40}$Ca of the upper mantle (Figure 44). This sample is from the Oka carbonatite complex, along with samples 9399 and 12162 which both plot within the upper mantle range. Sample 20346 also has an identical $^{87}Sr/^{86}Sr$ ratio to that of both other Oka samples which would indicate a genetic relationship and the same mantle source. If the source of sample 20346 matches the other Oka samples, some subsequent process or processes must have caused the difference in $\delta^{44/40}$Ca. Differences in the partial melting of carbonatite source material or melt extraction processes are possible candidates for investigation. Kang et al. (2016) demonstrated that $\delta^{44/40}$Ca was positively correlated with concentrations of elements favouring melts such as Lu and Yb in bulk peridotites. We see this same positive correlation in the bulk rock Oka carbonatite samples (Figure 45). Sample 20346 contains lower concentrations of Lu and Yb and a lower $\delta^{44/40}$Ca value compared to samples 9399 and 12162, perhaps implicating melting related processes such as melt extraction or partial melting as contributing factors.

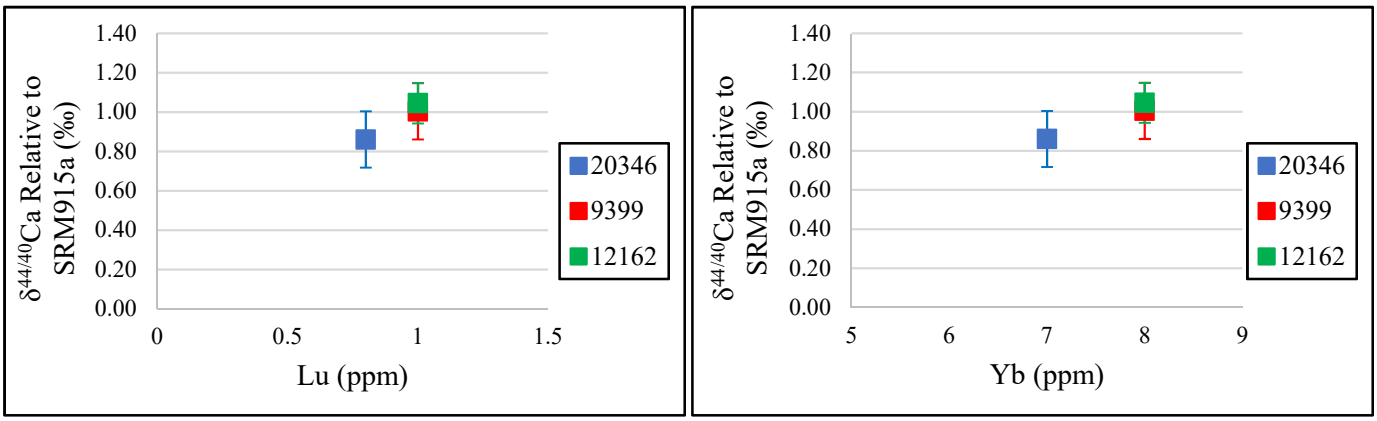

Figure 45 – Positive correlation between Lu and Yb concentrations and $\delta^{44/40}$Ca values in Oka carbonatite bulk rock samples.

The $\delta^{44/40}$Ca of samples 25865 and 20414 – both from the Phalaborwa carbonatite complex - plot well below the upper mantle average. These samples have significantly different $^{87}Sr/^{86}Sr$ ratios compared to the other carbonatite samples in this study – and compared to each other – indicating a different type of source material for these two samples (Table 34, Chapter 4). The $^{87}Sr/^{86}Sr$ ratio for 25865 (0.7064) indicates the enriched mantle 1 (EM1) mantle reservoir as a potential source, whereas the $^{87}Sr/^{86}Sr$ ratio for 20414 (0.7102) indicates the enriched mantle 2 (EM2) as a possible source (Zindler and Hart, 1986). The wide range of $^{87}Sr/^{86}Sr$ ratios in these Phalaborwa samples could be indicative of contamination by material with higher Sr isotopic ratios such as crustal material or interactions with later hydrothermal fluids, however, previous studies of Phalaborwa carbonatites argue against this due to a limited range of Nd-Hf isotopic variation (Wu et al., 2011). Zurevinski and Mitchell (2004) have argued that it is possible for carbonatite complexes to be formed by a mixture of multiple concurrent batches of carbonatitic magmas that are genetically-related but heterogeneous. Therefore, it is possible that the variations in both the $^{87}Sr/^{86}Sr$ ratios and the $\delta^{44/40}$Ca values of these Phalaborwa samples are the result of sampling different enriched mantle sources.

Sample 10673b is the only carbonatite sample in this study that plots above the average upper mantle $\delta^{44/40}$Ca. It also has the lowest $^{87}Sr/^{86}Sr$ ratio (0.7030) of any of the samples in this study (Table 34 in Chapter 4). This $^{87}Sr/^{86}Sr$ ratio still plots it as being sourced from the HIMU mantle reservoir like the Oka carbonatite samples but it is closer to a depleted mantle end member reservoir than any other sample in this study (Zindler and Hart, 1986). If the source for this

sample matches the upper mantle $\delta^{44/40}$Ca like other carbonatites in this study (10690, 12162, 9399, 25869) as well as one that plots just below (20346), other processes may be leading to the increased $\delta^{44/40}$Ca value. If we add this sample to the Lu (ppm) and Yb (ppm) versus $\delta^{44/40}$Ca plots in Figure 45, we see that it continues the same positive correlation trend (Figure 46). This again suggests the variations in $\delta^{44/40}$Ca that we see in these samples that originated from the same HIMU type mantle reservoir (according to their $^{87}Sr/^{86}Sr$ ratios) may be the result of varying degrees of source partial melting or carbonatite melt extraction processes.

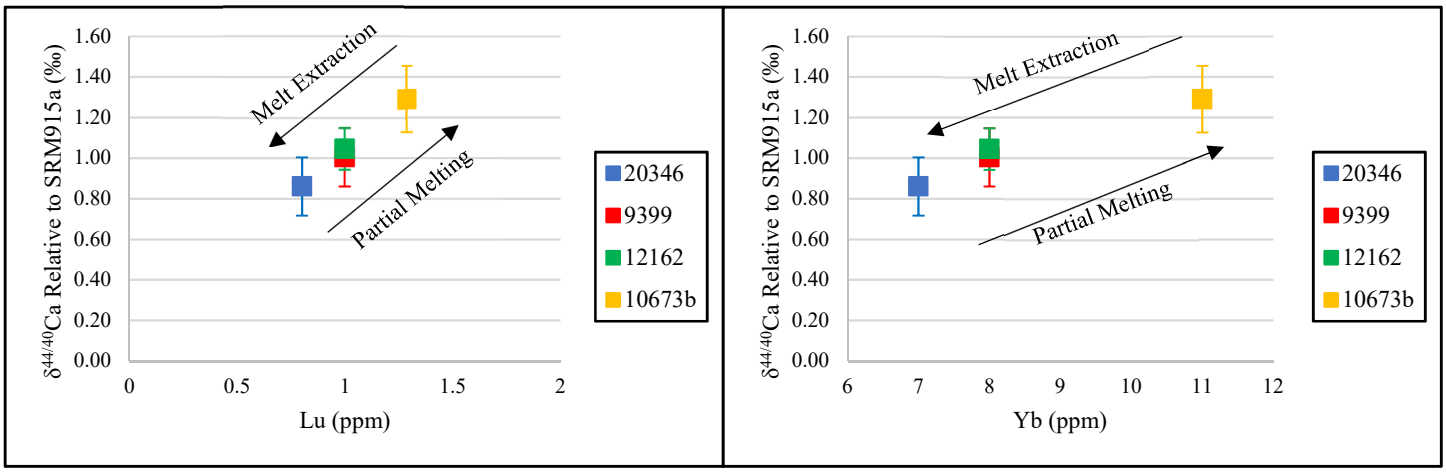

Figure 46 - Positive correlation between Lu and Yb concentrations and $\delta^{44/40}$Ca values in Oka carbonatite and Nemegos carbonatite bulk rock samples with HIMU type mantle reservoir origins.

In summary, it seems that the source effect found in the radiogenic Sr isotopes are not necessarily reflected in the $\delta^{44/40}$Ca values of the carbonatites analyzed in this study. This is supported by the wide range of $\delta^{44/40}$Ca values for carbonatites that originate from the same mantle reservoir according to their $^{87}Sr/^{86}Sr$ ratios (Figure 47). However, the $\delta^{44/40}$Ca values of these bulk carbonatite samples may be susceptible to modification by mantle processes. Analyzing additional well-characterized samples would help to clarify if $\delta^{44/40}$Ca values alone could be used to detect variations in mantle melting related processes for carbonatite samples that share the same type of mantle source. One additional note of importance is that these samples that were obtained from the Suffel Collection are all mineralized carbonatites whereas many of the carbonatite occurrences worldwide are not mineralized. Therefore, this study unintentionally sampled mineralized carbonatite samples and the influence of these mineralization processes on their $\delta^{44/40}$Ca values is unknown. It would be useful to analyze many

non-mineralized carbonatites along with mineralized carbonatites to see if any systematic differences exist.

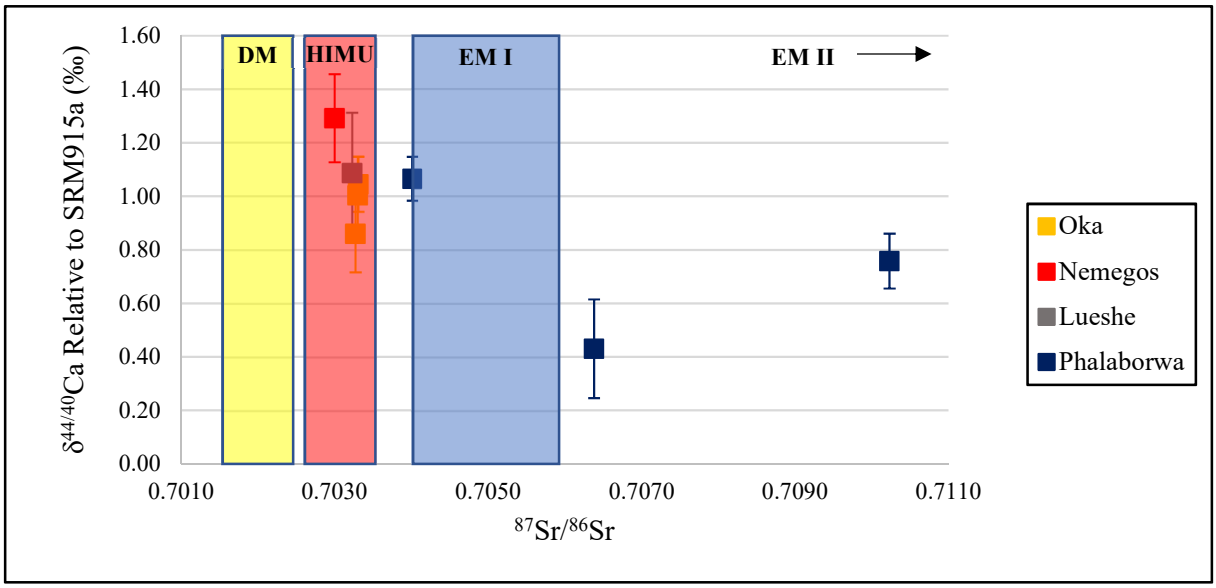

Figure 47 – $^{87}Sr/^{86}Sr$ ratios vs $\delta^{44/40}Ca$ values for bulk carbonatite samples in this study. Estimated Sr ratio ranges for mantle reservoirs overlain (Zindler and Hart, 1986). DM = Depleted Mantle, HIMU = High μMantle, EM I = Enriched Mantle I, EM II = Enriched Mantle II.

5.1.2 Cape Verde and Tamazert Carbonatites

This section focuses on the Cape Verde and Tamazert Carbonatites as a specific case study since they have already been examined recently in the research of Doucelance et al. (2014). Doucelance et al. (2014) used coupled cerium and neodymium isotopes to discuss whether the origin of the carbon in these oceanic carbonatites was primordial mantle carbon or the result of recycled marine carbonate via subduction. Their analyses and interpretations favoured the recycling of marine carbonates model, although they had difficulties in constraining the age and depth of this recycling.

Huang et al. (2011) have already showed that the Ca isotopic compositions of Hawaiian shield lavas can be used as evidence for the recycling of ancient marine carbonates into the mantle. If we use the same principles and concepts from their work, we can see if the Ca isotopic

compositions of these Cape Verde and Tamazert carbonatites supports the models of recycled marine carbonates.

If recycled ancient marine carbonates were part of the source material for these carbonatites, we would expect their $\delta^{44/40}$Ca values to be lower than the average for the upper mantle. Figure 48 compares the $\delta^{44/40}$Ca of the Cape Verde and Tamazert carbonatites to the upper mantle value. All the carbonatites plot below the upper mantle average as was expected by the recycled ancient marine carbonate model. If we adopt the same $\delta^{44/40}$Ca values for the upper mantle ($\delta^{44/40}$Ca = +1.05‰) and for ancient marine carbonates ($\delta^{44/40}$Ca = +0.20‰) as well as the same CaO concentrations for ancient carbonates and the mantle plume that were used by Huang et al. (2011), we can estimate the amount ancient marine carbonate that was added to the mantle source for these Cape Verde and Tamazert carbonatites. Table 42 provides the estimated amount of ancient marine carbonate added to the mantle source and the amount of the Ca budget that is contributed by this carbonate addition. Figure 49 illustrates the relationship between the amount of ancient marine carbonate added to a mantle source and the resulting $\delta^{44/40}$Ca (based on the model from Huang et al., 2011) with the calculated values for the Cape Verde and Tamazert carbonatites falling between the 0% and 5% end members.

The calculated amounts of ancient marine carbonates that would have needed to be added to the mantle source to yield the resulting $\delta^{44/40}$Ca values for these carbonatites ranges from 0.64% - 2.93%. This corresponds with approximately 10-35% of the total Ca in these samples contributed by marine carbonates (Table 42). The Ce-Nd isotopic compositions and ^{206}Pb/^{204}Pb isotopic ratios in Doucelance et al. (2014) correspond to a carbonate component addition in the order of a few %. Therefore, our results and calculations match up well and support the model of ancient marine carbonate recycling.

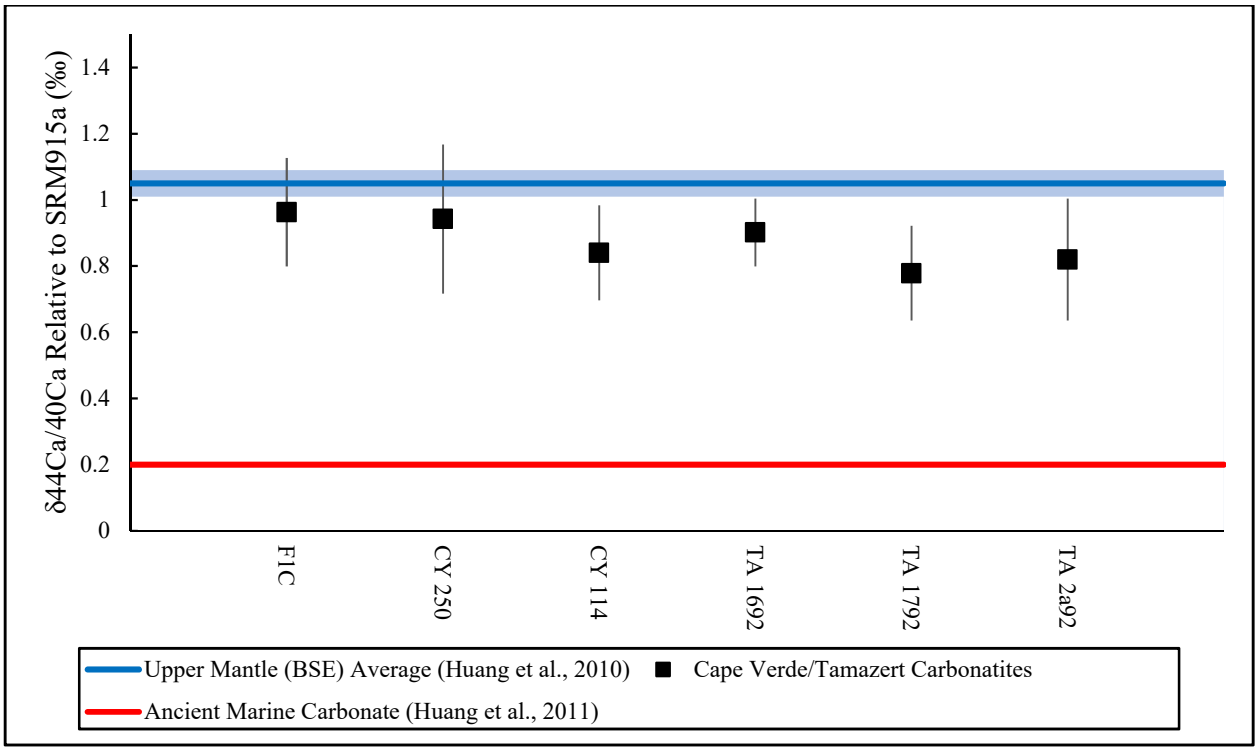

Figure 48 - Bulk rock $\delta^{44/40}$Ca values for Cape Verde and Tamazert carbonatites in this study compared to the BSE $\delta^{44/40}$Ca value of Huang et al. (2010).

Table 42 - Estimated amounts of ancient marine carbonate added to the mantle source for Cape Verde and Tamazert carbonatites and the amount of the total Ca budget contributed by this carbonate addition. Calculations are based on the calcium isotopic compositions measured in this study paired with the models and theory from Huang et al. (2011).

Location	Sample	$\delta^{44/40}$Ca relative to SRM915a	Carbonate added (%)	Ca budget from carbonate (%)
Fogo	**F1C**	+0.96	0.64	10.1
Brava	**CY 250**	+0.94	0.90	13.6
	CY 114	+0.84	2.17	27.9
Tamazert	**TA 1692**	+0.90	1.40	19.9
	TA 1792	+0.78	2.93	34.5
	TA 2a92	+0.82	2.42	30.2

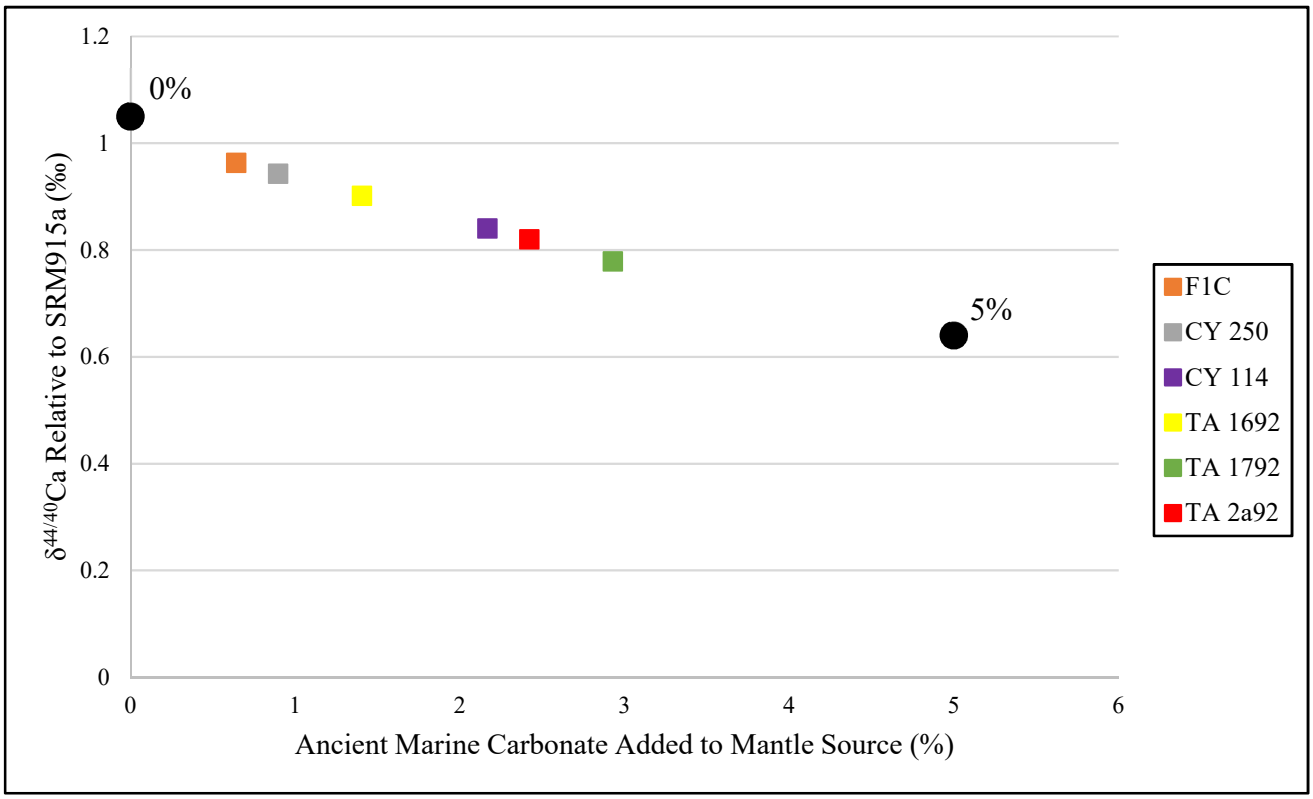

Figure 49 - Estimated amounts of ancient marine carbonate added to Cape Verde and Tamazert carbonatites with 0% and 5% end members plotted for reference.

5.1.3 Bulk Kimberlites and Related Peridotites

This section discusses the $\delta^{44/40}$Ca values of the one bulk rock kimberlite sample included in this study (R841), as well as one of the related bulk peridotite samples (16962). Figure 50 compares these samples to the average upper mantle $\delta^{44/40}$Ca value determined by Huang et al. (2010). Sample R841 plots within the range for the upper mantle whereas sample 16962 plots slightly below. Both samples have nearly identical $^{87}Sr/^{86}Sr$ ratios (0.7057 and 0.7055 respectively, Table 34 in Chapter 4) which correspond to the EM I reservoir as their mantle source. Since these samples appear to come from the same mantle source based on their strontium isotope ratios, perhaps we can implicate mantle melting processes as contributing factors to their $\delta^{44/40}$Ca differences as was shown to be a possibility for the carbonatite samples. Figure 51 plots the $\delta^{44/40}$Ca for each sample in relation to their Lu and Yb concentrations. Yet again we find that the processes of partial melting or melt extraction may be able to explain the $\delta^{44/40}$Ca variations in these samples. Especially when comparing the kimberlite to the peridotite sample it makes sense

that the kimberlite would be exposed to greater partial melting in its source material whereas the peridotite would be more likely to experience melt extraction processes.

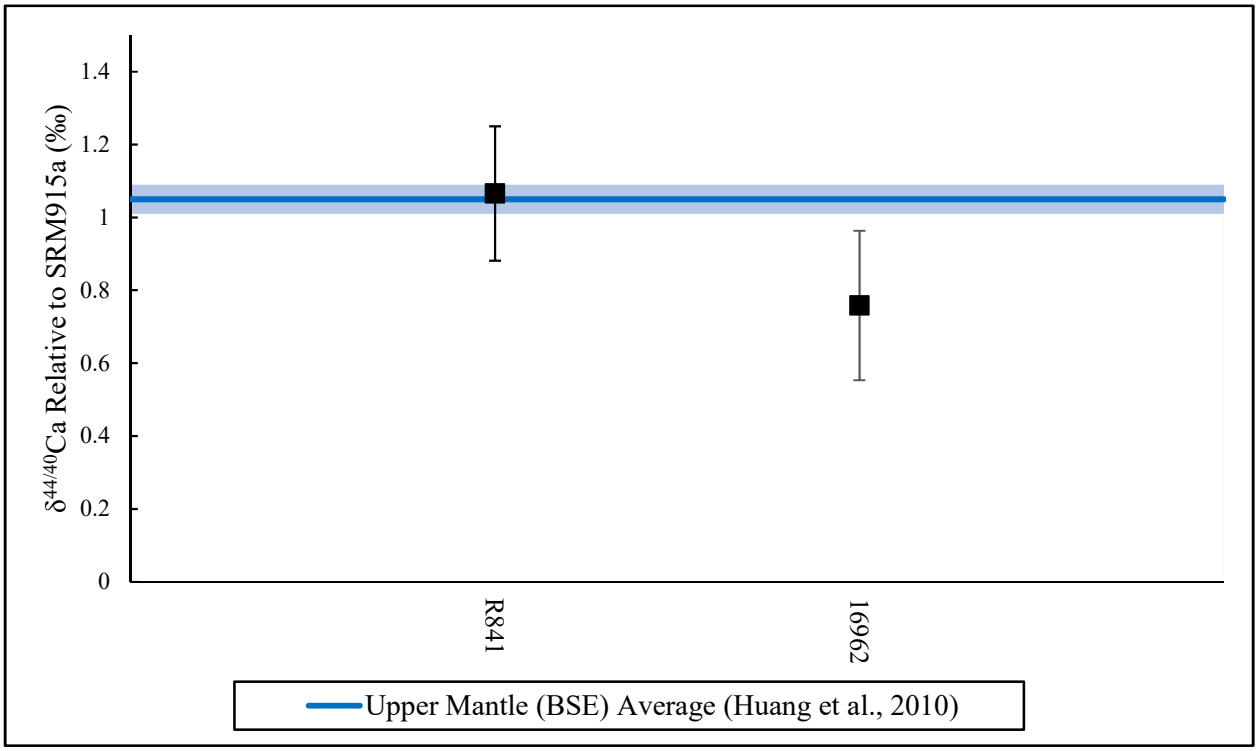

Figure 50 - Bulk rock $\delta^{44/40}$Ca values for Kimberley kimberlite (R841) and Kaapvaal peridotite (16962) in this study compared to the BSE $\delta^{44/40}$Ca value of Huang et al. (2010).

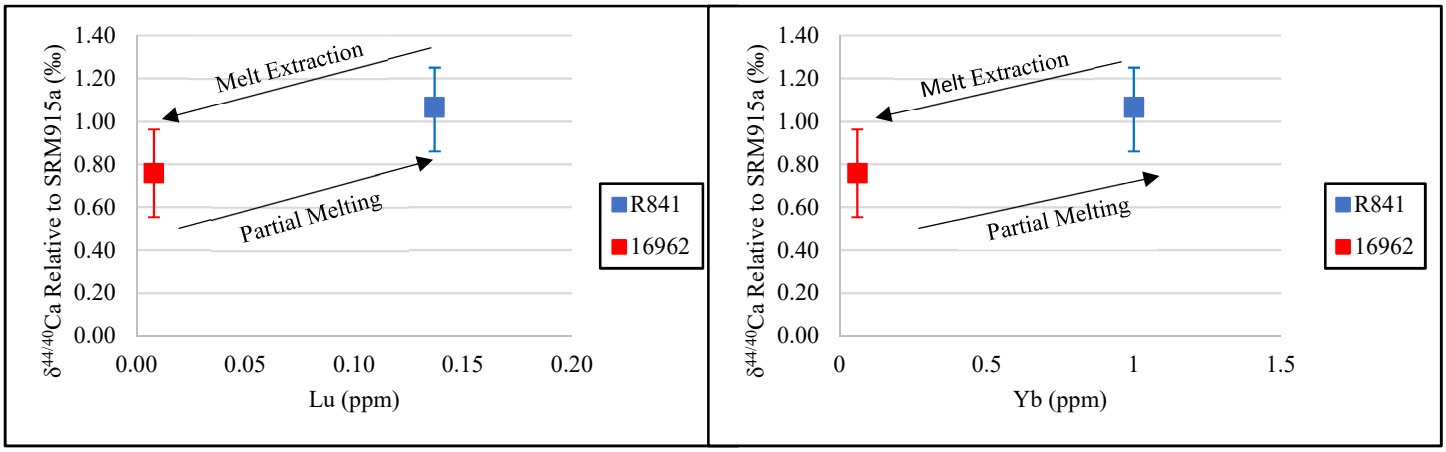

Figure 51 - Positive correlation between Lu and Yb concentrations and $\delta^{44/40}$Ca values in Kimberley kimberlite and Kaapvaal peridotite bulk rock samples with EM I type mantle reservoir origins.

5.1.4 Carbonate – Pyroxene Fractionation

The purpose of analyzing the Ca isotopic compositions of available Ca-bearing mineral separates from each sample is to help understand the systematics of inter-mineral fractionation for coexisting minerals in high-temperature igneous systems. Ca-O bond length is often the main contributing factor to fractionation between coexisting minerals. This has been shown for clinopyroxene and orthopyroxene pairs in high temperature systems (Huang et al. 2010) and calculated for carbonate minerals in low-temperature systems (Gussone et al., 2005), but the fractionation between coexisting high-temperature carbonates and pyroxenes has not been measured. Despite this, the expectation remains that differences in Ca-O bond lengths would be the main determinant of Ca isotopic fractionation between these minerals. Therefore, calcite is expected to yield heavier $\delta^{44/40}$Ca values than coexisting clinopyroxenes, but lighter $\delta^{44/40}$Ca values than coexisting orthopyroxenes. However, Table 33 and Figure 26 in Chapter 4 give the $\delta^{44/40}$Ca data for all coexisting calcite and pyroxene pairs and the results do not clearly support this prediction.

There are five total pairs of coexisting carbonate – pyroxene pairs that were analyzed in this study. Three were carbonatite samples (10673b, 10690, 9399), one was a kimberlite (R841), and one was a sample of marble from Bancroft. The major element compositions of each pyroxene and carbonate mineral separate can be found in Chapter 4 (Tables 22-24). There is quite a range of compositions for the pyroxenes analyzed in this study, making comparisons somewhat difficult. Samples BC-Cpx and R841-P are diopsides, 10690-P is an aegirine, 9399-P may be a wollastonite, and 10673b-P is an Fe-rich clinopyroxene often with many inclusions.

The Bancroft marble sample has identical $\delta^{44/40}$Ca values within error for both the calcite and clinopyroxene mineral components. Perhaps this is the result of some effect of metamorphism the sample has experienced. Since this sample is not a carbonatite, kimberlite, or peridotite, and the conditions under which it was metamorphosed are generally unknown, we will omit this sample from the rest of the interpretations in this section.

Samples R841, 10690 and 10673b all contained calcite – clinopyroxene pairs. We should expect the calcites to have heavier $\delta^{44/40}$Ca values than the clinopyroxenes based on Ca-O bond lengths, and we see that in sample 10673b and 10690, but not for R841-P. The estimated Ca-O bond length for wollastonite is 2.395 Å (Hesse, 1984) which is shorter than a typical clinopyroxene

and very similar to the estimated Ca-O bond length in a calcite but still slightly longer. Therefore, we would expect the $\delta^{44/40}$Ca of the wollastonite in sample 9399 to be close to the $\delta^{44/40}$Ca of the coexisting calcite but still slightly lower, but instead it is slightly higher.

There are too few samples and the pyroxenes are too variable in composition to make definitive arguments about coexisting calcite-pyroxene fractionation in these samples. However, there are a few trends that are noticeable in the data. Figure 52 shows a positive correlation between the Ca/Mg mole ratio in the pyroxenes and the $\Delta^{44/40}Ca_{carbonate - pyroxene}$ values. Ca/Mg mole ratio typically decreases as pyroxene composition moves from clinopyroxene to orthopyroxene. As the Ca/Mg ratio decreases in these pyroxenes, the $\Delta^{44/40}Ca_{carbonate - pyroxene}$ values get smaller, indicating more of the heavy Ca isotopes concentrating in the pyroxenes. Extrapolating this trend would yield more negative $\Delta^{44/40}Ca_{carbonate - pyroxene}$ values (i.e. pyroxene heavier than carbonate) for orthopyroxenes with low Ca-Mg mole ratios (Figure 53), thus fitting with the predictions based on Ca-O bond lengths.

Both Feng et al. (2014) and Kang et al. (2016) discussed the strong control of the chemical composition of orthopyroxenes (i.e. Ca content or Ca/Mg ratio) on the inter-mineral fractionation between Opx and Cpx. The patterns observed in this study suggest a strong compositional control on the inter-mineral fractionation that has been measured between the carbonates and pyroxenes. Despite the high variability in overall chemical composition in these pyroxenes, the Ca/Mg ratio appears to be a strong indicator of inter-mineral fractionation patterns.

Kang et al. (2016) also discuss the effect of temperature on Ca content in Opx and subsequently the $\Delta^{44/40}Ca_{Opx-Cpx}$ in their study and in Huang et al. (2010). For both data sets, they found that $\Delta^{44/40}Ca_{Opx-Cpx}$ was negatively correlated with increasing equilibrium temperatures. Kang et al. (2016) argued that the Ca content in Opx is controlled by the equilibrium temperature, and therefore, temperature controls the crystal chemistry of pyroxenes which subsequently exerts control on inter-mineral fractionation. If we apply this same theory to the data from this study, decreasing $\Delta^{44/40}Ca_{pyroxene-carbonate}$ or increasing $\Delta^{44/40}Ca_{carbonate-pyroxene}$ values may reflect an increase in equilibrium temperatures. With further studies and careful calibrations, $\Delta^{44/40}Ca_{carbonate - pyroxene}$ values could be used to estimate the temperatures and depths of formation for carbon-rich mantle rocks such as carbonatites and kimberlites.

However, another important point for consideration is the blocking temperatures or closure temperatures of different pyroxenes and carbonate minerals. Once the blocking temperature of a mineral has been reached, the crystal structure has formed sufficiently that the diffusion of isotopes is unlikely to continue. If the blocking temperatures of coexisting minerals is not the same, one of the mineral types may remain open to re-equilibration with infiltrating fluids or other minerals. This could result in coexisting carbonates and pyroxenes not being in isotopic equilibrium with respect to their Ca isotopes. Therefore, this should be considered in future investigations of this type.

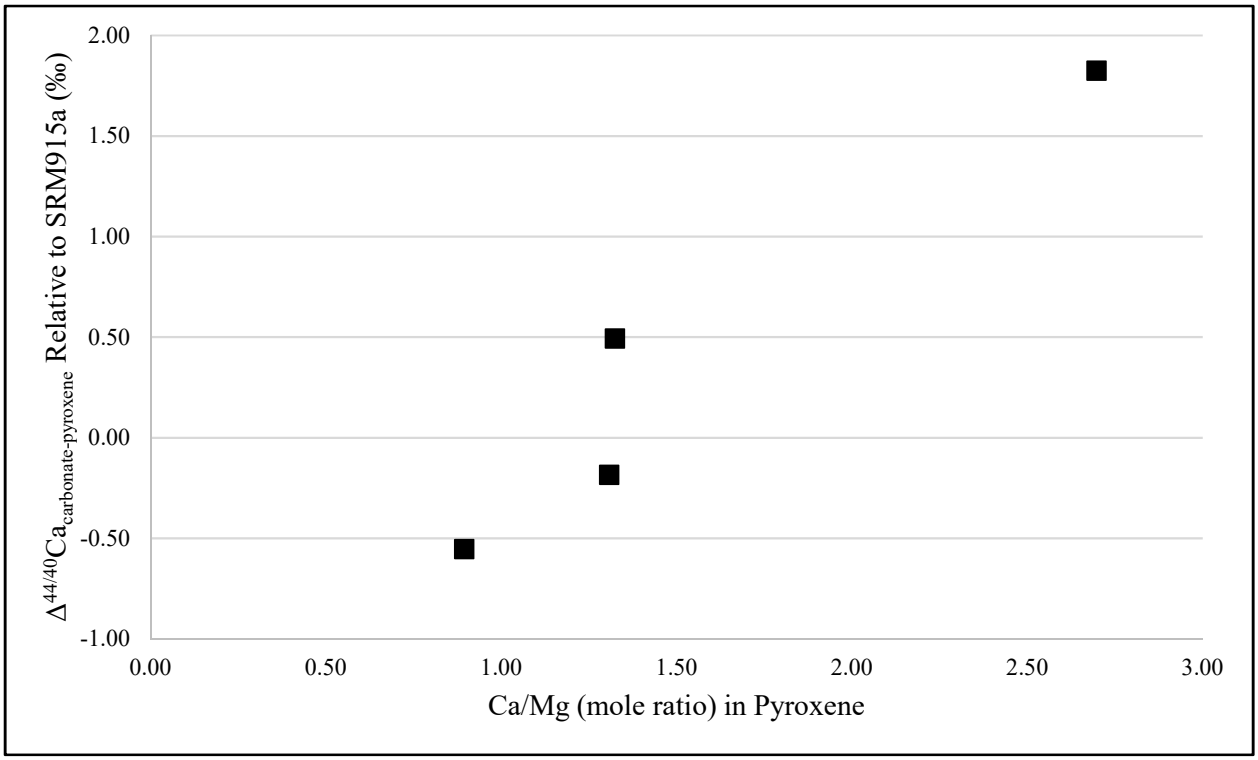

Figure 52 - Positive correlation between Ca/Mg ratio in pyroxene and $\Delta^{44/40}Ca_{carbonate\text{-}pyroxene}$

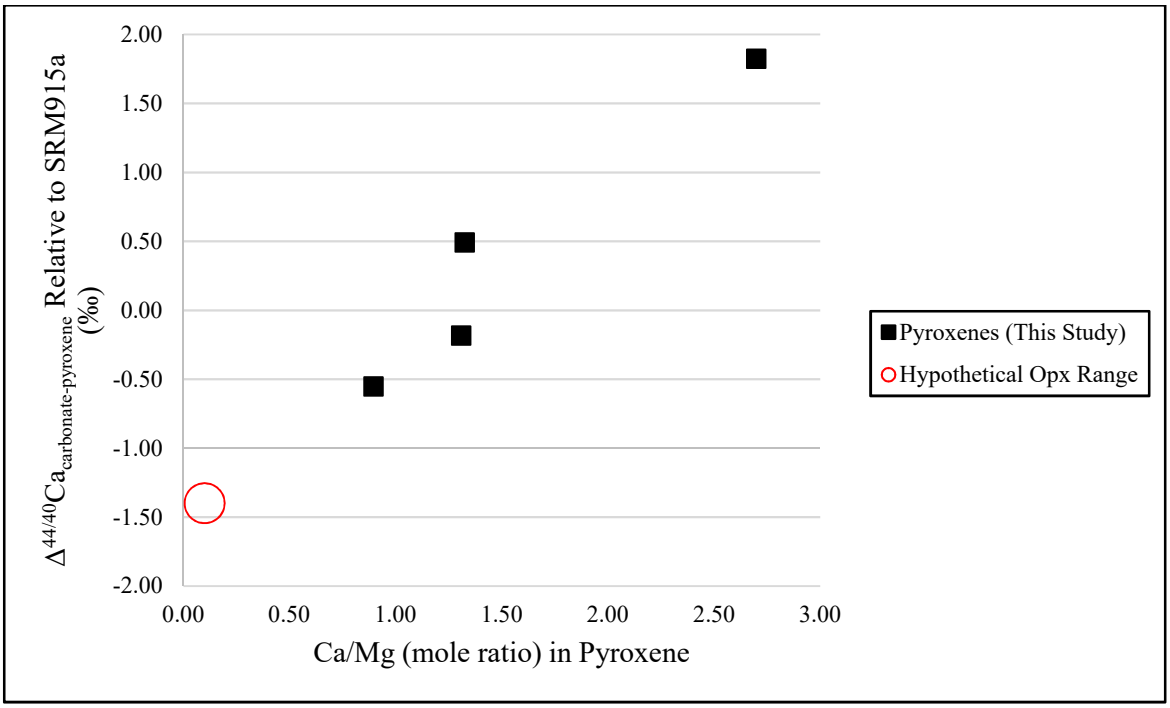

Figure 53 - Positive correlation between Ca/Mg ratio in pyroxene and $\Delta^{44/40}Ca_{carbonate\text{-}pyroxene}$ with extrapolated estimate for Opx.

5.1.5 Olivine – Pyroxene Fractionation

This study also included the analysis of two olivine samples (KH-Olv and SC-Olv) which coexisted with both clinopyroxenes and orthopyroxenes in the San Carlos and Kilbourne Hole mantle peridotites. There are extremely limited data published to date on olivine samples. One of the only instances of an olivine mineral separate analyzed for its Ca isotopic composition was in a recent work by Kang et al. (2016) in which it coexisted with both Cpx and Opx in a mantle peridotite and had a $\delta^{44/40}Ca$ that was identical to the Opx but higher than the Cpx. The olivines in this study were measured to have $\delta^{44/40}Ca$ values that were also higher than the coexisting Cpx in both samples. In the San Carlos peridotite, the olivine is slightly heavier in Ca isotopic composition than the Opx ($\delta^{44/40}Ca = +1.54 \pm 0.14‰$ compared to $\delta^{44/40}Ca = +1.37 \pm 0.14‰$) while in the Kilbourne Hole peridotite, the olivine was lighter than the coexisting Opx ($\delta^{44/40}Ca = +1.11 \pm 0.16‰$ compared to $\delta^{44/40}Ca = +1.56 \pm 0.23‰$). Since Kang et al. (2016) have shown that $\Delta^{44/40}Ca_{Opx\text{-}Cpx}$ decreases with increasing Ca/Mg in Opx, perhaps this same concept applies to $\Delta^{44/40}Ca_{Opx\text{-}Olivine}$. Figure 54 plots the Ca/Mg ratios in the San Carlos and Kilbourne Hole orthopyroxenes versus the $\Delta^{44/40}Ca_{Opx\text{-}Olivine}$ measured for these samples in this study. Although two data points is not a robust data set from which to draw conclusions, the same effect of

Ca/Mg ratios in Opx observed by Kang et al. (2016) appear to be present in the $\Delta^{44/40}Ca_{Opx\text{-}Olivine}$ values. Since there are not as many data to draw from, it appears olivines may be heavier or lighter than coexisting orthopyroxenes (perhaps depending on the chemical composition of the orthopyroxenes), but they do appear to match the existing, albeit limited, data and are heavier than coexisting clinopyroxenes.

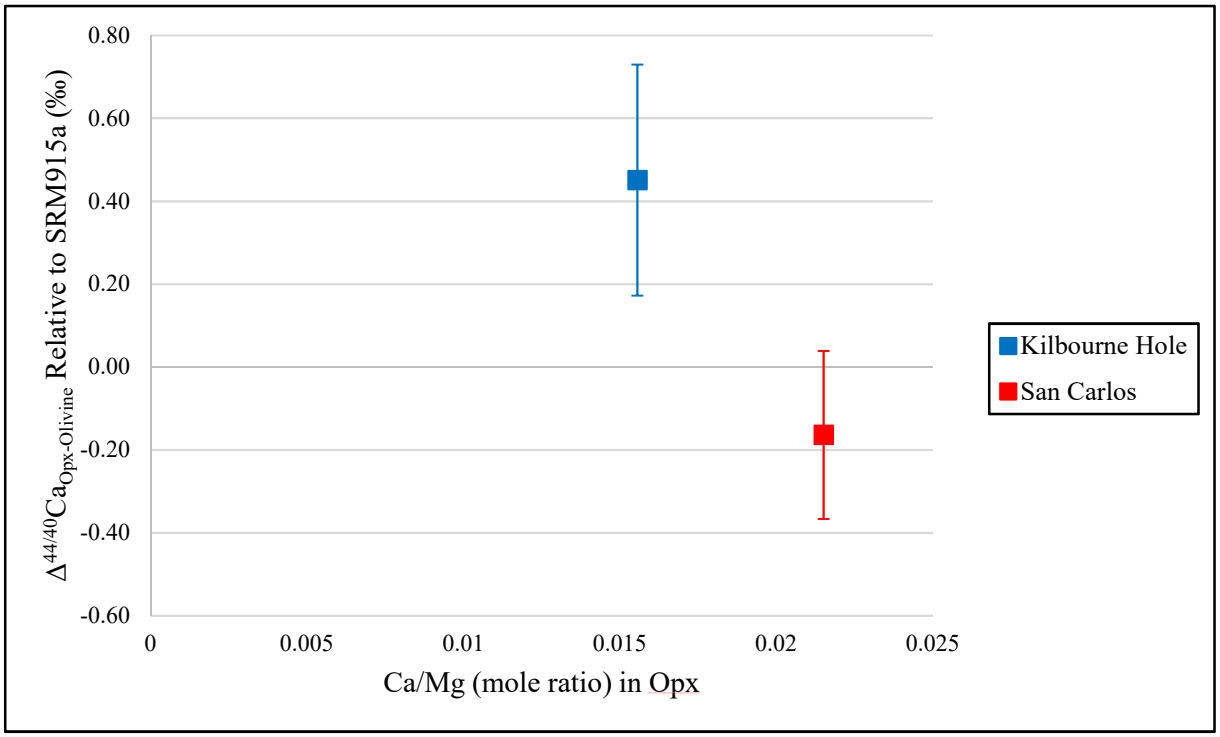

Figure 54 - Negative correlation between Ca/Mg ratio in Opx and $\Delta^{44/40}Ca_{Opx\text{-}Olivine}$.

5.2 Experimental Work

This study included the analysis of several high-pressure/high-temperature experiments with the goal of measuring the calcium isotopic fractionation between pyroxene and quenched melts of varying compositions to better understand and constrain the systematics of fractionation in natural systems.

5.2.1 Attainment of Equilibrium

Since the goal of the experiments was to measure isotopic fractionation between two phases, it is important that chemical and isotopic equilibrium was reached otherwise the analyses conducted could be measuring incomplete isotopic exchange between two phases that do not reflect upper

mantle chemical compositions. Attainment of chemical and isotopic equilibrium during each experimental run is of critical importance to the interpretation of the isotopic variations that are observed between the crystal and melt experimental phases. Although no experiment was conducted to specifically test that isotopic equilibrium was achieved during these experiments, the presence of homogeneous, unzoned pyroxenes (Figures 29,34,36 in Chapter 4) with compositions that were anticipated based on the composition of the starting materials used is suggestive of equilibrium conditions. Comparing the run times and P/T conditions of these experiments to those of Sossi and O'Neill (2017) also suggests they would have reached an equilibrium state. The experiments conducted by Sossi and O'Neill (2017) were similar in the sense that they were measuring isotopic fractionation between mineral phases and a fluid phase, and they determined that even after only 24 hours, their experiments had reached equilibrium. Our experiments were run for a minimum of 44 hours (up to 128 hours), and were also run at temperatures ranging from 325°C – 750°C higher than the 800°C run temperatures of Sossi and O'Neill (2017).

5.2.2 Experimentally Determined Fractionation Factors

If equilibrium conditions prevailed in the experiments, fractionation factors for the pyroxene versus melt phases of each experiment can be calculated. Table 43 gives the calculated values for these fractionation factors as well as the 1000lnα and Δ values. It is with these fractionation factors that we can begin to make some interpretations of the experimental data.

Table 43 - Crystals-Quenched melt fractionation factors for experimental samples.

Experiment Type	Experiment ID	P/T Conditions	Fractionation Factor ($\alpha_{Crystals - Melt}$)		1000ln α		$\Delta_{Crystals - Melt}$	
			$^{44/40}$Ca	$^{44/42}$Ca	$^{44/40}$Ca	$^{44/42}$Ca	$^{44/40}$Ca	$^{44/42}$Ca
Cpx + Carbonate Melt	B796	1250°C/3GPa	1.0004	1.0002	0.37	0.18	0.37	0.18
	B795	1350°C/3GPa	1.0006	1.0003	0.61	0.30	0.61	0.3
	B797	1450°C/3GPa	1.0013	1.0006	1.29	0.63	1.29	0.63
Cpx + Silicate Melt	A1325	1125°C/1GPa	1.0005	1.0002	0.45	0.22	0.45	0.22
Cpx + Carbonated Silicate Melt	Cbt-01	1375°C/3GPa	1.0015	1.0007	1.52	0.74	1.52	0.74
	Cbt-02	1440°C/5GPa	1.0021	1.0010	2.11	1.03	2.11	1.03
	M824	1440°C/5GPa	1.0027	1.0013	2.74	1.34	2.75	1.34

If we assume these are equilibrium fractionation factors, we can interpret the systematics of these fractionations using the available knowledge of how calcium isotopes fractionate between phases at high temperatures.

5.2.3 Ca-O Bond Lengths

Many of the recent studies involving inter-mineral fractionation of calcium isotopes at high temperatures have discussed the differences in Ca-O bonds lengths between different phases as a major contributing factor (e.g. Huang et al., 2010; Feng et al., 2014). As discussed in Chapter 1, shorter Ca-O bond lengths typically indicate stronger bonds which favour the heavier isotopes. An in-depth study of Ca-O bond lengths and Ca isotopes in various minerals such as the study conducted by Sossi and O'Neill for Fe-O bond lengths and iron isotopes does not currently exist. However, the studies by Huang et al. (2010) and Feng et al., (2014) looked at the Ca-O bond lengths in Opx versus Cpx in coexisting pyroxenes and used theoretical calculations that provide a basis for some interpretations. Also, while the current state of knowledge may not be robust, there is some information regarding the approximate Ca-O bond lengths in silicate and carbonate melts. Using this information, we can predict the direction in which calcium isotopes should fractionate between the minerals and melts in these experiments based on Ca-O bond lengths and compare these predictions to the results. Table 44 provides approximate Ca-O bond lengths for relevant mineral phases and melts.

Table 44 - Estimated Ca-O bond lengths for Ca-bearing minerals and melts. Opx, Cpx, and calcite bond lengths are from Huang et al. (2010), carbonate melt bond length from Genge et al. (1995), silicate melt bond length estimated from Sun et al. (2011).

Phase	Ca-O bond length (Å)
Orthopyroxene	2.15
Clinopyroxene	2.50
Calcite	2.32
Carbonate Melt	2.33
Silicate Melt	2.22

If the results were based purely on the assumption that the heavier isotopes of calcium would concentrate in the phase with the shorter Ca-O bond, then a negative correlation between Ca-O

bond length and $\delta^{44/40}$Ca is to be expected. However, plotting the $\delta^{44/40}$Ca values for each type of experiment against the approximate bond lengths of each experimental phase (Cpx and melt) illustrates a positive correlation (Figure 55). This suggests some other factors are at work in creating this fractionation between mineral and melt phases that is the opposite of what the Ca-O bond length theory predicts. Comparing the results of experiments Cbt-02 and M824 provides the only instance in which this line of reasoning may be relevant. Experiments Cbt-02 and M824 were run at the same P/T conditions and had the same starting material, yet experiment M824 produced some orthopyroxene and garnet crystals along with clinopyroxenes whereas Cbt-02 produced only clinopyroxenes. The appearance of Opx and garnet suggests that the temperature at the colder end of the capsule, which is situated at the opposite end to the thermocouple junction, may have been lower than in Cbt-02. The presence of garnet and orthopyroxene, while unintentional, verifies that the Cpx and carbonated silicate liquids in these experiments are indeed in equilibrium with a peridotite mineral assemblage. The addition of orthopyroxenes to the crystalline portion of M824 could explain its heavier calcium isotopic composition when compared to the Opx-free Cbt-02 crystals. In fact, if the crystals were purely Opx, the Ca-O bond length theory would predict a heavier crystal phase and lighter melt phase. However, the amount of orthopyroxene in M824 (~ 27% of crystal phase) is still outweighed by the amount of clinopyroxene (~ 64% of crystal phase) and the clinopyroxenes still account for the bulk of the Ca in the crystal phase (Cpx ≈ 91.3%, Opx ≈ 4.32%, Gt ≈ 4.34% of crystal phase Ca). Also, this still cannot account for the overall trend of heavier isotopes (larger $\delta^{44/40}$Ca values) accumulating in the crystal phases that is consistent across all the experiments.

In summary, current knowledge of the systematics of calcium isotopic fractionation between phases at high temperatures does not seem to be able to explain the fractionation trends found in these experiments. The general rule that shorter bond lengths and stronger bonds will concentrate the heavier isotopes of any element, calcium included, does not appear to be followed by these experiments. Additional factors need to be explored to uncover possible explanations.

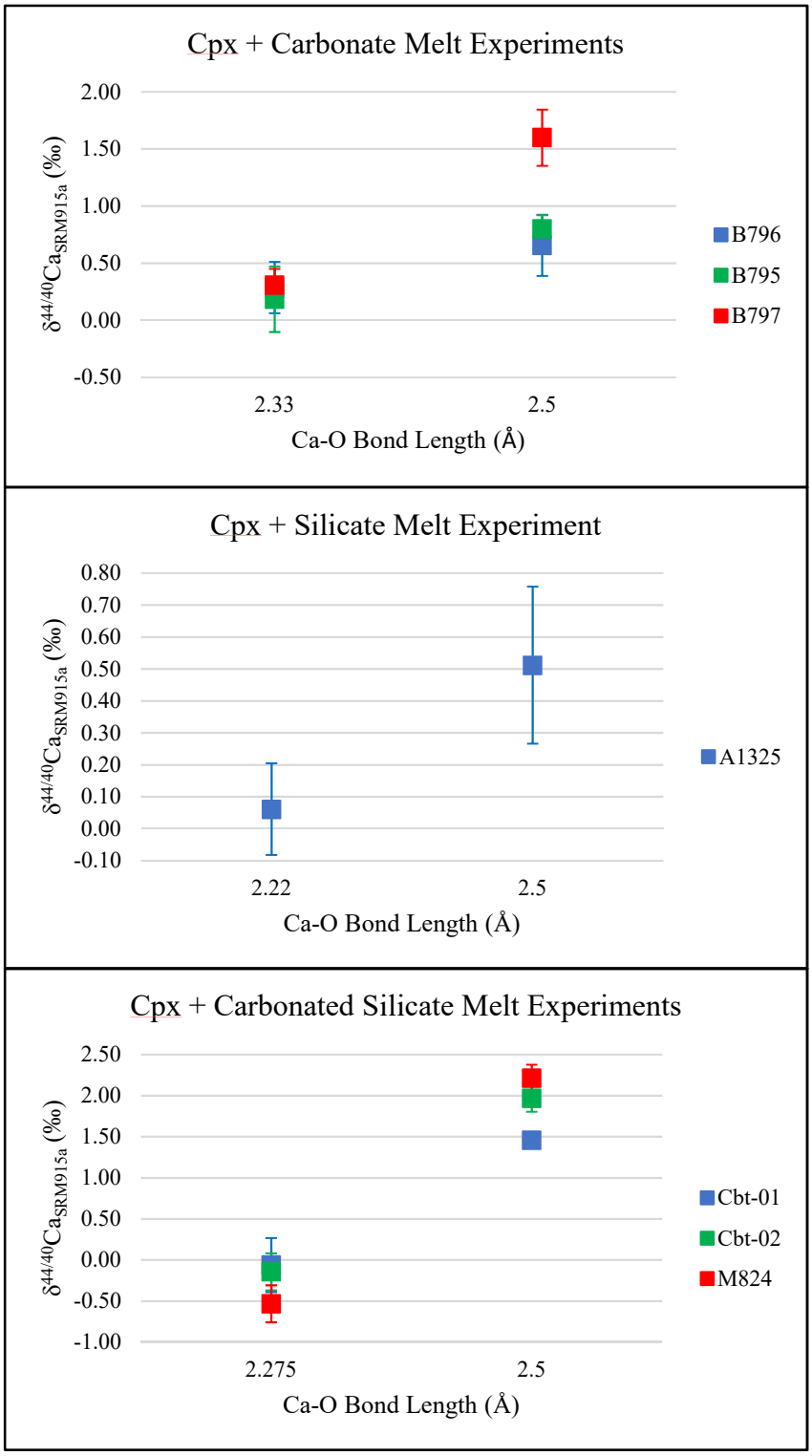

Figure 55 - Positive correlation between Ca-O bond length and $\delta^{44/40}$Ca for all experiments conducted.

5.2.4 Experimental Pyroxenes vs. Melts as a Proxy for BSE vs. Basalts

Looking at the $\delta^{44/40}$Ca values that have been published thus far for the Bulk Silicate Earth (BSE) (i.e. upper mantle) and terrestrial basalts leads to one possible interpretation of the relationship between the crystal and melt phases in the experiments. Figure 56 illustrates the $\delta^{44/40}$Ca values for the BSE and terrestrial basalts with the average $\delta^{44/40}$Ca values for the experimental crystal and melt phases for comparison. The BSE or upper mantle is slightly offset and heavier in its calcium isotopic composition compared to basalts. Although the size of the offset is increased by nearly an order of magnitude, we see the same pattern in the experimental data. This begins to make sense when we consider that some of the main Ca-bearing minerals in the Earth's upper mantle are pyroxenes and that basalts are a product of partial melting of the upper mantle. Additionally, the offset in the Cpx + Silicate Melt experiments ($\Delta^{44/40}Ca_{pyroxene\text{-}melt} = +0.45$) – likely representing the most common type of melt in the mantle – is less than the overall experimental average and closer to the offset found in nature. Although there have been studies published that indicate the lower $\delta^{44/40}$Ca values found in some basalts can be attributed to the recycling of ancient marine carbonates into their source material (e.g. Huang et al., 2011), $\delta^{44/40}$Ca variations in basalts have also been hypothesized to be caused by stable Ca isotopic fractionation during igneous processes. Additionally, the systematic trends in the data of Amini et al. (2009), strongly suggests a high temperature fractionation effect for Ca isotopes (Figure 57). While the results of these experiments do not necessarily indicate the mechanism that is driving the fractionation between the pyroxene and melt phases, it does support the theory that variations in basaltic and mantle rock $\delta^{44/40}$Ca values (specifically lower $\delta^{44/40}$Ca values) could be the result of calcium isotopic fractionation driven by igneous processes.

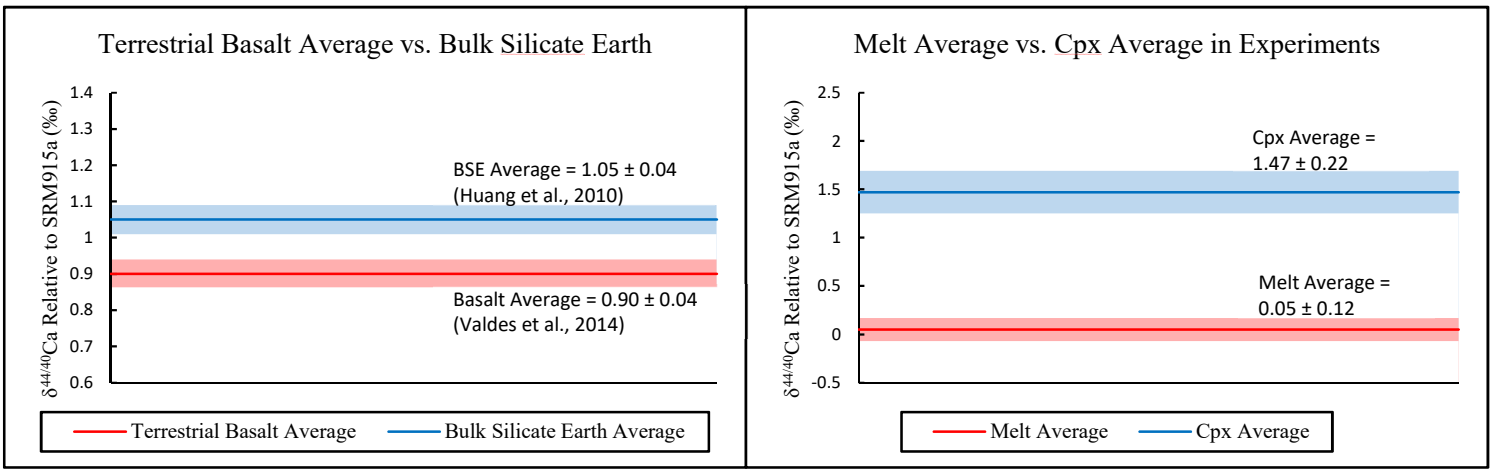

Figure 56 – $\delta^{44/40}$Ca values for BSE vs. terrestrial basalt average compared to the average $\delta^{44/40}$Ca values for Cpx vs. quenched melt in experiments.

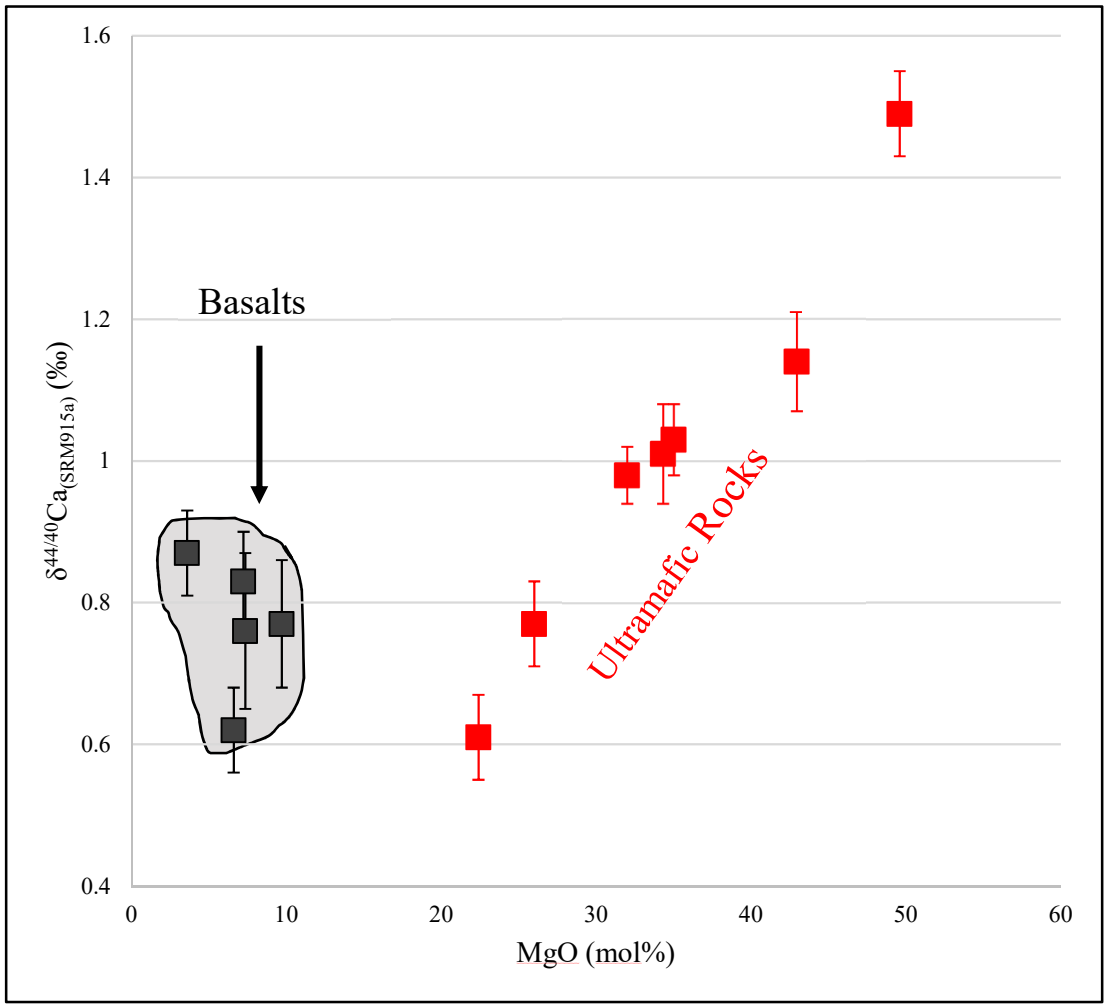

Figure 57 - Systematic trends in ultramafic rock $\delta^{44/40}$Ca data compared to basalts. Data from Amini et al. (2009).

To summarize thus far:

- If isotopic equilibrium conditions were achieved during our experiments, equilibrium fractionation factors for pyroxenes vs. melts can be estimated
- Estimated Ca-O bond lengths for the different experimental phases does not appear to be a good predictor of the direction or magnitude of fractionation.
- Experimental pyroxenes vs. melts may be a proxy for BSE vs. basalts in natural systems, and if so, the direction of fractionation in our experimental system correlates well to existing data for these natural systems.
- The mechanism or processes by which this fractionation occurs remains unknown.

5.2.5 Temperature Effect

The first general rule of equilibrium isotopic fractionation is the fractionation between two phases decreases with increasing temperatures as described by the relationship $1/T^2$. However, when we plot the fractionation between pyroxene and melt phases in these experiments we do not see this relationship. Figure 58 illustrates the relationship between temperature and the fractionation between experimental phases in the Cpx + Carbonated Silicate Melt experiments. We see an increase in the fractionation as the temperature increases, breaking the first rule of isotopic fractionation. However, there are other factors in play for this set of experiments, namely different pressures, different experimental apparatus (piston cylinder vs. multi-anvil), and different starting compositions.

This is where the Cpx + Carbonate Melt experiments are particularly important, since they were run at different temperatures but they all used a piston cylinder apparatus at the same pressure conditions, they all used the same starting materials, and they essentially all produced the same products (with B798 being the exception). Therefore, the effect of temperature can be more closely studied. Figure 59 shows this relationship between temperature and fractionation in the Cpx + Carbonate Melt experiments. The same trend of increasing fractionation with increasing temperature is even more evident in these experiments. Once again, this breaks the first general rule of equilibrium isotopic fractionation. So, either the experiments did not achieve equilibrium or there are other factors that are influencing the fractionation between the pyroxenes and melt

phases. Due to the evidence supporting the achievement of equilibrium during the experiments that has already been discussed, there must be other contributing factors to explain this fractionation trend.

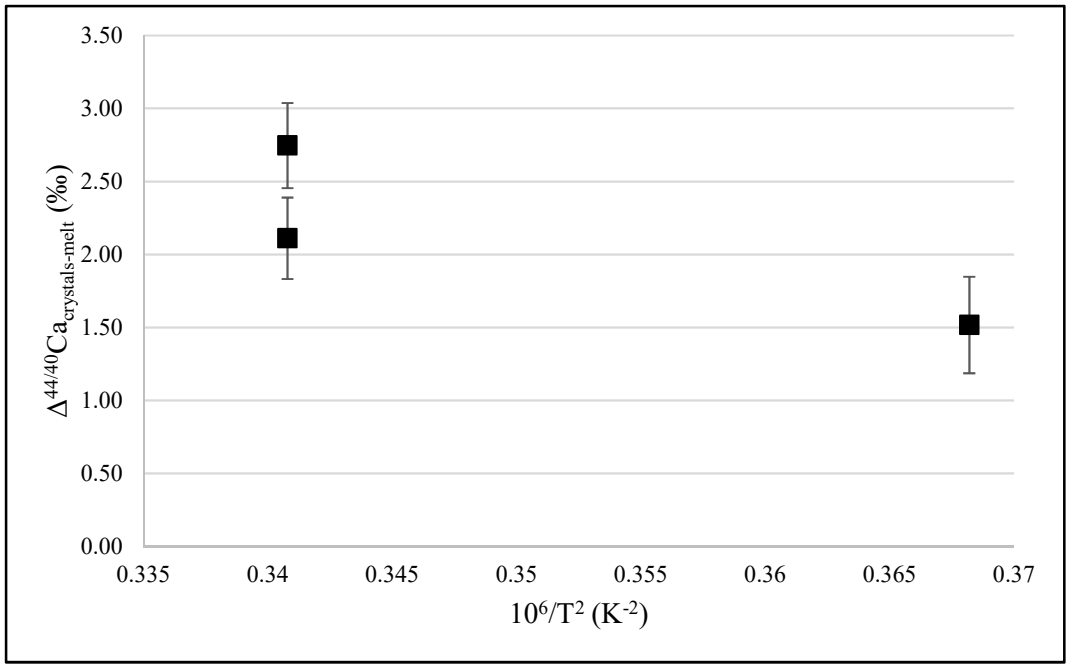

Figure 58 - Positive correlation between temperature and $\Delta^{44/40}Ca_{crystals\text{-}melt}$ in Cpx + Carbonated Silicate Melt experiments.

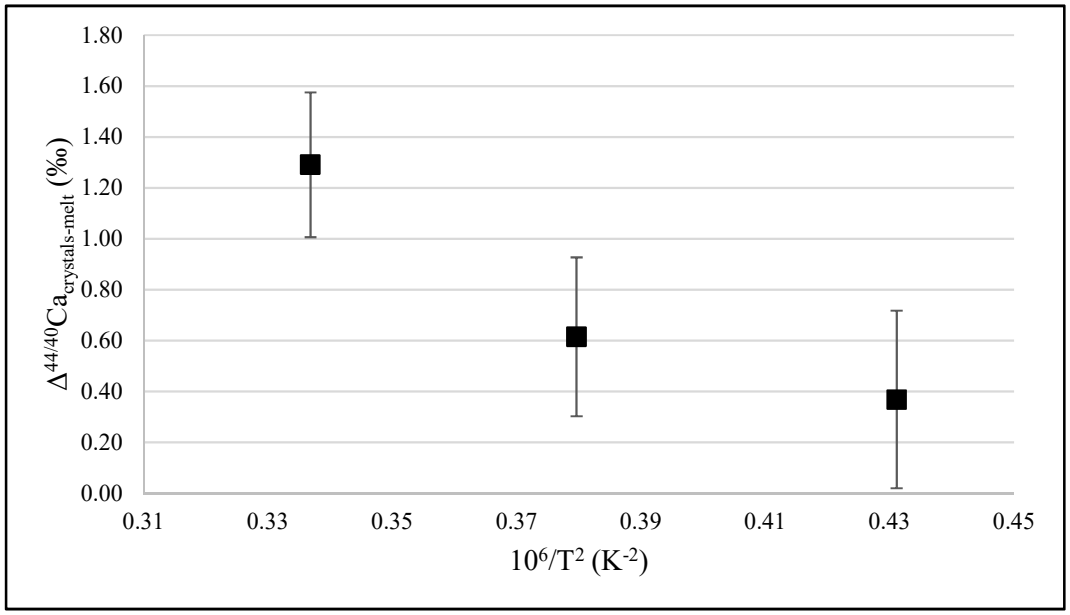

Figure 59 - Positive correlation between temperature and $\Delta^{44/40}Ca_{crystals\text{-}melt}$ in Cpx + Carbonate Melt experiments.

The Cpx + Carbonate Melt experiments were important for examining the effect of temperature because almost all other experimental conditions were the same. But, upon closer investigation, there was one additional factor that varied slightly amongst these experiments – the size of the experimental capsule itself. The exact size (i.e. length) of every experimental capsule was not measured but the mass of each sample was, and this can be used as a proxy for the length of the capsule since 3 mm diameter capsules were used for all the experiments. Based on sample masses and the lengths of several capsules that were measured, 10 mg of sample corresponds to approximately 1 mm of capsule length. In general, larger capsules were used for the higher temperature experiments to help ensure the formation of sufficient pyroxene crystals for isotopic analysis. Figure 60 illustrates the relationship between the mass of the experimental sample (representing the length of the capsule) and the fractionation between phases. There appears to be a positive correlation between the length of the experimental capsule and the magnitude of the fractionation between phases. Since increasing fractionation with increasing temperature goes against the general rules of isotopic fractionation, it seems much more logical that the fractionation is somehow related to the variations in capsule length.

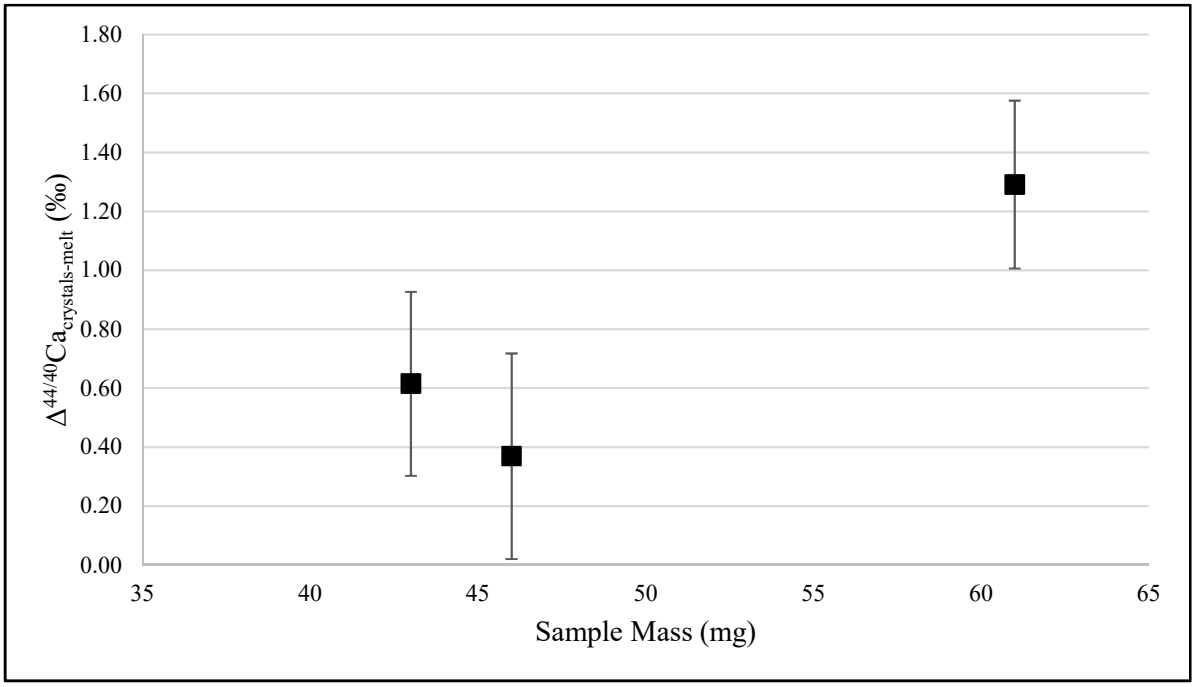

Figure 58 - Positive correlation between sample mass and $\Delta^{44/40}Ca_{crystals\text{-}melt}$ in Cpx + Carbonate Melt experiments.

To summarize:

- The magnitude of fractionation between phases in the different sets of experiments appears to be correlated positively with temperature.
- The magnitude of fractionation is also positively correlated with the length of the experimental capsule.
- Since one of the rules of isotopic fractionation is the $1/T^2$ relationship, perhaps there is a mechanism involving the length of the experimental capsule that can explain the otherwise contradictory correlation between fractionation and temperature in the experiments.

5.2.6 Thermal Diffusion

Thinking of a mechanism that involves the length of the experimental capsule as well as variations in temperature invoked the theory of isotopic fractionation by thermal diffusion recently studied by Richter et al. (2009) and Huang et al. (2010). The concept of isotopic fractionation of major elements by thermal (or Soret) diffusion was outlined in Chapter one but the main point to consider is that all major elements undergo isotopic fractionation in the same direction when a silicate melt is held under a temperature gradient, with the heavier isotopes concentrating at the cold end of the gradient. In a piston cylinder apparatus, the thermocouple that measures and helps regulate the temperature of the experiment is located near the top of the experimental capsule. This means that there is a 'hot spot' located near the top end of the capsule and, although the apparatus is designed to minimize this, there will be a slight decrease in temperature in areas within the capsule that are further from this hot spot. This means this effect will be amplified when the length of the experimental capsule is increased. We see this in the experiments of Richter et al. (2009) where they used a 10 mm long capsule that was purposely offset from the piston cylinder hot spot to set up a larger temperature gradient to measure the effects of thermal diffusion (Figure 61A). Conversely, when they wanted to measure the effects of chemical diffusion and minimize the effects of thermal diffusion, they used a smaller 5 mm long capsule (Figure 61B).

Thermal isotopic fractionation has not been observed in carbonatite or carbonated silicate melts. For thermal fractionation to be effective, the liquid phase must remain unstirred by convection. Low viscosity aqueous fluids likely remain sufficiently well-mixed through convective processes to eradicate thermal fractionation (e.g. Sossi and O'Neill, 2017). The melts in these experiments have significantly lower viscosity than silicate melts (Dobson et al., 1996; Genge et al., 1995), so it is not clear whether a stable compositional or isotopic profile could be maintained. Certain aspects of the experiments conducted in this study suggest, however, that thermal diffusion may be contributing to the measured isotopic fractionation patterns. Most importantly, the pyroxenes in each experiment formed in the bottom end of the experimental capsule where the temperature would be the lowest. This is the phase that is enriched in the heavier isotopes of calcium in every experiment and this effect is amplified when the length of the capsule (and therefore any temperature offset that exists within it) is increased. Especially when these observations are paired with the fact that the direction of fractionation between phases goes against predictions based on Ca-O bond lengths and defies the well-established $1/T^2$ relationship between fractionation and temperature, thermal diffusion driven isotopic fractionation seems to be a possible interpretation.

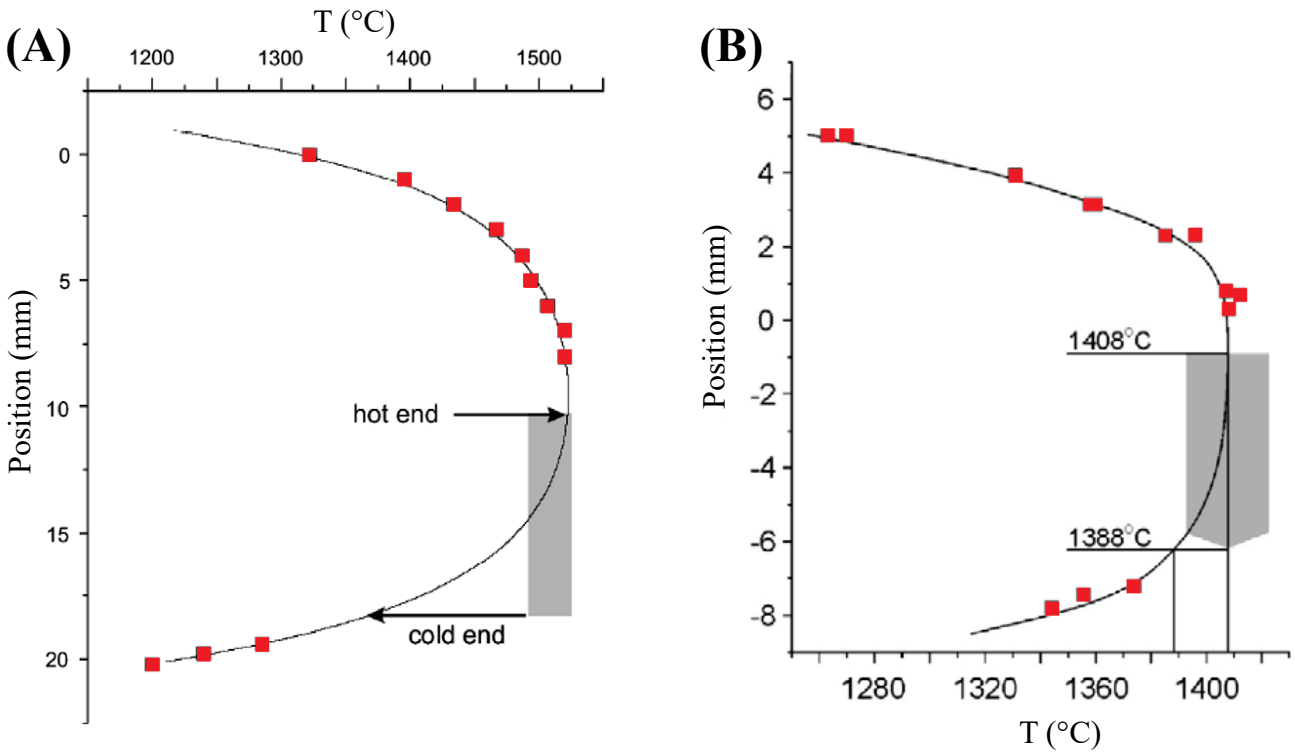

Figure 59 - Temperature gradients within a piston-cylinder apparatus. Figure from Richter et al. (2009)

The Fe isotopic composition of the Cpx + Carbonated Silicate Melt experiments was analyzed to test the hypothesis that the measured Ca isotopic fractionation is caused by thermal diffusion. When isotopic fractionation is driven by thermal diffusion, heavy isotopes of all major elements including Ca and Fe will concentrate in the cold end of the temperature gradient (Richter et al., 2009; Huang et al., 2010). Moreover, we can use relative magnitude of thermal fractionation of Ca and Fe measured by Huang et al. (2010) to predict the Fe fractionation (for silicate melts) that should accompany temperature-driven Ca isotopic fractionation. Therefore, if the Fe isotope fractionation pattern between experimental phases is in the order of that predicted from silicate melt studies, this would be consistent with thermal diffusion effects. If the Fe isotopes fractionated in the opposite direction to the Ca isotopes, this would essentially rule out thermal diffusion. Results showed that the heavier Fe isotopes were also enriched in the pyroxenes compared to the melt phases (Chapter 4), thus providing additional evidence in support of thermal diffusion.

Richter et al. (2009) and Huang et al. (2010) both provide estimates for the changes in $\delta^{44/40}$Ca and $\delta^{57/54}$Fe expected per °C caused by thermal diffusion. Table 45 provides these estimates for $\delta^{44/40}$Ca and $\delta^{57/54}$Fe based on these two studies, as well as the relationships between Ca and Fe including those in this study. These values were calculated based on the experiments of Richter and Huang which utilized large temperature gradients and long experimental capsules, but if we assume they are applicable to any size capsule and any range of ΔT we can use them to interpret the fractionations in our experiments.

Table 45 - Estimated rates of change to $\delta^{44/40}$Ca and $\delta^{57/54}$Fe caused by thermal diffusion compared to data from this study.

	Richter et al. (2009)		Huang et al. (2010)		Data from this study
	$^{44/40}$Ca	$^{57/54}$Fe	$^{44/40}$Ca	$^{57/54}$Fe	
‰/°C	0.064	0.033	0.061	0.036	
$^{44/40}$Ca/$^{57/54}$Fe	1.94		1.69		2.50

Since we did not measure the ΔT that would have existed within our experimental capsules, the Fe isotope measurements and the relationship between $\Delta^{44/40}$Ca and $\Delta^{57/54}$Fe were used to identify the possibility of thermal effects. Because the relative magnitudes of thermal gradient driven fractionation for different elements are proportional, considering the ratio of Ca fractionation vs Fe fractionation allows us to remove temperature from the equation: for fractionation in a temperature gradient, $\Delta^{44/40}$Ca/$\Delta^{57/54}$Fe is constant. Figure 62 illustrates the $\Delta^{44/40}$Ca/$\Delta^{57/54}$Fe relationship for the Cpx + Carbonated Silicate Melt experiments compared to the $\Delta^{44/40}$Ca/$\Delta^{57/54}$Fe caused by thermal diffusion according to Richter et al. (2009) and Huang et al. (2010). The line of best fit for our data is forced through the origin to better compare its slope to the slopes from Richter et al. (2009) and Huang et al. (2010). The positive correlation that is found in our experiments suggests that we cannot rule out the effects of thermal diffusion. Additionally, the slope of the $\Delta^{44/40}$Ca/$\Delta^{57/54}$Fe relationship is in the order of that observed in the thermal diffusion studies (Huang et al., 2010; Richter et al., 2009).

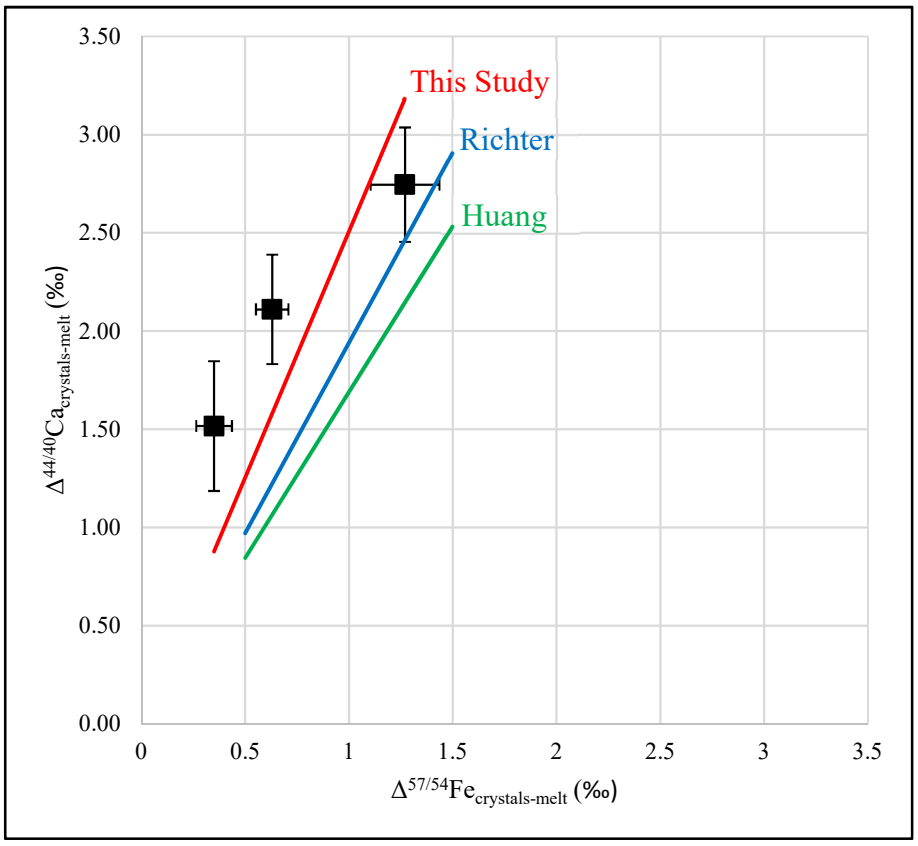

Figure 60 – $\Delta^{44/40}Ca/\Delta^{57/54}Fe$ relationship for the Cpx + Carbonated Silicate Melt experiments in this study compared to the $\Delta^{44/40}Ca/\Delta^{57/54}Fe$ caused by thermal diffusion according to Richter et al. (2009) and Huang et al. (2010)

Table 46 shows the estimated ΔT within our experimental capsules calculated using the average changes in $\delta^{44/40}Ca$ per °C according to Huang et al. (2010) and Richter et al. (2009) (Table 45) and based on the assumption that the $\Delta^{44/40}Ca_{crystal\text{-}melt}$ measured in each experiment is driven entirely by thermal diffusion. Essentially, Table 46 calculates the effective ΔT that explains the measured values according to thermal diffusion in silicate melts. The calculations show that increased effective ΔT corresponds with increased experimental temperature. The higher effective ΔT calculated for the Cpx + Carbonated Silicate Melt experiments corresponds to the use of the modified multi-anvil apparatus for these experiments which may be expected to have a slightly steeper temperature gradient. The conclusion here is that the calculated effective ΔT's are very reasonable, they increase with experimental temperature and are larger in the multi-anvil experiments, suggesting that thermal effects are a reasonable explanation for the $\Delta^{44/40}Ca_{crystal\text{-}melt}$ values that were measured in the experiments.

Table 46 – Estimated temperature variation within experimental capsules calculated based on the measured $\Delta^{44/40}Ca_{crystals\text{-}melt}$ in this study and effect of thermal diffusion driven fractionation for calcium isotopes averaged from Richter et al. (2009) and Huang et al. (2010).

Type of Experiment	Experiment ID	$\Delta^{44/40}Ca_{crystal\text{-}melt}$ (‰)	Estimated ΔT Within Experimental Capsule (°C)
Cpx + Carbonated Silicate Melt	Cbt-01	+1.52	24.3
	Cbt-02	+2.11	33.8
	M824	+2.75	43.9
Cpx + Carbonate Melt	B796	+0.37	5.9
	B795	+0.61	9.8
	B797	+1.29	20.7
Cpx + Silicate Melt	A1325	+0.45	7.2

If the $\Delta^{44/40}Ca_{crystal\text{-}melt}$ that was measured in our experiments is due to thermal effects, we can make some assumptions and describe two scenarios that can explain the mechanism behind this process occurring within the experiment. The assumptions are that the crystals are in the lower portion of the capsule, while the melt is in the upper half, and that the temperature within the capsule increases uniformly from bottom to top. Additionally, we assume all fractionation is driven by temperature and we analyze all melt from the top and all crystals from the bottom. Based on these assumptions, the two different scenarios that may exist are:

1. All the crystals are in equilibrium with the bottom of the melt pool (Figure 63A).
2. There is a vanishingly small melt fraction in the lower half of the capsule that allows temperature driven fractionation to persist throughout (Figure 63B).

In each scenario, $\Delta^{44/40}Ca$ is related to an effective ΔT, and if we use the rate of change to $\Delta^{44/40}Ca$ per °C from Huang et al. (2010) we can come up with equations that describe the fractionation from thermal effects in our experiments. The first scenario could be described by the following equation:

$$\Delta^{44/40}Ca = \text{capsule length} * \text{temperature gradient} * 0.061 / 4$$

This equation can be reduced further to give us:

$$\text{Effective } \Delta T = \text{capsule length} * \text{temperature gradient} / 4$$

Since scenario two allows for temperature driven fractionation to persist throughout the entire experimental capsule, the equations must be slightly modified to account for this larger degree of fractionation, giving us:

$$\Delta^{44/40}Ca = \text{capsule length} * \text{temperature gradient} * 0.061 / 2$$

And:

$$\text{Effective } \Delta T = \text{capsule length} * \text{temperature gradient} / 2$$

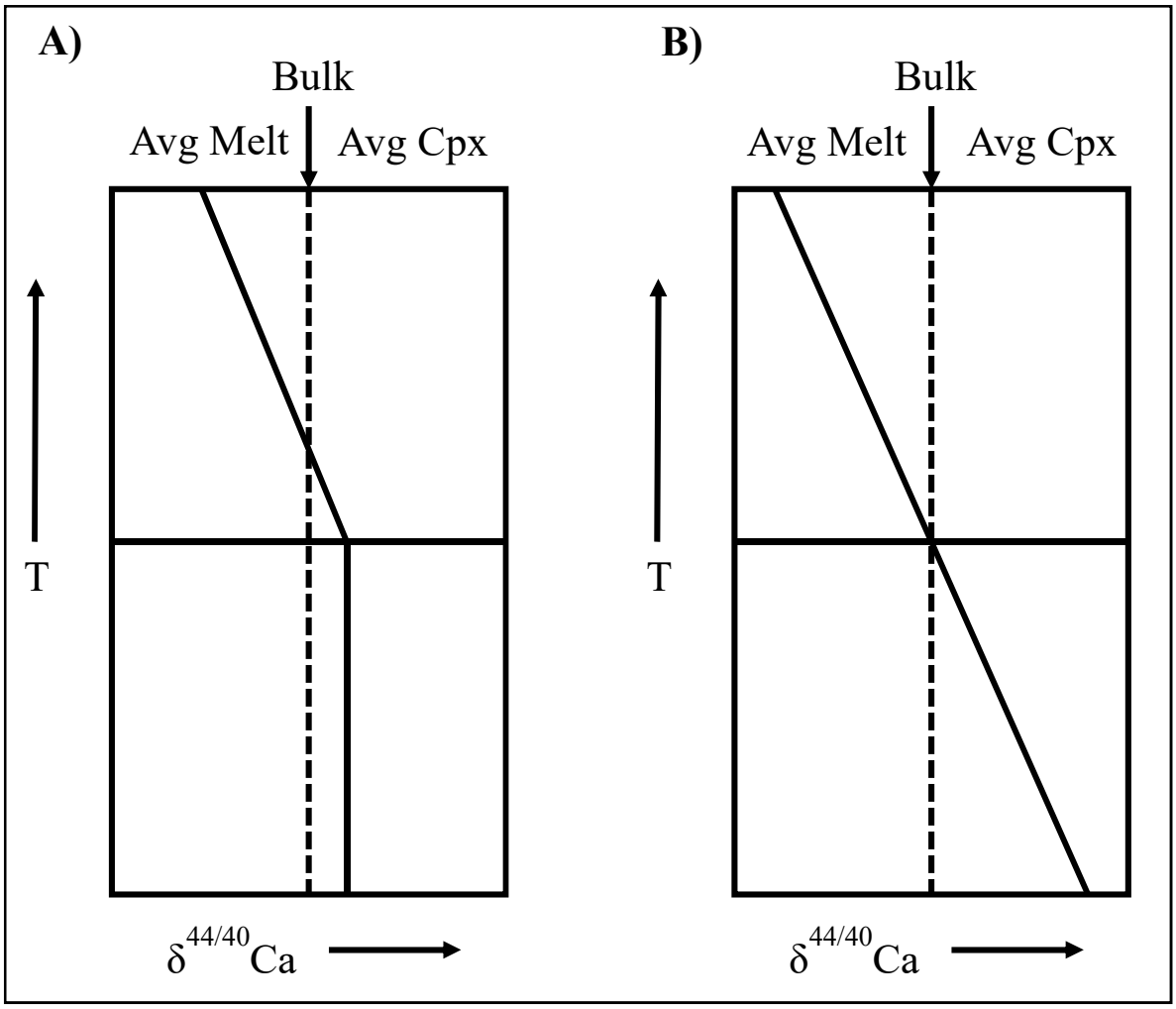

Figure 61 - Schematic of two possible scenarios describing the temperature driven fractionation in high pressure experiments.

Isotopic fractionation measured in all the high-pressure experiments may be thus caused by thermal fractionation in a temperature gradient. This effect has not been well recognised and may be a serious impediment to measuring equilibrium fractionation factors in high-temperature and

high-pressure experiments. There are only a few experimental studies that measure isotopic fractionation in systems that involve silicate melt (e.g., Shahar et al., 2008, 2009, 2011, 2015; Savage et al., 2015; Poitrasson et al., 2009; Hin et al., 2012, 2014), but these either do not consider the possible influence of thermal fractionation on their results, or maintain that thermal fractionation is an insignificant effect relative to the magnitude of measured fractionation.

This may help explain why there have been such mixed results in experimental studies of Fe isotope fractionation between metal and silicate melts. Whereas, Shahar et al. (2015) identified a significant fractionation between Fe-metal alloys and silicate melts, and computational predictions suggest there should be a measurable fractionation between metal and silicate (Polyakov and Mineev, 2000; Polyakov et al., 2007), Hin et al. (2012) found no fractionation between metal and silicate, and Poitrasson et al. (2009) also found no statistically significant fractionation.

Additionally, unlike this work, most studies of fractionation in systems involving silicate melts do not systematically investigate the effects or trends associated with temperature. For example, the data from Savage et al. (2015) suggest that there may be an increase in metal-silicate Cu isotope fractionation with increasing temperature, but this possibility is not explored, and the data is presented in a way that makes it difficult to identify this relationship.

It is important to note that proof of isotopic equilibrium conditions does not preclude thermal fractionation effects because they are also equilibrium effects. Many experimental studies will utilize methods of proving isotopic equilibrium such as the three-isotope exchange method used in Shahar et al. (2015). This method incorporated an ^{54}Fe isotopic spike to their Fe samples and allows for the terrestrial fractionation line (TFL) to be replaced by a secondary fractionation line (SFL) which has the same slope but a different intercept. At isotopic equilibrium, any phase that contains the isotope of interest will plot on the SFL, thus providing evidence of equilibrium fractionation effects. However, even methods such as this are unable to discriminate between phase driven and thermal driven fractionations, which illustrates the difficulty of separating the two effects in experimental work.

Adding to the difficulty of separating and identifying phase driven versus thermal driven fractionations in experimental work is the fact that experiments of this nature typically use larger than ideal capsules (as in this work). This is done to maximize the amount of material available

from each experimental phase for isotopic analyses. Especially if the isotope of interest is not a major element within one or more phases, the larger capsule sizes can be particularly necessary. Unfortunately, the larger the capsule, the more likely that a temperature offset can be generated between the top and bottom parts of the capsule. In addition, the details of capsule size and the spatial distribution of phases within the capsule are often not described by the authors of these type of studies, making it even more difficult to interpret the results and determine whether there is a possibility for thermal effects not previously identified in the work.

Shahar et al. (2015) measured the Fe isotope fractionation between Fe-metal and Fe-bearing silicate melt and found $\Delta^{57}Fe_{metal\text{-}silicate}$ values ranging from +0.12‰ to +0.43‰. This study warrants comparison because the capsules may have had mostly melt in the upper parts and mostly Fe-metal in the lower parts. If this was the case, their results may be showing thermal effects like our experiments. Despite not knowing the exact layout of the run products, nor the lengths of their capsules, the magnitude of their measured fractionations certainly aligns within the expected range of thermal diffusion driven fractionation. Using the estimated change in $\delta^{57/54}$Fe per °C given in Huang et al. (2010), the +0.12‰ to +0.43‰ range corresponds to a temperature offset of 3.3-11.9 °C, comparable to the calculated offsets in our experiments. It is important, therefore, in the light of this analysis, that future studies should consider in the experimental design how to minimise temperature gradients within the sample and provide sufficient documentation to assess the magnitude of potential thermal fractionation.

Chapter 6

6 Conclusion

This thesis has examined the Ca isotopic compositions of natural, mantle-derived samples, the fractionation between co-existing minerals in these rocks, and investigated the systematics of calcium isotopic fractionation in these systems through high-pressure and high-temperature experimentation. Previous research has explored calcium isotopes in mantle rocks, but has focused primarily on peridotites. Similarly, studies of inter-mineral calcium isotopic fractionation have only looked at Opx-Cpx mineral pairs. High pressure and temperature experimental work using calcium isotopes is very limited. Therefore, much of what was studied in this thesis was new and original research with little to which it can be compared. As such, the conclusions of this thesis serve as preliminary foundations for future works to expand and build upon. A summary of the main findings of this thesis follows:

- Ca isotopic composition of many bulk carbonatite samples matched that of the BSE value determined by Huang et al. (2010) based on Opx and Cpx in mantle peridotites. This may support the partial melting of carbonated peridotite as a carbonatite formation model.
- Ca isotopic composition of bulk carbonatites that varied from the BSE were correlated with concentrations of melt-favouring elements such as Lu and Yb. Based on this, decreased $\delta^{44/40}$Ca values may be an indicator of melt extraction processes, while increased $\delta^{44/40}$Ca may be a marker of increased partial melting in the carbonatite source material. These findings support the potential use of calcium isotopes as geochemical tracers of mantle processes related to melting and magmatism.
- The calcium isotopic composition of the Cape Verde and Tamazert carbonatite samples confirmed the findings of previous studies which pointed to the addition of ancient marine carbonates into the carbonatite source.
- Calcium isotopic fractionation between coexisting carbonate and pyroxene minerals in this study existed over a wide range but was correlated with the Ca/Mg ratio in the pyroxenes. This suggests the Ca-O bond length in the pyroxenes plays a critical role in determining the direction and magnitude of fractionation between the two mineral phases.

However, the sample set was limited, and additional coexisting carbonate-pyroxene mineral pairs should be examined to better constrain this relationship.

- Olivines analyzed for their calcium isotopic composition measured heavier than coexisting Cpx but were heavier and lighter than coexisting Opx depending on the sample.
- Experiments yielded consistently heavier calcium isotopic compositions in the pyroxenes than in the quenched melts in all experiments. The direction of fractionation between phases appeared to be contrary to that predicted based on the available information on the estimated Ca-O bond lengths in the pyroxenes and melts. The magnitude of the fractionation between the two phases was positively correlated with temperature when it typically should be negatively correlated based on the $1/T^2$ relationship. Whether the fractionation that was measured is the result of equilibrium isotopic fractionation between pyroxene and quenched melt or whether other factors are influencing the results is undetermined. Iron isotopic fractionation between pyroxenes and quenched melt in the Cpx + Carbonated Silicate Melt experiments suggested that thermal diffusion may have influenced the direction and magnitude of fractionation in the experiments. However, not enough evidence exists to definitively conclude in favour of diffusion driven fractionation or equilibrium fractionation between the two phases. Additional experimentation is required.
- Other experimental studies of fractionation in systems involving silicate melts often do not measure other isotopes besides the one of interest. Comparing Ca and Fe isotopes in the same experiments as was done in this study provides an important measure that shows whether the results may be consistent with fractionation in a temperature gradient.

6.1 Future Natural Sample Work

Future work with natural samples should continue to assess mantle-derived samples for their calcium isotopic compositions to further characterize the calcium isotopic composition of the mantle. Additional well-characterized carbonatite samples should be carefully selected for analysis to continue the research conducted in this study and build a larger data set from which to make interpretations. Samples that include co-existing Ca-bearing mineral phases should be

sought out for analysis to add to the developing understanding of the systematics of inter-mineral calcium isotopic fractionation in high-temperature systems. Coupled with continued experimental work, these samples should prove to be of great value.

6.2 Future Experiments

Future experimental work to investigate the fractionation between pyroxenes and melts of varying compositions will need to be designed very carefully to minimize and account for the effects of thermal diffusion. Minimizing the size of the experimental capsule should help minimize the delta T within the sample and therefore minimize the effects of thermal diffusion. Based on the estimated temperature profile within the piston cylinder experimental capsule of Richter et al. (2009) illustrated in Figure 60, minimizing the capsule size to <2mm may be sufficient to limit the temperature gradient to a few degrees (°C) or less. However, even a 2°C ΔT could result in $\delta^{44/40}$Ca fractionations up to 0.13‰ between hot and cold ends of the capsule. Therefore, precise estimates of the temperature gradients that exist within any given piston cylinder apparatus should be made before running these types of experiments to be able to accurately correct for thermal diffusion effects. Alternatively, a rocking piston cylinder or multi-anvil apparatus could be used to run these types of experiments to maintain convection within the capsule and keep the experiment mixed, thus avoiding the need for a stable temperature profile.

In addition to this, the thermal diffusion experiments conducted by Richter et al. (2009) and Huang et al. (2010), measured the effect using only silicate melts. Many of the assumptions made here are based on the effect of thermal diffusion in silicate melts being similar to its effect in carbonate melts or carbonated silicate melts. However, experiments that measured the effect of thermal diffusion in melts of varying compositions would be useful in determining the validity of these assumptions.

As well as accounting for thermal diffusion in all future experiments involving isotopic analyses of major elements, revisiting previous experiments of this kind should also be of importance. Since temperature gradients exist to varying degrees in all piston cylinder apparatus, the results and interpretations of previous isotopic analyses of experimental materials must take this into

account. For example, the experiments by Sossi and O'Neill (2017) used the fractionation between minerals and a buffering fluid within their experimental capsules to determine the Fe fractionation factors between common Fe-bearing mantle minerals. They indicate they believed the maximum temperature gradient within their capsules to be 12°C, which could result in Fe isotopic fractionations up to $\delta^{57/54}Fe = +0.40‰$. Sossi and O'Neill (2017) reported $\Delta^{57/54}Fe_{mineral\text{-}fluid}$ values that ranged from −0.14‰ to +0.45‰ yet made no mention of any potential effects that thermal diffusion could have had on these results. However, their buffering fluid was an iron-chloride solution and not a silicate melt, so the effect of thermal diffusion may be minimized by convection of this fluid, but these are all topics worthy of investigation.

Despite the concerns that thermal diffusion may present for experimental work, a study investigating inter-mineral equilibrium fractionation factors, much like the one Sossi and O'Neill (2017) conducted for Fe isotopes, could be carried out for Ca isotopes in numerous Ca-bearing mineral phases. Experiments of this type to determine inter-mineral Ca fractionation factors would be important for interpreting the growing number of natural sample data sets. They may also help with designing and interpreting experiments to measure the fractionation between minerals and melts such as this one.

References

Amini, M., Eisenhauer, A., Böhm, F., Holmden, C., Kreissig, K., Hauff, F., & Jochum, K.P., 2009. Calcium isotopes ($\delta^{44/40}$Ca) in MPI-DING reference glasses, USGS rock powders and various rocks: Evidence for ca isotope fractionation in terrestrial silicates. Geostand. Geoanal. Res. 33, 231-247.

Amsellem, E., Moynier, F., Pringle, E. A., Bouvier, A., Chen, H. and Day, J. M., 2017. Testing the chondrule-rich accretion model for planetary embryos using calcium isotopes. Earth Planet. Sci. Lett. 469, 75-83.

Amundsen, H.E.F., 1987. Evidence of liquid immiscibility in the upper mantle. Nature 327, 692-695.

Andersen, T., 2008. Qassiarssuk Complex, Gardar Rift, southwest Greenland. Can. Mineral. 46, 933-950.

Anderson, D.L., 1989. Composition of the Earth. Science 243, 367-370.

Begg, G.C., Griffin, W.L., Natapov, L.M., O'Reilly, S.Y., Grand, S.P., O'Neill, C.J., Hronsky, J.M.A., Poudjom Djomani, Y., Swain, C.J., Deen, T., Bowden, P., 2009. The lithospheric architecture of Africa: seismic tomography, mantle petrology and tectonic evolution. Geosphere 5, 23-50.

Bell, K., Blenkinsop, J., 1980. Ages and initial ^{87}Sr-^{86}Sr ratios from alkalic complexes of Ontario. In: Pye, E.G., Geoscience Research Grant Program, summary of research, 1979-1980. Ontario Geological Survey, Miscellaneous Paper 93, pp. 16-23.

Bellon, H., Pouclet, A., 1980. Datations K/Ar de quelques laves du Rift-Ouest de l'Afrique Centrale; implication sur l'evolution magmatique et structurale. Geol. Rundsch. 69, 49-62.

Berner, R. A., 2004. The Phanerozoic Carbon Cycle, Oxford Univ. Press, Oxford, U. K.

Bouabdellah, M., Hoernle, K., Kchit, A., Duggen, S., Hauff, F., Klugel, A., Lowry, D., Beaudoin, G., 2010. Petrogenesis of the Eocene Tamazert continental carbonatites (Central High Atlas, Morocco): Implications for a common source for the Tamazert and Canary and Cape Verde Island carbonatites. J. Petrol. 51, 1655-1686.

Brooker, R.A., Hamilton, D.L., 1990. Three-liquid immiscibility and the origin of carbonatites. Nature 346, 459-462.

Brooker, R.A., Kjarsgaard, B.A., 2011. Silicate-carbonate liquid immiscibility and phase relations in the system SiO_2-Na_2O-Al_2O_3-CaO-CO_2 at 0.1-2.5 GPa with applications to carbonatite genesis. J. Petrol. 52, 1281-1305.

Brown, E.H., Blackwell, D.L., Christenson, B.W., Rasse, F.I., Haugerud, R.A., Jones, J.T., Leiggi, P.A., Morrison, M.L., Rady, P.M., Reller, G.J., Sevigny, J.H., Silverberg, D.S., Smith, M.T., Sondergaard, J.N., Zieler, C.B., 1987. Geologic Map of the Northwest Cascades. Geol. Soc. Am. Map Chart Ser., MC-61.

Canil, D., 1990. Experimental study bearing on the absence of carbonate in mantle-derived xenoliths. Geology 18, 1011-1013.

Chapman, J.B., Mason, T.F.D., Weiss, D.J., Coles, B.J., Wilkinson, J.J., 2006. Chemical separation and isotopic variations of Cu and Zn from five geological reference materials. Geostand. Geoanal. Res. 30, 5-16.

Chen, W., Simonetti, A., 2014. Evidence for the multi-stage petrogenetic history of the Oka Carbonatite Complex (Quebec, Canada) as recorded by perovskite and apatite. Minerals 4, 437-476.

Chen, W., Kamenetsky, V.S., Simonetti, A., 2013. Evidence for the alkaline nature of parental carbonatite melts at Oka complex in Canada. Nat. Commun. 4, 2687.

Church, A.A., Jones, A.P., 1995. Silicate-Carbonate Immiscibility at Oldoinyo-Lengai. J. Petrol. 36, 869-889.

Clement, C.R., Skinner, E.M., Hawthorne, J.B., Kleinjan, L., Allsopp, H.L., 1979. Precambrian ultramafic dykes with kimberlite affinities in the Kimberley area. In: Boyd, F.R., Meyer, H.O.A. (Eds.), Kimberlites, Diatremes and Diamonds: their Geology, Petrology and Geochemistry. Proceedings of the Second International Kimberlite Conference, Vol. 1. Washington, DC: American Geophysical Union, pp. 101-110.

Colla, C.A., Wimpenny, J., Yin, Q-Z., Rustad, J.R., Casey, W.H., 2013. Calcium-isotope fractionation between solution and solids with six, seven or eight oxygens bound to Ca(II). Geochim. Cosmochim. Acta 121, 363-373.

Dalton, J.A., Presnall, D.C., 1998. Carbonatitic melts along the solidus of model lherzolite in the system CaO-MgO-Al2O3-SiO2-CO2 from 3 to 7 GPa. Contrib. Mineral. Petrol. 131, 123-135.

Dasgupta, R., Hirschmann, M.M., Withers, A.C., 2004a. Deep global cycling of carbon constrained by the solidus of anhydrous, carbonated eclogite under upper mantle conditions. Earth Planet. Sci. Lett. 227, 73-85.

Dasgupta, R., Hirschmann, M.M., Dellas, N., 2004b. The effect of bulk composition on the solidus of carbonated eclogite from partial melting experiments at 3 GPa. Contrib. Mineral. Petrol. 149, 288-305.

Dasgupta, R., Mallik, A., Tsuno, K., Withers, A.C., Hirth, G., Hirschmann, M.M., 2013. Carbon-dioxide-rich silicate melt in the Earth's upper mantle. Nature 493, 211-215.

Dawson, J.B., 1998. Peralkaline nephelinite-natrocarbonatite relationships at Oldoinyo Lengai, Tanzania. J. Petrol. 39, 2077-2094.

de Wit, M.J., Roering, C., Hart, R.J., Armstrong, R.A., de Rone, C.E.J., Green, R.W.E., Tredoux, M., Peberdy, E., Hart, R.A., 1992. Formation of an Archean continent. Nature 357, 553-562.

Deines, P., 1989. Stable isotope variations in carbonatites. In: Bell, K. (Ed.), Carbonatites: Genesis and Evolution. Unwin Hyman, London, pp. 301-359.

Deines, P., 2002. The carbon isotope geochemistry of mantle xenoliths. Earth Sci. Rev. 58, 247-278.

DePaolo, D.J., 2004. Calcium isotopic variations produced by biological, kinetic, radiogenic and nucleosynthetic processes. Rev. Mineral Geochem. 55, 255-288.

Denaeyer, M.E., 1970. Rapports isotopiques δ O et δ C conditions d'affleurement des carbonatites de l'Afrique centrale. Compt. Rend. Acad. Sc. Paris 270, 2155-2158.

Dennis, K.J., Schrag, D.P., 2010. Clumped isotope thermometry of carbonatites as an indicator of diagenetic alteration. Geochim. Cosmochim. Acta 74, 4110-4122.

Dobson, D.P., Jones, A.P., Rabe, R., Sekine, T., Kurita, K., Taniguchi, T., Kondo, T., Kato, T., Shimomura, O., Urakawa, S., 1996. In-situ measurement of viscosity and density of carbonate melts at high pressure. Earth Planet. Sci. Lett. 143, 207-215.

Donnelly, C.L., Griffin, W.L., O'Reilly, S.Y., Pearson, N.J., Shee, S.R., 2011. The Kimberlites and related rocks of the Kuruman Kimberlite Province, Kaapvaal Craton, South Africa. Contrib. Mineral. Petrol. 161, 351-371.

Doucelance, R., Hammouda, T., Moreira, M., Martins, J.C., 2010. Geochemical constraints on depth of origin of oceanic carbonatites: The Cape Verde case. Geochim. Cosmochim. Acta 74, 7261-7282.

Doucelance, R., Bellot, N., Boyet, M., Hammouda, T., Bosq, C., 2014. What coupled cerium and neodymium isotopes tell us about the deep source of oceanic carbonatites. Earth Planet. Sci. Lett. 407, 175-186.

Eggler, D.H., 1973. Effect of CO2 on the melting of peridotite. Carnegie Institution of Washington Yearbook 73pp. 215-224.

Eggler, D.H., 1974. Peridotite –carbonate relations in the system CaO –MgO –SiO2 –CO2. Carnegie Institution of Washington Yearbook 74pp. 468-474.

Eggler, D.H., 1975. Composition of the partial melt of carbonated peridotite in the system CaO-MgO-SiO2-CO2. Carnegie Institution of Washington Yearbook 75pp. 623-626.

Eggler, D.H., 1976. Does CO2 cause partial melting in the low-velocity layer of the mantle? Geology 4, 69-72.

Eggler, D.H., 1978. The effect of CO2 upon partial melting of peridotite in the system Na2O-CaO-Al2O3-MgO-SiO2-CO2 to 35 kb, with an analysis of melting in a peridotite-H2O-CO2 system. Am. J. Sci. 278, 305-434.

Eggler, D.H., 1987a. Discussion of recent papers on carbonated peridotite, bearing on metasomatism and magmatism: an alternative. Earth Planet. Sci. Lett. 82, 398-400.

Eggler, D.H., 1987b. Discussion of recent papers on carbonated peridotite, bearing on metasomatism and magmatism: final comment. Earth Planet. Sci. Lett. 82, 403.

Eggler, D.H., Baker, D.R., 1982. Reduced volatiles in the system C-O-H: implications to mantle melting, fluid formation and diamond genesis. In: Akimoto, S., Manghnani, M.H. (Eds.), High-pressure Research in Geophysics. Center for Academic Publications Japan, Tokyo, pp. 237-250.

Fantle, M.S., DePaolo, D.J., 2005. Variations in the marine Ca cycle over the past 20 million years. Earth Planet. Sci. Lett. 237. 102-117.

Fantle, M.S., Tipper, E.T., 2014. Calcium isotopes in the global biogeochemical Ca cycle: Implications for development of a Ca isotope proxy. Earth-Sci. Rev. 129, 148-177.

Feng, C., Qin, T., Huang, S., Wu, Z., Huang, F., 2014. First-principles investigations of equilibrium calcium isotope fractionation between clinopyroxene and Ca-doped orthopyroxene. Geochim. Cosmochim. Acta 143, 132-142.

Feng, L., Zhou, L., Yang, L., DePaolo, D.J., Tong, S.-Y., Liu, Y.-S., Owens, T.L., Gao, S., 2017. Calcium isotopic compositions of sixteen USGS reference materials. Geostand. Geoanal. Res. 41, 93-106.

Field, M., Stiefenhofer, J., Robey, J., Kurszlaukis, S., 2008. Kimberlite-hosted diamond deposits of southern Africa: A review. Ore Geol. Rev. 34, 33-75.

Freestone, I.C., Hamilton, D.L., 1980. The role of liquid immiscibility in the genesis of carbonatites — An experimental study. Contrib. Mineral. Petrol. 73, 105-117.

Frey, F.A., Prinz, M., 1978. Ultramafic inclusions from San Carlos, Arizona: Petrologic and geochemical data bearing on their petrogenesis. Earth Planet. Sci. Lett. 38, 129-176.

Frost, D.J., McCammon, C.A., 2008. The redox state of Earth's mantle. Annu. Rev. Earth Planet. Sci. 36, 389-420.

Gaillard, F., Malki, M., Iacono-Marziano, G., Pichavant, M., Scaillet, B., 2008. Carbonatite melts and electrical conductivity in the asthenosphere. Science 322, 1363-1365.

Genge, M.J., Price, G.D., Jones, A.P., 1995. Molecular dynamics simulations of $CaCO_3$ melts to mantle pressures and temperatures: implications for carbonatite magmas. Earth Planet. Sci. Lett. 131, 225-238.

Gittins, J., 1989. The origin and evolution of carbonatite magmas. In: Bell, K. (Ed.), Carbonatites: Genesis and Evolution. Unwin Hyman, London, pp. 580-600.

Gittins, J., Jago, B.C., 1998. Differentiation of natrocarbonatite magma at Oldoinyo Lengai volcano, Tanzania. Mineral. Mag. 62, 759-768.

Gold, D.P., 1972. The Monteregian Hills: ultra-alkaline rocks and the Oka carbonatite complex. 24th International Geology Congress Guidebook B-11.

Gold, D.P., Eby, G.N., Bell, K., Vallée, M., 1986. Carbonatites, diatremes and ultra-alkaline rocks in the Oka area, Québec. Geological Association of Canada Guidebook 21.

Gold, D.P., Vallée, M., and Charette, J-P., 1967. Economic geology and geophysics of the Oka alkaline complex, Québec. Can. Min. Metall. Bull. 60, 1131-1144.

Griffith, E.M., Schauble, E.A., Bullen, T.D., Paytan, A., 2008. Characterization of calcium isotopes in natural and synthetic barite. Geochim. Cosmochim. Acta. 72, 5641-5658.

Gudfinnsson, G.H., Presnall, D.C., 2005. Continuous gradations among primary carbonatitic, kimberlitic, melilititic, basaltic, picritic, and komatiitic melts in equilibrium with garnet lherzolite at 3-8 GPa. J. Petrol. 46, 1645-1659.

Gussone, N., Böhm, F., Eisenhauer, A., Dietzel, M., Heuser, A., Teichert, B.M.A., Reitner, J., Wörheide, G., Dullo, W.-C., 2005. Calcium isotope fractionation in calcite and aragonite. Geochim. Cosmochim. Acta. 69, 4485-4494.

Gussone, N., Eisenhauer, A., Heuser, A., Dietzel, M., Bock, B., Böhm, F., Spero, H.J., Lea, D.W., Bijma, J., Nägler T.F., 2003. Model for kinetic effects on calcium isotope fractionation (δ^{44}Ca) in inorganic aragonite and cultured planktonic foraminifera. Geochim. Cosmochim. Acta, 67, 2375-1382.

Halama, R., Vennemann, T., Siebel, W., Markl, G., 2005. The Gronnedal-Ika carbonatite-syenite complex, South Greenland: carbonatite formation by liquid immiscibility. J. Petrol. 46, 191-217.

Hammouda, T., 2003. High pressure melting of carbonated eclogites experimental constraints on carbon recycling and storage in the mantle. Earth Planet. Sci. Lett. 214, 357-368.

Hammouda, T., Keshav, S., 2015. Melting in the mantle in the presence of carbon: Review of experiments and discussion on the origin of carbonatites. Chem. Geol. 418, 171-188.

Harmer, R.E., Gittins, J., 1998. The Case for Primary, Mantle-derived Carbonatite Magma. J. Petrol. 39, 1895-1903.

Harmer, R.E., Lee, C.A., Eglington, B.M., 1998. A deep mantle source for carbonatite magmatism; evidence from the nephelinites and carbonatites of the Buhera district, SE Zimbabwe. Earth Planet. Sci. Lett. 158, 131-142.

Hazen, R. M., Hemley, R. J., Mangum, A. J., 2012. Carbon in Earth's interior: Storage, cycling, and life, Eos Trans. AGU, 93(2), 17.

Hesse, K.-F., 1984. Refinement of the crystal structure of wollastonite-2M (parawollastonite). Z. Kristallogr. 168, 93-98.

Heuser, A., Eisenhauer, A., 2008. The calcium isotope composition ($\delta^{44/40}$Ca) of NIST SRM 915b and NIST SRM 1486. Geostand. Geoanal. Res. 32, 311-315.

Hin, R.C., Schmidt, M.W., Bourdon, B., 2012. Experimental evidence for the absence of iron isotope fractionation between metal and silicate liquids at 1 GPa and 1250 to 1300 °C and its cosmochemical consequences. Geochim. Cosmochim. Acta 93, 164-181.

Hin, R.C., Fitoussi, C., Schmidt, M.W., Bourdon, B., 2014. Experimental determination of the Si isotope fractionation factor between liquid metal and liquid silicate. Earth Planet. Sci. Lett. 387, 55-66.

Hindshaw R. S., Reynolds B. C., Wiederhold J. G., Kretzschmar R. and Bourdon B., 2011. Calcium isotopes in a proglacial weathering environment: Damma glacier, Switzerland. Geochim. Cosmochim. Acta 75, 106-118.

Hornig-Kjarsgaard, I., 1998. Rare earth elements in sovitic carbonatites and their mineral phases. J. Petrol. 39, 2105-2121.

Huang, F., Chakraborty, P., Lundstrom, C.C., Holmden, C., Glessner, J.J.G., Kieffer, S.W., Lesher, C.E., 2010. Isotope fractionation in silicate melts by thermal diffusion. Nature 464, 396-400.

Huang, F., Lundstrom, C.C., Glessner, J., Ianno, A., Boudreau, A., Li, J., Ferre, E.C., Marshak, S., DeFrates, J., 2009. Chemical and isotopic fractionation of wet andesite in a temperature gradient: Experiments and models suggesting a new mechanism of magma differentiation. Geochim. Cosmochim. Acta 73, 729-749.

Huang, S., Farkas, J., Jacobsen, S.B., 2010. Calcium isotopic fractionation between clinopyroxene and orthopyroxene from mantle peridotites. Earth Planet. Sc. Lett. 292, 337-344.

Huang, S., Farkaš, J., Jacobsen, S.B., 2011. Stable calcium isotopic compositions of hawaiian shield lavas: Evidence for recycling of ancient marine carbonates into the mantle. Geochim. Cosmochim. Acta 75, 4987-4997.

Huang, S., Farkas, J., Yu, G., Petaev, M.I., Jacobsen, S.B., 2012. Calcium isotopic ratios and rare earth element abundances in refractory inclusions from Allende CV3 chondrite. Geochim. Cosmochim. Acta 77, 252-265.

Huang, S., Jacobson, S.B., 2017. Calcium isotopic compositions of chondrites. Geochim. Cosmochim. Acta 201, 364-376.

Irving, A., 1980. Petrology and geochemistry of composite ultramafic xenoliths in alkali basalts and implications for magmatic processes within the mantle. Am. J. Sci. 280, 389-426.

Jacobson, A.D., Andrews, M.G., Lehn, G.O., Holmden, C., 2015. Silicate versus carbonate weathering in Iceland: New insights from Ca isotopes. Earth Planet. Sci. Lett. 416, 132-142.

Javoy, M., 1997. The major volatile elements of the Earth: Their origin, behavior, and fate. Geophys. Res. Lett. 24, 177-180.

Javoy, M., Pineau, F., Iiyama, I., 1978. Experimental determination of the isotopic fractionation between gaseous CO2 and carbon dissolved in tholeiitic magma. Contrib. Mineral. Petrol. 67, 35-39.

Jones, A.P., 1989. Upper mantle enrichment by kimberlite or carbonatitic magmatism. In: Bell, K. (Ed.), Carbonatites: Genesis and Evolution. Unwin Hyman, London, pp. 448-463.

Jones, A.P., Genge, M., Carmody, L., 2013. Carbonate melts and carbonatites. Rev. Mineral. Geochem. 75, 289-322.

Kaminsky, F., Wirth, R., Schreiber, A., Thomas, R., 2009. Nyerereite and nahcolite inclusions in diamond: evidence for lower-mantle carbonatitic magmas. Mineral. Mag. 73, 797-816.

Kang, J-T., Ionov, D.A., Liu, F., Zhang, C-L., Golovin, A.V., Qin, L-P., Zhang, Z-F., Huang, F., 2017. Calcium isotopic fractionation in mantle peridotites by melting and metasomatism and Ca isotope composition of the Bulk Silicate Earth. Earth Planet. Sci. Lett. 474, 128-137

Kang, J-T., Zhu, H-L., Liu, Y-F., Liu, F., Wu, F., Hao, Y-T., Zhi, X-C., Zhang, Z-F., Huang, F., 2016. Calcium isotopic composition of mantle xenoliths and minerals from Eastern China. Geochim. Cosmochim. Acta, 174, 335-344.

Keshav, S., Gudfinnsson, G.H., 2013. Silicate liquid-carbonatite liquid transition along the melting curve of model, vapor-saturated peridotite in the system CaO-MgO-Al2O3-SiO2-CO2 from 1.1 to 2 GPa. J. Geophys. Res. 118, 3341-3353.

Kjarsgaard, B., Hamilton, D.L., 1988. Liquid immiscibility and the origin of alkali-poor carbonatites. Mineral. Mag. 52, 43-55.

Kjarsgaard, B., Hamilton, D.L., 1989. The genesis of carbonatites by immiscibility. In: Bell, K. (Ed.), Carbonatites: Genesis and Evolution. Unwin Hyman, London, pp. 388-404.

Kjarsgaard, B., Peterson, T., 1991. Nephelinite-carbonatite liquid immiscibility at Shombole volcano, East Africa: Petrographic and experimental evidence. Mineral. Petrol. 43, 293-314.

Kramm, U., Maravic, H.V., Morteani, G., 1997. Neodymium and Sr isotopic constraints on the petrogenetic relationships between carbonatites and cancrinite syenites from the Lueshe Alkaline Complex, east Zaire. J. Afr. Earth Sci. 25, 55-76.

Kruckenberg, S.C., Tikoff, B., Toy, V.G., Newman, J., Young, L.I., 2013. Strain localization associated with channelized melt migration in upper mantle lithosphere: Insights from the Twin Sisters ultramafic complex, Washington, USA. J. Struct. Geol. 50, 133-147.

Lancelot, J.R., Allegre, C.J., 1974. Origin of carbonatitic magma in the light of the Pb-U-Th isotope system. Earth Planet. Sci. Lett. 22, 233-238.

Lee, W.J., Wyllie, P.J., 1997. Liquid immiscibility between nephelinite and carbonatite from 1.0 to 2.5 GPa compared with mantle melt compositions. Contrib. Mineral. Petrol. 127, 1-16.

Lehn, G.O., Jacobson, A.D., 2015. Optimization of a ^{48}Ca-^{43}Ca double-spike MC-TIMS method for measuring Ca isotope ratios ($\delta^{44/40}$Ca and $\delta^{44/42}$Ca): limitations from filament reservoir mixing. J. Anal. At. Spectrom. 30, 1571-1581.

Lehn, G.O., Jacobson, A.D., Holmden, C., 2013. Precise analysis of Ca isotope ratios ($\delta^{44/40}$Ca) using an optimized ^{43}Ca-^{42}Ca double-spike MC-TIMS method. Int. J. Mass Spectrom. 351, 69-75.

Le Maitre, R.W., 2002. Igneous Rocks: A Classifiation and Glossary of Terms. Cambridge University Press, Cambridge, UK.

Le Roex, A.P., Bell, D.R., Davis, P., 2003. Petrogenesis of group I kimberlites from Kimberley, South Africa: Evidence from bulk-rock geochemistry. J. Petrol. 44, 2261-2286.

Lowdon, J.A., Stockwell, C.H., Tipper, H.W., Wanless, R.K., 1963. Age determinations and geological studies. Geological Survey of Canada, Paper 62-17, pp. 83-84.

Ludwig, C., 1856. Diffusion zwischen ungleich erwarmten Orten gleich zusammengesetzter Losungen. Sitz. Math. Naturwiss. Classe Kaiserlichen Akad. Wiss. 20, 539.

Luth, R.W., 1999. Carbon and carbonates in the mantle. In: Fei, Y., Bertka, C.M., Mysen, B.O. (Eds.), Mantle Petrology: Field Observations and High Pressure Experimentation. A Tribute to Francis (Joe) Boyd. Geochem. Soc. Spec. Publ. 6, pp. 297-316.

Macris, C.A., Young, E.D., Manning, C.E., 2013. Experimental determination of equilibrium magnesium isotope fractionation between spinel, forsterite, and magnesite from 600 to 800° C. Geochim. Cosmochim. Acta 118, 18-32.

Madeira, J., Mata, J., Mourao, C., Brum da Silveira, A., Martins, S., Ramalho, R., Hoffmann, D.L., 2010. Volcano-stratigraphic and structural evolution of Brava Island (Cape Verde) based on ^{40}Ar/^{39}Ar, U-Th and field constraints. J. Volcanol. Geotherm. Res. 196, 219-235.

Magna, T., Gussone, N., Mezger, K., 2015. The calcium isotope systematics of Mars. Earth Planet. Sci. Lett. 430, 86-94.

Marty B., Alexander, CMO'D, Raymond, S.N., 2013. Primordial origins of Earth's carbon. Rev. Mineral. Geochem. 75, 149-181.

Masaki, Y., Yuka, H., Naoko, N., Hirogo, K., 2005. Rb-Sr, Sm-Nd ages of the Phalaborwa Carbonatite Complex, South Africa. Polar Geosci. 18, 101-113.

Mata, J., Moreira, M., Doucelance, R., Ader, M., Silva, L.C., 2010. Noble gas and carbon isotopic signatures of Cape Verde oceanic carbonatites. Implications for carbon provenance. Earth Planet. Sci. Lett. 291, 70-83.

Mattey, D.P., 1991. Carbon dioxide solubility and carbon isotope fractionation in basaltic melt. Geochim. Cosmochim. Acta 55, 3467-3473.

Mattey, D.P., Taylor, W.R., Green, D.H., Pillinger, C.T., 1990. Carbon isotopic fractionation between CO2 vapour, silicate and carbonate melts: an experimental study to 30 kbar. Contrib. Mineral. Petrol. 104, 492-505.

McDonough, W.F., Sun, S.-s., 1995. The composition of the Earth. Chem. Geol. 120, 223-253.

Mitchell, R.H., 2005. Carbonatites and carbonatites and carbonatites. Can. Mineral. 43, 2049-2068.

Montelli, R., Nolet, G., Dahlen, F.A., Masters, G., 2006. A catalogue of deep mantle plumes: new results from finite-frequency tomography. Geochem. Geophys. Geosyst. 7.

Moynier, F., Fujii, T., 2017. Calcium isotope fractionation between aqueous compounds relevant to low-temperature geochemistry, biology and medicine. Sci. Rep. -UK, 7, 44255.

Mysen, B.O., 1983. The structure of silicate melts. Annu. Rev. Earth Planet. Sci. 11, 75-97.

Mysen, B.O., Fogel, M.L., Morrill, P.L., Cody, G.D., 2009. Solution behavior of reduced C-O-H volatiles in silicate melts at high pressure and temperature. Geochim. Cosmochim. Acta 73, 1696-1710.

Nasraoui, M., Bilal, E., 2000. Pyrochlores from the Lueshe carbonatite complex (Democratic Republic of Congo): a geochemical record of different alteration stages. J. Asian Earth Sci. 18, 237-251.

Nelson, D.R., Chivas, A.R., Chappell, B.W., McCulloch, M.T., 1988. Geochemical and isotopic systematics in carbonatites and implications for the evolution of ocean-island sources. Geochim. Cosmochim. Acta 52, 1-17.

Novella, D., Keshav, S., Gudfinnsson, G.H., Ghosh, S., 2014. Melting phase relations of model carbonated peridotite in the system CaO-MgO-Al2O3-SiO2-CO2 from 2 to 3 GPa and further indication of possible unmixing between carbonatite and silicate liquids. J. Geophys. Res. 119, 2780-2800.

Owen, L.B., Faure, G., 1977. Rb-Sr dating of the Lackner Lake Complex, northern Ontario. Precambrian Res. 5, 299-303.

Anthony, E.Y., Poths, J., 1992. 3He surface exposure dating and its implications for magma evolution in the Potrillo volcanic field, Rio Grande Rift, New Mexico, USA. Geochim. Cosmochim. Acta 56, 4105-4108.

Phalaborwa Mining Company Limited Mine Geological and Mineralogical staff, 1976. The geology and the economic deposit of copper, iron, and vermiculite in the Phalabor igneous complex. Econ. Geol. 71, 177-192.

Pineau, F., Javoy, M., 1969. Determination des rapports isotopiques $^{18}O/^{16}O$ et $^{13}C/^{12}C$ dans diverses carbonatites. Implications genetiques. Compt. Rend. 269, 1930-1933.

Poitrasson, F., Roskosz, M., Corgne, A., 2009. No iron isotope fractionation between molten alloys and silicate melt to 2000 C and 7.7 GPa: experimental evidence and implications for planetary differentiation and accretion. Earth Planet. Sci. Lett. 278, 376-385.

Polyakov, V.B., Mineev, S.D., 2000. The use of Mössbauer spectroscopy in stable isotope geochemistry. Geochim. Cosmochim. Acta 64, 849-865.

Polyakov, V.B., Clayton, R.N., Horita, J., Mineev, S.D., 2007. Equilibrium iron isotope fractionation factors of minerals: reevaluation from the data of nuclear inelastic resonant X-ray scattering and M ssbauer spectroscopy. Geochim. Cosmochim. Acta 71, 3833-3846.

Ragan, D.M., 1961. The geology of the Twin Sisters dunite in the Northern Cascades, Washington. Ph.D. thesis, Seattle, University of Washington, p. 87.

Richter, F.M., Watson, E.B., Mendybaev, R.A., Dauphas, N., Georg, B., Watkins, J., Valley, J., 2009. Isotopic fractionation of the major elements of molten basalt by chemical and thermal diffusion. Geochim. Cosmochim. Acta 73, 4250-4263.

Richter, F.M., Watson, E.B., Mendybaev, R.A., Teng, F-Z., Janney, P.E., 2008. Magnesium isotope fractionation in silicate melts by chemical and thermal diffusion. Geochim, Cosmochim. Acta 72, 206-220.

Rohrbach, A., Schmidt, M.W., 2011. Redox freezing and melting in the Earth's deep mantle resulting from carbon-iron redox coupling. Nature 472, 209-212.

Russell, W.A., Papanastassiou, D.A., 1978. Calcium isotope fractionation in ion-exchange chromatography. Anal. Chem. 50, 1151-1154.

Russell, W.A., Papanastassiou, D.A., Tombrello, T.A., 1978. Ca isotope fractionation on the Earth and other solar system materials. Geochim. Cosmochim. Acta 42, 1075-1090.

Savage, P.S., Moynier, F., Chen, H., Shofner, G., Siebert, J., Badro, J., Puchtel, I.S., 2015. Copper isotope evidence for large-scale sulphide fractionation during Earth's differentiation. Geochem. Persp. Let. 1, 53-64.

Schauble, E., 2004. Applying stable isotope fractionation theory to new systems. In: Johnson, C.M., Beard, B., Albarede, F. (Eds.), Reviews in Mineralogy & Geochemistry, v. 56, Geochemistry of Non-traditional Stable Isotopes. Mineralogical Society of America.

Schauble, E.A., 2011. First-principles estimates of equilibrium magnesium isotope fractionation in silicate, oxide, carbonate and hexaaquamagnesium (2+) crystals. Geochim. Cosmochim. Acta 75, 844-869.

Schiller, M., Paton, C., Bizzarro, M., 2012. Calcium isotope measurement by combined HR-MC-ICPMS and TIMS. J. Anal. At. Spectrom. 27, 38-49.

Schmitt, A.-D., Stille, P. 2005. The source of calcium in wet atmospheric deposits: Ca-Sr isotope evidence. Geochim. Cosmochim. Acta 69, 3463-3468.

Shahar, A., Young, E.D., Manning, C.E., 2008. Equilibrium high-temperature Fe isotope fractionation between fayalite and magnetite: an experimental calibration. Earth Planet. Sci. Lett. 268, 330-338.

Shahar, A., Ziegler, K., Young, E.D., Ricolleau, A., Schauble, E.A., Fei, Y.W., 2009. Experimentally determined Si isotope fractionation between silicate and Fe metal and implications for Earth's core formation. Earth Planet. Sci. Lett. 288, 228-234.

Shahar, A., Hillgren, V.J., Young, E.D., Fei, Y., Macris, C.A., Dent, L., 2011. High-temperature Si isotope fractionation between iron metal and silicate. Geochim. Cosmochim. Acta 75, 7688-7697.

Simon, J.I., DePaolo, D.J., 2010. Stable calcium isotopic compositions of meteorites and rocky planets. Earth Planet. Sci. Lett. 289, 457-466.

Simon, J.I., DePaolo, D.J., Moynier, F., 2009. Calcium isotope composition of meteorites, Earth, and Mars. Astrophys. J. 702, 707-715.

Skulan, J., DePaolo, D.J., Owens, T.L., 1997. Biological control of calcium isotopic abundances in the global calcium cycle. Geochim. Cosmochim. Acta 61, 2505-2510.

Soret, C., 1879. Sur l'etat d'equilibre que prend au point de vue de sa concentration une dissolution saline primitivement homohene dont deux parties sont portees a` des temperatures differentes. Arch. Sci. Phys. Nat. 2, 48-61.

Sossi, P.A., O'Neill, H.S.C., 2017. The effect of bonding environment on iron isotope fractionation between minerals at high temperature. Geochim. Cosmochim. Acta 196, 121-143.

Sparks, R.S.J., Brooker, R.A., Field, M., Kavanagh, J., Schumacher, J.C., Walter, M.J., White, J., 2009. The nature of erupting kimberlite melts. Lithos 112, 429-438.

Streckeisen, A., 1980. Classification and nomenclature of volcanic rocks, lamprophyres, carbonatites and melilitic rocks. IUGS Subcomission on the Systematics of Igneous Rocks. Geol. Rundsch. 69, 194-207.

Sun, N., Stixrude, L., de Koker, N., Karki, B.B., 2011. First principles molecular dynamics simulations of diopside ($CaMgSi_2O_6$) liquid to high pressure. Geochim. Cosmochim. Acta 75, 3792-3802.

Sweeney, R.J., 1994. Carbonatite melt compositions in the Earth's mantle. Earth Planet. Sci. Lett. 128, 259-270.

Symons, D.T.A., 1989. Paleomagnetism of the 1.1 Ga Lackner Lake Complex and tectonics of the Kapuskasing Structural Zone. Can. J. Earth Sci. 26, 1778-1783.

Taylor, H. P., Freebees, J., Degens, E. T., 1967. Oxygen and carbon isotope studies of carbonatites from the Laacher See district, West Germany, and Alno district, Sweden. Geochim. Cosmochim. Acta 31, 407-430.

Tera, F., Eugster, O., Burnett, D.S., Wasserburg, G.J., 1970. Comparative study of Li, Na, K, Rb, Cs, Ca, Sr and Ba abundances in achondrites and in Apollo 11 lunar samples. Proceedings of the Apollo 11 Lunar Science Conference, Vol. 2, pp. 1637-1657.

Thompson, G.A., Robinson, R., 1975. Gravity and magnetic investigation of the Twin Sisters dunite, Northern Washington. Geol. Soc. Am. Bull. 86, 1413-1422.

Treiman, A.H., Essene, E.J., 1985. The Oka carbonatite complex, Québec: geology and evidence for silicate-carbonate liquid immiscibility. Am. Mineral. 70, 1101-1113.

Ulmer, P., Sweeney, R.J., 2002. Generation and differentiation of group II kimberlites: Constraints from a high-pressure experimental study to 10 GPa. Geochim. Cosmochim. Acta 66, 2139-2153.

Urey, H.C., 1947. The thermodynamic properties of isotopic substances. J. Chem. Soc. 562-581.

Valdes, M.C., Moreira, M., Foriel, J., Moynier, F., 2014. The nature of Earth's building blocks as revealed by calcium isotopes. Earth Planet. Sci. Lett. 394, 135-145.

van Keken, P.E., Kiefer, B., Peacock, S.M., 2002. High-resolution models of subduction zones: implications for mineral dehydration reactions and the transport of water into the deep mantle. Geochem. Geophys. Geosyst. 3, 1056.

Veizer, J., Bell, K., Jansen, S.L., 1992. Temporal distribution of carbonatites. Geology 20, 1147-1149.

Wallace, M.E., Green, D.H., 1988. An experimental determination of primary carbonatite magma composition. Nature 335, 343-346.

White, B.S., Wyllie, P.J., 1992. Solidus reactions in synthetic lherzolite-H2O-CO2 from 20-30 kbar, with applications to melting and metasomatism. J. Volcanol. Geotherm.I. Res. 50, 117-130.

Williams, W.J.W., 1999. Evolution of quaternary intraplate mafic lavas from the Potrillo volcanic field, USA, and the San Quintin volcanic field, Mexico. Univ Texas El Paso. Unpub. PhD dissertation, p 186.

Wilson, S.A., 1997. The collection, preparation and testing of USGS reference material BCR-2, Columbia River, Basalt, U.S. Geological Survey Open-File Report 98-00x.

Withers, A.C., Hirschman, M.M., Tenner, T.J., 2011. The effect of Fe on olivine H_2O storage capacity: Consequences for H_2O in the martian mantle. Am. Mineral. 96, 1039-1053.

Wolf, J.A., 1994. Physical properties of carbonatite magmas inferred from molten salt data, and application to extraction patterns from carbonatite-silicate magma chambers. Geol. Mag. 131, 145-153.

Wombacher, F., Eisenhauer, A., Heuser, A., Weyer, S., 2009. Separation of Mg, Ca and Fe from geological reference materials for stable isotope ratio analyses by MC-ICP-MS and double-spike TIMS. J. Anal. At. Spectrom. 24, 627-636.

Woolley, A.R., Bailey, D.K., 2012. The crucial role of lithospheric structure in the generation and release of carbonatites: geological evidence. Mineral. Mag. 76, 259-270.

Woolley, A.R., Kempe, D.R.C., 1989. Carbonatites: Nomenclature, average chemical compositions and element distribution. In: Bell, K. (Ed.), Carbonatites: Genesis and Evolution. Unwin Hyman, London, pp. 1-14.

Woolley, A.R., Kjarsgaard, B.A., 2008. Carbonatite occurrences of the world: map and database. Geological Survey of Canada Open File # 5796, 28 p.

Wu, F-Y., Yang, Y-H., Li, Q-L., Mitchell, R.H., Dawson, J.B., Brandl, G., Yuhara, M., 2011. In situ determination of U-Pb ages and Sr-Nd-Hf isotopic constraints on the petrogenesis of the Phalaborwa carbonatite Complex, South Africa. Lithos 127, 309-322.

Wyllie, P.J., Huang, W.L., 1975a. In fluence of mantle CO2 in the generation of carbonatites and kimberlites. Nature 257, 297-299.

Wyllie, P.J., Huang, W.L., 1975b. Peridotite, kimberlite, and carbonatite explained in the system CaO-MgO-SiO2-CO2. Geology 3, 621-624.

Wyllie, P.J., Huang, W.L., 1976a. Carbonation and melting reactions in the system CaO-MgO-SiO2-CO2 at mantle pressures with geophysical and petrological applications. Contrib. Mineral. Petrol. 54, 79-107.

Wyllie, P.J., Huang, W.L., 1976b. High CO2 solubilities in mantle magmas. Geology 4, 21-24.

Yaxley, G.M., Brey, G.P., 2004. Phase relations of carbonate-bearing eclogite assemblages from 2.5 to 5.5 GPa: implications for petrogenesis of carbonatites. Contrib. Mineral. Petrol. 146, 606-619.

Yaxley, G.M., Green, D.H., 1994. Experimental demonstration of refractory carbonate-bearing eclogite and siliceous melt in the subduction regime. Earth Planet. Sci. Lett. 128, 313-325.

Ying, J., Zhou, X., Zhang, H., 2004. Geochemical and isotopic investigation of the Laiwu–Zibo carbonatites from western Shandong Province, China, and implications for their petrogenesis and enriched mantle source. Lithos 75, 413-426.

Young, E.D., Manning, C.E., Schauble, E.A., Shahar, A., Macris, C.A., Lazar, C., Jordan, M., 2015. High-temperature equilibrium isotope fractionation of non-traditional stable isotopes: Experiments, theory, and applications. Chem. Geol. 395, 176-195.

Xirouchakis, D., Hirschmann, M.M., Simpson, J.A., 2001. The effect of titanium on the silica content and on mineral-liquid partitioning of mantle-equilibrated melts. Geochim. Cosmochim. Acta 65, 2201-2217.

Zhao, D., 2007. Seismic images under 60 hotspots: search for mantle plumes. Gondwana Res. 12, 335-355.

Zhao, X., Zhang, Z., Huang, S., Liu, Y., Li, X., Zhang, H., 2017. Coupled extremely light Ca and Fe isotopes in peridotites. Geochim. Cosmochim. Acta 208, 368-380.

Zindler, A., Hart, S.R., 1986. Chemical geodynamics. Ann. Rev. Earth Planet. Sci. 14, 493-571.

Zurevinski, S.E., Mitchell, R.H., 2004. Extreme compositional variation of pyrochlore-group minerals at the Oka carbonatite complex, Quebec: evidence of magma mixing? Can. Mineral. 42, 1159-1168.

Appendix A

Category	Group	Sample	$\delta^{44/40}$Ca	2se	Reference
Carbonaceous Chondrites	CM2	Murchison	+0.84	0.05	Valdes et al., 2014
	CM2	Murray	+0.75	0.07	Valdes et al., 2014
	CM2	Murchison	+0.60	0.04	Simon and DePaolo, 2010
	CM2	Murchison	+0.72	0.04	Huang and Jacobsen, 2017
	CM	PCA 02012	+0.55	0.19	Amsellem et al., 2017
	CM2	Cold Bokkeveld	+0.36	0.13	Amsellem et al., 2017
	CM	PCA 02010	+0.77	0.12	Amsellem et al., 2017
	CM2	Murchison	+0.59	0.09	Wombacher et al., 2009
	CV3	Allende	+0.55	0.10	Valdes et al., 2014
	CV3	Vigarano	+0.33	0.18	Valdes et al., 2014
	CV3	Allende	+0.49	0.05	Simon and DePaolo, 2010
	CV3	Allende	+0.28	0.05	Huang and Jacobsen, 2017
	CV3	Allende	+0.26	0.07	Amsellem et al., 2017
	CV3	Allende replicate	+0.10	0.05	Amsellem et al., 2017
	CV3	Allende replicate	+0.44	0.08	Amsellem et al., 2017
	CO3.3	Felix	+1.19	0.13	Valdes et al., 2014
	CO3.4	Ornans	+0.76	0.03	Valdes et al., 2014
	CO3.5	Lance	+0.95	0.08	Valdes et al., 2014
	CO3.8	Isna	+0.99	0.04	Valdes et al., 2014
	CR2	RBT 04133	+0.27	0.04	Valdes et al., 2014
	CR2	Asuka 881595	+0.47	0.10	Amsellem et al., 2017
	CI	Orgueil	+0.65	0.05	Valdes et al., 2014
	CI1	Orgueil	+0.75	0.08	Huang and Jacobsen, 2017
	CI1	Orgueil	+0.45	0.04	Amsellem et al., 2017
	CI1	Yamato 980115	+0.93	0.02	Amsellem et al., 2017
Ordinary Chondrites	LL4	Soko-Banja	+0.95	0.10	Valdes et al., 2014
	LL5	Olivenza	+0.97	0.16	Valdes et al., 2014
	LL6	Cherokee Springs	+0.96	0.08	Valdes et al., 2014
	LL5	Paragould	+0.92	0.05	Simon and DePaolo, 2010
	L6	Bruderheim	+0.96	0.03	Simon and DePaolo, 2010
	LL6	St. Severin	+0.98	0.04	Simon and DePaolo, 2010
	O, L6	Bruderham	+0.98	0.07	Huang and Jacobsen, 2017
	O, L6	Peace River	+0.83	0.11	Huang and Jacobsen, 2017
	O, H6	Guarena	+0.91	0.03	Huang and Jacobsen, 2017
	O, H3	Grady (1937)	+0.92	0.04	Huang and Jacobsen, 2017
Enstatite Chondrites	EH3	Qingzhen	+0.99	0.07	Valdes et al., 2014
	EH3	Kota-Kota	+1.01	0.01	Valdes et al., 2014

	EH4	Abee	+0.98	0.02	Valdes et al., 2014
	EH4	Indarch	+0.95	0.03	Valdes et al., 2014
	EH5	St. Marks	+0.90	0.09	Valdes et al., 2014
	EH3	Indarch	+1.13	0.04	Simon and DePaolo, 2010
	EH3	Sahara 97096	+1.18	0.04	Simon and DePaolo, 2010
	EH3	Qingzhen	+1.16	0.05	Simon and DePaolo, 2010
	EH4	Abee	+1.25	0.05	Simon and DePaolo, 2010
	EH3	KLE 98300	+1.29	0.05	Simon and DePaolo, 2010
	EL3	MAC 88136	+1.48	0.05	Simon and DePaolo, 2010
	EH	Abee	+0.90	0.02	Huang and Jacobsen, 2017
	EH	Indarch	+0.96	0.02	Huang and Jacobsen, 2017
	EH6	Indarch	+1.06	0.15	Amsellem et al., 2017
	EL6	Khairpur	+0.91	0.03	Amsellem et al., 2017
Achondrites	Aubrite	Khor Temiki	+0.88	0.03	Valdes et al., 2014
	Aubrite	Norton County 1	+1.08	0.05	Valdes et al., 2014
	Aubrite	Norton County 2	+0.88	0.05	Valdes et al., 2014
	Aubrite	Cumberland Falls	+0.96	0.05	Valdes et al., 2014
	Aubrite	Bustee	+0.96	0.06	Valdes et al., 2014
	Angrite	Angra dos Reis	+0.88	0.05	Simon and DePaolo, 2010
	Diogenite	Bilanga	+0.95	0.05	Simon and DePaolo, 2010
	Eucrite	Juvinas	+0.89	0.04	Simon and DePaolo, 2010
	Aubrite	Norton County	+1.01	0.07	Simon and DePaolo, 2010
Lunar, Apollo samples	Ilmenite basalt	10057	+0.81	0.09	Valdes et al., 2014
	Olivine basalt	12012	+1.05	0.04	Valdes et al., 2014
	Basalt	14053	+0.76	0.06	Valdes et al., 2014
	Basalt	15016	+0.91	0.05	Valdes et al., 2014
	Green glass	15426	+0.88	0.08	Valdes et al., 2014
	Basalt	10017	+0.87	0.04	Simon and DePaolo, 2010
	Green glass	15427	+1.09	0.04	Simon and DePaolo, 2010
	Green glass	15427	+1.04	0.04	Simon and DePaolo, 2010
Martian	Orthopyroxenite	ALH 84001	+1.01	0.05	Simon and DePaolo, 2010
	Shergottite	Zagami	+0.97	0.05	Simon and DePaolo, 2010
	Enriched shergottites	LAR 06319	+0.93	0.14	Magna et al., 2015
		Los Angeles 001	+0.99	0.02	
		NWA 856	+0.91	0.06	
		NWA 1068	+0.90	0.02	
		RBT 04262	+0.90	0.07	
		Shergotty	+1.14	0.10	
		Zagami	+0.71	0.01	
		ALHA 77005	+1.05	0.01	

	Intermediate shergottites	EETA 79001A	+1.05	0.03	
		Y-000097	+0.98	0.07	
	Depleted shergottites	NWA 5990	+0.95	0.04	
		NWA 6162	+0.90	0.01	
		SaU 005	+0.80	0.06	
		Y-980459	+1.08	0.05	
	Nakhlites	Lafayette	+0.94	0.07	
		MIL 03346	+0.89	0.04	
		Nakhla	+0.81	0.01	
		NWA 817	+0.79	0.07	
		NWA 5790	+0.82	0.04	
		Y-000593	+1.04	0.05	
	Chassignites	Chassigny	+1.06	0.10	
		NWA 2737	+0.74	0.07	
	Orthopyroxenite	ALH 84001	+1.06	0.07	
Allende Chondrules	CV3	EA1	+1.12	0.10	Amsellem et al., 2017
	CV3	EA2	+1.12	0.06	
	CV3	EA3	+1.16	-	
	CV3	EA4	+1.21	0.12	
	CV3	EA5	+1.11	0.08	
	CV3	EA6	+1.00	0.15	
	CV3	EA7	+1.01	0.15	

Appendix B

Category	Sample	$\delta^{44/40}$Ca	2se	Reference
	BHVO-2	+0.83	0.07	Amini et al., 2009
	BHVO-2	+0.87	0.03	Valdes et al., 2014
	BHVO-2	+0.80	0.03	Kang et al., 2017
	BHVO-2	+0.90	0.05	Magna et al., 2015
	BHVO-2	+0.79	0.08	Schiller et al., 2012
	BHVO-2	+0.77	0.10	Feng et al., 2017
	BHVO-1	+0.96	0.05	Huang et al., 2011
	BHVO-1	+0.87	0.06	Schiller et al., 2012
	BHVO-1	+0.77	0.10	Feng et al., 2017
	BHVO-1	+0.78	0.08	Lehn and Jacobson, 2015
	Kilauea BHVO-1	+1.00	0.12	Huang et al., 2010
	BHVO	+0.80	0.05	Amsellem et al., 2017
	BIR-1	+0.77	0.09	Amini et al., 2009
	BIR-1	+0.89	0.04	Valdes et al., 2014
	BIR-1	+0.84	0.03	Kang et al., 2017
	BIR-1	+0.79	0.06	Schiller et al., 2012
	BIR-1	+0.79	0.12	Feng et al., 2017
	BIR-1	+0.82	0.20	Wombacher et al., 2009
Basalts	BCR-2	+0.87	0.06	Amini et al., 2009
	BCR-2	+0.87	0.18	Valdes et al., 2014
	BCR-2	+0.82	0.03	Kang et al., 2017
	BCR-2	+0.87	0.08	Schiller et al., 2012
	BCR-2	+0.92	0.40	Wombacher et al., 2009
	BCR-2	+0.79	0.12	Feng et al., 2017
	BCR-2	+0.91	0.04	Amsellem et al., 2017
	BCR	+0.82	0.05	Colla et al., 2013
	BCR-1	+0.82	0.05	Simon and DePaolo, 2010
	DNC-1	+0.79	0.06	Schiller et al., 2012
	DNC-1	+0.82	0.08	Feng et al., 2017
	Mauna Kea SR 687	+0.89	0.13	Huang et al., 2010
	Mauna Kea SR 700	+0.94	0.06	Huang et al., 2010
	SR700	+0.94	0.05	Huang et al., 2011
	Mauna Kea SR 685	+0.97	0.13	Huang et al., 2010
	SR685	+0.92	0.08	Huang et al., 2011
	Mahukona 72-1	+1.03	0.13	Huang et al., 2010
	72-1	+1.02	0.04	Huang et al., 2011
	Mahukona 72-5	+0.91	0.13	Huang et al., 2010

	Oslo Rift Nephelinites			
	S36/S01	+1.06	0.13	Huang et al., 2010
	KL2-G	+0.70	0.07	Amini et al., 2009
	KL2	+0.76	0.07	Amini et al., 2009
	ML3B-G	+0.72	0.05	Amini et al., 2009
	ML3B	+0.62	0.06	Amini et al., 2009
	SRM688	+0.86	0.05	Valdes et al., 2014
	151-09-9	+0.85	0.09	Valdes et al., 2014
	KBD 408-702	+1.05	0.11	Valdes et al., 2014
	CV-SN98-01	+0.81	0.10	Valdes et al., 2014
	BM1962 128 (114)	+0.81	0.09	Valdes et al., 2014
	BV2	+0.93	0.13	Valdes et al., 2014
	BM1911 1626 (11)	+0.89	0.03	Valdes et al., 2014
	SH 25	+0.90	0.08	Valdes et al., 2014
	Eruption 1931	+0.87	0.04	Valdes et al., 2014
	AG 132	+1.07	0.11	Valdes et al., 2014
	AG 36	+1.06	0.02	Valdes et al., 2014
	MO50 CP112	+0.96	0.05	Valdes et al., 2014
	NIC-SC2	+1.02	0.04	Simon and DePaolo, 2010
	Average host basalts	+0.63	0.06	Zhao et al., 2017
	KOO-1	+0.75	0.03	Huang et al., 2011
	KOO-7	+0.76	0.02	Huang et al., 2011
	KOO-10	+0.75	0.05	Huang et al., 2011
	KM-1	+0.77	0.03	Huang et al., 2011
	KSDP-9	+0.92	0.06	Huang et al., 2011
	KSDP-71	+0.83	0.06	Huang et al., 2011
	D19-9	+0.90	0.05	Huang et al., 2011
	BE-N	+0.69	0.25	Wombacher et al., 2009
	9149	+0.80	0.04	Jacobson et al., 2015
	22038	+0.81	0.04	Jacobson et al., 2015
	9297	+0.80	0.04	Jacobson et al., 2015
	9265	+0.79	0.04	Jacobson et al., 2015
	709	+0.82	0.04	Jacobson et al., 2015
	4685	+0.79	0.04	Jacobson et al., 2015
	W-2	+0.70	0.08	Feng et al., 2017
	HSDP-R452	+1.04	0.12	Skulan et al., 1997
	HSDP-R160	+1.54	0.25	Skulan et al., 1997
	IO-14	+1.04	0.19	Skulan et al., 1997
	IO-38	+0.97	0.10	Skulan et al., 1997
	D54G	+0.87	0.07	DePaolo, 2004

	KOO-10	+1.03	0.22	DePaolo, 2004
	KOO-21	+1.10	0.19	DePaolo, 2004
	KOO-55	+1.11	0.14	DePaolo, 2004
	GUG-6	+1.41	0.22	DePaolo, 2004
	ALV-1833	+1.03	0.23	DePaolo, 2004
	HK-02	+1.04	0.26	DePaolo, 2004
	HU-24	+0.88	0.23	DePaolo, 2004
	HK-11	+0.83	0.27	DePaolo, 2004
	HU-05	+1.34	0.16	DePaolo, 2004
	HSDP 452	+1.04	0.12	DePaolo, 2004
	HSDP 160	+1.54	0.25	DePaolo, 2004
	IO-14	+1.04	0.19	DePaolo, 2004
	IO-38	+0.97	0.10	DePaolo, 2004
	SUNY MORB	+0.98	0.03	DePaolo, 2004
	SUNY MORB	+0.93	0.12	DePaolo, 2004
	EH12	+0.88	0.11	Amsellem et al., 2017
	EH12 replicate	+0.88	0.04	Amsellem et al., 2017
	EH12 replicate	+0.83	0.05	Amsellem et al., 2017
	EH15	+0.80	0.02	Amsellem et al., 2017
	EW 9309 10D	+0.86	0.09	Amsellem et al., 2017
Felsic Rocks	ATHO-G	+0.87	0.08	Amini et al., 2009
	Tsm-2G	+0.84	0.05	Simon and DePaolo, 2010
	RGM-1	+0.89	0.03	Feng et al., 2017
	RGM-2	+0.80	0.13	Feng et al., 2017
	92DLV-113	+1.29	0.20	Skulan et al., 1997
	92DLV-113	+1.11	0.20	DePaolo, 2004
	Lake Co. Obsidian	+0.97	0.05	DePaolo, 2004
	StHs6/80-G	+0.75	0.05	Amini et al., 2009
	StHs6/80	+0.77	0.11	Amini et al., 2009
	AGV-2	+0.77	0.10	Valdes et al., 2014
	AGV	+0.53	0.05	Colla et al., 2013
	AGV-2	+0.79	0.09	Feng et al., 2017
	T1-G	+0.80	0.06	Amini et al., 2009
	T1	+0.72	0.10	Amini et al., 2009
	G-2	+0.59	0.07	Valdes et al., 2014
	92-12-29	+1.05	0.22	Skulan et al., 1997
	94-02-05	+1.22	0.08	Skulan et al., 1997
	76DSH-8	+1.32	0.24	Skulan et al., 1997
	76DSH-8	+1.09	0.21	Skulan et al., 1997
	76DSH-8	+0.93	0.06	Skulan et al., 1997

	92-12-29	+1.05	0.22	DePaolo, 2004
	94-02-05	+1.22	0.24	DePaolo, 2004
	76DSH-8	+1.32	0.21	DePaolo, 2004
	76DSH-8	+1.09	0.21	DePaolo, 2004
	76DSH-8	+0.93	0.06	DePaolo, 2004
Bulk Peridotites	BM90/21-G	+1.01	0.07	Amini et al., 2009
	BM90/21	+1.01	0.09	Amini et al., 2009
	PCC-1	+1.14	0.07	Amini et al., 2009
	PCC	+1.20	0.05	Amsellem et al., 2017
	Ts-53389	+0.94	0.06	Kang et al., 2017
	S-17	+0.94	0.02	Kang et al., 2017
	313-8	+0.99	0.08	Kang et al., 2017
	S-4	+0.95	0.03	Kang et al., 2017
	313-102	+0.92	0.08	Kang et al., 2017
	stz-1	+0.93	0.02	Kang et al., 2017
	S-37	+0.93	0.02	Kang et al., 2017
	S-1	+0.92	0.08	Kang et al., 2017
	S-14	+0.96	0.06	Kang et al., 2017
	S-21	+0.92	0.06	Kang et al., 2017
	stz-2	+0.90	0.07	Kang et al., 2017
	S-15	+0.90	0.09	Kang et al., 2017
	S-2	+0.95	0.05	Kang et al., 2017
	313-104	+0.97	0.08	Kang et al., 2017
	S-16	+0.97	0.09	Kang et al., 2017
	S-22	+0.98	0.07	Kang et al., 2017
	S-62	+1.09	0.06	Kang et al., 2017
	621-16	+1.07	0.09	Kang et al., 2017
	BN-8	+1.03	0.06	Kang et al., 2017
	419/09	+0.79	0.03	Kang et al., 2017
	S-29	+0.72	0.04	Kang et al., 2017
	105/03	+0.61	0.09	Kang et al., 2017
	H-25	+0.55	0.01	Kang et al., 2017
	107/03	+0.96	0.08	Kang et al., 2017
	KC-137/08	+0.25	0.01	Kang et al., 2017
	4230-16	+0.89	0.07	Kang et al., 2017
	U85	+0.83	0.04	Kang et al., 2017
	4230-19	+0.88	0.06	Kang et al., 2017
	YY09-47	+0.86	0.13	Zhao et al., 2017
	YY11-06	+0.89	0.09	Zhao et al., 2017
	YY09-07	+0.92	0.09	Zhao et al., 2017

	YY09-05	−0.08	0.07	Zhao et al., 2017
	YY09-05	+0.09	0.14	Zhao et al., 2017
	YY09-28	+0.22	0.10	Zhao et al., 2017
	YY09-28	+0.24	0.14	Zhao et al., 2017
	YY09-24	+0.58	0.09	Zhao et al., 2017
	YY09-18	+0.66	0.06	Zhao et al., 2017
	YY09-27	+0.70	0.09	Zhao et al., 2017
	JP-1	+1.15	0.03	Magna et al., 2015
	LZ0604B	+1.08	0.06	Amsellem et al., 2017
	LZ0604B replicate	+1.17	0.11	Amsellem et al., 2017
Clinopyroxenes	San Carlos Cpx	+1.04	0.04	Huang et al., 2010
	Kilbourne Hole Cpx	+0.98	0.04	Huang et al., 2010
	P-1	+0.77	0.03	Kang et al., 2016
	P-9	+0.71	0.06	Kang et al., 2016
	P-10	+0.96	0.04	Kang et al., 2016
	P-15	+0.91	0.04	Kang et al., 2016
	H-3	+0.82	0.03	Kang et al., 2016
	H-16	+0.92	0.05	Kang et al., 2016
	LHLS-4	+0.94	0.12	Kang et al., 2016
	LHLS-6	+1.03	0.12	Kang et al., 2016
	LHLS-10	+0.83	0.12	Kang et al., 2016
	89CN	+0.96	0.05	Simon and DePaolo, 2010
	90DH	+0.97	0.07	Simon and DePaolo, 2010
	YY09-47	+0.86	0.12	Zhao et al., 2017
	YY11-06	+0.88	0.06	Zhao et al., 2017
	YY09-07	+0.92	0.03	Zhao et al., 2017
	YY09-05	−0.09	0.07	Zhao et al., 2017
	YY09-28	+0.25	0.07	Zhao et al., 2017
	YY09-24	+0.58	0.07	Zhao et al., 2017
	YY09-18	+0.67	0.05	Zhao et al., 2017
	YY09-27	+0.69	0.08	Zhao et al., 2017
Orthopyroxenes	San Carlos Opx	+1.40	0.07	Huang et al., 2010
	Kilbourne Hole Opx	+1.73	0.09	Huang et al., 2010
	P-1	+1.77	0.01	Kang et al., 2016
	P-9	+1.82	0.01	Kang et al., 2016
	P-10	+0.95	0.05	Kang et al., 2016
	P-15	+1.12	0.09	Kang et al., 2016
	H-3	+1.44	0.10	Kang et al., 2016
	H-16	+1.05	0.05	Kang et al., 2016
	LHLS-4	+1.34	0.12	Kang et al., 2016

	LHLS-6	+1.31	0.12	Kang et al., 2016
	LHLS-10	+1.21	0.12	Kang et al., 2016
	YY09-47	+0.90	0.04	Zhao et al., 2017
	YY11-06	+1.01	0.06	Zhao et al., 2017
	YY09-07	+0.88	0.09	Zhao et al., 2017
	YY09-05	+0.22	0.02	Zhao et al., 2017
	YY09-28	−0.24	0.06	Zhao et al., 2017
	YY09-24	+0.44	0.06	Zhao et al., 2017
	YY09-18	+0.59	0.03	Zhao et al., 2017
	YY09-27	+0.70	0.06	Zhao et al., 2017
Olivine	P-15	+1.16	0.08	Kang et al., 2016
Dunites	DTS-1	+1.59	0.09	Huang et al., 2010
	DTS-1	+1.49	0.06	Amini et al., 2009
	DTS-1	+1.51	0.13	Feng et al., 2017
	DTS-2	+1.20	0.11	Feng et al., 2017
Calcites	500 (spar)	+1.14	0.04	Jacobson et al., 2015
	6917 (spar)	+0.91	0.04	Jacobson et al., 2015
	7906 (spar)	+1.10	0.04	Jacobson et al., 2015
	10303 (spar)	+0.98	0.04	Jacobson et al., 2015
	11622 (spar)	+1.22	0.04	Jacobson et al., 2015
	15239 (spar)	+1.24	0.04	Jacobson et al., 2015
	NI 4320	+1.17	0.04	Jacobson et al., 2015
	NI 4525	+0.92	0.04	Jacobson et al., 2015
	NI 1582	+1.27	0.04	Jacobson et al., 2015
	NI 10784	+1.06	0.04	Jacobson et al., 2015
	Bulandstindur	+1.08	0.04	Jacobson et al., 2015
	NI 14632 (spar)	+0.85	0.04	Jacobson et al., 2015
	NI 14231	+1.18	0.04	Jacobson et al., 2015
	B9435	+0.68	0.04	Jacobson et al., 2015
	Sturlugata	+0.77	0.04	Jacobson et al., 2015
Bulk Carbonatites	SARM 40	+0.87	0.04	Schiller et al., 2012
	COQ-1	+0.71	0.11	Feng et al., 2017
Carbonatites Silicate Phase	82LM66A	+0.87	0.02	Amini et al., 2009
	83HV26	+0.69	0.04	Amini et al., 2009
Carbonatites Carbonate Phase	82LM66A	+0.67	0.05	Amini et al., 2009
	83HV26	+0.74	0.04	Amini et al., 2009

Curriculum Vitae

Name: Matthew Maloney

Post-secondary Education and Degrees:

University of Toronto
Toronto, Ontario, Canada
2006-2011 B.A. Honours (English)

The University of Toronto
Toronto, Ontario, Canada
2013-2015 B.Sc. Honours with Distinction (Geoscience & Biology)

The University of Western Ontario
London, Ontario, Canada
2015-2018 M.Sc. (candidate) Geology & Planetary Science

Honours and Awards:

Dean's List
University of Toronto
2013-2014 and 2014-2015

Related Work Experience

Teaching Assistant
The University of Western Ontario
2015-2017

Publications:

Maloney, M., Withers, A.C., Bouvier, A., Georg, R.B. (2017) *Experimental Constraints on Calcium Isotopic Fractionation in Carbonated Melts,* Poster presented at the Centre for Planetary Science and Exploration (CPSX) Space Day, April 6, 2017.

Maloney, M., Withers, A.C., Bouvier, A., Georg, R.B. (2017) *Experimental Constraints on Calcium Isotopic Fractionation in Carbonated Melts,* Oral Presentation given at the 16th Advances in Earth Sciences Research Conference (AESRC) March 31-April 2, 2017.

Svensson, M.J.O., Maloney, M., Duff, S., Osinski, G.R. (2017) *Laser Induced Breakdown Spectroscopy (LIBS) as a Simulated Stand-Off Geochemical Analysis Instrument in the CanMars 2016 MSR Analogue Mission,* Poster presented at the Lunar and Planetary Science Conference, March 20-24, 2017.

Mittelholz, A., Maloney, M., Osinski, G.R. (2016) *The Use of Raman Spectroscopy for the 2015 CanMars MSR Analogue Mission,* Poster presented at the 47th Lunar and Planetary Science Conference, March 21-25, 2016.